THE UNIVERSITY *of* EDINBURGH

This thesis has been submitted in fulfilment of the requirements for a postgraduate degree (e.g. PhD, MPhil, DClinPsychol) at the University of Edinburgh. Please note the following terms and conditions of use:

This work is protected by copyright and other intellectual property rights, which are retained by the thesis author, unless otherwise stated.
A copy can be downloaded for personal non-commercial research or study, without prior permission or charge.
This thesis cannot be reproduced or quoted extensively from without first obtaining permission in writing from the author.
The content must not be changed in any way or sold commercially in any format or medium without the formal permission of the author.
When referring to this work, full bibliographic details including the author, title, awarding institution and date of the thesis must be given.

CARDIOVASCULAR MAGNETIC RESONANCE AND POSITRON EMISSION TOMOGRAPHY IN THE ASSESSMENT OF AORTIC STENOSIS.

Jacek Kwiecinski

MD, MSc

Thesis presented for the degree of Doctor of Philosophy at

the University of Edinburgh

2019

To Szubi, Ziomik and Ziomi

Table of Contents

List of Tables

List of Figures

Declaration

This thesis represents the research I performed at the Centre for Cardiovascular Sciences, Clinical Research Imaging Centre, and the Cedars Sinai Medical Center between September 2015 and October 2018.

I was personally involved in every aspect of the work as reported herein. However, in keeping with the collaborative nature of such studies, I received and acknowledge help from other sources. Data for chapters 3,5 was collected by Dr Calvin Chin by summer 2015. I was involved in recruitment for this study during my master's in medical science by research studies (September 2014 to August 2015). For chapter 5 I analyzed all the data of the Edinburgh cohort and drafted the manuscript together with Dr Lionel Tastet. For chapter 4 I was personally responsible for managing the animals, mini pump preparation, imaging and data analysis. Surgical mini pump implantation was performed by Gary Borthwick and magnetic resonance imaging was supervised by Dr Maurits Jansen and Dr Ross Lennen.

Chapters 6 and 7 have been drafted by me under the supervision of Dr Piotr Slomka and Dr Daniel Berman during the 3rd year of my PhD which I spent in California. I recruited patients who underwent imaging at Cedars Sinai Medical Center and analyzed all the relevant data including imaging performed at Severance Hospital (Yonsei University) by Dr Mijin Yun and the University of Edinburgh by Dr Philip Adamson.

Chapters 1, 3, 6 and 7 have all been published and chapters 4 and 5 are under review for publication in peer-reviewed medical journals. I was the first author for chapters 3, 4, 6 and 7, and first co-authors for chapters 1 and 5. This thesis has not been accepted in any previous applications for a degree and all sources of information have been acknowledged. The research was undertaken in accordance with the Declaration of Helsinki, all procedures conformed to Home Office guidance on the

use of the animals (Scientific Procedures) Act of 1986 and were approved by the South East Scotland Ethics Committee, the University of Edinburgh Animal Welfare and Ethical Review Board. This thesis has not been submitted for any other degree or professional qualification.

Acknowledgements

This thesis has been conducted under the primary supervision of Dr Maurits Jansen and Dr Marc Dweck. This body of work would not have been possible without their vision and personal dedication. Their mentorship has been invaluable and has played a major role in my academic achievements. The preclinical study would not be possible without the guidance of Dr Gillian Gray. Likewise, in the clinical aortic stenosis projects Dr Calvin Chin and Dr Russel Everett played a key role. Throughout my studies I was fortunate to meet researchers who were always keen to share their expertise. Dr Mike Millar and Lyndsey Boswell from Immunodetection and Histological Imaging at the Centre for Reproductive Health have provided me with expert know-how and guided me through the perils of biopsy samples processing and analysis. Dr Calum Gray and Dr Giorgos Papanastasiou from the Clinical Research Imaging Centre have been pivotal in facilitating image analysis of the acquired data.

Over the course of my research I have had the opportunity to work closely as part of an international collaboration and would like to use this opportunity to acknowledge the help, support and friendship I experienced. It was a pleasure to collaborate with Dr Marie-Annick Clavel and Lionel Tastet from the University Laval, Quebec City, Canada. During the 3rd year of my studies I had the unique privilege to become a member of the Cardiac Imaging Research Team at Cedars Sinai Medical Center, Los Angeles, California. Dr Daniel Berman, Dr Piotr Slomka and Dr Damini Dey have created a wonderful environment for research excellence. Thanks to them the 10 months spent in California have been incredibly productive. I look forward to working with them in the future.

None of this would be however possible if it was not for the generosity of the Polish School of Medicine Memorial Fund which in 2014/15 supported my master's degree at the University of Edinburgh and then magnanimously enabled me to continue my studies at the University of Edinburgh as a PhD student. Additionally the manager of

the fund Dr Maria Dlugolecka Graham has provided a wealth of opportunities to discover the incredible legacy of the Polish-Scottish relationships. Thanks to her dedication, hard work and positive attitude the 4 years I spent in Edinburgh have proved to be much more than just an incredible scientific experience.

I would like to thank my family for their invaluable support over the years I dedicated to research. My parents have played a key role in shaping my thinking as well as my career, and I struggle to find the words to express my gratitude towards them. Finally, I would like to thank my wife Agnieszka and my daughter Ania for their unconditional love, willingness to travel over the Atlantic and continuous encouragement, without them this accomplishment would not be possible.

Abstract

Background

Aortic stenosis is not only characterized by progressive valve narrowing but also by the hypertrophic response of the left ventricle that ensues. In this most common valvular condition novel imaging approaches (cardiovascular magnetic resonance [CMR] and positron emission tomography [PET]) have shown promise in the assessment of disease progression and risk stratification. The central aim of this thesis was to investigate the potential of CMR imaging to refine risk prediction and to improve the imaging protocol of ^{18}F-sodium fluoride PET for aortic stenosis.

Methods and Results

Asymmetric wall thickening in aortic stenosis

In a prospective observational cohort study, 166 patients with aortic stenosis (age 69, 69% males, mean aortic valve area 1.0±0.4cm2) and 37 age and sex-matched healthy volunteers underwent phenotypic characterisation with comprehensive clinical, imaging and biomarker evaluation. Asymmetric wall thickening on both echocardiography and cardiovascular magnetic resonance was defined as regional wall thickening ≥13 mm and >1.5-fold the thickness of the opposing myocardial segment.

Asymmetric wall thickening was observed in 26% (n=43) of patients with aortic stenosis using magnetic resonance and 17% (n=29) using echocardiography. Despite similar demographics, co-morbidities, valve narrowing, myocardial hypertrophy and fibrosis, patients with asymmetric wall thickening had increased cardiac troponin I and brain natriuretic peptide concentrations (both p<0.001). Over 28 [22, 33] months of follow-up, asymmetric wall thickening was an independent predictor of aortic valve

replacement or death whether detected by magnetic resonance (HR=2.15; 95 CI 1.29 to 3.59; p=0.003) or echocardiography (HR=1.79; 95 CI 1.08 to 3.69; p=0.021).

Animal model of pressure overload

We performed serial Cardiac Magnetic Resonance (CMR) imaging every 2-week in 31 mice subjected to pressure overload (continuous angiotensin II infusion) for 6 weeks and investigated reverse remodelling by repeating CMR 1 month following normalization of afterload (n=9). Cine CMR was used to measure left ventricular volumes, mass, and systolic function whilst myocardial fibrosis was assessed using indexed ECV (iECV) calculated from T1-relaxation times acquired with a small animal modified look-locker inversion recovery sequence.

During the initial phase of increased pressure afterload indices of left ventricular hypertrophy (0.091 [0.083, 0.105] vs 0.123 [0.111, 0.138] g) and myocardial fibrosis (iECV: 0.022 [0.019, 0.024] vs 0.022 [0.019, 0.024] mL) increased in line with blood pressure measurements (65.1±12.0 vs 84.7±9.2 mmHg) whilst left ventricular ejection fraction (LVEF, 59.3 [57.6, 59.9] vs 46.9 [38.5, 49.6] %) deteriorated significantly (all $p \leq 0.01$ compared to baseline).

During the reverse remodelling phase blood pressure normalized (68.8±5.4 vs 65.1±12.0 mmHg, p=0.42 compared to baseline). Whilst LV mass (0.108 [0.098, 0.116] vs 0.091 [0.083, 0.105] g) and iECV (0.034 [0.032, 0.036] vs 0.022 [0.019, 0.024] mL) improved both remained elevated compared to baseline ($p<0.05$). Similarly, the LVEF remained impaired 51.1 [42.9, 52.8] vs 59.3 [57.6, 59.9] %, p=0.03. There was a strong association between LVEF and iECV values during pressure overload ($r=-0.88$, $p<0.001$).

Gender differences in aortic stenosis

Two hundred forty-nine patients (66±13 years, 30% women) with at least mild AS were recruited from two prospective observational cohort studies and underwent comprehensive Doppler echocardiography and CMR exams. On CMR, T1 mapping was used to quantify extracellular volume (ECV) fraction as a marker of diffuse fibrosis, and late gadolinium enhancement (LGE) was used to assess focal fibrosis.

There was no difference in age between women and men (66±15 vs 66±12 years, p=0.78). However, women presented a better cardiovascular risk profile than men with less hypertension, dyslipidemia, diabetes, and coronary artery disease (all p≤0.10). As expected, LV mass index measured by CMR was smaller in women than in men (p<0.0001). Despite fewer comorbidities, women presented larger ECV fraction [29.0 (27.4-30.6) vs. 26.8 (25.1-28.7) %, p<0.0001] and similar LGE [4.5 (2.3-7.0) vs. 2.8 (0.6-6.8) %, p=0.20] than men. In multivariable analysis, female sex remained an independent determinant of higher ECV fraction and LGE (both p≤0.05).

Prior CT angiography for PET

Forty-five patients (age 67.1±6.9 years, 76% males) underwent CTA (CTA1) and combined ^{18}F-NaF PET/CTA (CTA2) imaging within 14 [10,21] days. We fused CTA1 from visit one with ^{18}F-NaF PET from the second visit (PET) and compared visual pattern of activity, maximal standard uptake values (SUVmax) and target to background (TBR) measurements on (PET/CTA1) fused versus hybrid (PET/CTA2) data.

On PET/CTA2, 226 coronary plaques were identified. Fifty-eight coronary segments from 28 (62%) patients had high ^{18}F-NaF uptake (TBR>1.25), whilst 168 segments had lesions with ^{18}F-NaF TBR ≤1.25. Uptake in all lesions was categorized identically on co-registered PET/CTA1. There was no significant difference in ^{18}F-NaF uptake values between PET/CTA1 and PET/CTA2 (SUVmax: 1.16±0.40 vs. 1.15±0.39,

p=0.53; TBR:1.10±0.45 vs. 1.09±0.46, p=0.55). The intraclass correlation coefficient for SUVmax and TBR was 0.987 (95%CI 0.983 to 0.991) and 0.986 (95%CI 0.981 to 0.992). There was no fixed or proportional bias between PET/CTA1 and PET/CTA2 for SUVmax and TBR. Cardiac motion correction of PET scans improved reproducibility with tighter 95% limits of agreement (±0.14 for SUVmax and ±0.15 for TBR vs. ±0.20 and ±0.20 on diastolic imaging; p<0.001).

Delayed PET imaging

Twenty patients (67±7years old, 55% male) with stable coronary artery disease underwent coronary CT angiography and PET/CT both 1 h and 3 h after the injection of 266.2±13.3 MBq of ^{18}F-NaF. We compared the visual pattern of coronary uptake, maximal background (blood pool) activity, noise, standard uptake values (SUVmax), corrected SUV (cSUVmax) and target to background (TBR) measurements in lesions defined by CTA on 1h vs 3h post injection ^{18}F-NaF PET.

On 1h PET 26 CTA lesions with ^{18}F-NaF PET uptake were identified in 12 (60%) patients. On 3h PET we detected ^{18}F-NaF PET uptake in 7 lesions which were not identified on the 1h PET. The median cSUVmax and TBR values of these lesions were 0.48 [interquartile range (IQR) 0.44-0.51] and 1.45 [IQR, 1.39-1.52] compared to -0.01 [IQR, -0.03-0.001] and 0.95 [IQR, 0.90-0.98] on 1h PET, both p<0.001. Across the entire cohort 3h PET SUVmax values were similar to 1h PET measurements 1.63 [IQR, 1.37-1.98] vs. 1.55 [IQR, 1.43-1.89], p=0.30 and the background activity was lower 0.71 [IQR, 0.65-0.81] vs. 1.24 [IQR, 1.05-1.31], p<0.001. On 3h PET, the TBR values, cSUVmax and the noise were significantly higher (2.30 [IQR, 1.70-2.68] vs 1.28 [IQR, 0.98-1.56], p<0.001; 0.38 [IQR, 0.27-0.70] vs 0.90 [IQR, 0.64-1.17], p<0.001 and 0.10 [IQR, 0.09-0.12] vs. 0.07 [IQR, 0.06-0.09], p=0.02). The median cSUVmax and TBR values increased by 92% (range: 33-225%) and 80% (range: 20-177%).

Conclusions

In aortic stenosis, asymmetric wall thickening is associated with adverse prognosis, in this condition there are significant differences in the fibrosis burden between male and female patients and the adverse remodeling of the ventricle can be reproduced in a simple animal model of pressure overload. For ^{18}F-NaF PET utilizing a CT angiography acquired before the PET acquisition enables adequate uptake quantification and delayed emission scanning facilitates image analysis.

Lay Summary

Aortic stenosis is the most common heart valve condition in the western world. In this disease the aortic valve (which allows blood to exit the heart and stops blood flowing back into the heart after a contraction) through a process involving inflammation and progressive calcium formation, becomes narrowed. The progressive narrowing of the aortic valve leads to an increased strain on the heart muscle which has to work increasingly hard to pump blood through the stenotic valve. Over time the heart muscle thickens to maintain performance, but eventually the heart fails, and the valve has to be replaced.

In the past decade novel imaging approaches for diagnosing and monitoring the progression of aortic stenosis have emerged. These include cardiovascular magnetic resonance imaging which enables in depth characterization of the heart muscle and ^{18}F-sodium fluoride positron emission tomography (PET) in combination with computed tomography which holds promise in predicting the progression of valve calcifications. The overall aim of this thesis was to investigate the heart muscle response to aortic stenosis using cardiovascular magnetic resonance and improve the ^{18}F-sodium fluoride positron emission tomography imaging protocol.

Asymmetric wall thickening

In a cohort of 166 patients with aortic stenosis we evaluated the prevalence and prognostic significance of asymmetric wall thickening on echocardiography which is the most accessible tool for heart imaging and using cardiovascular magnetic resonance imaging.

Asymmetric wall thickening was observed in 26% (n=43) of patients with aortic stenosis using magnetic resonance and 17% (n=29) using echocardiography. Despite similar demographics, valve narrowing and conventional heart muscle characteristics, patients with asymmetric wall thickening had increased markers of heart strain. In

longitudinal observation of patients, asymmetric wall thickening was an independent predictor of aortic valve replacement or death whether detected by magnetic resonance or echocardiography.

Animal model of the heart muscle changes in aortic stenosis

We performed serial cardiac magnetic resonance imaging every 2-week in 31 mice subjected to a continuous infusion of a drug which raises blood pressure for 6 weeks and investigated recovery by repeating imaging 1 month following normalization of blood pressure.

During the initial phase of the experiment measures of heart muscle thickening and fibrosis increased in line with blood pressure measurements whilst the heart performance deteriorated significantly. During the recovery phase blood pressure normalized, but parameters of muscle thickening and fibrosis remained higher than at baseline. The changes in fibrosis both in the initial and the recovery phase of the experiment predicted the later changes in heart performance.

Gender differences in aortic stenosis

Two hundred forty-nine patients with aortic stenosis were recruited from two cohort studies and underwent comprehensive echocardiography and cardiovascular magnetic resonance exams. There was no difference in age between women and men. However, women presented a better cardiovascular risk profile than men with less hypertension, dyslipidemia, diabetes, and coronary artery disease. Despite a favorable risk profile, women presented with more fibrosis than men.

Prior computed tomography angiography for positron emission tomography

Forty-five patients underwent computed tomography and combined ^{18}F-sodium fluoride PET with computed tomography imaging within 2 weeks. We fused computed

tomography from visit one with ^{18}F-sodium fluoride PET from the second visit and compared visual pattern and measures of ^{18}F-sodium fluoride activity on the PET fused with computed tomography from the first visit versus single visit data.

We found no significant difference in ^{18}F-sodium fluoride activity values between the single visit and prior computed tomography datasets. Using the visit one computed tomography the generated fused datasets enabled quantification of ^{18}F-sodium fluoride PET. The reproducibility of such results is enhanced by motion correction of PET data. The proposed approach may enable a practical method for the selection of high-risk patients for ^{18}F-sodium fluoride PET scan based on results from an initial CTA scan.

Delayed PET imaging

Twenty patients underwent combined PET with computed tomography imaging 1 hour and 3 hours after injection of ^{18}F-sodium fluoride. We compared the visual pattern and measures of ^{18}F-sodium fluoride activity on 1 hour versus 3 hours after injection PET imaging.

Compared to 1-hour imaging on the 3 hours after injection scan we detected more areas of increased ^{18}F-sodium fluoride activity. The most commonly used measures of ^{18}F-sodium fluoride activity were on average 92% higher on 3 hours after tracer injection PET imaging. Likewise, the image quality improved as a result facilitating distinguishing increased PET tracer activity.

Conclusions

In summary in aortic stenosis asymmetric wall thickening is a distinct form of heart adaptation which is associated with higher risk of rapid disease progression. In aortic stenosis fibrosis as seen on magnetic resonance imaging is different between women

and men. The sequence of events which is characteristic for aortic stenosis can be reproduced in a small animal model. For ^{18}F-sodium fluoride PET utilizing a computed tomography scan from an imaging session before the PET enables accurate evaluation of tracer activity. For this imaging modality prolonging the interval between tracer injection and PET imaging facilitates image analysis.

Abbreviations

^{18}F-NaF	^{18}F-sodium fluoride
AS	Aortic stenosis
CMR	Cardiovascular magnetic resonance
CT	Computed tomography
CTA	Computed tomography angiography
ECV	Extracellular volume fraction
iECV	Indexed extracellular volume fraction
HR	Hazard ratio
ICC	Intraclass correlation coefficients
IQR	Interquartile range
LGE	Late gadolinium enhancement
LV	Left ventricle
PET	Positron emission tomography
SUV	Standard uptake value
TAVI	Transluminal aortic valve implantation
TBR	Target to background ratio

Chapter 1. Introduction

Excerpts from this chapter have been published in the review article by Lassen ML*, Kwiecinski J* and Slomka P. Gating approaches in cardiac PET imaging *PET Clinics.* 2019 (in press)

Dweck MR, Kwiecinski J. Emerging Sex Differences in Aortic Stenosis. *JACC Cardiovascular Imaging* 2019 Jan;12(1):106-108.

*Denotes equal contribution

Calcific aortic valve stenosis (AS) is the most common form of valve disease and a major health care burden (Thaden, Nkomo, & Enriquez-Sarano, 2014). This condition is characterized by progressive narrowing of the valve and while the disease originates in the valve, the development of symptoms and adverse events in aortic stenosis also relates to how the left ventricle adapts to the associated increase in afterload (Carabello Blase, 2013). Aortic stenosis triggers a hypertrophic response in the myocardium that initially restores wall stress and maintains cardiac performance, but eventually leads to decompensation, driving the transition to heart failure, symptoms and ultimately death (Dweck, Boon, & Newby, 2012; Hein et al., 2003). Interestingly, only a weak association exists between the severity of valve obstruction and the magnitude of the hypertrophic response, making it important that both processes are considered independently (M. R. Dweck, S. Joshi, et al., 2012).

1.1 Prevalence

Aortic stenosis is the most prevalent form of valve disease in developed countries, which with an ageing population, is projected to treble by 2050 (Eveborn, Schirmer, Heggelund, Lunde, & Rasmussen, 2013; Nkomo et al., 2006). In a recent meta-analysis which encompassed 7 large population-based studies, it was estimated that in the western world over 12% of those age ≥75 years have stenosed aortic valves (Osnabrugge et al., 2013). Another recent study showed that the incidence of severe AS increases with age and reaches 2–3% in patients over 65 years of age (Brian R. Lindman et al., 2016). While in the past this condition was primarily a results of rheumatic heart disease, nowadays calcific aortic stenosis occurs in elderly patients and is a prolonged degenerative process (Mitchell, Sackett, Hunzicker, & Levine, 1954).

1.2 Clinical management

Despite the widespread prevalence of aortic stenosis, we lack medical therapies capable of modifying disease progression or halting ventricular decompensation. Currently patient management consists of watchful waiting until patients with severe stenosis develop evidence of left ventricular decompensation, either in the form of symptoms or a reduction in ejection fraction(Baumgartner et al., 2017; Nishimura Rick et al., 2017). At this point, mortality rates rise rapidly and aortic valve replacement (AVR) is recommended (Ross & Braunwald, 1968). Without aortic valve replacement outcome of symptomatic AS subjects is extremely poor, with survival rates as low as 50% at 2 years and 20% at 5 years (Horstkotte & Loogen, 1988).

1.3 Natural history of Aortic Stenosis

Deterioration of the valve leaflets (cusps) was long regarded as a 'wear and tear' process which over time leads to calcium deposition. More recently this progressive degeneration has been carefully studied and as a result it is now widely appreciated that aortic stenosis is governed by a series of processes including: inflammation and deposition of lipids and calcium (M Otto, Kuusisto, D Reichenbach, Gown, & D O'Brien, 1994; Tania A. Pawade, Newby, & Dweck, 2015). The latter originate as regions of microcalficiation which co-localize with lipid deposits. These microscopic deposits are believed to promote further hydroxyapatite formation creating a positive feedback loop wherein calcification and inflammation aggravate one another(Nadra et al., 2005; Rajamannan et al., 2002; Weiss Robert, Ohashi, Miller Jordan, Young Stephen, & Heistad Donald, 2006). With foci of calcification established within the valve it appears that the disease enters a self-perpetuating cycle of injury and calcification (Mohler Emile et al., 2001; Rajamannan et al., 2003). It was proposed that calcific deposits lead to a mechanical leaflet compliance mismatch resulting in mechanical injury which results in further inflammatory response(Tania A. Pawade et

al., 2015). Ultimately these processes lead to severe valve narrowing which is associated with an 80% 5-year risk of progression to valve replacement, heart failure or death (Otto et al., 1997).

Since AVR is the only available therapy for AS, appropriate timing of the intervention is crucial. In every day clinical practice, it is either symptoms or a decrease in LV ejection fraction that triggers intervention (Baumgartner et al., 2017; Nishimura Rick et al., 2017). Unfortunately, identifying ventricular decompensation is problematic as symptoms are frequently difficult to assess in the elderly and a fall in ejection fraction occurs late and is often irreversible (Braunwald, 1990; Chizner, Pearle, & deLeon, 1980; Marc R. Dweck et al., 2012; Lassnigg et al., 2013; Turina, Hess, Sepulcri, & P Krayenbuehl, 1987).

The rationale for a symptom-guided approach to AS is based largely on the landmark manuscript by Ross and Braunwald: well known to cardiologists worldwide (Ross & Braunwald, 1968). That manuscript, however, is now 50 years old, based largely upon retrospective observational/post-mortem data, and comprised predominantly male patients who on average developed symptoms at 60 years of age. Whether symptoms remain the best guide to LV decompensation and the timing of AVR in modern clinical practice is starting to be questioned(Kang, Park, et al., 2010; Kang, Rim, et al., 2010; Pellikka et al., 2005).

Modern AS patients are certainly older, making symptom assessment even more challenging because of both their extensive co-morbidities and their limitations to physical exertion. Is the patient breathless because of valve disease or anemia or obstructive pulmonary disease? Similarly, is the patient who walks carefully with a stick truly asymptomatic? These issues have prompted many investigators to seek more objective biomarkers of LV decompensation to help guide the timing of AVR (Calvin W. L. Chin, Anoop S. V. Shah, et al., 2014). Several of these biomarkers are under active investigation including blood biomarkers (e.g., troponin, Btype natriuretic

peptide), echocardiographic strain data, and electrocardiograph changes as well as the mid-wall fibrosis on cardiac magnetic resonance (Attias et al., 2013; Clavel, Malouf, et al., 2014; Dahou et al., 2015; Dweck et al., 2011; Kearney et al., 2012). Importantly, these myocardial biomarkers provide more powerful prediction of long-term outcomes after AVR than traditional valve assessments, indicating that the health of the myocardium at the time of surgery is a key determinant of long-term prognosis.

Our current management strategy for aortic stenosis has major limitations that would be fundamentally enhanced by:

(i) an improved understanding of the mechanisms underlying valve calcification and left ventricular decompensation,

(ii) the development of novel medical therapies that could halt or regress the disease process and

(iii) the identification of objective biomarkers of valve decompensation that can better guide AVR.

1.4 Non-invasive imaging of Aortic Stenosis

In the past decade non-invasive imaging techniques have enabled researchers to further characterize aortic stenosis (Chambers et al., 2016; Calvin W. L. Chin, Vassilis Vassiliou, et al., 2014; Dulgheru et al., 2016). In particular cardiovascular magnetic resonance (CMR), computed tomography (CT) and positron emission tomography (PET) have improved our understanding of the natural history of this valvular condition. The findings of observational trials focused on AS have provided hope that we now might be able to detect subtle progression within the valve and myocardium. Further, since assessment of the disease can be so accurate, nowadays performing interventional trials, testing new medication approaches can benefit from imaging-

derived endpoints. Ultimately it is believed that the aforementioned imaging modalities could help clinicians better decide on the timing of aortic valve replacement.

1.4.1 Insights from non-invasive imaging

1.4.1.1 Aortic Stenosis – disease of the myocardium

In conditions associated with left ventricular pressure overload such as aortic stenosis and hypertension, myocyte size and myocardial wall thickness increase to restore wall stress (M. R. Dweck, S. Joshi, et al., 2012). This hypertrophic response is initially adaptive maintaining cardiac output and systolic function. However, as hypertrophy increases, the left ventricle ultimately decompensates, leading to progressive impairment in ventricular performance and the development of symptoms and adverse cardiovascular events (B. A. Carabello, 2002; Gunther & Grossman, 1979). Preliminary histological studies have indicated that this pathologic transition from ventricular adaptation to decompensation is driven primarily by two processes: myocyte death and myocardial fibrosis (Hein et al., 2003). Myocyte death takes the form of oncosis (similar to necrosis) and apoptosis and is accompanied by signs of cellular stress manifest as increased autophagy (Kostin et al., 2003; Vigliano et al., 2011). Although the trigger for these events remains unclear, it has been proposed that progressive myocyte cell death relates to neurohumoral mediators, such as angiotensin II and norepinephrine (Antonini-Canterin et al., 2003; Cote et al., 2010; Fujisaka et al., 2013; Helske et al., 2004). Alternatively, myocardial ischemia may act as the trigger, itself occurring as a consequence of increased myocardial oxygen demand (due to the increased myocardial mass and afterload) and reduced coronary reserve (due to impaired microcirculatory perfusion and inadequate expansion of coronary capillary density)(Galiuto et al., 2006; Marcus et al., 1983). Replacement

myocardial fibrosis is believed to occur in response to this cell death. Such fibrosis is irreversible and its accumulation in the left ventricle leads to progressive impairment of myocardial relaxation (diastolic dysfunction) and contraction (systolic dysfunction) driving the clinical progression to heart failure (Azevedo et al., 2010; Shirani, Pick, Roberts, & Maron, 2000; Weidemann et al., 2009)(Figure 1).

Figure 1. The transition from a normal heart to LV decompensation in aortic valve stenosis. Potential biomarkers are shown in italic.

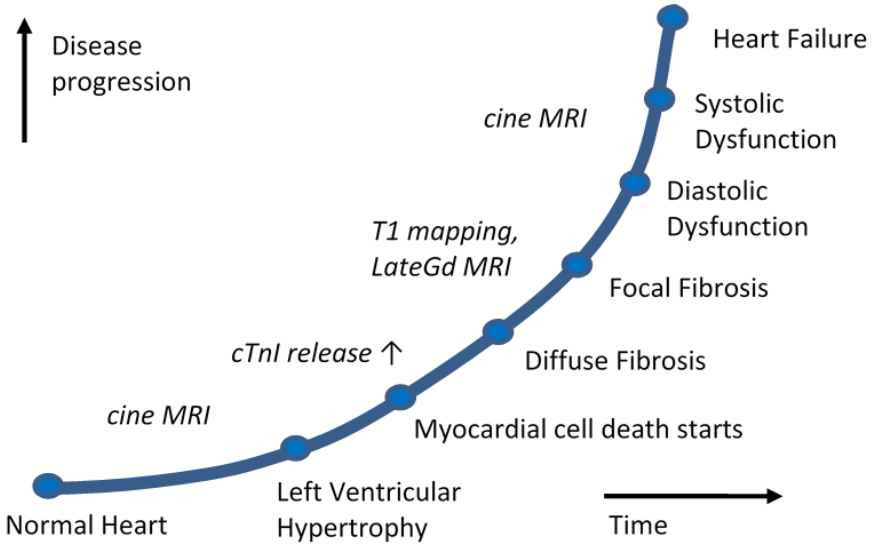

1.4.1.2 Cardiovascular Magnetic Resonance Late Gadolinium Enhancement for Imaging Replacement Fibrosis

Dedicated cardiovascular magnetic resonance (CMR) techniques have been developed for the direct visualization and quantification of myocardial fibrosis in patients and animal models (Lluri et al., 2017; Vassiliou et al., 2017). These involve the administration of gadolinium contrast, which accumulates in regions of fibrosis and increases signal in these areas on T1-weighted scans. On this basis, late gadolinium enhancement can identify replacement fibrosis within the decompensating myocardium in a mid-wall pattern that is easily differentiated from prior myocardial infarction.

Several MRI studies have investigated the role of late gadolinium enhancement in aortic stenosis and confirmed that the mid-wall pattern acts as a direct measure of left ventricular decompensation (Dweck et al., 2011; Lluri et al., 2017; Vassiliou et al., 2017). In a recent study consisting of 143 patients with moderate to severe aortic stenosis, Dweck et al. demonstrated that mid-wall fibrosis was present in a third of subjects and was associated with an advanced hypertrophic response and other markers of ventricular decompensation. Moreover, mid-wall fibrosis acted as an independent predictor of mortality providing incremental prognostic value over and above that of the ejection fraction. Indeed, patients with mid-wall fibrosis had an 8-fold increase in all-cause mortality compared to those without, despite similar aortic stenosis severity and coronary artery disease burden (Dweck et al., 2011). Similar findings have been observed in patients following AVR, with the presence of mid-wall late gadolinium enhancement being associated with adverse ventricular remodelling and worse peri-operative and long-term outcomes following surgery (Barone-Rochette et al., 2014; Quarto et al., 2012). Interestingly, replacement myocardial fibrosis as detected by cardiovascular magnetic resonance does not appear to be reversible following AVR suggesting that once observed in the ventricle, surgery

should be considered early before further irreversible fibrosis develops (Barone-Rochette et al., 2014). Late gadolinium enhancement CMR appears to hold major advantages as a biomarker of left ventricular decompensation because of its ability to measure directly the key pathological process driving the ventricle towards heart failure. On this basis it was proposed it could become the central tool used in clinical practice to decide upon the timing of AVR. This hypothesis is currently tested in the context of the Early Valve Replacement Guided by Biomarkers of LV Decompensation in Asymptomatic Patients With Severe Aortic Stenosis (NCT03094143) randomized controlled trial.

1.4.1.3 Computed Tomography

The extent of aortic valve calcification can be assessed with non-invasive imaging. While echocardiography has been used to estimate the calcific burden for several decades more recently computed tomography has been utilized in this context (Cioffi et al., 2013; Rosenhek et al., 2004). This imaging modality is advantageous over conventional echocardiography as it provides superior reproducibility (Messika-Zeitoun et al., 2004). Applying the widely utilized coronary calcium score protocol, an electrocardiography-gated non-contrast CT provides information regarding the density, volume and mass of macroscopic calcium deposits within the valve (T. Pawade et al., 2018). Employing such methodology, it was shown that the calcific burden measured in Agatston Units (AU) is closely correlated with hemodynamic echocardiography derived measurements which up to date are considered the golden standard for stenosis assessment (Agatston et al., 1990; Koos, Kuhl, Muhlenbruch, & Mahnken, 2006; F. Liu et al., 2006). Furthermore, more recently gender specific thresholds for severe aortic stenosis have been proposed. From a cohort of 646 patients moderate to severe aortic stenosis patients Clavel et al. focused on those in whom echocardiographic findings were discordant (the calculated valve area and peak or mean velocity showed discrepancies classifying patients as having

moderate/severe disease). The authors showed that a threshold of 1275 AU in women and 2065 AU in men enables distinguishing severe aortic stenosis (Clavel et al., 2013). Moreover, utilization of these cut-off values for dichotomizing subjects was shown to act as an independent predictor of overall mortality (Clavel, Pibarot, et al., 2014). More recently these promising thresholds were further validated in an international multicenter registry which included a wide range of patient populations, who underwent imaging on different scanner vendors (T. Pawade et al., 2018).

The aforementioned studies suggest that computed tomography calcium scoring can be used for grading disease severity in aortic stenosis. This method provides insights into disease progression and can be used for risk stratification. Importantly while this approach enables disease burden assessment it does not allow for the assessment of calcification activity. Techniques that could monitor calcification activity are therefore desired.

1.5 Left ventricular remodeling on cardiovascular magnetic resonance imaging

1.5.1 Patterns of left ventricular remodeling

In aortic stenosis the narrowing the valve leads to a hypertrophic response in the myocardium. As a result, myocytes enlarge and the left ventricular wall thickness and the overall mass increases. While initially wall stress is restored and systolic function can be maintained ultimately the hypertrophic response is maladaptive as it has been already linked to adverse outcome (Cioffi et al., 2011; Cioffi & Stefenelli, 2002; Gosse, 2005; Gradman & Alfayoumi, 2006). Importantly there are wide differences in the degree of hypertrophy among patients with similar valve obstruction (M. R. Dweck, S. Joshi, et al., 2012). Moreover, distinct patterns of remodeling have been also reported. These have been described taking into consideration imaging measures of LV mass, the diastolic volumes and the relative wall thickness (which takes into account both wall thickness and the end-diastolic cavity dimension (Cioffi & Stefenelli, 2002; Ganau et al., 1992). The four classical patterns of LV remodeling in AS are: normal ventricular geometry, concentric remodeling, concentric hypertrophy, and eccentric hypertrophy. Although both concentric remodeling and hypertrophy are considered as a physiological response to the increased afterload, this pattern of remodeling can be maladaptive (R. Capoulade et al., 2017). This is largely due to the development of myocardial fibrosis and irreversible myocardial dysfunction associated with it (Gaasch & Zile, 2011; Milano et al., 2012). Previous studies showed that severe LV hypertrophy is associated with adverse outcome both in subjects before aortic valve replacement and those in whom the stenosed valve has been removed (Cioffi et al., 2011; D. Cramariuc, Gerdts, Davidsen, Segadal, & Matre, 2010; Duncan et al., 2008; Greve et al., 2012; Holme et al., 2012; B. R. Lindman et al., 2014; Orsinelli, Aurigemma, Battista, Krendel, & Gaasch, 1993; Rieck et al., 2012).

1.5.1.1 Patterns of Left Ventricular Remodeling and Outcome

To date, only one study assessed the impact of different LV remodeling patterns on all-cause mortality in AS patients with preserved LV ejection fraction. In a total of 747 consecutive aortic stenosis patients Capoulade et al. showed that on echocardiography concentric hypertrophy is the most prevalent pattern of LV remodeling and can be found in over 50% of subjects (R. Capoulade et al., 2017). Concentric remodeling was detected in 23% of patients and eccentric hypertrophy was rare and found in 9% of cases. The study also demonstrated that older age, obesity, hypertension and more severe AS are associated with higher prevalence of concentric hypertrophy. Interestingly over a median of 6.4 years of follow-up this pattern of remodeling was independently associated with increased mortality even after adjustment for the factors mentioned above and for AVR. The six-year survival rate for concentric hypertrophy patients was 61% compared to 70% for a normal or eccentric LV pattern and 71% for concentric remodeling. The authors concluded that concentric hypertrophy may be associated with an outcome penalty despite successful AVR. The findings of the study support the usefulness of LV remodeling assessment for improving risk stratification in AS patients with preserved LVEF.

The aforementioned study has not addressed all relevant questions regarding the hypertrophic response in aortic stenosis. For instance, asymmetric wall thickening which has been also reported in AS patients was not reported in the analysis (Hess et al., 1983a; Tuseth, Cramariuc, Rieck, Wachtell, & Gerdts, 2010). Actually, up to date this pattern of remodeling has not been considered by a vast majority of studies assessing the LV hypertrophic response in AS and as a result both its true prevalence and more importantly its impact on outcome have not been well understood. Moreover, when compared to cardiovascular magnetic resonance the assessment of left ventricular remodeling and hypertrophy by echocardiography has several

limitations. The former technique was shown to be more robust and reproducible in measuring left ventricular mass, volume and wall thickness (M. S. Maron et al., 2009; Myerson, Bellenger, & Pennell, 2002). Despite these clear advantages of CMR imaging we lack studies utilizing this superior modality for evaluating asymmetric wall thickening in AS.

1.5.2 The role of diffuse myocardial fibrosis

While in aortic stenosis replacement fibrosis quantified with late gadolinium enhancement on CMR is already established as a marker of adverse prognosis only recently an approach for assessing diffuse fibrosis was described (Barone-Rochette et al., 2014; Herrmann et al., 2018; Vassiliou et al., 2017). CMR T1 mapping showed hope in this regard (D. R. Messroghli, Greiser, Frohlich, Dietz, & Schulz-Menger, 2007; Daniel R. Messroghli et al., 2004; Piechnik et al., 2010). The highlight of this technique is that compared to late gadolinium enhancement, T1-mapping generates an image of the myocardium based on the T1 relaxation time, which is a magnetic property of a given tissue and does not rely on relative signal differences. This is particularly relevant as diffuse fibrosis is believed to be a process involving the entire ventricle and therefore its assessment cannot require remote tissue as reference. The initial approach which was introduced by Messroghli et al., which is now known as native T1-mapping has evolved over the past years. Back in 2008 the partition coefficient which is a ratio of the T1 relaxation times in the myocardium and bloodpool after the administration of a gadolinium-based contrast agent was described (Jerosch-Herold et al., 2008). The authors showed that patients with dilated cardiomyopathy have higher partition coefficients than controls and suggested this might be due to expansion of the extracellular matrix presumably in the form of interstitial fibrosis. More recently, the extracellular volume fraction (ECV), a measure which takes into consideration both pre and post contrast T1 relaxation values

corrected by the blood-pool contrast load and hematocrit was developed (A. S. Flett et al., 2010). Importantly it was shown that this novel measure reflects the diffuse fibrosis burden quantified on endomyocardial biopsies.

1.5.2.1 T1-mapping in Aortic Stenosis

Using standardized methodology on a cohort of AS patients Chin et al have systematically compared commonly used T1 measures at multiple time points and in multiple regions across the left ventricle (C. W. L. Chin et al., 2014). The authors showed that pre-contrast T1 was limited by an inability to differentiate patients with aortic stenosis from healthy volunteers and post-contrast myocardial T1 lacked sufficient scan–rescan reproducibility. In comparison, the partition coefficient and the ECV demonstrated excellent reproducibility and were increased in patients with aortic stenosis when compared with healthy volunteers.

Other studies suggested that pre-contrast T1 relaxation times can provide important insights in AS subjects. Bull et al demonstrated that non-contrast T1 values measured using the ShMOLLI CMR sequence correlate well with percentage collagen volume fraction as measured on histology in patients with AS. In their study, non-contrast T1 values in AS increased with disease severity (Bull et al., 2013). In a prospective observational longitudinal study of 127 consecutive patients with moderate or severe AS followed up for a median of 27.9 months Lee et al showed that T1 mapping derived measures predicts outcome in individuals with aortic stenosis. The native T1 values were predictors of outcome independent of an established risk score (EuroSCORE II) and replacement fibrosis on CMR. On multivariate Cox regression analysis, every 20-ms increase in native T1 was independently associated with a 28% increase risk of all-cause mortality and heart failure hospitalization (H. Lee et al., 2018).

Further data on the prognostic value of ECV has been also published. The ECV was linked with outcome as Nadijiri et al showed that in patient pre- and post-transcatheter

aortic valve replacement ECV acts as a predictor of adverse events (Nadjiri et al., 2016). Chin et al evaluated both extracellular expansion and replacement fibrosis in the myocardium of patients with aortic stenosis and healthy control subjects and showed that both are closely associated with the magnitude of the hypertrophic response, the presence of LV dysfunction, the functional capacity of the patient, and, ultimately, clinical outcome. The authors proposed a new classification of AS patients based purely on CMR derived assessment of the myocardium. Subjects were divided into three groups, those with: normal myocardium, extracellular expansion, and replacement myocardial fibrosis. Across these groups the investigators demonstrated a stepwise increase in all-cause mortality and concluded that T1-mapping has the potential to detect early, subclinical ventricular decompensation in aortic stenosis and ultimately might be able to guide decisions regarding the timing of aortic valve replacement (C. W. L. Chin et al., 2017).

It is believed that diffuse fibrosis quantified with CMR has the potential to greatly improve our understanding of left ventricular decompensation (Nagel & Chandrashekhar, 2018; Neubauer & Bull, 2017). Assessment of the expansion of diffuse fibrosis can potentially provide valuable insights into disease progression at a stage when LV function is still maintained. Ultimately it was speculated that T1 mapping indices could potentially predict LV decompensation in AS patients and assist in guiding the optimal timing of valve replacement.

1.5.2.2 Challenges associated with longitudinal studies of fibrosis development

Elucidating the exact time course of events in aortic valve stenosis with the aim of better understanding the timing and sequence in which diffuse fibrosis progress under pressure overload and regresses after load normalization is challenging. This is

primarily because collecting aortic stenosis natural history data in patients would take very many years if not decades (Rosenhek et al., 2010).

Preclinical models are an alternative approach that have the potential to provide desired insights (Camacho, Fan, Liu, & He, 2016; Ku, Huelnhagen, Niendorf, & Pohlmann, 2018). The potential benefits of using an animal model are several fold. Firstly, the time when the trigger to hypertrophy started is known - this is impossible to gauge in human patients as aortic stenosis progresses over several years before manifesting clinically usually at the time of auscultation or echocardiography. The fact that the exact disease onset is known enables monitoring how the hypertrophic response develops and how the myocardium eventually decompensates. A second advantage is the much quicker time course that this sequence occurs over in laboratory animals (rodents). Finally, animal models allow for correlating the information provided by non-invasive biomarkers with detailed histological examination of the entire myocardium at multiple different time points. This therefore overcomes the sampling error associated with human biopsy samples, which are difficult to obtain in the earlier stages of disease and may not be representative of the left ventricle as a whole, given that remodelling often demonstrates regional variation (M. R. Dweck, S. Joshi, et al., 2012). Importantly given the fact that preclinical CMR offers excellent spatial and temporal resolution and enables acquisition of cinematographic and T1 mapping data the techniques for identifying LV decompensation are directly translatable to humans and are therefore of direct clinical relevance (Figure 2).

Figure 2. Examples of various MRI sequences. Structural and functional MRI. A - B: 2-chamber and 4-chamber cine scans of a mouse heart after induction of myocardial infarction. C and D, short-axis cine scan of the same animal at end-diastole and end-systole, resp. Ejection fraction: 20%. E: LateGd MRI of the same mouse. Signal enhancement demarcating the infarct is clearly visible. F. MOLLI T1-mapping scan raw data and fitted T1-maps before (G) and after (H) the injection of Gd of a rat heart and corresponding signal intensity curves fitted to calculate T1 values.

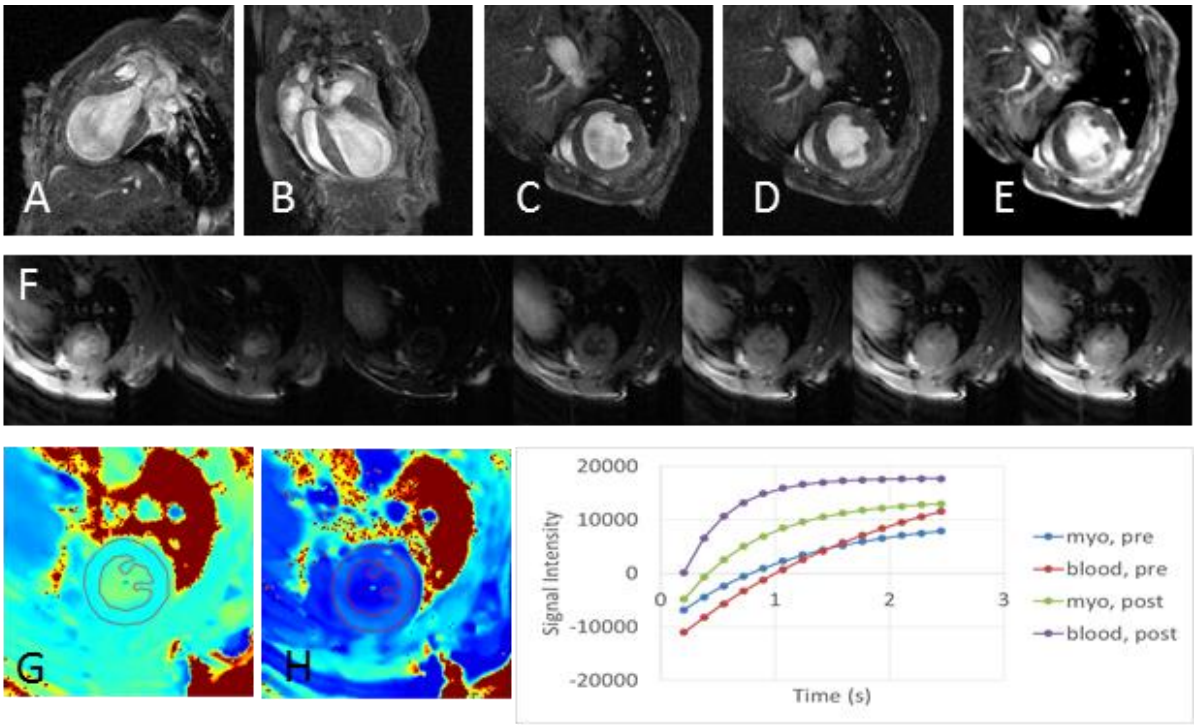

1.5.3 Gender discrepancies in aortic stenosis

Interestingly in the past decade, important sex differences in the pathophysiology of AS are beginning to emerge, perhaps related to the influences of testosterone (Aurigemma & Gaasch, 1995; Carroll et al., 1992; P. S. Douglas et al., 1995; Rohde et al., 1997; Villari et al., 1995; Zhu et al., 2016). Most notably, recent data have suggested that women need less valvular calcium than men to develop severe AS (Aggarwal et al., 2013). Importantly, after taking into account that women have smaller bodies and smaller LVOT, even after normalization for these factors women present lower aortic valve calcium density than men for similar AS severity. This difference between sexes is also related to a steeper slope of AS severity increase with any given aortic valve calcium load or density increase in women than in men. Therefore, while valvular calcification is the mechanism of AS in both men and women, there are important pathophysiological differences between men and women that warrant specific clinical approaches and further research into disease mechanisms specific to each sex (Aggarwal et al., 2013).

To date multiple studies showed that for a given degree of valve narrowing males present with a more pronounced LV hypertrophic response. Initial echocardiographic data showed that cardiac adaptation to aortic stenosis seems to be influenced by gender with males presenting larger left ventricular volumes and higher wall tension (Bech-Hanssen et al., 1999). These findings have been recently corroborated in cardiac magnetic resonance imaging studies (Dweck et al., 2012). While data on the myocardial response to pressure overload is largely concordant some discrepancies regarding the prognosis following successful aortic valve replacement in males versus females have been reported. In the SEAS study, women and men had similar rates of AS progression and AS-related events (Cramariuc et al., 2015). However, in that study women had lower total mortality and a ischaemic cardio-vascular event rate than men independent of confounders. Additionally, recently superior LV hypertrophy

regression and outcome were reported in elderly women compared with men undergoing transcutaneous aortic valve replacement from the prospective Placement of Aortic Transcatheter Valve (PARTNER) trial (Williams et al., 2014). In line with these findings Fuchs et al showed that although women referred to AVR are older and more symptomatic, operative and long-term mortality are not increased. In the oldest age group of 79 years and older, women even have a better outcome, presumably due to a longer mean life expectancy (Fuchs et al., 2010).

On the other hand, in a retrospective study involving 577 consecutive patients who underwent aortic valve replacement Caballero-Borrego et al demonstrated that women more often suffered acute myocardial infarction perioperatively, had a low cardiac output in the postoperative period and experienced greater perioperative mortality than men (Caballero-Borrego et al., 2009). In line with these findings in a separate elegant analysis Pibarot et al. (2009) showed that the mismatch of patient and prosthesis, greater ventricular hypertrophy and the underestimation of symptoms in women are possible causes of the greater mortality in women with AVR. Another reason for less favorable outcomes in females might be the fact that women are more often present with paradoxical low flow low gradient aortic stenosis which is associated worse outcome, especially when treated medically (Hachicha et al., 2007 & Barasch et al., 2008).

Intriguing data derived from cardiovascular magnetic resonance imaging has been reported by Singh et al. According to this recent study gender differences may also exist in both the remodeling response of the left ventricle and in the development of symptoms. The authors provided cardiac magnetic resonance, transthoracic echocardiography, and biomarker analysis of 174 patients (133 men and 41 women) with moderate to severe AS coupled with detailed assessment of symptom status at baseline and after follow-up (Singh et al., 2017). With the data acquired across

multiple expert centers across the United Kingdom the authors demonstrated that, despite a similar severity of aortic valve narrowing, men had higher indexed left ventricular mass, increased LV volumes, and more concentric remodeling. Importantly, these differences in the degree of LV remodeling persisted after correction for size differences between the sexes and in a multivariable analysis. Having in mind that similar findings were reported in previous studies, it appears that for a given degree of AS men develop more advanced cardiac remodeling than women (Dobson et al., 2016; M. R. Dweck, S. Joshi, et al., 2012; J. M. Lee et al., 2015).

1.5.3.1 Gender difference in myocardial fibrosis

Aside from the degree of hypertrophy, recent data suggests that further differences can be found in the degree of myocardial fibrosis. Singh et al have shown that men might have more LV late gadolinium enhancement and scarring than women. In part, these differences can be related to previous myocardial infarction (not unexpected given the sex differences in coronary artery disease), but in the study there was also a numerical difference in the mid-wall pattern of scarring that is more specific to AS. Similarly, men had increased levels of blood biomarkers related to fibrosis and reduced markers of LV performance (ejection fraction, longitudinal strain, circumferential strain)(Singh et al., 2017). While these findings are of interests it is important to have in mind that despite being a multicenter study, there were only 41 females included in the analysis. With the Singh et al study somewhat limited by sample size and with many of the fibrosis observations of borderline significance larger studies are now required for confirmation. In particular, these could assess whether the mid-wall pattern of late gadolinium enhancement is indeed more prevalent in men and elucidate the information provided by T1 mapping, which appears to be conflicting.

1.5.3.2 Gender discrepancies in the development of symptoms and outcome

The second key insight provided in the paper by Singh et al is the demonstration that, despite the more advanced LV remodeling and decompensation observed in men, it was women who were more likely to develop symptoms necessitating aortic valve replacement (AVR). Similar findings were reported in a recent report by Capoulade et al. In an echocardiographic study of 747 consecutive AS patients followed up for 6.4 years the most prevalent pattern of LV remodeling – concentric hypertrophy was independently associated with increased risk of mortality in women, but not in men (R. Capoulade et al., 2017). While the association of adverse outcome and concentric hypertrophy persisted in the entire cohort, the fact that this relationship showed gender discrepancies supports the view that a sex specific approach in aortic stenosis is justified.

The paper by Singh et al. also elucidates the relationship between symptom development and novel biomarkers of LV decompensation including Btype natriuretic peptide, echocardiographic strain and mid-wall fibrosis on cardiac magnetic resonance (Attias et al., 2013; Dahou et al., 2015; Kearney et al., 2012). On univariate analysis, symptom development prompting AVR was not associated with indexed LV mass, myocardial perfusion parameters, ejection fraction, myocardial strain assessments, or the presence/volume of mid-wall late gadolinium enhancement. Although symptom development was associated with B-type natriuretic peptide in men, it was not in women. Moreover, despite men having greater evidence of LV remodeling and decompensation by the vast majority of measures, it was women who developed symptoms more quickly and therefore proceeded to aortic valve replacement (Singh et al., 2017).

The uncoupling of symptoms and markers of LV remodeling raises important questions. Can we rely on symptom development in modern clinical practice to guide AVR timing? Perhaps it is the biomarkers that are unreliable? Are we operating too

late in men, allowing them to develop excessive myocardial scarring? Ultimately, such questions regarding the optimal timing of surgery are not well answered by observational studies and will only be fully addressed in the context of randomized controlled trials. Fortunately, several such trials are under way (e.g., Early Valve Replacement Guided by Biomarkers of LV Decompensation in Asymptomatic Patients With Severe Aortic Stenosis [NCT03094143], Evaluation of Transcatheter Aortic Valve Replacement Compared to Surveillance for Patients With Asymptomatic Severe Aortic Stenosis [NCT03042104]), examining whether alternative strategies might improve the timing of AVR compared with symptom development. These randomized clinical trials are long overdue and their results highly anticipated.

While we await these trials to report their findings the gender discrepancies in the fibrosis burden, in particular, in the T1-mapping derived measurements could easily be evaluated on large multicenter registry data. Up to date only one single center study showed a statistically significant difference in measures of diffuse fibrosis (Treibel, Kozor, et al., 2018). In a cohort of 168 patients with symptomatic severe AS referred for surgical AVR men showed more extracellular matrix expansion, calculated as the product of LV myocardial volume and ECV (28.5±8.8 ml/m2 vs. 21.4±6.3 ml/m2 and a higher burden of replacement fibrosis as assessed with LGE (16.5±11.2 g vs. 10.5±8.9 g) than women. In the study, men more frequently showed concomitant coronary artery disease, which could partly explain increased myocardial fibrosis compared with women. Given the overall less favorable remodeling pattern and ventricular phenotype with more concentric and eccentric hypertrophy as well as lower LV ejection fraction, higher NTproBNP and hsTnT in men compared to women it is intriguing why only in females the maladaptive remodeling is associated with impaired survival after aortic valve replacement (J. M. Brown et al., 2009; Morris et al., 1994; Onorati et al., 2014; Petrov et al., 2014; Stamou et al., 2012).

1.6. Calcification activity on ^{18}F-sodium fluoride PET

^{18}F – sodium fluoride has been used for decades in nuclear medicine to image bone malignancies (Jadvar, Desai, & Conti, 2015). In the skeleton, fluoride binding is facilitated through a chemical reaction with hydroxyapatite, a crystalline structure that is commonly known as the bone mineral. Importantly hydroxyapatite is also the main component of vascular atherosclerosis and valvular calcifications (Monte Blau, Ganatra, & Bender, 1972). In the context of cardiovascular imaging the binding of ^{18}F-NaF to microcalcification was studied in histological samples of human carotid plaques on three levels: with electron microscopy, autoradiography, and µPET/CT(Irkle et al., 2015; Vesey et al., 2017). It was demonstrated that ^{18}F-NaF binds preferentially to microcalcification beyond the resolution of µCT and co-localizes to regions of active mineralization within vascular tissue. The preferential binding to microcalcification is likely due to the high surface area of hydroxyapatite in regions where this nanocrystal builds up (Gasser, Voegel, & Gramain, 1993; J. Lin, Raghavan, & Fuerstenau, 1981).

This imaging modality gained interest in the context of detecting cardiovascular calcification within coronary arteries, the abdominal aorta, carotid arteries and the aortic valve (M. R. Dweck, M. W. L. Chow, et al., 2012; M. R. Dweck, C. Jones, et al., 2012; Forsythe et al., 2018; Lee et al., 2017; T. A. Pawade et al., 2016; Vesey et al., 2017). It was shown that ^{18}F-Fluoride is readily taken up by the valves of patients with aortic stenosis and on histology correlates with markers of calcification activity (Dweck et al., 2014). The ability to monitor calcification activity is particularly of interest as the calcific burden of the valve has been already linked to outcome (Clavel, Pibarot, et al., 2014; T. Pawade et al., 2018). With such encouraging initial studies nowadays ^{18}F-NaF is utilized in randomized clinical trials evaluating therapies aimed at slowing the progression of aortic valve calcifications (Study Investigating the Effect of Drugs Used to Treat Osteoporosis on the Progression of Calcific Aortic Stenosis -

NCT02132026 and Bicuspid Aortic Valve Stenosis and the Effect of vitamin K2 on Calcium metabolism on ^{18}F-NaF PET/MRI - NCT02917525).

Aside from being able to predict progression of native aortic valve disease ^{18}F-NaF PET has been recently shown to be a robust tool for imaging patients who underwent surgical aortic valve replacement. In our recent study we have identified ^{18}F-NaF PET as the first noninvasive technique capable of detecting early bioprosthetic valve degeneration and of predicting future valve dysfunction (Cartlidge et al., 2019). In an extensive histological and state of the art ex vivo imaging validation we demonstrated increased ^{18}F-NaF uptake in each of the failed bioprosthetic aortic valves examined, with PET activity colocalizing to areas of calcification, pannus, thrombus, and disrupted tissue architecture on histology. When applied to patients in the clinical setting, ^{18}F-NaF PET identified early valve degeneration beyond the resolution of echocardiography or CT and outperformed conventional surveillance methods in predicting the development of new valvular dysfunction and overt valve failure within the 2-year follow-up period. ^{18}F-NaF PET, appears to be a readily applicable measure of valve degeneration with the potential to transform how we monitor and treat the expanding population of patients living with surgical bioprosthetic valves.

Given the growing population of patients who undergo transluminal aortic valve replacement (TAVR) and the finite lifespan of the implanted bioprothesis an imaging approach which would enable prediction of structural TAVR deterioration is desirable. While a combined CT angiography and ^{18}F-NaF PET appear to be ideally suited for monitoring degeneration of TAVR, imaging TAVR presents unique challenges. After TAVR deployment, leaflets of the native valve are displaced against the aortic wall making it difficult to discern PET tracer uptake within the implanted bioprosthesis from the native valve. Similarly, distinguishing TAVR calcifications from stent struts and native valve calcium requires high quality CT angiography. In view of these peculiarities to date data regarding imaging TAVR with PET is in short supply.

Despite the growing enthusiasm, ^{18}F-NaF cardiovascular PET remains a complex and challenging imaging approach. Before this promising modality reaches its full potential, several limitations need to be addressed (Thomas & Haraszti, 2014). These include small target lesions size, which for adequate count statistics requires long emission scanning. The duration of emission scanning has been set at 30 minutes and increases the risk of inter-scan patient motion as subjects may find it difficult to remain immobilized over the entire length of the acquisition. The measured uptake is also adversely affected by blurring of the tracer signal in target lesions by cardiorespiratory motion which occurs as a result of physiological tidal breathing and heart contractions. To reduce the effect of motion gating can by employed. To date it has only been widely utilized to ameliorate cardiac motion, with end-diastolic imaging (25% of PET counts) used for image analysis. Additionally, with the need for anatomical reference when evaluating uptake ^{18}F-NaF PET requires multifaceted experience staff to acquire CT angiography. In view of the small target lesions size, joint effects of cardiorespiratory motion ^{18}F-NaF PET would undoubtedly benefit from refinement of image acquisition, reconstruction and analysis.

1.6.1 Delayed PET Imaging of cardiovascular disease

The benefit of delayed PET acquisition for the detection of disease is widely appreciated in oncological applications with ^{18}F-fluorodeoxyglucose (FDG)(Caoduro et al., 2013; Kubota et al., 2004; W. Y. Lin, Tsai, & Hung, 2005; Nishiyama et al., 2005). There is good agreement that because background activity decreases on delayed imaging, the image quality improves. The lower background activity is a critical feature and advantage of delayed imaging, because it increases target to background ratios (Cheng, Torigian, Zhuang, & Alavi, 2013; Houshmand et al., 2016). It has been shown that a longer time window from injection to acquisition translates

to higher signal to noise and therefore facilitates visual analysis providing higher diagnostic accuracy (Kubota et al., 2001). For coronary PET imaging, it was suggested that the optimal timing for acquisition with FDG is 2.5-3h after tracer administration (Rudd et al., 2002).

In the 1970s when ^{18}F-NaF was first used for bone scanning, Blau et al suggested that the optimal scanning time for ^{18}F-NaF is 2-4 hours post injection (M. Blau, Nagler, & Bender, 1962). Nevertheless, whole-body ^{18}F-NaF PET is nowadays most often performed with imaging commencing 60 minutes after injection (Czernin, Satyamurthy, & Schiepers, 2010; Grant et al., 2008; Hawkins et al., 1992; Segall et al., 2010). In case of ^{18}F-NaF PET bone imaging, since ^{18}F-NaF has faster blood clearance and higher bone uptake compared to 99mTc-methylene diphosphonate, the SNM practice guideline recommends emission scanning for the axial skeleton as soon as 30-45 minutes after injection in patients with normal renal function to decrease the overall time of the study. However, a longer waiting time of 90-120 minutes was recommended to acquire high-quality images of the extremities (Segall et al., 2010).

In cardiovascular PET, in most studies to date assessing ^{18}F-NaF uptake in atherosclerotic plaques and aortic valves, acquisition was performed 1-hour (1h) after tracer administration (Derlin et al., 2010; Derlin, Toth, et al., 2011; Derlin, Wisotzki, et al., 2011; Joshi et al., 2014). Although semi-quantitative analysis is feasible with 1h images, it can be difficult to discriminate plaques with ^{18}F-NaF uptake from noise. In fact, compared to uptake in the bony skeleton, ^{18}F-NaF uptake due to active microcalcification formation in coronary plaque and valve leaflets is very small in amount. Recently, it has been speculated that the optimal time for atherosclerotic plaque imaging with ^{18}F-sodium fluoride might differ from the 1h post injection time-point used for bone imaging (Derlin, Wisotzki, et al., 2011).

Longer delays for cardiovascular ^{18}F-NaF PET imaging were evaluated by only one study to date. Blomberg et al. concluded that delayed ^{18}F-NaF PET imaging does not improve quantification of vascular calcification. However, the authors measured only overall heart ^{18}F-NaF activity (including blood pool) by placing regions of interest around the entire cardiac silhouette on ungated PET/CT images (excluding ^{18}F-NaF activity originating from bones and cardiac valves) and averaged the SUV values derived from all slices. The study was performed without cardiac gating and motion correction. Further, with 2.5-minute scan time and a 2.2 MBq dose of ^{18}F-NaF per kilogram of body weight the authors had approximately 16 times less counts compared to recent studies and ongoing clinical trials (which utilize a ~3.4MBq per kg dose and 30-min long acquisitions)(Björn A. Blomberg et al., 2014).

There remains a need to comprehensively assess whether the optimal timing for ^{18}F-NaF cardiovascular PET is 1h post injection imaging. In particular the potential benefits of a delayed acquisition should be investigated.

1.6.2 Anatomical reference for ^{18}F-sodium fluoride uptake quantification

Regardless of the delay from tracer injection to image acquisition in order to measure ^{18}F-NaF uptake anatomical reference is essential. For cardiovascular PET two approaches have been proposed (Bellinge, Francis, Majeed, Watts, & Schultz, 2018). The lesion specific method of analysis utilizes coronary CT angiography for anatomical reference (Joshi et al., 2014; Lee et al., 2017). Regions of interest can be delimited around coronary plaques so that single areas of increased tracer uptake are considered. Such an approach has several advantages as it provides lesion specific information: it enables assessing plaque composition and it can be used for guiding revascularization as luminal stenosis can also be evaluated. When compared to a global coronary method of analysis it is not prone to false positive findings in patients

with non-coronary ^{18}F-NaF uptake. This approach is however more challenging from an acquisition point of view as it requires prospective ECG-gating of the PET acquisition, moreover CT and PET datasets need to be co-registered which is not always trivial. Furthermore, the lesion specific approach is highly dependent on the quality of the coronary CT angiography. The latter relies upon the staff expertise and the quality of the CT component of the hybrid PET/CT scanner.

A more straightforward approach for ^{18}F-NaF uptake quantification has also been described. The global coronary method of analysis utilizes the low-dose CT data acquired for attenuation correction purposes (Alavi, Werner, & Høilund-Carlsen, 2017; Beheshti et al., 2011; B. A. Blomberg et al., 2015). Regions of interest are drawn around the entire heart and as a result both the PET acquisition and image analysis are simplified. There is no need for prospective ECG gating and the radiation dose is smaller. Image analysis can be performed by readers without experience in reporting coronary angiography. Unfortunately, this approach has several limitations. First of all, its specificity is suboptimal in all patients presenting with non-coronary ^{18}F-NaF uptake. For instance, it can be very difficult to distinguish valvular calcification that lays in close proximity from coronary plaques. This is often the case for the left main stem and aortic valve or the circumflex artery and the mitral annulus (Bellinge et al., 2018). Further since the global method does not provide insights into coronary anatomy it cannot be used to inform invasive angiography. Finally, because this approach averages the signal from the entire coronary vasculature it does not allow for appreciating single plaque activity and therefore fails to depict high-risk/ vulnerable plaques.

While there are multiple advantages of using CT angiography for anatomical reference for analyzing ^{18}F-NaF uptake it has several limitations which hamper its practical implementation into a meaningful clinical workflow. To date studies have utilized CT angiography acquired using hybrid PET/CT scanners during a single

imaging session. This approach, however, does not lend itself to patient selection for imaging based on prior CT angiography findings. If the ^{18}F-NaF imaging becomes part of a clinical assessment strategy, it is likely that patients should be selected for ^{18}F-NaF PET based on the findings of a CT angiography performed for clinical purposes. Another key limitation of the single session hybrid PET/CTA protocol is that it may not allow for the use of optimal CT equipment for CT angiography which may only be available on standalone CT scanners. Finally, the use of hybrid PET/CTA requires multi-faceted staff expertise in both PET and coronary CT angiography during a single session. An acquisition protocol which would enable taking full advantage of CT angiography and in the same time mitigate the aforementioned limitations is desirable.

1.6.3 Image reconstruction and optimal measure for ^{18}F- sodium fluoride PET.

Another potential aspect of ^{18}F-NaF PET which requires attention is image reconstruction. It is widely recognized that successful imaging of microcalficiations requires not only an ideal radiotracer that reflects the biology of the disease but also the technology and a measurement system that is both accurate and precise. While in the near future improved spatial resolution and implementation of partial-volume correction on future PET/CT scanners may to some degree improve accuracy of ^{18}F-NaF PET, nowadays incorrect reconstruction approaches may distort the study results (Jacobo Cal-Gonzalez et al., 2018).

The number of iterations, the use of filtering, applying point spread functions as well as taking full advantage of the time of flight and resolution recovery techniques all have a profound impact on the uptake values (Huet, Burg, Le Guludec, Hyafil, & Buvat, 2015; Jaskowiak, Bianco, Perlman, & Fine, 2005). In a recent study Doris et al. showed how particular settings affect the signal to noise ratio and influence image

quality. The authors demonstrated that while more iterations and no post-filtering result in higher SUVmax and TBR values, such images are excessively noisy and difficult to interpret (Mhairi K. Doris et al., 2018). It appears that standardization of reconstruction parameters would be an important step in disseminating ^{18}F-NaF PET as it would enable making direct comparisons between centers. Uniform reconstruction parameters would also allow for establishing reference values (Figure 3).

Figure 3. The effect of different PET reconstructions on visual image quality in the original diastolic, summed and motion-corrected images in a patient with a positive culprit lesion in the left main coronary artery. The PET reconstruction using 4 iterations and 5-mm post-filtering was considered to provide superior image quality (TBR=1.92 for motion-corrected image). This figure was originally published in JNC under the Creative Commons Attribution 4.0 International License (http://creativecommons.org/licenses/by/4.0/). Doris MK, Otaki Y, Krishnan SK et al.: Optimization of reconstruction and quantification of motion-corrected coronary PET-CT. J Nucl Cardiol. 2018 © The Author(s) 2018.

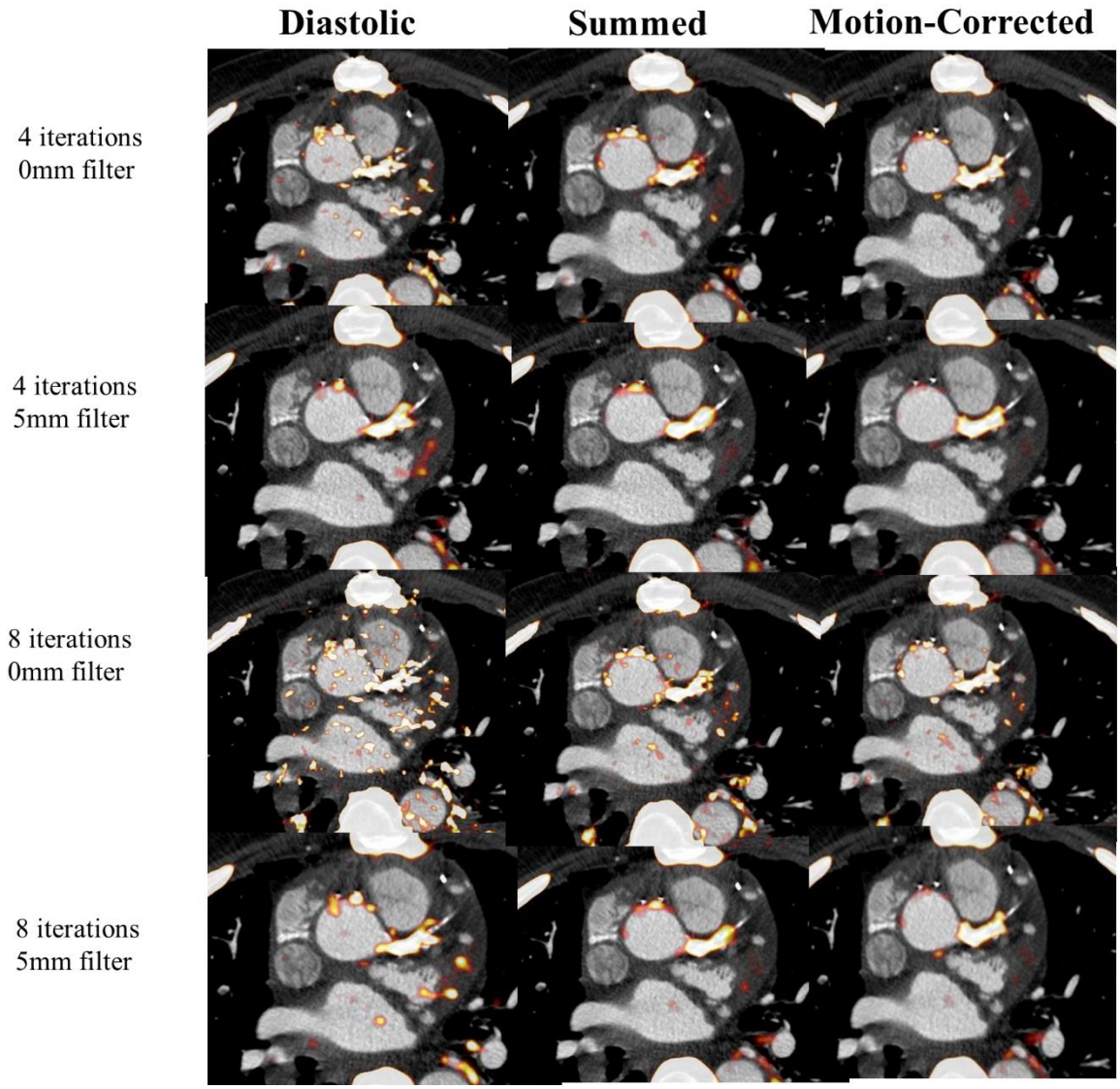

Similarly, standardization of the uptake measurement utilized would be beneficial. While target to background ratios (TBR) remain the most widely used measure, in the context of coronary imaging usually maximal TBR values (derived by dividing the target's maximum SUV by the background mean) are used, at the same time for aortic valve mean TBR values have been shown to be more reproducible. Pawade et al. have systematically investigated the image analysis of ^{18}F-fluoride PET imaging of the aortic valve. The authors showed that improved scan-rescan reproducibility can be achieved using mean TBR measurements in the valve (percentage error ±10%). They concluded that this encouraging reproducibility might have implications for

application to future clinical trials, with ^{18}F-fluoride potentially providing a useful imaging end-point of drug efficacy (T. A. Pawade et al., 2016).

While in cardiovascular PET TBR has been widely utilized, in patients undergoing PET/CT imaging for the initial staging or treatment response evaluation of malignancies the maximum standardized uptake value (SUVmax) is the most commonly used parameter for measuring lesion activity (Boellaard, Krak, Hoekstra, & Lammertsma, 2004; Thie, 2004). Recently Chen et al pointed out that despite the broad application of TBR in the literature, particularly in the field of atherosclerosis PET imaging, its biologic significance and physiologic or mathematic explanation have not been provided (Chen & Dilsizian, 2015). Huet et al argued that blood activity adds to plaque activity because of the spatial blurring of PET images (which occurs as a result of the imperfect spatial resolution)(Huet et al., 2015). It was suggested that to correct for blood uptake, subtraction of venous SUV from arterial SUV would be a more rational solution than dividing the 2 measured values. The rational supporting this approach is the fact that the clearance of PET tracers from the venous blood pool can be quite variable from subject to subject, as it depends on multiple factors. As a result, dividing the vascular wall SUV with the venous blood pool SUV may introduce more variability and confusion to the TBR measurement than confidence (Chen & Dilsizian, 2015).

1.6.4 Gating for cardiovascular PET

Positron emission tomography images are affected by physiological patient motion which degrades the images qualitatively and quantitatively. Three distinct motion patterns can be observed in cardiac PET scans: cardiac contraction, respiratory motion, and patient repositioning during the acquisition.

Aside from the development of novel tracers, the improvement in the clinical assessment of cardiac disease has partly been facilitated through the continuous

improvement in the spatial resolution of the PET systems, which in current PET/CT systems offer resolutions of 2-5 mm at full-width at half maximum (FWHM)(J. Cal-Gonzalez et al., 2018; Rahmim, Rousset, & Zaidi, 2007). Correction for point spread function as well as time-of-flight imaging has become standard in many modern PET systems, which offer improved localization of the annihilation event and, thus, improved spatial recovery of the tracer distribution (Armstrong, Tonge, & Arumugam, 2014; Conti, 2011; Dasari et al., 2018; Slomka, Pan, Berman, & Germano, 2015). The high-resolution PET systems, in theory, permit accurate delineation of abnormal areas with a precision similar to the PET scanner's spatial resolution (Blankstein et al., 2014; Nensa et al., 2018; Rubeaux, Doris, Alessio, & Slomka, 2017). Unfortunately, high-resolution imaging of the myocardium and foci of microcalcification within the coronary arteries and the aortic valve is hampered by motion during the acquisitions (Nehmeh & Erdi, 2008). The detrimental impact of motion during the PET-acquisition was recognized already in 1982 when it was proposed to divide the PET-data into motion-limited bins based on the respiratory/cardiac phase (Terpogossian, Bergmann, & Sobel, 1982).

Since then several studies have investigated the effects of cardiac and respiratory motion (Chander et al., 2008; Manber et al., 2016; Rubeaux, Joshi, Dweck, Fletcher, Motwani, Thomson, Germano, Dey, Li, et al., 2016; Teras et al., 2010; Thielemans et al., 2014). Despite the fact that all motion patterns have equally detrimental effects on image quality, to date the focus has been primarily on cardiac contraction(Dawood et al., 2009; Shechter, Resar, & McVeigh, 2006). One reason for this is the potential need for additional equipment to track motion patterns. The availability of ECG has facilitated employing cardiac gating into clinical practice.

1.6.4.1 Cardiac gating

Nowadays in the clinical setting usually 3-lead ECG is utilized (Nekolla, Dinges, & Rischpler, 2013). With the lead data being directly transferred to the scanner both retrospective and prospective gating of the acquired PET is feasible. The use of 3-lead electrocardiograms (ECG) is relatively easy, cheap and has been shown to be reproducible in many studies (Nekolla et al., 2013). Aside from the gating functionality it also serves to monitor the patient during the acquisition. The acquired ECG signal employs the R-wave as a reference to estimate the cardiac phase in which each coincidence was acquired, ultimately allowing the data to be sorted into near motion-free cardiac gates (Figure 4). Cardiac gating in most modern systems is performed retrospectively. Prospective gating is mainly used in older PET systems where listmode storage is not feasible and relies on defining phases in relation to the peak of the R wave. Such phases can be defined as preceding the R wave (backward gating) of occurring after it (forward gating). In both scenarios, the annihilation events can be sorted into predefined sinogram buffers and reconstructed once the acquisition is completed.

Figure 4. Principle of ECG-gating, here shown using a 10-bin ECG-gating. The acquired PET-data for each R-R interval is divided into a user-specified number of phases of the cardiac contraction.

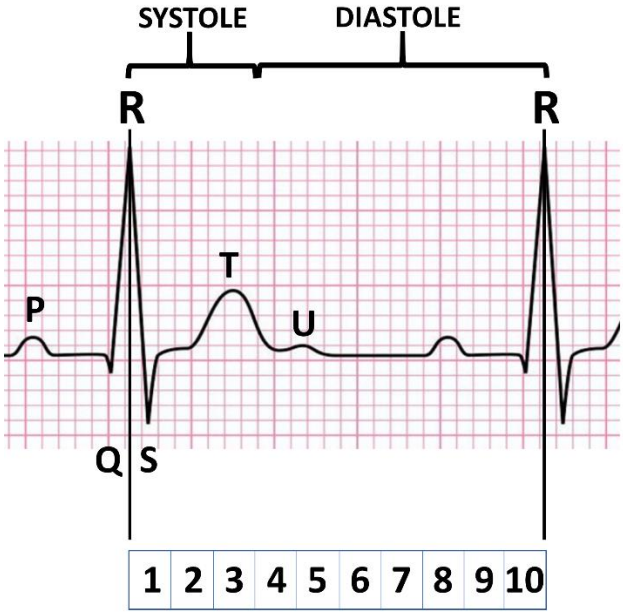

Cardiac gating can serve two functions: (1) it can be used for motion compensation of the myocardium and (2) for functional assessment of the myocardium (Le Meunier et al., 2011). The functional assessment provides both diagnostic and prognostic value in the clinical assessment of global cardiac function (left ventricular ejection fraction, LVEF), regional wall motion abnormalities and myocardial dyssynchrony (AlJaroudi et al., 2012; Pazhenkottil et al., 2011). The motion-compensated images are mainly used for research purposes while the functional assessments are used in the clinical routine. Analyses of the functional parameters have shown that an increase in LVEF (from baseline to peak stress) is inversely related to the magnitude of ischemia and the extent of angiographic CAD (T. L. Y. Brown, Merrill, Volokh, & Bengel, 2008; Dorbala et al., 2007). In patients with multivessel CAD, LVEF often shows a blunted response or can even drop on stress imaging. The change in LVEF during peak stress has been shown to have value for risk prediction (Dorbala et al., 2009; Lertsburapa et al., 2008). Importantly, cardiac gating has been proven a strong tool as a first approach in the assessment in the coronary plaques as the coronary arteries can shift up to 26 mm during the cardiac cycle (Figure 5A)(Dilsizian et al., 2016; Rubeaux, Joshi, Dweck, Fletcher, Motwani, Thomson, Germano, Dey, Berman, et al., 2016). ECG gating can be also leveraged to perform cardiac motion correction and therefore compensate for heart contractility. This approach has already been shown to improve signal to noise and TBR of coronary plaques (Figure 5B)(Rubeaux, Joshi, Dweck, Fletcher, Motwani, Thomson, Germano, Dey, Li, et al., 2016). More recently Doris et al showed that a similar algorithm can be utilized for aortic valve ^{18}F-NaF imaging. In a feasibility study the authors demonstrated that such motion correction improves both signal to noise and target to background ratios (M. K. Doris et al., 2017).

Figure 5. Displacement of the coronary arteries during the cardiac contraction. The right coronary artery shifts by 8-26 mm during cardiac contraction - yellow arrows (A). Motion correction of physiological motion of the right coronary artery (B). Systolic excursion of the tricuspid annular plane leads to displacement of the PET signal during the cardiac cycle (zoomed area of interest in blue squares). The difference in the shift of PET from reference is shown on the end-systolic (top-right) and late-diastolic (mid right) images. Green arrows represent the vectors of mid RCA motion. By co-registration of all PET data to the reference end-diastolic gate, the final motion corrected image is corrected for the 14mm mid RCA motion (bottom-right). Panel B of this figure was originally published in JNC under the Creative Commons Attribution 4.0 International License (http://creativecommons.org/licenses/by/4.0/). Doris MK, Otaki Y, Krishnan SK et al.: Optimization of reconstruction and quantification of motion-corrected coronary PET-CT. J Nucl Cardiol. 2018 © The Author(s) 2018.

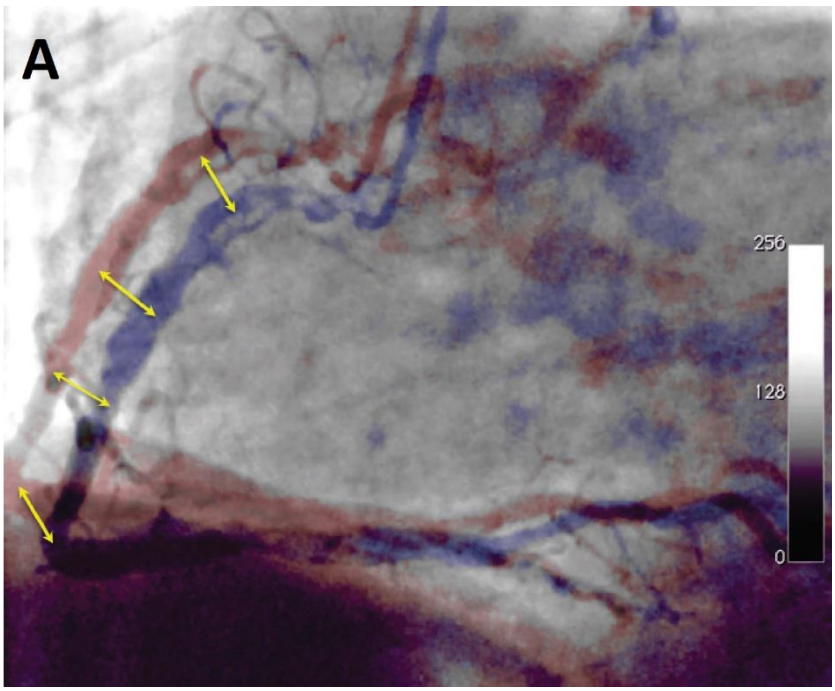

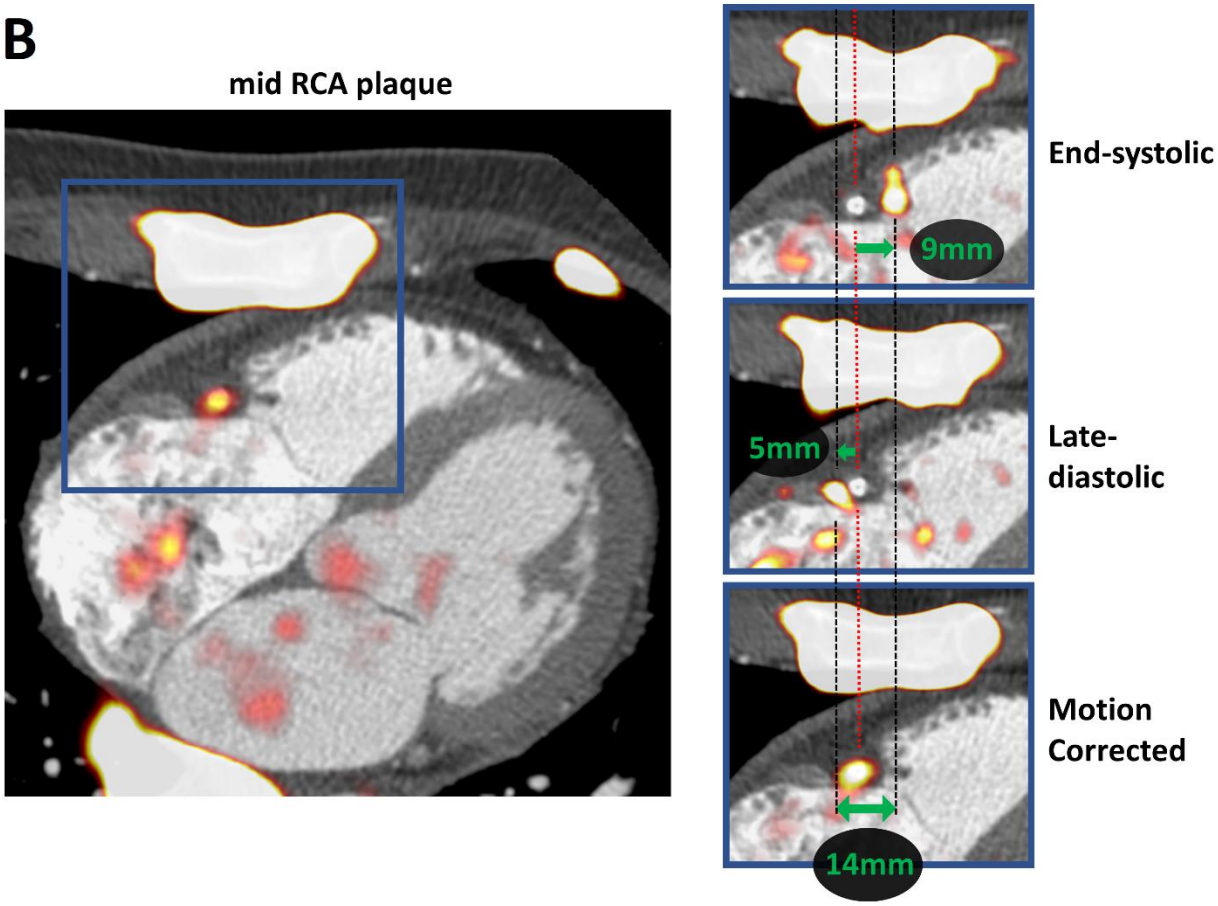
B
mid RCA plaque
End-systolic
9mm
Late-
diastolic
5mm
Motion
Corrected
14mm

1.6.4.2 Respiratory gating

Respiratory gating is desired in the clinical settings to improve image quality but is not often utilized in many modern systems which only allow for one form of gating during the reconstruction (ECG or respiratory gating). In systems facilitating dual-physiological trigger events (cardiorespiratory signals), the respiratory signal may be extracted using external markers such as piezo-electric respiratory belts or infra-red systems (Nehmeh & Erdi, 2008). Other solutions employing spirometers, and measurements of the nasal temperature/humidity have also been successfully tested (Buther et al., 2009). Respiratory gating employing external markers has several drawbacks. These include: a time-consuming imaging setup , potential malfunction during the acquisition and rather rigid monitoring of the respiratory signal which results in less robust monitoring in patients with changes in the respiratory baseline (Giraud & Garcia, 2010; M. L. Lassen, Rasmussen, Christensen, Kjaer, & Hasbak, 2017; C. Liu, Pierce, Alessio, & Kinahan, 2009). Owing to the complex setups, the introduction of respiratory gating is still mainly a tool applied in research-studies primarily in centers with technical personnel who can maintain the systems.

1.6.4.2.1 Data driven respiratory gating

To overcome the drawbacks of the external markers, the tendency in recent research is to replace the external markers using data-driven methods (Adam L. Kesner et al., 2014). The data-driven methods offer several benefits over the use of external markers: First, the data-driven methods do not require frequent calibrations as they extract the respiratory signal directly from the list files. Second, they allow for ad-hoc correction of all acquisitions acquired in listmode format, whereas careful planning is needed when using external markers. A third benefit is that the data-driven methods do not require the user to buy any additional hardware, which can be costly both to acquire and install.

In addition, the data-driven methods, in general, have the potential of facilitating accurate gating in patients with changes in the respiratory baseline, a frequent problem in myocardial perfusion imaging where stress scans are performed after administration of pharmaceutical agents. The common agents (adenosine, dipyridamole, and regadenoson) all have short half-lives, which require optimized stressing protocols such that the maximum effect is obtained during the infusion of the PET-tracer. Given the fast roll-off effect of the pharmaceuticals, it is not uncommon to encounter changes in the respiratory base-line during the acquisition (Memmott, Tonge, Saint, & Arumugam, 2018; Watt & Routledge, 1985). If not corrected for, the change in the respiratory baseline might introduce a degradation of the gated images in comparison to the non-gated images (Gould, 2017). Here, data-driven gating approaches allow for tailored gating-approaches that fits the stress-imaging protocol and, thus, have the potential of outperforming the use of the external markers which often are calibrated to the respiratory baseline at the beginning of the acquisition (Dawood, Buther, Lang, Schober, & Schafers, 2007; M. L. Lassen et al., 2017).

1.6.4.2.2 Sensitivity based methods

The first attempts at extracting information of the respiratory motion directly from the PET-raw data (list files) were proposed by Bundschuh et al and He et al (Bundschuh et al., 2007; He et al., 2008). These methods, in brief, are based on the heterogeneous sensitivity profiles that exist in all PET-systems. The sensitivity profile is partly introduced by the geometry of the system and partly by the detector materials used (Eriksson et al., 2007). Owing to the geometry in the PET system, the highest sensitivity is obtained in the center of the field of view. Heterogeneous objects moving in and out of the center field of view will result in changes in the obtained count rates equivalent to the motion in the scanners axial direction. For patient scans, the

heterogeneous uptake rates are obtained through differences in the tracer distribution as well as differences in the linear attenuation coefficients in the lungs and diaphragm.

1.6.4.2.3 Center-of-Mass/centroid-of-mass based methods

The center-of-mass or centroid-of-mass (CoM) based approaches have gained substantial interest in imaging of organs with focal uptake and high contrast to background ratio, such as myocardial scans and in studies of non-small cell lung cancers. Several methods relying on this assessment have been proposed, using either the full field of view or through detection of localized motion vector fields (Buther et al., 2009; Buther et al., 2010). The CoM assessment, in brief, evaluates the centroid of the counts obtained in the region of interest using single-slice rebinned sinograms (SSRB), which are marked by the user in most cases (Daubewitherspoon & Muehllehner, 1987). The SSRB algorithm, in short, is an algorithm that compresses the full 3D sinograms into a reduced 3D sinogram. By performing the compression, the noise is reduced and provides a more stable respiratory signal. This omits the varying sensitivity profiles and, thus, provides a more stable measurement of the respiratory cycle even for lesions slightly misplaced from the center of the systems field of view.

1.6.4.2.4 Sinogram Fluctuation model

The sinogram fluctuation model evaluates the fluctuations obtained in sinograms with short time duration (~500ms). Following their binning, the sinograms can be evaluated for the periodicity of the signal changes in each of the short time-duration datasets, thus, permitting extraction of the respiratory signal using only data with frequencies within the normal respiratory range (2-9 s periodicity)(A. L. Kesner & Kuntner, 2010).

1.6.4.2.5 Respiratory gating: Phase vs amplitude

Once acquired, the respiratory signal can be used for gating in multiple ways where phase-based/time-based (similar to the ECG-based gating approaches) and amplitude-based gating are the two most common approaches (Figure 6)(Dawood et al., 2007).

1.6.4.2.5.1 Time-based / Phase-based gating

The phase-based method is the most simplistic method of the two, where each respiratory phase is divided into a user-defined number of phases, each with equal time-duration (Dawood et al., 2007). This ensures homogeneous noise-levels for all gates, which is beneficial in the subsequent analyses. Unfortunately, this method does not allow for differentiating between normal tidal breathing and sudden excessive in/expiratory breath-holds or changes in the respiratory baseline.

1.6.4.2.5.2 Amplitude-based gating

The amplitude-based gating offers more accurate gating than the time-based/phase-based gating approach. Despite the superiority in providing high spatial differentiation of data from different respiratory amplitudes, this technique also has its limitations. The highly dynamic range of respiratory signals often hampers its functionality and, thus, most often requires truncation or discarding of data outside the normal range to ensure enough counts to provide clinical image-qualities. In addition, the asynchronous respiratory cycle will often introduce inhomogeneities in the noise-characteristics in the resulting gated images with the best quality often obtained in the end-expiratory phase. Due to this, it has been proposed to use the optimal respiratory gate, which only employs data from the end-expiratory phase – known as

the optimal respiratory phase, which typically can contain up to 35% of all image counts (C. Liu et al., 2010).

Figure 6. Time-based (phase-based) gating and amplitude-based gating techniques demonstrated using 4 respiratory gates. Time-based method divides the data into equally time-divided bins that will have the same noise properties (equal time-duration, A). Amplitude-based gating divides the data into bins with the same respiratory amplitude, and thereby pose the risk of having noise-variated gates in the following assessments, as can be observed for the third respiratory cycle which does not reach the same amplitude as the preceding cycles (B).

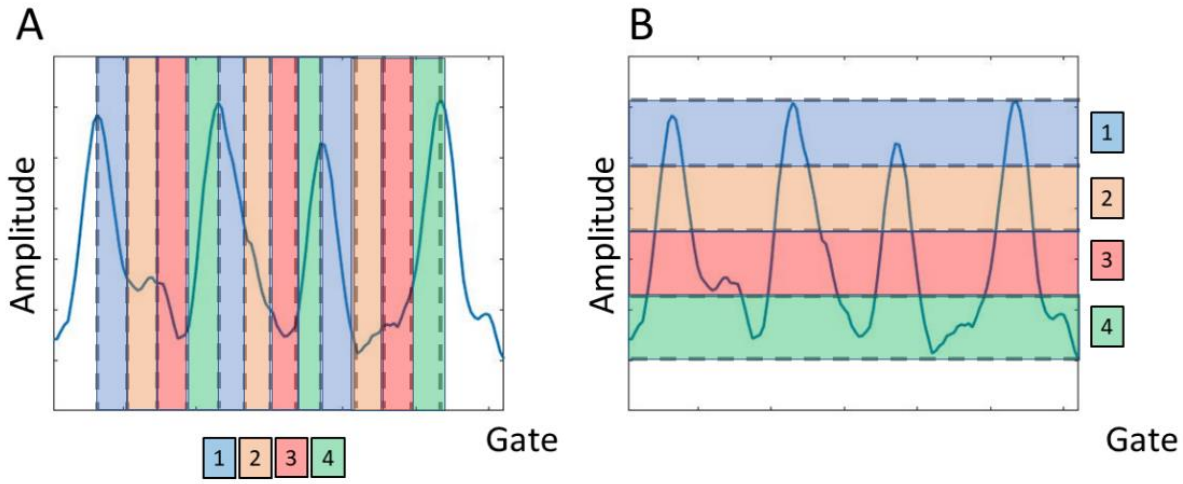

1.6.4.3 Dual gating

The single gating techniques have been proven suboptimal for many PET-scans as the non-corrected motion-pattern is still embedded in the resulting images. Dual-gating approaches, which combine the cardiorespiratory motion, have been proposed (Gigengack et al., 2012; Hyun, Gerlach, Rubeaux, & Slomka, 2017; Lamare et al., 2014; Teras et al., 2010). The combination of the two gating techniques ensures virtually motion-free images, with only little intra-gate motion present (Figure 7). Unfortunately, this requires sufficient image quality (count rates per single gate) in the subsequent reconstructions, as often up to 16-64 gates are being utilized. The exact number depends on how many respiratory and cardiac gates are used (N Respiratory gates × N cardiac gates) with N being the number of the respective gates (Martinez-Moller, Zikic, et al., 2007; Slomka, Rubeaux, et al., 2015).

Figure 7. Dual-gating scheme. Example of a dual gating scheme employing 4 ECG and 8 respiratory bins, which creates a total of 24 virtually motion-free images. Each of the gated images can be co-registered to obtain images with reduced noise properties when compared to the noise in each individual gate. This research was originally published in JNM. Slomka PJ, Rubeaux M, Le Meunier L, et al. Dual-Gated Motion-Frozen Cardiac PET with Flurpiridaz F18. J Nucl Med. 2015;56(12):1876-1881. © SNMMI.

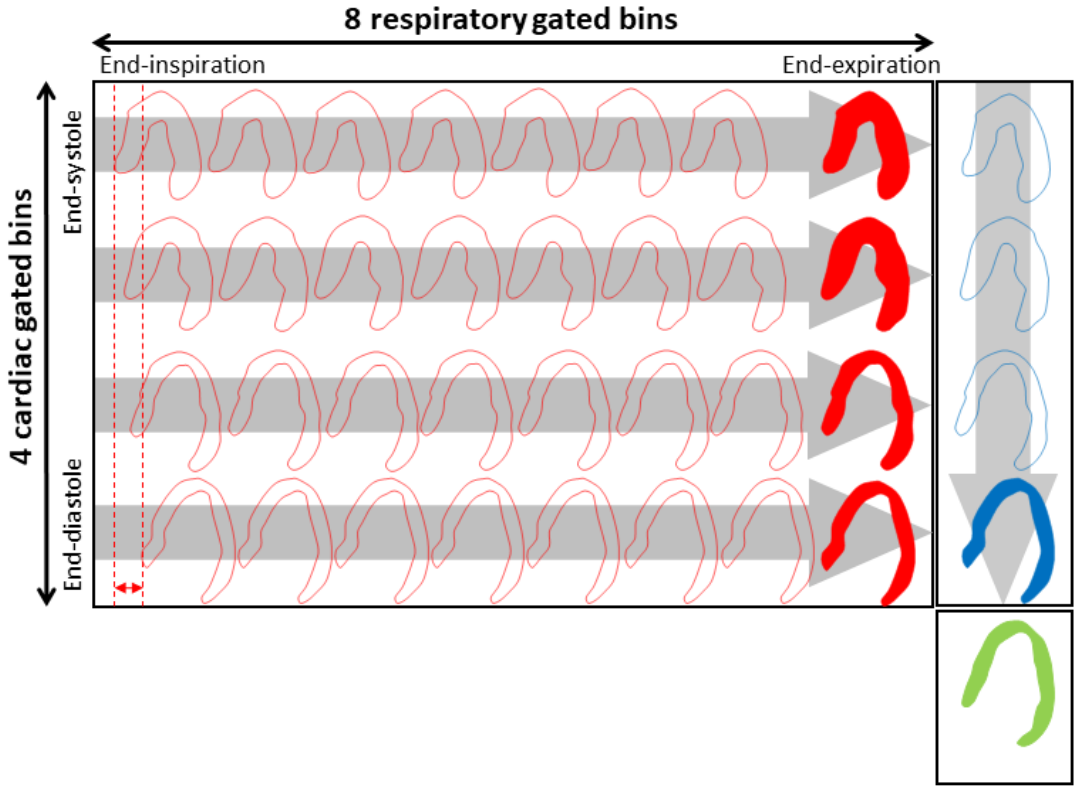

1.6.4.4 PET attenuation correction issues resulting from motion

Attenuation correction (AC) is an important prerequisite for absolute quantification in all PET imaging. Several attenuation correction techniques have been proposed, depending on the modality (PET-only, PET/CT or PET/MRI)(Chesler, 1971; Kinahan, Hasegawa, & Beyer, 2003; Martinez-Moller et al., 2009). Several drawbacks and limitations have been described for the AC maps, disregarding the acquiring modality. The drawbacks include both physiological and technical aspects such as beam-

hardening, misalignment, truncation as well as non-physiological artifacts. In the context of gating, especially the misalignment artifacts are particularly relevant.

Misalignment of the PET-emission data and the AC-images can be classified either as repositioning events where the patient moves between the acquisition of the AC maps and the PET-emission data, differences between the respiratory-gated PET-images and the corresponding AC maps or as breathing during the AC acquisition (Figure 8)(Gould et al., 2007; Martin Lyngby Lassen et al., 2017; Martinez-Moller, Souvatzoglou, Navab, Schwaiger, & Nekolla, 2007).

Respiratory motion during the PET-images translates the heart up by up to a few centimeters. Due to the fast acquisition times of the AC images (a few seconds in CT), respiratory motion during the acquisition is often not a problem regardless whether a free-breathing or end-expiratory breath-hold acquisition protocol is utilized (Beyer et al., 2016). Employing cine CT for PET/CT has been suggested (Pan et al., 2006). This allows reconstructing a respiratory-averaged AC map with the same displacements as obtained during the cine CT acquisition.

Figure 8. Displacement of PET-emission data and the attenuation correction (AC) maps (A) can cause local changes of more than 80% in the quantitative assessment (B, C). Correction for the misalignment of the AC maps and PET-data reduced the extent and severity of the hypometabolic region (D, E). The displacements can be introduced through respiratory motion during the PET-acquisition or by patient repositioning between the acquisition of the AC map and the PET data. This figure was originally published in JNC under the Creative Commons Attribution 4.0 International License (http://creativecommons.org/licenses/by/4.0/). Lassen ML, Rasul S, Beitzke D, et al.: Assessment of attenuation correction for myocardial PET imaging using combined PET/MRI. J Nucl Cardiol. 2017:1-12 © The Author(s) 2017.

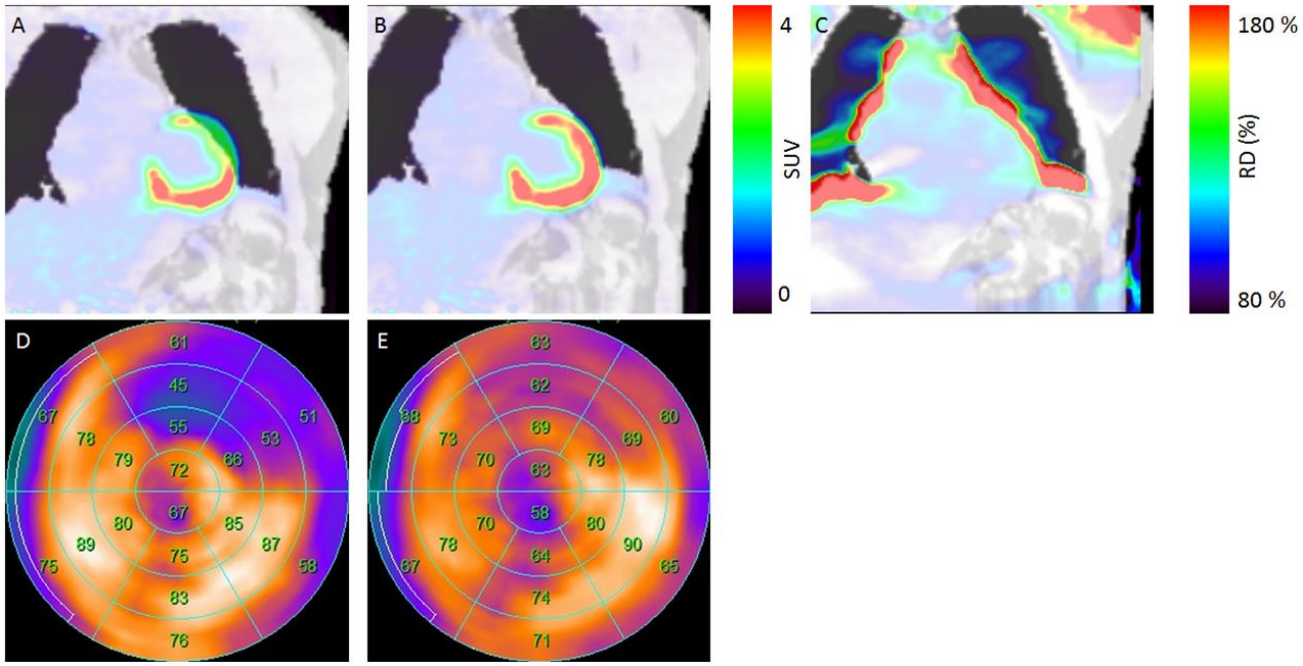

1.6.4.5 Future directions

Cardiorespiratory motion has been investigated by many researchers and several gating approaches have been proposed. The use of external markers has been used in the conventional assessment of the displacement during the acquisition. However, recent trends indicate that data-driven gating techniques are an emerging technology that will permit marker-less motion detection in clinical routine. These gating techniques mainly focus on respiratory motion detection, though cardiac gating might also be possible as demonstrated for the first time in 2009(Buther et al., 2009; Adam L. Kesner et al., 2014). While these established techniques might replace the conventional external marker methods, the potential of data-driven detection of patient repositioning events is another interesting field of research. A recent pilot study has shown that such techniques are feasible in coronary plaque studies, in which gross patient motion has a detrimental effect on the quantitative accuracy (Martin Lyngby Lassen et al., 2018). Furthermore, it is believed that also tracer-kinetic studies for novel PET-tracers which scanning protocols can last up to one hour or more will benefit from patient repositioning detection, ultimately enabling triple-gating or application of sophisticated combinations of various gating techniques (Piccinelli, Votaw, & Garcia, 2018).

Moreover, the use of gated images is expected to be implemented in motion compensation techniques, either during or before image-reconstruction. This will improve the image quality of the static images, where accurate definition of pathophysiological changes can be difficult in the gated images due to the increased noise levels. By correcting for the motion during image-reconstruction, it is possible to obtain a fully motion compensated image with the spatial resolution similar to gated images, with the noise characteristics of the static image-acquisitions. In addition, the motion compensated images can also reduce the respiratory blur in the ECG-gated reconstructions and, thus, lead to improved quantification of left ventricular volumes

for function assessments. Therefore, gating will become increasingly important in the future not only for the definition motion but also in the pursuit of accurate assessment of physiological parameters.

1.7 Thesis aims and hypotheses

The over-arching aim of this multimodal thesis is to investigate the potential of cardiovascular magnetic resonance imaging to refine risk prediction and to improve the imaging protocol of ^{18}F-NaF PET for aortic stenosis.

The aims of the thesis are:

1. To assess asymmetric wall thickening in patients with aortic stenosis using both cardiovascular magnetic resonance and echocardiography and characterize the factors associated with this pattern of remodelling, its relationship with markers of left ventricular decompensation and to evaluate its prognostic implications.

2. To develop a mouse model of left ventricular hypertrophy and reverse remodelling in response to a reversible state of increased left ventricular afterload. Ultimately, we aimed to create a model to provide insight in to the optimal timing for aortic valve implantation.

3. To assess the gender differences and determinants of diffuse and focal myocardial fibrosis in patients with aortic stenosis.

4. To assess the feasibility of utilizing a previously acquired CT angiography with a subsequent PET-only ^{18}F-NaF scan for the evaluation of cardiac ^{18}F-NaF PET uptake.

5. To quantitatively assess whether delayed 3-hour post-injection state-of-the-art PET scanning improves image quality and ^{18}F-NaF uptake measurements.

The hypotheses of the thesis are:

1. Asymmetric wall thickening is a distinct pattern of LV remodeling under pressure overload and particular imaging modalities differ in their capacity to depict it.

2. By inducing increased afterload mice hearts undergo adverse remodeling which resembles the transition from a normal heart to decompensation as observed in patients with aortic stenosis.

3. The burden of diffuse and replacement fibrosis is different in females compared to males suffering from aortic stenosis.

4. CT angiography acquired before ^{18}F-NaF PET used for anatomical reference enables reliable assessment of the PET tracer uptake.

5. Delayed: 3-hour post injection ^{18}F-NaF PET improves image quality and uptake measurements compared to a 1-hour post injection acquisition.

Chapter 2. Methods

2.1 Overview

Chapters 3 and 5 have been based on an analysis of ongoing prospective observational cohort studies. Chapter 4 was a preclinical study conducted on small rodents (mice). Chapters 6 and 7 have been based on data collected for a randomized controlled trial and multicenter prospective observational study. The specific study designs and methodology for each of the cohorts are described in detail in the following chapters. Below I present an overview of the patient populations and imaging modalities utilized in these studies.

2.2 Patient population

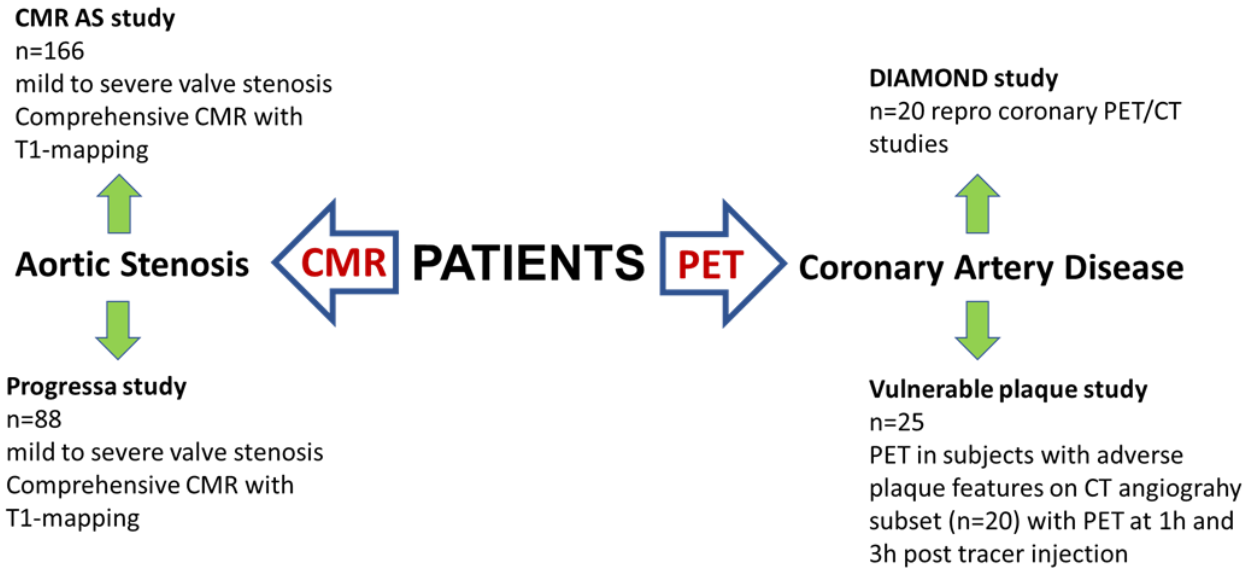

Figure 9. Overview of patient cohorts included in the studies conducted as part of the thesis.

2.2.1 Patients with Aortic Stenosis

2.2.1.1 *Inclusion criteria*

Patients with at least mild AS (peak aortic jet velocity [Vpeak] ≥2.0 m/s) were recruited from two prospective observational cohort studies (Metabolic Determinants of the Progression of Aortic Stenosis (PROGRESSA) NCT01679431; Quebec Heart and Lung Institute and Role of Fibrosis in Aortic Stenosis NCT01755936; Edinburgh Heart Centre, United Kingdom)

2.2.1.2 *Exclusion criteria*

We excluded patients with other forms of valvular heart disease (moderate or severe in nature), end-stage heart failure, advanced malignancies or other comorbidities with a life expectancy < 2 years, cardiomyopathies (including previous myocarditis), and contraindications to gadolinium enhanced magnetic resonance, such as ferromagnetic foreign bodies and estimated glomerular filtration rate< 30mL/min/1.73 m2. Coronary artery disease was defined as previous myocardial infarction, documented evidence of myocardial ischaemia or a> 50% stenosis of the coronary artery lumen.

2.2.2 Patients with Coronary Artery Disease

We recruited patients within a prespecified reproducibility substudy of an ongoing randomized clinical trial - DIAMOND (Dual antiplatelet therapy to Inhibit coronary Atherosclerosis and MyOcardial injury in patients with Necrotic high-risk coronary plaque Disease) and an observational study of stable patients with borderline coronary stenosis in the main epicardial vessels on CTA and high-risk plaque features by visual and quantitative plaque analysis – Vulnerable Plaque study.

2.2.2.1 *Inclusion criteria*

For DIAMOND patient inclusion required the presence of multi-vessel coronary artery disease (defined as at least two major epicardial vessels with any combination of either >50% luminal stenosis, or previous revascularization (percutaneous coronary intervention or coronary artery bypass graft surgery on invasive angiography in the context of stable coronary artery disease.

In the vulnerable plaque study patient inclusion required a coronary HRP defined by having at least three of the following adverse plaque features by quantitative plaque analysis of CTA performed for clinical purposes in stable subjects: 1) positive remodeling (remodeling index >1.1); 2) low attenuation plaque (LAP) (<30 HU); 3) obstructive coronary stenosis defined by a vessel stenosis ≥50% or contrast density difference (the difference between the lumen opacity proximal and distal to the plaque) ≥25% (13); 4) plaque volume >100mm3 or plaque burden (lesion volume normalized to the vessel volume) ≥40%; 5) spotty calcification on visual CTA assessment. Those who displayed HRP on CTA were invited to participate in a research ^{18}F-NaF PET-CT scan.

2.2.2.2 Exclusion criteria

For the DIAMOND trial exclusion criteria included an acute coronary syndrome within the previous 12 months, renal dysfunction (eGFR ≤30 mL/min/1.73 m2) and contraindication to iodinated contrast agents.

From the second cohort we excluded patients younger than 18 years, with elevated creatinine>1.5 mg/dL, pregnant or breastfeeding females, subjects with significant arrhythmia including multiple premature ventricular or atrial contractions, patients with an ejection fraction <35% or class III congestive heart failure. Finally, individuals who had a known iodine contrast allergy, were unable to take beta blockers or were unable to provide informed consent were also excluded.

2.3 Magnetic Resonance Imaging

Imaging was performed with 1.5 and 3 Tesla scanners (Quebec: Philips Achieva or Philips Ingenia, Philips Healthcare, Best, The Netherlands; Edinburgh: Magnetom Verio, Siemens AG, Erlangen, Germany). A balanced steady-state free precession sequence was used for short-axis cine imagining.

T1 mapping was performed using the Modified Look-Locker Inversion recovery sequence for the assessment of diffuse myocardial fibrosis. Short-axis T1 maps of the mid-cavity were acquired in diastole before and 20min after the administration of 0.1mmol/kg of gadobutrol (Gadovist, Bayer Pharma AG, Germany) using a dedicated 32-channel anterior-posterior cardiac array.

Late gadolinium enhancement (LGE) was used for detection of focal replacement fibrosis. Acquisition was performed between 8 and 15 min after gadobutrol (Gadovist, Bayer Pharma AG, Germany) administration using an inversion recovery fast gradient-echo sequence and a phase sensitive inversion recovery sequence in two phase-encoding directions in order to distinguish true enhancement from artefact. The inversion time was optimized to achieve adequate nulling of the myocardium.

2.3.1 Image analysis

Image analysis was performed offline (cvi42, Circle Cardiovascular Imaging Inc., Calgary, Canada) in core laboratories using standardized approaches by trained operators supervised by Eric Larose in Quebec and Marc Dweck in Edinburgh following the current guidelines (Le Ven et al., 2016). The left ventricular longitudinal function was determined by measuring the difference in mitral annular displacement between end-systole and end-diastole. On short-axis cine images, epicardial and endocardial contours were carefully identified and planimetered in end-systole and end-diastole for left ventricular volume quantification. The left ventricular mass was calculated from the total myocardial volume (excluding trabeculations and papillary muscles) multiplied by the density of the myocardium (1.05 g/mL). All volumes and mass values were indexed to body surface area (calculated using the Du Bois formula). Focal replacement fibrosis and extracellular volume (ECV) fraction were assessed using late gadolinium enhancement (LGE) and T1 mapping respectively. LGE was performed 15 min following administration of gadobutrol (Gadovist, Bayer Pharma AG, Germany; 0.2 mmol/kg [Quebec], 0.1 mmol/kg [Edinburgh]). The presence of LGE was determined both qualitatively and quantitatively, and its distribution recorded. T1 mapping was performed using the Modified Look-Locker Inversion Recovery (C. W. L. Chin et al., 2017).

2.4 Echocardiography

All participants underwent a transthoracic echocardiographic examination for the assessment of aortic stenosis and cardiac function on iE33, Philips Medical Systems, The Netherlands. The severity of aortic stenosis was classified on the basis of the aortic jet peak velocity, the mean pressure gradient and the aortic valve area derived using the continuity equation. All assessments were conducted in accordance with European Association of Echocardiography/American Society of Echocardiography (ASE) guidelines (Baumgartner et al., 2009). Transmitral early (E) and late diastolic velocities and deceleration time were measured at the tips of mitral valve leaflets using pulse wave Doppler. Pulse-wave tissue Doppler imaging was used to evaluate the early (e') diastolic velocities of the medial and lateral mitral annulus. Diastolic function was determined using the E/e' ratio. The left ventricular mass was calculated using wall thickness measurements and cavity dimensions (ASE formula) and indexed to body surface area (Lang et al., 2015). Cut-off values of 115 g/m2 for males and 95 g/m2 for females were used to distinguish subjects with left ventricular hypertrophy.

2.5 Positron emission tomography – computed tomography imaging

2.5.1 Coronary CT angiography

Diamond trial patients had the coronary CT angiography (CTA) scan performed on the 128-slice Biograph mCT scanner (Siemens Medical Systems, Erlangen, Germany) using the following settings: 330 ms rotation time, 100 or 120kV (depending on body mass index), 160-245 mAs. The second cohort underwent CTA on a dual source CT scanner (Definition; Siemens Medical Systems, Erlangen, Germany). The scan parameters were as follows: 330 ms gantry rotation time, reference tube current of 400 mAs per rotation, and a tube voltage of 120 kVp. Patients in both cohorts received beta blockers (orally or intravenously) to achieve a target heart rate <60beats/min and sublingual nitrates. A bolus of 60-100 mL of contrast (300-400 mgI/mL; Iomeron) was power injected intravenously at 6 mL/s, after determining the appropriate trigger delay with a test bolus of 20 mL contrast. Transverse images were reconstructed using filtered back projection with 0.75/0.6 mm slice thickness, 0.4 mm increment and a medium-soft convolution kernel.

2.5.2 ^{18}F-sodium fluoride PET

Prior to the PET imaging, 250 MBq of ^{18}F-sodium fluoride was injected intravenously and patients rested in a quiet environment for 60 minutes. Because emission scanning was followed by CTA during that hour subjects were administered with beta-blockers. Patients were acquired on 2 different PET/CT scanners 128-slice Biograph mCT, Siemens Medical Systems (DIAMOND cohort) and 128-slice Discovery 710 (GE Healthcare, Milwaukee, WI, USA (Cohort 2). In both cohorts low-dose CT attenuation correction scan (120 kV, 50 mAs, 3 mm slice thickness), a 30-min single bed position PET acquisition with ECG-gating in list mode was performed. Image corrections were applied for attenuation, dead time, scatter, and random coincidences. In DIAMOND patients PET data were reconstructed using a Siemens implementation of iterative reconstruction algorithm (Ultra-HD; with Point Spread function correction and time of flight reconstruction, matrix 256, Gaussian filter of 5 mm and 2 iterations and 21 subsets). In Cohort 2 data were reconstructed with GE implementation of iterative reconstruction algorithm (Sharp IR with Point Spread function correction and time of flight reconstruction, matrix 256, Gaussian filter of 5 mm and 4 iterations and 24 subsets)(Mhairi K. Doris et al., 2018).

In both cohorts, a CTA was obtained on the hybrid scanner with patient remaining on the table in the same position. In Cohort 1 identical acquisition and reconstruction parameters as CTA1 were utilized with imaging performed on the same scanner. In Cohort 2 CTA (CTA2) was acquired with rotation time 350ms, tube voltage 120 kV, tube current 150-250 mAs) and reconstructed using an adaptive statistical iterative reconstruction algorithm with 0.625 mm thick slices, a 0.625 mm increment and a medium-soft convolution kernel

2.5.2.1 Motion Correction

Cardiac motion correction was performed for the PET/CT images. This novel technique compensates for coronary artery motion by aligning all gates to the end-diastolic position, thus allowing utilization of radioactivity throughout the cardiac cycle. This method has been shown to reduce image noise and improve target to background ratios (Rubeaux, Joshi, Dweck, Fletcher, Motwani, Thomson, Germano, Dey, Li, et al., 2016). In the first step of motion correction, anatomic coronary artery data was extracted from coronary CTA by applying a vessel tracking algorithm based on Bayesian maximal paths (Autoplaque version 2.0). Second, a diffeomorphic mass-preserving image registration algorithm was used to align the 10 gates of PET data to the end-diastolic gate (FusionQuant Software, Cedars Sinai Medical Center, Los Angeles). After motion correction, the 10 gates were summed together to build a motion-free image containing counts from the entire PET acquisition.

2.5.3 Image analysis

Coronary ^{18}F-NaF image analysis was performed on axial images using FusionQuant software. PET and CTA reconstructions were reoriented, fused and systematically co-registered in all 3 planes. Key points of reference were the sternum, vertebrae, blood pool in the ventricles and the great vessels. For each scan, plaque activity was measured by delimiting 3-dimensional volumes of interest on lesions. On motion corrected images all segments with coronary plaque (at least a >25% stenosis) that were suitable for Autoplaque analysis (had a lumen diameter ≥2 mm) were interrogated. The maximum standard uptake value (SUVmax) was recorded from these regions. Background blood pool activity was measured by delimiting a cylindrical volume of interest (radius = 10 mm, thickness = 5 mm) in the right atrium on the level of the right coronary artery orifice. Target to background ratios (TBRs) were calculated by dividing SUVmax by averaged background blood pool activity.

Coronary plaques were considered positive for ^{18}F-NaF if they presented with focal tracer uptake arising from the coronary plaque which followed the course of the vessel in three dimensions over more than one slice and had a TBR>1.25.

2.6 Preclinical model of pressure overload

Continuous angiotensin II infusion is an established model of pressure overload heart disease (Lawrence et al., 1963 & Brown et al., 1981). It has been successfully used for evaluating the impact of particular genes on angiotensin mediated hypertension, the vascular results of angiotensin II including: abdominal aorta aneurysms progression, the impact of oxidative stress on the cardiovascular system and atherosclerosis development (Cassis et al., 1999; Rateri et al., 2011; Daugherty et al., 2000; Kawada et al., 2002; Bruemmer et al., 2003 & Weiss et al., 2001).

In our study we used this well described model for exploring the myocardial response to pressure overload and reverse remodeling which occurs after load normalization with advanced cardiac imaging. To date such data is not available and hence we lack detailed insights into the adverse remodeling which occurs under pressure overload. With serial imaging our study aimed to explore the complex interplay between left ventricular hypertrophy, concomitant diffuse and focal fibrosis and LV decompensation.

2.6.1 Study Protocol

Thirty-one male C57BL/6J mice (Envigo, UK) were subjected to a continuous Angiotensin II infusion at a 480±34ng/kg/min dose. Animals were split into three groups with varying duration of infusion: 2 weeks (n=5), 4 weeks (n=3), 6 weeks (n=23). Additionally, 9 animals of those receiving Angiotensin II for 6 weeks were kept for 28 days after the infusion came to an end to monitor reverse remodelling after relief of the increased afterload. Nine animals received sterile saline infusion instead of angiotensin II and these comprised the control group.

All animals underwent serial CMR imaging to assess left ventricular structure and function as well as myocardial fibrosis. CMR was performed initially at baseline before the onset of pressure overload, and then every 2-weeks during Angiotensin II infusion.

In a subgroup, CMR was performed a final time 4 weeks after the end of infusion. At the end of the final imaging session, animals were culled by exsanguination under deep anaesthesia with the heart stored for further analysis. Throughout the experiments, animals were on a regular chow diet, we housed 5 mice per cage in a 12h:12h light/dark cycle in animal facilities at the University of Edinburgh. All procedures conformed to Home Office guidance on the use of the animals (Scientific Procedures) Act of 1986 and were approved by the University of Edinburgh Animal Welfare and Ethical Review Board.

2.6.2 Animal model of pressure overload

To subject animals to pressure overload, subcutaneously implanted osmotic minipumps (Alzet, Cupertino, CA) were used (Gong et al., 2014). Minipumps were prepared to deliver Angiotensin II (Sigma-Aldrich, Darmstadt, Germany) at the rates and over a time which is characteristic for a given pump model. Implantation was performed surgically under anaesthesia. To monitor pressure overload animals underwent serial blood pressure measurements. These were carried using the Letica LE 5002 Non-Invasive Blood Pressure System (Panlab, Cornellá, Spain) which operates on the same basis as clinically used sphygmomanometers (tail cuff method). Prior to the start of the experimental protocol mice were trained to tail cuff plethysmography in order to decrease the load of stress related to taking the measurements and to improve reproducibility. During the experimental period animals were subjected to plethysmography after every imaging session. After 2 preliminary measurements, at least three recordings of systolic, diastolic and mean arterial pressure per animal were recorded.

2.6.3 Histology

After the final imaging session, animals were kept under anaesthesia and euthanized. Hearts were removed and transferred into 10% neutral buffered formalin (Cellstor, CellPath, Newton, UK) for fixation for at least 20 hours. Subsequently hearts were processed and embedded in paraffin in a short axis orientation so that the sections cut would all show the ventricle lumen. Slides were stained in a 0.1% sirius red solution in saturated picric acid (Picrosirius red, Sigma, Dorset, UK). Slide images were acquired on the AxioScan Z1 (Carl Zeiss, Oberkochen, Germany) and analysed using a dedicated software package Image-Pro Premiere 9.1 (MediaCybernetics, Rockville, MD, USA) using tissue specific threshold. The area of fibrosis was expressed as a percentage of the total myocardium area.

2.6.4 Preclinical magnetic resonance imaging

All MRI scans were performed on a 7 Tesla preclinical horizontal-bore MRI system (Agilent Technologies, Yarnton, UK) equipped with a 33mm inner diameter radiofrequency coil for mice (Rapid Biomedical, Rimpar, Germany).

Prior to imaging animals were anaesthetised using isoflurane and an Anicath 26G cannula (Millpledge Veterinary, Clarborough, UK) was placed intraperitoneally for administration of the gadolinium-based contrast agent. Animals were placed in an MRI cradle with electrocardiogram (ECG) leads placed subcutaneously. The animals were positioned supine with hearts in the centre of the coil, and in the centre of the MRI scanner. A pressure transducer was placed under the torso for constant monitoring of respiration (MR-compatible Small Animal Monitoring and Gating System, SA Instruments, Stony Brook, NY), and a rectal probe was inserted to monitor and maintain body temperature at 37 ± 0.5 °C via a feedback-controlled warm air system. Throughout the imaging session special care was taken to keep the heart rate stable at 530-600 beats/min and maintain a respiratory rate at 45-75 breaths/min.

Scout images were taken to confirm correct positioning and to orientate 1.0 mm short axis slices covering the heart. T1 mapping was performed using a Small Animal Modified Look-Locker Inversion recovery sequence with short-axis T1 maps of the mid-cavity acquired in systole (Daniel R. Messroghli et al., 2004). Such T1-mapping datasets before and after contrast injection were acquired at end-systole with the following imaging parameters: repetition time (TR): 2.8 ms, echo time (TE): 1.4 ms, trigger delay (TD): 40-60ms individually adjusted according to the equation TD=(RR interval/2) - 15ms, initial inversion time (TI) 130-165ms according to the formula: TD + RR interval, matrix size 128 x 128, field of view: 30 x 30 mm, number of signal averages: 8, flip angle: 10°, slice thickness 1.5 mm. Eight phase-encoding echos were acquired per segment. Subsequently gadobenate dimeglimine was injected via the intraperitoneal cannula, before a second T1-mapping dataset was acquired at 20

minutes post-injection. During the time between the T1-mapping acquisitions, cine images were acquired in the same orientation for structural and functional assessment. The short axis, vertical and horizontal long axis cardiac images were acquired using an ECG triggered and respiratory-gated gradient echo sequence (TR/TE = 5.2/1.3 ms, flip angle: 15°) with gradient and radiofrequency spoiling. Eighteen phases were acquired with a field of view of 30x30 mm, a 128x128 matrix, and 2 averages were used. For the left ventricular short axis, nine consecutive 1-mm-thick slices were acquired, which encompassed the entire heart from base to apex. Late gadolinium enhancement imaging was performed between 12 and 18 minutes after contrast administration with a short-axis cardiac-gated T1-weighted gradient echo inversion-recovery scan with the following imaging parameters: TR: 595ms, TE: 1.45 ms, field of view: 30 x 30 mm, number of signal averages: 4, inversion time: 560 ms, flip angle: 90°, nine 1 mm thick slices covering the entire left ventricle.

2.6.4.1 Image analysis

Data were analysed using certified software (cvi42, Circle CVI, Calgary, Alberta, Canada). The short axis cine images of the LV were used for the assessment of left ventricular volumes, mass and ejection fraction. The epicardial and endocardial contours were carefully identified and planimetered in end-systole and end-diastole for left ventricular volume quantification. The left ventricular mass was calculated from the total myocardial volume (excluding trabeculations and papillary muscles) multiplied by the density of the myocardium (1.05 g/mL). Maximal wall thickness was evaluated in all 17 segments of the LV from cine images of the LV in end-diastole (1). For diffuse fibrosis, we calculated the extracellular volume fraction (ECV%) derived from pre- and post-contrast myocardial T1 values corrected for blood-pool T1. The ECV% was calculated according to: ECV% = partition coefficient x [1-hematocrit]; where partition coefficient = [ΔR1myocardium/ΔR1blood-pool] and ΔR1 = (1/post-contrast T1-1/pre-contrast T1). In order to evaluate the total amount of interstitial fibrosis in each animal, we calculated the indexed ECV (iECV) in each animal using the following equation: ECV% x left ventricular myocardial volume, where left ventricular myocardium volume = left ventricular mass divided by the gravity of myocardium (1.05g/ml). To avoid blood-pool contamination and partial volume effects we used a mid-myocardial region of interest for the T1-mapping analysis. A two-pixel wide myocardium and ventricular boundary zone was excluded from all applicable slices. Late gadolinium enhancement was used for detection of focal replacement fibrosis. Where present, it was quantified as an area of myocardium with a signal intensity exceeding the threshold of two standard deviations above the mean value of normal myocardium. All areas of inversion artefact or myocardial regions contaminated by blood pool or epicardial fat were excluded.

2.6.4.2 Reproducibility of T1 mapping measurements

Since T1-mapping for exploring the extracellular myocardial compartment in small rodents is not a well-established technique prior to conducting the main study we performed experiments aimed at optimizing the acquisition protocol. In particular we were interested to explore how stable are the T1 post relaxation times following contrast injection. By carrying out repeated modified look-locker inversion recovery acquisitions we found that as soon as 20 minutes after intraperitoneal injection of a gadolinium-based contrast agent T1 relaxation times plateau and remained stable up to 50 minutes post injection. To reduce the length of acquisition (and hence limit the time our experimental animals were anesthetized) we decided to conduct imaging at 20 min post contrast agent infusion.

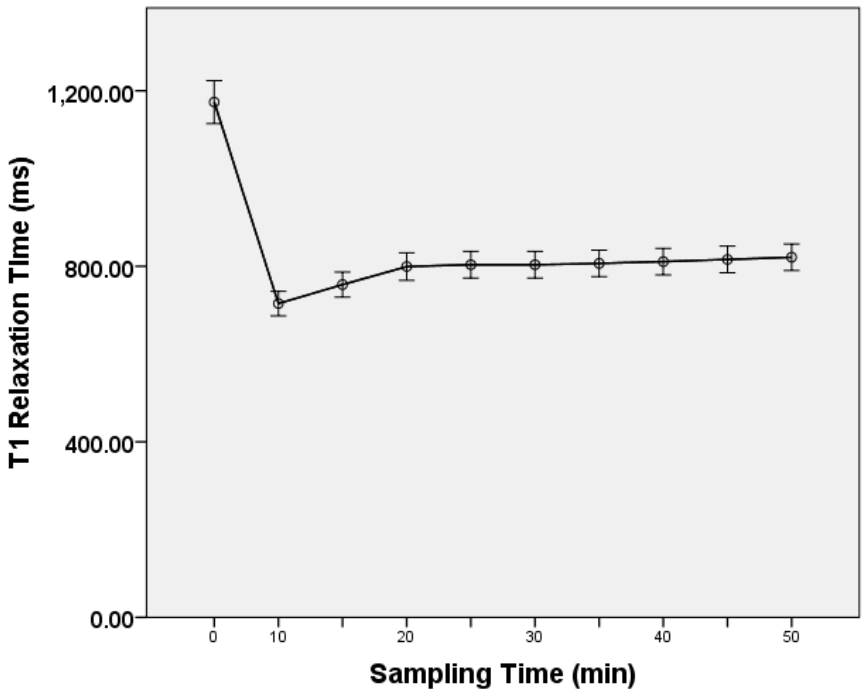

Figure 10. Variation of myocardium T1 relaxation. Post-contrast T1 values are dramatically reduced with the administration of contrast, followed by an exponential increase in values towards baseline. Significant changes in T1 were observed in the first 20 min following contrast administration, while a plateau phase was observed between 20 and 50 min where values remained relatively unchanged.

2.7 Statistical analysis

Continuous variables were tested for distribution with the Shapiro-Wilk test. Data are presented as mean±SD, median [interquartile range] or percentages were appropriate. Differences between variables were assessed with the use of a 2-sided Student T test, paired Student T test, ANOVA or the Mann-Whitney, Wilcoxon rank-sum and the Kruskall–Wallis test were appropriate. We presented all categorical variables as percentages and used the chi-square test for comparison. We used Bland-Altman plots to visualize reproducibility of PET tracer uptake measurements. The 95% normal range for differences between sets of SUV and TBR measurements (the limits of agreement) were estimated by multiplying the SD of the mean difference by 1.96 (W. A. Weber, Ziegler, Thödtmann, Hanauske, & Schwaiger, 1999). Intra-class correlation coefficients with 95% confidence intervals (CIs) were calculated for PET/CTA1 vs. PET/CTA2 scan variation. The Pitman-Morgan test was used to compare the homogeneity of variance between uptake measurements derived from diastolic gate and motion corrected datasets. In our per lesion analysis we assumed independence of lesions within patients. In the outcome analysis of patients with aortic stenosis we used Kaplan–Meier curves to elucidate the survival distributions with regard to all cause mortality and AVR. Differences in the outcome of patients with and without given remodeling patterns were assessed using the log-rank test. A Cox proportional hazard regression with adjustment for potential confounders was performed to determine the predictors of worse outcome. A 2-sided p value <0.05 was regarded as statistically significant. Statistical analysis was performed with SPSS software (version 24, SPSS, Inc., Chicago, Illinois).

Chapter 3. Adverse Prognosis Associated with Asymmetric Myocardial Thickening in Aortic Stenosis.

Published by Kwiecinski J*, Chin CWL*, Everett RJ, White AC, Semple S, Yeung E, Jenkins WJ, Shah ASV, Koo M, Mirsadraee S, Lang CC, Mills N, Prasad SK, Jansen MA, Japp AG, Newby DE, Dweck MR. Adverse prognosis associated with asymmetric myocardial thickening in aortic stenosis. Eurpean Heart J Cardiovasc Imaging. 2018 Mar 1;19(3):347-356.

*denotes equal contribution

3.1 Summary

Asymmetric wall thickening has been described in patients with aortic stenosis. However, it remains poorly characterised and its prognostic implications are unclear. We hypothesized this pattern of adaptation is associated with advanced remodelling, left ventricular decompensation and a poor prognosis.

In a prospective observational cohort study, 166 patients with aortic stenosis (age 69, 69% males, mean aortic valve area 1.0±0.4cm2) and 37 age and sex-matched healthy volunteers underwent phenotypic characterisation with comprehensive clinical, imaging and biomarker evaluation. Asymmetric wall thickening on both echocardiography and cardiovascular magnetic resonance was defined as regional wall thickening ≥13 mm and >1.5-fold the thickness of the opposing myocardial segment.

Although no control subject had asymmetric wall thickening, it was observed in 26% (n=43) of patients with aortic stenosis using magnetic resonance and 17% (n=29) using echocardiography. Despite similar demographics, co-morbidities, valve narrowing, myocardial hypertrophy and fibrosis, patients with asymmetric wall thickening had increased cardiac troponin I and brain natriuretic peptide concentrations (both $p<0.001$). Over 28 [22, 33] months of follow-up, asymmetric wall thickening was an independent predictor of aortic valve replacement or death whether detected by magnetic resonance (HR=2.15; 95 CI 1.29 to 3.59; P=0.003) or echocardiography (HR=1.79; 95 CI 1.08 to 3.69; p=0.021).

Asymmetric wall thickening is common in aortic stenosis and is associated with increased myocardial injury, left ventricular decompensation and adverse events. Its presence may help identify patients likely to proceed quickly towards AVR.

3.2 Introduction

Aortic stenosis is not only characterised by progressive valve narrowing but also by the hypertrophic response of the left ventricle that ensues(Carabello Blase, 2013). Indeed the development of symptoms and adverse events appears as much related to events in the myocardium as the valve(Marc R. Dweck et al., 2012). New techniques for assessing adverse patterns of remodelling are therefore of major interest (Calvin W. L. Chin, Vassilis Vassiliou, et al., 2014).

Echocardiography is the most common imaging technique to assess patients with aortic stenosis and can provide assessments of wall thickness that can be used to calculate left ventricular mass index. Cardiovascular magnetic resonance is less widely employed but provides the gold standard assessment of left ventricular mass and wall thickness with the unique ability to identify myocardial fibrosis. Asymmetric wall thickening is most commonly associated with hypertrophic cardiomyopathy (B. J. Maron, 2002; M. S. Maron et al., 2009). However this form of remodelling has recently been described in patients with increased afterload such as hypertension and aortic stenosis (M. R. Dweck, S. Joshi, et al., 2012; B. J. Maron et al., 1977; Panza & Maron, 1988; Tuseth et al., 2010). An initial magnetic resonance study suggested that asymmetric wall thickening could be observed in around a quarter of patients. However this study was hampered by referral bias and did not involve detailed tissue characterization (M. R. Dweck, S. Joshi, et al., 2012). Echocardiographic studies have suggested a lower prevalence of around 10%, with the prognostic implications of this observation remaining unclear (B. J. Maron et al., 1977; Panza & Maron, 1988).

In this study, we sought to assess asymmetric wall thickening in patients with aortic stenosis using both cardiovascular magnetic resonance and echocardiography. In particular, we aimed to investigate in depth the factors associated with an asymmetric

pattern of wall thickening, its relationship with other markers of left ventricular remodelling and decompensation and to assess its prognostic implications.

3.3 Methods

3.3.1 Patient Population

We performed a prospective observational cohort study of stable subjects with mild, moderate and severe aortic stenosis recruited from the Edinburgh Heart Centre. All patients who attended the institution between March 2012 and August 2014 were invited to participate. We excluded patients with other forms of valvular heart disease (moderate or severe in nature), end-stage heart failure, advanced malignancies or other comorbidities with a life expectancy <2 years, cardiomyopathies (including previous myocarditis) and contraindications to gadolinium-enhanced magnetic resonance, such as ferromagnetic foreign bodies and estimated glomerular filtration rate <30 mL/min/1.73 m2. Coronary artery disease was defined as previous myocardial infarction, documented evidence of myocardial ischemia or a >50% stenosis of the coronary artery lumen. The blood sampling and analysis protocols are described in the supplementary data.

Both the clinical and imaging assessments were carried out at the Clinical Research Facility and the Clinical Research Imaging Centre, Edinburgh. The study was conducted in accordance with the Declaration of Helsinki and approved by the local research committee. Written informed consent was obtained from all enrolled patients.

3.3.2 Cardiovascular Magnetic Resonance

Cardiovascular magnetic resonance was performed using a 3T scanner (MAGNETOM Verio, Siemens Healthcare GmbH, Erlangen, Germany). A balanced steady-state free precession sequence was used for short-axis cine imagine of the left ventricle and assessment of left ventricular volumes, mass and ejection fraction (Argus software, Siemens AG, Healthcare Sector). LV longitudinal function was determined by measuring the difference in mitral annular displacement between end-systole and end-diastole. On short-axis cine images epicardial and endocardial contours were carefully identified and planimetered in end-systole and end-diastole for left ventricular volume quantification. The left ventricular mass was calculated from the total myocardial volume (excluding trabeculations and papillary muscles) multiplied by the density of the myocardium (1.05 g/mL). All volumes and mass values were indexed to body surface area (calculated using the Du Bois formula). The left ventricular mass/volume ratio (M/V) was calculated by dividing the left ventricular mass by the left ventricular end-diastolic volume. This parameter indexes the left ventricular mass to cavity size, with M/V values >1.16 g/mL identifying patients with a relative increase in wall thickness (M. R. Dweck, S. Joshi, et al., 2012). Left ventricular hypertrophy was defined as an indexed left ventricular mass ≥95th centile of the normal range corrected for age and gender (Petersen et al., 2017). Maximal wall thickness was evaluated in all 17 segments of the left ventricle from cine images of the left ventricle in end-diastole (again excluding ventricular trabeculations). Asymmetric left ventricular wall thickening was defined as a regional wall thickening ≥13 mm that was also ≥1.5-fold the thickness of the opposing myocardial segment (M. R. Dweck, S. Joshi, et al., 2012). Such criteria had to be fulfilled on two adjacent short-axis magnetic resonance cine images.

3.3.3 Fibrosis Assessment

Late gadolinium enhancement was used for detection of focal replacement fibrosis. Acquisition was performed between 8 and 15 min after gadobutrol (Gadovist, Bayer Pharma AG, Germany) administration using an inversion recovery fast gradient-echo sequence and a phase-sensitive inversion recovery sequence in two phase-encoding directions in order to distinguish true enhancement from artefact. The inversion time was optimized to achieve adequate nulling of the myocardium. The presence of LGE was evaluated visually by two experienced operators (MRD and CWLC). Where present, it was quantified using QMASS software (Medis, Leiden, The Netherlands) as an area of myocardium with a signal intensity exceeding the threshold of 2 standard deviations above the mean value of normal myocardium. All areas of inversion artefact or myocardial regions contaminated by blood pool or epicardial fat were excluded.

T1 mapping was performed using the Modified Look-Locker Inversion recovery sequence for the assessment of diffuse myocardial fibrosis. Short-axis T1 maps of the mid-cavity were acquired in diastole before and 20 min after the administration of 0.1 mmol/kg of gadobutrol (Gadovist, Bayer Pharma AG, Germany) using a dedicated 32-channel anterior-posterior cardiac array. T1 maps were analysed using OsiriX 4.1.1 software (Geneva, Switzerland). For diffuse fibrosis, we calculated the extracellular volume fraction (ECV) derived from pre- and post-contrast myocardial T1 values corrected for blood-pool T1 and hematocrit. The ECV was calculated according to: ECV = partition coefficient x [1-hematocrit], where partition coefficient = [ΔR1myocardium/ΔR1blood-pool] and ΔR1 = (1/post-contrast T1-1/pre-contrast T1). In order to evaluate the total amount of interstitial fibrosis in our study cohort, we calculated the indexed fibrosis volume (IFV) in each patient using the following equation: ECV x left ventricular myocardial volume corrected for the body surface area.

3.3.4 Echocardiography

All participants underwent a transthoracic echocardiographic examination for the assessment of aortic stenosis and cardiac function on iE33, Philips Medical Systems, The Netherlands. The severity of aortic stenosis was classified on the basis of the aortic jet peak velocity, the mean pressure gradient and the aortic valve area derived using the continuity equation. All assessments were conducted in accordance with European Association of Echocardiography / American Society of Echocardiography (ASE) guidelines (Baumgartner et al., 2009). Trans-mitral early (E) and late diastolic velocities and deceleration time were measured at the tips of mitral valve leaflets using pulse wave Doppler. Pulse-wave tissue Doppler imaging was used to evaluate the early (e') diastolic velocities of the medial and lateral mitral annulus. Diastolic function was determined using the E/e' ratio. The left ventricular mass was calculated using wall thickness measurements and cavity dimensions (ASE formula) and indexed to body surface area (Lang et al., 2015). Cut-off values of 115 g/m2 for males and 95 g/m2 for females were used to distinguish subjects with left ventricular hypertrophy. Relative wall thickness (RWT) calculated according to the formula: RWT=2PWTd/LVEDD (PWTd posterior wall thickness at end-diastole; LVEDD left ventricle end-diastolic dimension) was used in a similar fashion to M/V to classify subjects into the different patterns of remodelling and hypertrophy (Table 1). To assess the presence of asymmetric wall thickening both long and short-axis images were screened by two experienced operators blinded to the magnetic resonance data (AGJ and JK). Similar to magnetic resonance assessments asymmetric left ventricular wall thickening was defined as a regional wall thickening ≥13 mm that was also ≥1.5-fold the thickness of the opposing myocardial segment.

3.3.5 Patterns of Left Ventricular Adaptation

Using both echocardiography and CMR we categorized patients with aortic stenosis into six groups of anatomic adaptation based on the left ventricular mass index, the indexed left ventricular end-diastolic volume, M/V and the presence of asymmetric wall thickening (M. R. Dweck, S. Joshi, et al., 2012). Normal ventricular structure, concentric remodelling, asymmetric remodelling, concentric hypertrophy, asymmetric hypertrophy and eccentric hypertrophy (Table 1).

Table 1. Magnetic resonance and echocardiographic definitions of six patterns of left ventricular adaption in aortic stenosis. Asymmetric wall thickening on both modalities was defined by a maximal wall thickness ≥13 mm that was also ≥1.5-fold the thickness of the opposing myocardial segment.

		Concentric Wall Thickening		**Asymmetric Wall Thickening**		
	Normal Ventricle	Concentric remodelling	Concentric hypertrophy	Asymmetric remodelling	Asymmetric hypertrophy	Eccentric hypertrophy
MAGNETIC RESONANCE						
LV mass index, above age & gender normal values	-	-	✓	-	✓	✓
LV Mass/EDV ≥1.16 g/mL	-	✓	✓	✓	✓	-
Asymmetric wall thickening	-	-	-	✓	✓	-
LVEDVi above age & gender normal values	-	-	-	-	-	✓
ECHOCARDIOGRAPHY						
LV mass index, ≤95 g/m^2 for females ≤115 g/m^2 for males		-	✓	-	✓	✓
Relative wall thickness >0.42	-	✓	✓	✓	✓	-
Asymmetric wall thickening	-	-	-	✓	✓	-

LVEDVi, left ventricular end diastolic volume indexed to body surface; LV, left ventricular;

3.3.6 Blood sampling and analysis

Plasma cardiac troponin I (cTnI) concentrations were measured using the Abbott Architect Stat high-sensitivity cTnI assay (Abbott Laboratories, Abbott Park, Il, USA). The lower limit of detection of this assay is 1.2 ng/L whilst the 99th centile from the reference population is 16ng/L for females and 34ng/L for males. We have previously shown that the analytical variability of the Architect Stat assay is low with a coefficient of variation for duplicate samples of 10% at 6 ng/L.1 Brain natriuretic peptide (BNP) concentrations were measured using the Triage BNP assay (Biosite, Inc., San Diego, CA, USA). The inter-assay coefficient of variation was 10% at 28.8 pg/mL, with a detection range of 5–1300 pg/mL.

3.3.7 Clinical Endpoints

The primary endpoint of the study was aortic valve replacement and all-cause mortality. In the subgroup of subjects that subsequently underwent aortic valve replacement, we determined the impact of asymmetric thickening on 30-day peri-operative cardiovascular outcomes (myocardial infarctions, congestive heart failure, new episodes of atrial or ventricular arrhythmia, perivalvular leaks, permanent pacemaker insertion, cardiac tamponade). Patients that underwent AVR were censored for survival analysis and considered as withdrawn alive. All the mortality, surgery and in-hospital complications data were obtained from the National Strategic Tracing Service, which is a national database for all National Health Service patients in United Kingdom.

3.3.8 Statistical analysis

We assessed the distribution of all continuous variables using the Shapiro-Wilk test, and presented them as mean±standard deviation or median (interquartile range). Comparisons were made using one-way analysis-of-variance to compare continuous parametric data and the Kruskall–Wallis test for non-parametric data. Chi-square

tests were used for categorical baseline characteristics. The association between biomarkers and asymmetric wall thickening was assessed using linear regression analyses with adjusting for potential confounders. Kaplan-Meier curves were used to elucidate the survival distributions with regard to all-cause mortality and AVR. Differences in the outcome of patients with and without asymmetric wall thickening were assessed using the log-rank test. A Cox proportional hazard regression with adjustment for potential confounders was performed to determine the predictors of worse outcome. A two-sided $P<0.05$ was considered statistically significant. All statistical analysis has been performed using SPSS Version 20 (IBM Corp., Armonk, NY, USA) and GraphPad Prism Version 5.0 (GraphPad Software, San Diego, CA, USA).

3.4 Results

3.4.1 Study population

The study group comprised 166 patients with aortic stenosis (69 [63,75] years old, 68% males) and 37 age- and sex-matched healthy volunteers (68 [63,74] years; 65% males). In the patient group, 34 (20%) had mild, 45 (27%) moderate, and 87 (53%) severe aortic stenosis. The mean peak aortic jet velocity and aortic valve area were 3.8±0.9 m/s and 1.0±0.4cm2 respectively. Among patients with aortic stenosis, 4 (2%) had an ejection fraction <50% (45±2%). Overall 112 (67%) patients had a history of hypertension (mean systolic blood pressure 151±21 mmHg), 25 (15%) had diabetes mellitus and 59 (35%) had coronary artery disease. A comprehensive overview of patients' demographics, aortic stenosis severity, left ventricular characteristics and co-morbidities can be found in Tables 2-7.

Table 2. Comparison of patient characteristics between those with concentric wall thickening and asymmetric wall thickening on magnetic resonance.

	Concentric Wall Thickening (n=67)	**Asymmetric Wall Thickening (n=43)**	**P Value**
BASELINE CHARACTERISTICS			
Age, years	70 [65,77]	72 [67,75]	0.56
Males, n (%)	52 (77)	31 (72)	0.52
CAD, n (%)	22 (33)	20 (47)	0.16
Diabetes, n (%)	9 (13)	7 (16)	0.80
Hyperlipidaemia, n (%)	38 (57)	22 (51)	0.84
Hypertension, n (%)	48 (72)	33 (77)	0.56
SBP, mmHg	150±20	153±22	0.53
Six-minute walk, distance (m)	369±96	358±124	0.64
Symptomatic AS, n (%)	16 (24)	14 (32)	0.31
ECHOCARDIOGRAPHY			
AVA, cm^2	0.8 [0.7,1.1]	0.8 [0.7,1.0]	0.15
AVA indexed, cm^2/m^2	0.44 [0.38,0.58]	0.43 [0.36,0.50]	0.08
Dimensionless index	0.25 [0.21,0.30]	0.23 [0.19,0.28]	0.06
Vm, m/s	3.9 [3.4,4.5]	4.2 [3.8,4.8]	0.01
MPG, mmHg	35 [24,44]	41 [34,50]	0.01
- Mild, n (%)	10 (15)	1 (2)	0.02
- Moderate, n (%)	18 (27)	9 (22)	0.47
- Severe, n (%)	39 (58)	33 (76)	0.05
Indexed SV <35mL/m^2, n (%)	13 (19)	9 (21)	0.85
E/A	0.81 [0.68, 1.00]	0.82 [0.63, 1.16]	0.68
Deceleration Time	206 [169, 254]	217 [196, 247]	0.41

E/e'	12.6 [9.8,16.7]	14.2 [11.5,18.5]	0.05
LVOT Vm, m/s	1.0 [0.9,1.1]	1.0 [0.9,1.2]	0.29
Bicuspid Aortic Valve n (%)	26 (39)	14 (33)	0.51
CARDIOVASCULAR MAGNETIC RESONANCE			
Indexed EDV, mL/m^2	67 [60,74]	68 [62,78]	0.15
Indexed ESV, mL/m^2	22 [16,26]	22 [18,26]	0.42
Indexed SV, mL/m^2	46±9	48±9	0.26
Indexed SV <35mL/m^2, n (%)	6 (9%)	4 (8%)	0.94
Max Wall Thickness, mm	12 [10,13]	16 [14,17]	<0.001
Indexed left ventricular mass, g/m^2	92 [81,103]	96 [80,106]	0.49
Left ventricular mass/EDV, g/mL	1.34 [1.24,1.56]	1.36 [1.21,1.50]	0.39
Mid-wall Fibrosis, n (%)	25 (37)	21 (48)	0.24
Extracellular volume fraction, %	27.6±2.9	28.1±2.6	0.29
Indexed Fibrosis volume, mL/m^2	24.5 [20.7,29.4]	26.6 [21.1,30.4]	0.28
Ejection fraction, %	68 [64,72]	67 [64,73]	0.92
Longitudinal function, mm	11.8±3.0	11.1±2.6	0.18
BIOMARKERS			
HS-cTnI, ng/L	6.6 [4.3,10.38]	13.5 [8.1,32.8]	<0.001
BNP, pg/mL	20.9 [8.1,51.8]	56.3 [25.5,112]	<0.001
OUTCOMES			
Combined Primary Outcome, n (%)	34 (51)	35 (81)	0.001
AVR, n (%)	28 (42)	31 (72)	0.002
Aortic Stenosis - related death, n (%)	2 (3)	2 (5)	0.78
All cause death, n (%)	7 (10)	6 (14)	0.58

CAD, coronary artery disease; SBP, systolic blood pressure; MPG, mean pressure gradient; LVOT, left ventricular outflow track; EDV, end diastolic volume; ESV, end systolic volume; SV, stroke volume; HS-cTnI, high-sensitivity cardiac troponin I; AVR, aortic valve replacement

3.4.2 Cardiovascular magnetic resonance

3.4.2.1 Patterns of left ventricular adaptation

Using magnetic resonance criteria, thirty-nine patients with aortic stenosis (23%) had normal left ventricular structure. Thirty-four (20%) patients with aortic stenosis had left ventricular remodelling with 22 having a concentric pattern (13%) and 12 (7%) an asymmetric pattern. Among the 93 (58%) patients with left ventricular hypertrophy, the most frequently occurring adaptation pattern was concentric left ventricular hypertrophy detected in 45 individuals (27%), whilst asymmetric left ventricular hypertrophy was observed in 31 subjects (19%). Seventeen (10%) patients with aortic stenosis had an eccentric pattern of hypertrophy, with these patients often having associated aortic regurgitation (n=13), mitral regurgitation (n=2) or a history of myocardial infarction (n=2). All 37 healthy volunteers that comprised the control group had normal left ventricular structure.

3.4.2.2 Asymmetric Wall Thickening

Overall 43 (26%) of our patients with aortic stenosis demonstrated evidence of asymmetric wall thickening on magnetic resonance (Figure 9). Twelve patients had asymmetric remodelling and 31 had asymmetric hypertrophy. Importantly none of the healthy volunteers exhibited such a pattern of left ventricular adaptation. The site of asymmetric wall thickening was almost universally in the septum: at the basal level in 33 patients (77% of those with asymmetric wall thickening) and at the mid-cavity in 27 (63%) (Figure 10A). In 2 patients (5%) the regional wall thickening was observed in the anterior wall, it was never observed in the lateral or inferior walls. In 13 patients (30%) regional thickening affected just 1 segment of the 17-segment model, 16 subjects (37%) had 2 segments of asymmetric thickening whilst 14 patients (33%) had 3 or 4 affected segments.

Table 3. Baseline characteristics of patients with different forms of remodelling and hypertrophy on magnetic resonance.

	Normal ventricle (n=39)	**Concentric remodelling (n=22)**	**Asymmetric remodelling (n=12)**	**Concentric hypertrophy (n=45)**	**Asymmetric hypertrophy (n=31)**	**Eccentric hypertrophy (n=17)**	**P Value**
BASELINE CHARACTERISTICS							
Age, years	69 [55,.75]	71 [66,.76]	72 [67,.73]	70 [64,.78]	72 [66,.77]	68 [65,.77]	0.40
Males, n (%)	21 (58)	20 (91)	10 (83)	32 (71)	21 (68)	9 (56)	0.06
CAD, n (%)	12 (33)	7 (32)	5 (42)	15 (33)	15 (48)	4 (21)	0.49
Diabetes, n (%)	5 (14)	5 (23)	0 (0)	4 (9)	7 (23)	3 (16)	0.31
Hyperlipidaemia, n (%)	13 (37)	13 (59)	8 (67)	20 (44)	14 (45)	7 (39)	0.34
Hypertension, n (%)	20 (56)	17 (77)	9 (75)	31 (69)	24 (77)	11 (58)	0.22
SBP, mmHg	147±23	149±18	148±20	151±22	155±22	154±19	0.71
Six minute walk, distance (m)	424±73	368±63	380±90	370±111	345±135	389±50	0.04
Symptomatic AS, n (%)	4 (10)	6 (27)	3 (25)	10 (22)	11 (35)	3 (18)	0.26
ECHOCARDIOGRAPHY							

Vm, m/s	3.0 [2.5, 3.8]	3.5 [2.9, 3.9]	4.1 [3.9, 4.6]	4.1 [3.5, 4.6]	4.2 [3.8, 4.9]	3.7 [3.2, 4.0]	<0.001
MPG, mmHg	20 [14, 32]	28 [17, 37]	40 [36, 46]	36 [28, 48]	41 [31, 54]	27 [22, 38]	<0.001
- Mild, n (%)	19 (49)	5 (23)	1 (8)	5 (11)	0	0	<0.001
- Moderate, n (%)	9 (23)	8 (36)	2 (17)	10 (22)	7 (23)	9 (53)	0.265
- Severe, n (%)	8 (21)	9 (41)	9 (75)	30 (67)	24 (77)	8 (47)	<0.001
AVA, cm^2	1.0 [0.8, 1.3]	1.0 [0.8, 1.2]	0.8 [0.7, 1.0]	0.8 [0.7, 1.0]	0.8 [0.7, 1.0]	1.0 [0.8, 1.1]	0.002
AVA indexed, cm^2/m^2	0.55 [0.45, 0.71]	0.52 [0.41, 0.63]	0.45 [0.35, 0.49]	0.41 [0.37, 0.49]	0.42 [0.34, 0.51]	0.50 [0.43,0.59]	0.001
Dimensionless index	0.32 [0.25, 0.41]	0.28 [0.24, 0.32]	0.23 [0.19, 0.25]	0.24 [0.19, 0.30]	0.24 [0.19, 0.29]	0.25 [0.23, 0.32]	<0.001
Indexed SV $<35mL/m^2$, n (%)	8 (22)	7 (31)	3 (25)	6 (14)	6 (19)	3 (16)	0.60
E/A	0.96 [0.74, 1.24]	0.77 [0.69, 1.05]	0.71 [0.52, 0.97]	0.84 [0.70, 1.00]	0.89 [0.65, 1.16]	1.11 [0.80, 1.25]	0.013
Deceleration Time, ms	188 [167, 225]	206 [163,277]	217 [150,246]	198 [171, 250]	227 [187, 248]	186 [166, 231]	0.050
E/e'	11.4 [8.9, 13.7]	11.0 [9.0, 12.8]	12.4 [10.4, 16.9]	13.9 [11.0, 19.0]	15.1 [11.8, 22.5]	12.4 [11.2, 16.0]	0.005
LVOT Vm, m/s	1.0 [0.9, 1.1]	1.0 [0.9, 1.1]	0.9 [0.9, 1.1]	1.0 [0.9, 1.2]	1.0 [0.9, 1.2]	0.9 [0.9, 1.2]	0.82

Bicuspid Aortic Valve n (%)	13 (36)	8 (36)	3 (25)	18 (40)	11 (35)	4 (21)	0.75
CARDIOVASCULAR MAGNETIC RESONANCE							
Indexed EDV, mL/m^2	68 [60, 77]	61 [50, 68]	61 [50, 67]	69 [62, 78]	75 [64, 84]	88 [71, 114]	<0.001
Indexed ESV, mL/m^2	24 [20, 27]	17 [13, 23]	18 [14, 22]	22 [18, 27]	24 [21, 27]	26 [24, 40]	<0.001
Indexed SV, mL/m^2	45±8	42±7	42±7	47±10	50±9	59±12	<0.001
Indexed SV <35mL/m^2, n (%)	2 (6%)	2 (9%)	2 (16%)	4 (9%)	2 (6%)	0 (0%)	NA
Ejection fraction, %	66 [62, 68]	70 [64, 73]	69 [66, 75]	67 [63, 71]	67 [64, 72]	65 [62, 69]	0.08
Longitudinal function, mm	13.5±2.6	13.0±2.6	11.0±2.5	11.1±3.0	11.1±2.6	13.6±2.8	<0.001
Max Wall Thickness, mm	8 [6, 9]	10 [9, 12]	15 [14,16]	12 [11, 14]	17 [15, 18]	10 [8, 12]	<0.001
Indexed left ventricular mass, g/m^2	64 [59, 77]	80 [73, 87]	78 [75, 83]	98 [92, 108]	101 [93, 114]	96 [78, 104]	<0.001
Left ventricular mass/EDV, g/mL	0.97 [0.89, 1.05]	1.27 [1.22, 1.46]	1.30 [1.22,.1.48]	1.42 [1.28, 1.62]	1.41 [1.20, 1.51]	1.03 [0.93, 1.07]	<0.001
Mid-wall Fibrosis, n (%)	5 (14)	4 (18)	2 (17)	21 (47)	19 (61)	8 (50)	<0.001

Extracellular volume fraction, %	27.2±2.0	26.5±1.8	26.4±1.7	28.1±3.1	28.8±2.5	28.4±3.0	0.003
Indexed Fibrosis volume, mL/m^2	17.5 [16.3, 20.0]	20.8 [18.4, 23.6]	20.0 [18.9, 22.5]	27.2 [23.9, 31.8]	28.1 [26.1, 32.3]	23.6 [21.0, 28.7]	<0.001
BIOMARKERS							
HS-cTnI, ng/L	3.1 [1.5, 4.3]	5.3 [3.7, 7.4]	13.5 [7.4, 33.0]	8.0 [4.4,15.2]	13.8 [8.2, 28.0]	6.3 [3.3, 9.9]	<0.001
BNP, pg/mL	21.9 [8.3,.40.1]	13.6 [5.9,.33.9]	27.2 [14.0,.41.4]	21.6 [11.0,.54.1]	65.6[30.2,123.8]	27.5 [8.4,.56.3]	0.001
OUTCOMES							
Combined Primary Outcome, n (%)	6 (15)	11 (50)	10 (83)	23 (51)	25 (81)	6 (38)	<0.001
AVR, n (%)	6 (15)	9 (41)	9 (75)	19 (42)	22 (71)	6 (38)	<0.001
AS-related death, n (%)	0	1 (5)	0	1 (2)	2 (6)	0	NA
All-cause death, n (%)	0	2 (9)	1 (8)	5 (11)	5 (16)	1 (6)	0.09

CAD, coronary artery disease; SBP, systolic blood pressure; MPG, mean pressure gradient; LVOT, left ventricular outflow track; EDV, end diastolic volume; ESV, end systolic volume; SV, stroke volume; HS-cTnI, high-sensitivity cardiac troponin I; AVR, aortic valve replacement

Figure 11. Asymmetrical Wall Thickening on Both Magnetic Resonance and Echocardiography. Images demonstrating asymmetric wall thickening in patients with aortic stenosis. Cardiovascular magnetic resonance short-axis cine images showing an abnormally thickened septum: in a patient with asymmetric remodelling (A) and two subjects with asymmetric hypertrophy (B) & (C). Echocardiographic parasternal long-axis images demonstrating thickening of the septum in two further patients with asymmetric remodelling (D) & (E). Echocardiographic apical 4-chamber image in a subject with asymmetric hypertrophy (F).

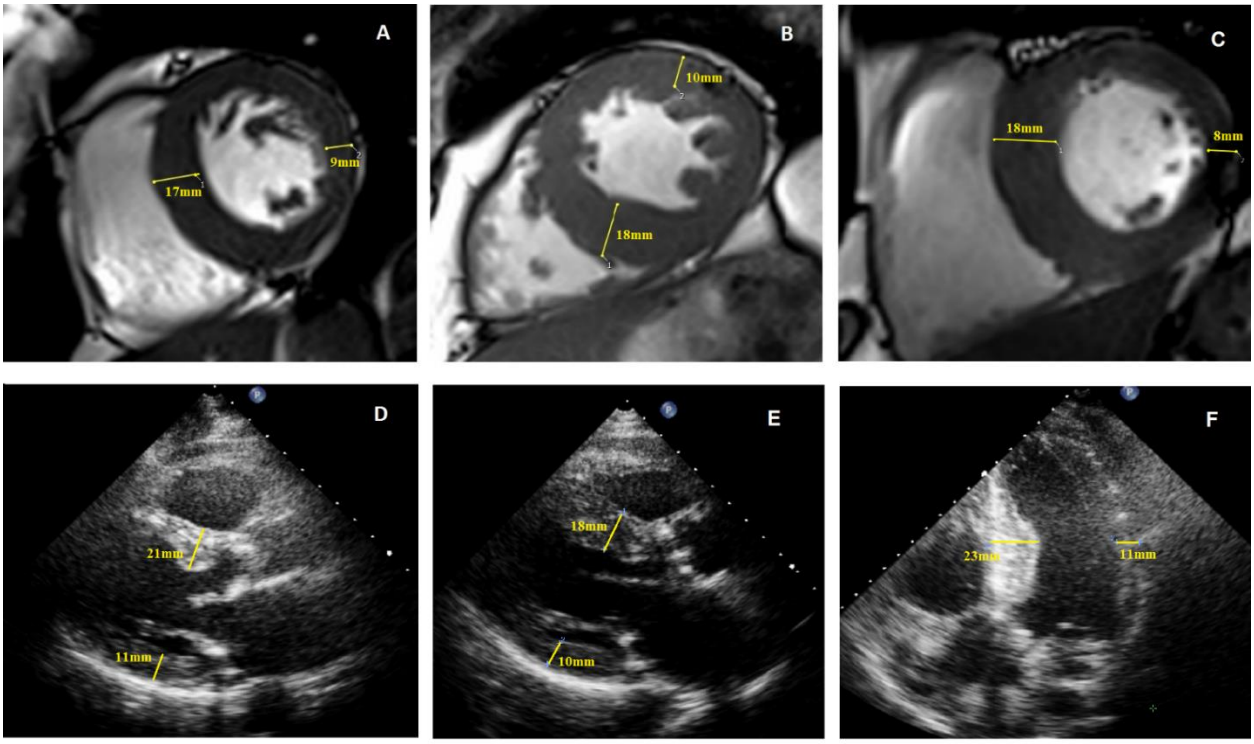

We compared patients with asymmetric wall thickening on CMR to patients with concentric patterns of remodelling or hypertrophy (Table 2). As expected, patients in the asymmetric group had increased maximal wall thickness compared to the concentric groups (16 [14,17] vs. 12 [10,13] mm, p<0.001) but interestingly they also had similar aortic stenosis severity. Indeed, there was no difference between the groups in terms of the aortic valve area (0.8 [0.7,1.1] *vs.* 0.8 [0.7,1.0] cm^2, respectively, p=0.15), the indexed aortic valve area (0.43 [0.36,0.50] *vs*. 0.44 [0.38,0.58] cm^2/m^2, p=0.08) nor the dimensionless index (0.25 [0.21,0.30] *vs.* 0.23 [0.19,0.28], p=0.06). Whilst slightly higher peak aortic jet velocities (4.2 [3.8,4.8] *vs.* 3.9 [3.4,4.5] m/s, p=0.01) and mean gradients (41([34,50] vs. 35 [24,44], p 0.01) were observed in those with asymmetric wall thickening these differences were small. No differences were observed between the two groups in terms of comorbidities, the magnitude of the hypertrophic response nor the degree of myocardial fibrosis (all p>0.15). Despite these similarities patients with an asymmetric pattern had double the plasma concentrations of troponin I (13.5 [8.1,32.8] vs. 6.6 [4.3,10.4] ng/L, p<0.001) and BNP (56.3 [25.5,112.2] vs. 20.9 [8.1,51.8] pg/mL, p<0.001) compared to subjects with concentric wall thickening. Indeed asymmetric wall thickening was associated with both troponin and BNP levels independent of age, sex, systolic blood pressure, aortic stenosis severity and left ventricular mass index (p<0.001)(Figure 11).

3.4.2.3 Asymmetric wall thickening resolution

Out of the 31 subjects with asymmetric wall thickening who underwent aortic valve replacement, 12 had a repeat magnetic resonance imaging 1-year following surgery. In these patients the left ventricular mass index decreased on repeat imaging (from 97 [86,102] to 68 [65, 80] g/m^2; p<0.001) as did maximum wall thickness (from 15 [14,16] to 13 [11,14] mm; p=0.006) with an observed tendency to reduced high-sensitivity troponin I levels (from 9.0 [4.9,20.8] to 4.0 [1.8,10.0] ng/L; p=0.073) (Figure 10B). Overall 6 of the 12 patients had complete resolution of their regional wall thickening and no longer fulfilled criteria for asymmetric wall thickening.

Figure 12. Prevalence, Distribution and Resolution after Aortic Valve Replacement of Asymmetric Wall Thickening. (A) 17-segment model of the left ventricle demonstrating the site of asymmetric wall thickening as detected by both magnetic resonance and echocardiography. Magnetic resonance was more sensitive in detecting asymmetric wall thickening (43 cases) than echocardiography (29 cases). On both modalities asymmetric wall thickening was almost universally confined to the basal and mid-cavity segments of the septum. (B) Patient with asymmetric wall thickening at baseline, which resolved when magnetic resonance was repeated 1 year after aortic valve replacement.

A

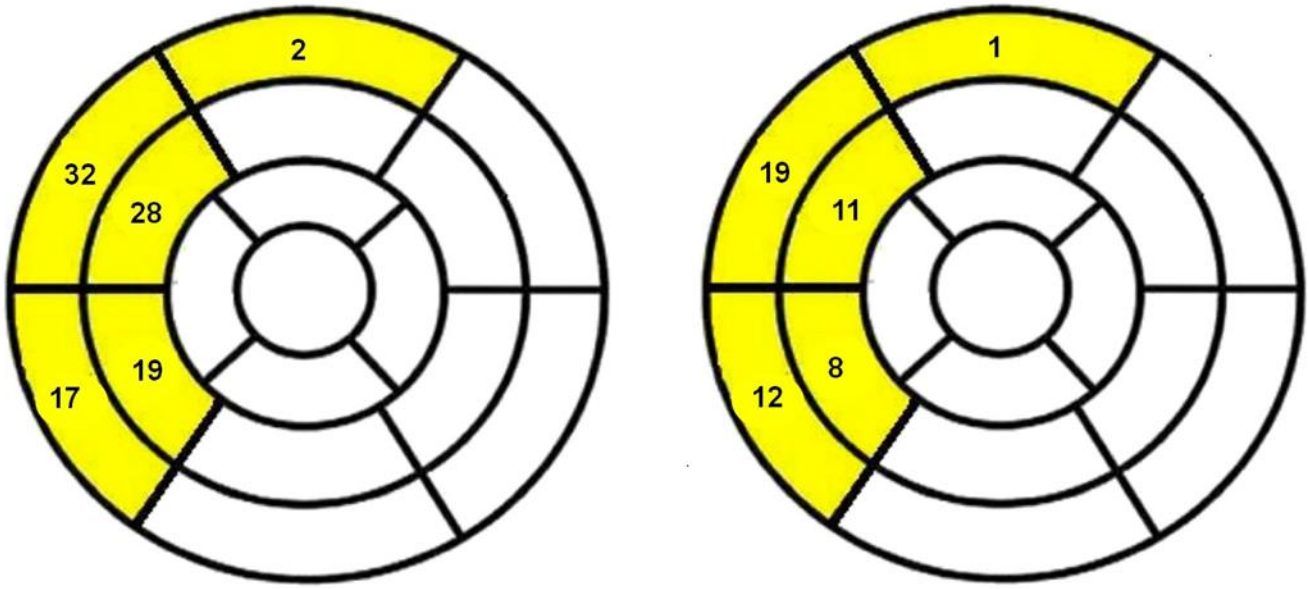
Magnetic resonance (n=43)
2
32
28
19
17
Echocardiography (n=29)
1
19
11
8
12

B

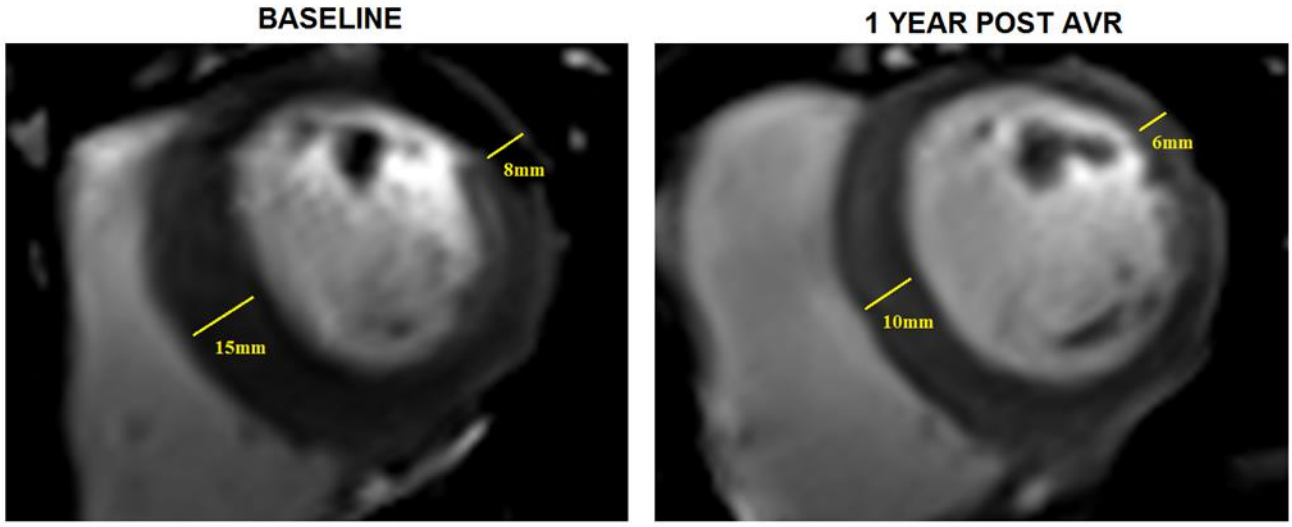
BASELINE
8mm
15mm
1 YEAR POST AVR
6mm
10mm

Figure 13. Characteristics of Patients with Asymmetric vs Concentric Wall Thickening.

Boxplots presenting: Aortic Valve Area (A), Indexed Left Ventricular Mass (B), High Sensitivity Cardiac Troponin I (C) and Brain Natriuretic Peptide (D) concentrations in aortic stenosis patients with asymmetric and concentric patterns of wall thickening. Despite no difference in AVA and left ventricular mass index (p=0.15 and p=0.49 respectively) patients with asymmetric wall thickening had higher cardiac troponin and BNP levels than those with concentric wall thickening (p<0.001).

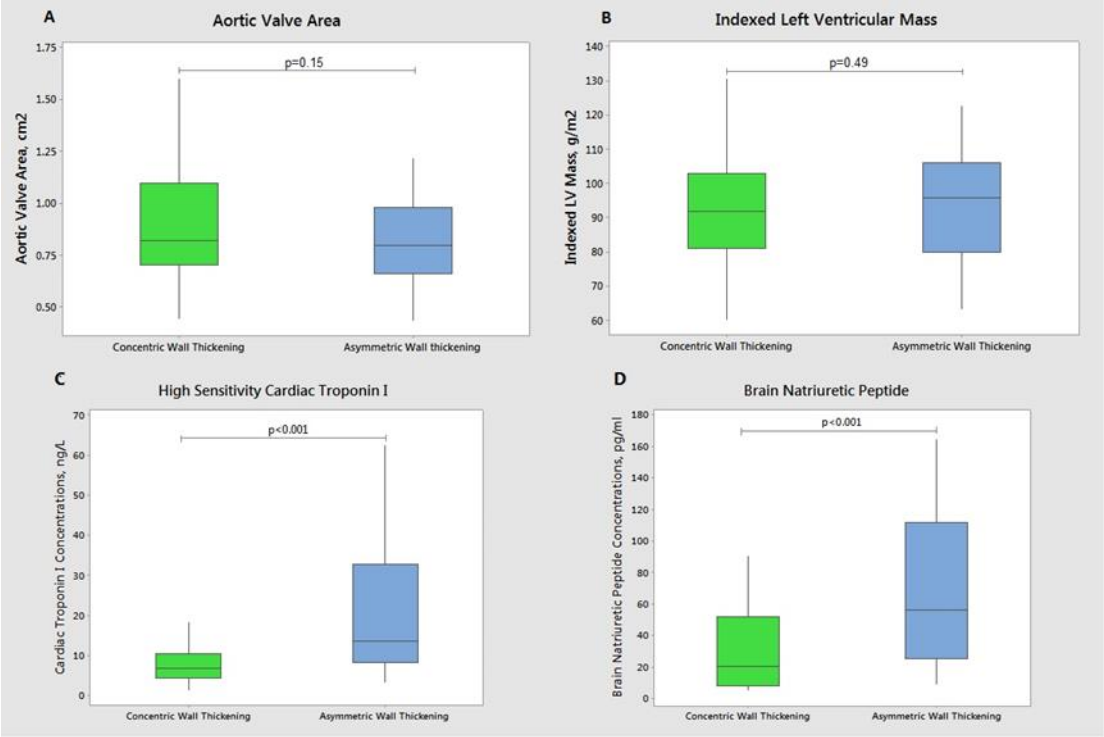

3.4.2.4 Fibrosis

Asymmetric wall thickening was associated with higher ECV and replacement fibrosis compared to healthy controls and AS subjects with a normal left ventricle (28.1±2.6% and 48% vs 26.5±1.3% & 0% and 27.2±2.0 & 14% respectively, all $p<0.05$). Interestingly there was no significant difference in the fibrosis burden between subjects with an asymmetric and concentric pattern of LV adaptation (28.1±2.6% and 48% vs 27.6±2.9 and 37%, $p=0.29$ and $p=0.24$ respectively).

Table 4. Comparison of patient characteristics between subjects with left ventricular remodelling and left ventricular hypertrophy on magnetic resonance. Patients with eccentric hypertrophy were excluded.

	Left ventricular remodelling (n=34)	**Left ventricular hypertrophy (n=76)**	**P Value**
BASELINE CHARACTERISTICS			
Age, years	71 [67, 75]	72 [65, 78]	0.78
Males, n (%)	30 (88)	53 (70)	0.03
CAD, n (%)	12 (35)	30 (39)	0.68
Diabetes, n (%)	5 (15)	11 (14)	0.97
Hyperlipidaemia, n (%)	21 (62)	34 (45)	0.10
Hypertension, n (%)	26 (76)	55 (72)	0.65
SBP, mmHg	148±19	152±21	0.33
Six minute walk, distance (m)	374±73	360±121	0.47
Symptomatic AS, n (%)	9 (26)	21 (27)	0.90
ECHOCARDIOGRAPHY			
AVA, cm^2	0.9 [0.8, 1.1]	0.8 [0.7, 1.0]	0.07
AVA indexed, cm^2/m^2	0.45 [0.40, 0.57]	0.42 [0.37, 0.51]	0.10
Dimensionless index	0.25 [0.23, 0.31]	0.24 [0.20, 0.30]	0.26
Vm, m/s	3.9 [2.5, 3.8]	4.2 [3.7, 4.8]	0.01
MPG, mmHg	35 [21.0, 42]	38 [29, 50]	0.01
- Mild, n (%)	6 (18)	5 (7)	0.09

- Moderate, n (%)	10 (29)	17 (22)	0.43
- Severe, n (%)	18 (53)	54 (71)	0.07
Indexed SV <35mL/m^2, n (%)	10 (29)	12 (16)	0.11
E/A	0.74 [0.65, 1.01]	0.85 [0.69, 1.10]	0.46
Deceleration Time, ms	211 [160, 256]	214 [178, 247]	0.67
E/e'	11.6 [9.6, 13.9]	14.2 [11.5, 19.5]	0.001
LVOT Vm, m/s	0.9 [0.9, 1.1]	1.0 [0.9, 1.1]	0.21
Bicuspid Aortic Valve n (%)	11 (32)	29 (38)	0.56
CARDIOVASCULAR MAGNETIC RESONANCE			
Indexed EDV, mL/m^2	61 [50, 67]	72 [63, 80]	<0.001
Indexed ESV, mL/m^2	17 [14, 23]	23 [19, 27]	<0.001
Indexed SV, mL/m^2	42±6	48±9	0.001
Indexed SV <35mL/m^2, n (%)	4 (11%)	6 (8%)	0.52
Ejection fraction, %	70 [64, 74]	67 [63, 72]	0.036
Longitudinal function, mm	12.3±2.7	11.1±2.8	0.046
Max Wall Thickness, mm	11 [9, 14]	14 [12, 16]	0.001
Indexed left ventricular mass, g/m^2	79 [73, 86]	99 [92, 110]	<0.001
Left ventricular mass/EDV, g/mL	1.28 [1.22, 1.45]	1.41 [1.26, 1.58]	0.017
Mid-wall Fibrosis, n (%)	6 (18)	40 (53)	<0.001
Extracellular volume fraction, %	26.4±1.8	28.4±2.9	<0.001
Indexed Fibrosis volume, mL/m^2	20.3 [18.7, 23.2]	27.7 [24.4, 32.1]	<0.001
BIOMARKERS			
HS-cTnI, ng/L	6.9 [4.7, 11.6]	9.5 [5.0, 18.5]	0.12

BNP, pg/mL	16.5 [7.9, 37.8]	41.1 [15.0, 81.7]	0.01
OUTCOMES			
Combined Primary Outcome, n (%)	21 (62)	48 (63)	0.89
AVR, n (%)	18 (53)	41 (54)	0.92
AS-related death, n (%)	1 (3)	3 (4)	0.88
All cause death, n (%)	3 (9)	10 (13)	0.51

CAD,coronary artery disease; SBP, systolic blood pressure; MPG, mean pressure gradient; LVOT, left ventricular outflow track; EDV, end diastolic volume; ESV, end systolic volume; SV, stroke volume; HS-cTnI, high-sensitivity cardiac troponin I; AVR, aortic valve replacement

3.4.3 Echocardiography.

Using echocardiographic criteria 26 aortic stenosis patients (16%) had normal left ventricular structure. Thirty-two (19%) had left ventricular remodelling whilst 108 (65%) exhibited left ventricular hypertrophy, of whom 9 (6%) had eccentric hypertrophy. Overall echocardiography demonstrated good agreement with magnetic resonance in terms of determining the pattern of left ventricular adaptation (all $p>0.10$ for a difference, Table 5).

Table 5. Comparison of patient characteristics between subjects with asymmetric wall thickening on echocardiography and cardiovascular magnetic resonance imaging.

	Asymmetric Wall Thickening (Echocardiography) (n=29)	**Asymmetric Wall Thickening (magnetic resonance) (n=43)**	**P Value**
BASELINE CHARACTERISTICS			
Age, years	73 [69,.81]	72 [67,.75]	0.39
Males, n (%)	19 (65)	31 (72)	0.58
CAD, n (%)	17 (58)	20 (47)	0.33
Diabetes, n (%)	5 (17)	7 (16)	0.87
Hyperlipidaemia, n (%)	17 (58)	22 (51)	0.58
Hypertension, n (%)	23 (80)	33 (77)	0.74
SBP, mmHg	152±21	153±22	0.91
Six-minute walk, distance. (m)	365±127	358±124	0.92
Symptomatic AS, n (%)	13 (45)	16 (37)	0.52
ECHOCARDIOGRAPHY			
AVA,.cm^2	0.8 [0.6, 1.0]	0.8 [0.7, 1.0]	0.77
AVA indexed,.cm^2/m^2	0.45 [0.32, 0.51]	0.43 [0.36, 0.50]	0.91
Dimensionless index	0.23 [0.19, 0.30]	0.23 [0.19, 0.28]	0.49
Vm,.m/s	4.4 [4.0, 5.1]	4.2 [3.9, 4.9]	0.60
MPG, mmHg	45 [35, 60]	41 [35, 50]	0.54

- Mild, n (%)	0	1 (2)	NA
- Moderate, n (%)	4 (14)	9 (21)	0.43
- Severe, n (%)	25 (86)	33 (77)	0.32
Indexed SV <35mL/m^2, n (%)	6 (21)	9 (21)	0.87
E/A	0.79 [0.61, 1.12]	0.82 [0.63, 1.16]	0.65
Deceleration Time	223 [200, 247]	217 [196, 247]	0.73
E/e'	16.8 [12.8, 24.4]	14.2 [11.5, 18.5]	0.27
LVOT Vm,.m/s	1.0 [0.9, 1.2]	1.0 [0.9, 1.2]	0.60
Bicuspid Aortic Valve n (%)	7 (24)	14 (33)	0.59
CARDIOVASCULAR MAGNETIC RESONANCE			
Indexed EDV, mL/m^2	71 [64, 80]	68 [62, 78]	0.40
Indexed ESV, mL/m^2	22 [18, 25]	22 [18, 26]	0.80
Indexed SV, mL/m^2	50±10	48±9	0.32
Indexed SV <35mL/m^2, n (%)	2 (7%)	4 (8%)	0.94
Ejection fraction, %	68.[65, 72]	67.[64, 73]	0.78
Longitudinal function, mm	10.9±2.5	11.1±2.6	0.84
Max Wall Thickness, mm	16 [15, 18]	16 [14, 17]	0.55
Indexed left ventricular mass, g/m^2	101 [89, 113]	96 [80, 106]	0.32
Left ventricular mass/EDV, g/mL	1.37 [1.24, 1.56]	1.36 [1.21, 1.50]	0.63
Mid-wall Fibrosis, n (%)	13 (44)	21 (48)	0.44
Extracellular volume fraction, %	28.7±2.7	28.1±2.6	0.46
Indexed Fibrosis volume, mL/m^2	24.9 [20.4, 28.7]	26.6 [21.1, 30.4]	0.19
BIOMARKERS			

HS-cTnI,.ng/L BNP,.pg/mL	13.5 [8.0, 32.5] 64.7 [28.1, 130.5]	13.5 [8.1, 32.8] 56.3 [25.5, 112]	0.71 0.24
OUTCOMES			
Combined Primary Outcome, n (%) AVR, n (%) AS-related death, n (%) All cause death, n (%)	23 (79) 20 (69) 1 (4) 3 (10)	35 (81) 31 (72) 2 (5) 6 (14)	0.55 0.53 NA 0.74

CAD, coronary artery disease; SBP, systolic blood pressure; MPG, mean pressure gradient; LVOT, left ventricular outflow track; EDV, end diastolic volume; ESV, end systolic volume; SV, stroke volume; HS-cTnI, high-sensitivity cardiac troponin I; AVR, aortic valve replacement

We were interested whether echocardiography was similarly able to detect asymmetric wall thickening. Short-axis images of the left ventricle were either unavailable or non-interpretable in 31 subjects, in whom analysis was based solely on the parasternal and apical long-axis images. Overall 29 of the 166 patients with aortic stenosis exhibited asymmetric wall thickening (17%), again it was not observed in the control patients. Compared to magnetic resonance (which served as the gold standard in this analysis) echocardiography was less sensitive (67%) but showed excellent specificity (100%) in detecting patients with asymmetric wall thickening. Half (n=8, 57%) of the patients with asymmetric wall thickening on magnetic resonance that were missed by echocardiography had non-interpretable short-axis echo images. At the segment level echocardiography missed 47 (48%) of the segments with asymmetric thickening detected by magnetic resonance, although the distribution of this thickening was similar to magnetic resonance: confined to the septum with the exception of 1 patient with anterior wall involvement (Figure 10A). Importantly despite the relatively lower sensitivity, patients with asymmetric wall thickening on echocardiography again demonstrated troponin and BNP concentrations that were more than double the values in patients with concentric wall thickening (troponin I 13.5 [8.0,32.5] vs 5.3 [3.6,11.2] ng/L, p=0.001; and BNP 64.7 [28.1,130.5] vs 24.3 [10.2,52.9] pg/mL, p<0.001) (Tables 6 and 7).

Table 6. Baseline characteristics of patients with different forms of remodelling and hypertrophy on echocardiography.

	Normal ventricle (n=25)	**Concentric remodelling (n=37)**	**Asymmetric remodelling (n=4)**	**Concentric hypertrophy (n=68)**	**Asymmetric hypertrophy (n=25)**	**Eccentric hypertrophy (n=8)**	**P Value**
BASELINE CHARACTERISTICS							
Age, years	67 [62, 73]	70 [65, 77]	73 [71, 83]	70 [63, 75]	72 [67, 78]	74 [67, 78]	0.18
Males, n (%)	13 (52)	23 (62)	4 (100)	52 (76)	17 (68)	5 (63)	0.12
CAD, n (%)	4 (16)	12 (32)	2 (50)	22 (32)	12 (48)	3 (38)	0.07
Diabetes, n (%)	4 (16)	4 (11)	0 (0)	10 (15)	4 (16)	2 (25)	NA
Hyperlipidaemia, n (%)	8 (32)	16 (43)	4 (100)	32 (47)	13 (52)	2 (25)	0.24
Hypertension, n (%)	15 (60)	21 (78)	3 (75)	42 (62)	22 (88)	8 (100)	0.04
SBP, mmHg	150±24	151±22	147±19	149±20	154±21	155±24	0.47
Six minute walk, distance (m)	397±89	375±132	375±45	378±92	373±119	384±71	0.05
ECHOCARDIOGRAPHY							
Vm, m/s	3.6 [2.9, 4.1]	3.5 [2.8, 3.9]	3.9 [3.4, 4.0]	4.0 [3.3, 4.5]	4.5 [4.0, 4.8]	3.8 [3.1, 4.2]	<0.001

MPG, mmHg	25 [16, 36]	25 [16, 37]	36 [26, 41]	38 [26, 44]	44 [35, 57]	35 [16, 41]	<0.001
AVA, cm^2	1.0 [0.8, 1.3]	1.0 [0.8, 1.2]	1.0 [0.8, 1.1]	0.8 [0.7, 1.1]	0.8 [0.7, 1.0]	1.0 [0.8, 1.1]	0.087
AVA indexed, cm^2/m^2	0.53 [0.45, 0.68]	0.53 [0.40, 0.70]	0.51 [0.35, 0.62]	0.46 [0.38, 0.58]	0.45 [0.34, 0.49]	0.50 [0.43, 0.64]	0.042
Dimensionless index	0.29 [0.25, 0.38]	0.27 [0.24,0.34]	0.23 [0.19, 0.25]	0.24 [0.19, 0.30]	0.24 [0.19, 0.29]	0.25 [0.23, 0.32]	0.001
Indexed SV <35mL/m^2, n (%)	6 (24)	9 (24)	1 (25)	14 (20)	3 (12)	0 (0)	0.38
E/A	1.01 [0.79, 1.26]	0.79 [0.69, 1.08]	0.73 [0.52, 0.99]	0.82 [0.70, 1.08]	0.85 [0.68, 1.14]	1.11 [0.80, 1.25]	0.063
Deceleration Time	188 [167, 225]	206 [163,277]	217 [150,246]	198 [171, 250]	227 [187, 248]	186 [166, 231]	0.15
E/e'	12.9 [10.3, 14.9]	11.6 [8.7, 13.8]	13.1 [10.3, 16.3]	12.6 [10.6, 18.0]	16.6 [12.1, 22.4]	12.3 [8.7, 19.8]	0.027
LVOT Vm, m/s	1.0 [0.9, 1.1]	1.0 [0.9,1.1]	1.0 [0.9, 1.1]	0.9 [0.8, 1.1]	0.9 [0.9, 1.2]	0.9 [0.9, 1.1]	0.82
Bicuspid Aortic Valve n (%)	9 (36)	8 (22)	1 (25)	28 (41)	8 (32)	3 (37)	0.46
CARDIOVASCULAR MAGNETIC RESONANCE							
Indexed EDV, mL/m^2	63 [59, 74]	64 [57, 71]	64 [52, 80]	74 [62, 86]	75 [67, 89]	89 [72, 114]	0.001

Indexed ESV, mL/m^2	21 [18, 25]	22 [17, 25]	21 [14, 24]	25 [21, 29]	22 [19, 28]	26 [24, 40]	0.02
Indexed SV, mL/m^2	45±8	43±7	45±10	50±11	51±9	59±12	0.004
Indexed SV $<35mL/m^2$, n (%)	2 (8%)	2 (5%)	1 (25%)	5 (7%)	2 (8%)	0 (0%)	NA
Ejection fraction, %	69 [65, 73]	67 [64, 70]	70 [65, 74]	66 [63, 71]	67 [64, 74]	64 [60, 69]	0.187
Longitudinal function, mm	13.3±3.4	13.0±2.5	10.9±3.3	12.2±3.0	10.9±2.3	10.8±1.8	0.002
Max Wall thickness (mm)	8 [6, 9]	10 [9, 12]	15 [14,16]	12 [11, 14]	17 [15, 18]	9 [8, 11]	<0.001
Indexed LV mass, g/m^2	69 [60, 77]	74 [68, 89]	84 [75, 99]	97 [91, 108]	101 [91, 115]	95 [83, 104]	<0.001
LV mass/EDV, g/mL	0.99 [0.92, 1.06]	1.22 [1.17, 1.32]	1.31 [1.20, 1.51]	1.36 [1.18, 1.53]	1.41 [1.19, 1.53]	1.03 [0.94, 1.09]	0.014
Mid-wall Fibrosis, n (%)	3 (12)	9 (33)	1 (25)	27 (40)	16 (64)	3 (38)	<0.001
Extracellular volume fraction, %	27.1±2.5	27.7±2.3	26.6±1.1	27.8±2.7	28.9±2.6	26.7±3.3	0.003

Indexed Fibrosis volume, mL/m^2	17.5 [16.7, 22.0]	20.1 [17.7, 24.6]	22.9 [19.0, 27.0]	26.0 [20.7, 30.9]	28.1 [25.7, 33.9]	23.8 [19.9, 27.4]	<0.001
BIOMARKERS							
HS-cTnI, ng/L	3.4 [1.7, 4.9]	4.5 [2.5, 9.1]	6.8 [3.9, 14.5]	7.0 [3.9, 11.4]	14.8 [9.6, 38.3]	6.7 [4.9, 11.0]	<0.001
BNP, pg/mL	17.8 [5.9, 30.2]	19.1 [7.0, 38.4]	29.4 [26.9, 43.2]	27.5 [14.8, 63.4]	72.9 [30.8, 141.8]	29.7 [16.4, 72.3]	0.001
OUTCOMES							
Combined Primary Outcome, n (%)	10 (40)	10 (27)	4 (100)	34 (50)	18 (72)	5 (62)	0.001
AVR, n (%)	9 (15)	8 (22)	4 (100)	30 (44)	15 (60)	5 (62)	0.005
AS-related death, n (%)	0	1 (3)	0	1 (1)	2 (8)	0	NA
All-cause death, n (%)	0	2 (5)	0	7 (10)	4 (16)	1 (12)	NA

CAD, coronary artery disease; SBP, systolic blood pressure; MPG, mean pressure gradient; LVOT, left ventricular outflow track; EDV, end diastolic volume; ESV, end systolic volume; SV, stroke volume; HS-cTnI, high-sensitivity cardiac troponin I; AVR, aortic valve replacement

Table 7. Comparison of patient characteristics between asymmetric and concentric wall thickening diagnosed using echocardiography. Patients with eccentric hypertrophy were excluded.

	Asymmetric Wall Thickening (Echocardiography) (n=29)	**Concentric Wall Thickening (Echocardiography) (n=105)**	**P Value**
BASELINE CHARACTERISTICS			
Age, years	73 [69, 81]	70 [63, 74]	0.13
Males, n (%)	19 (65)	79 (71)	0.58
CAD, n (%)	17 (58)	37 (33)	0.03
DM, n (%)	5 (17)	18 (16)	0.89
Hyperlipidaemia, n (%)	17 (58)	48 (43)	0.16
Hypertension, n (%)	23 (80)	72 (65)	0.17
SBP, mmHg	152±21	151±21	0.76
Six minute walk, distance (m)	365±127	381±100	0.60
ECHOCARDIOGRAPHY			
AVA, cm^2	0.8 [0.6, 1.0]	0.9 [0.7, 1.2]	0.050
AVA indexed, $cm^{2/}m^2$	0.45 [0.32, 0.51]	0.44 [0.36, 0.56]	0.28
Dimensionless index	0.23 [0.19, 0.30]	0.26 [0.23, 0.32]	0.049
Vm, m/s	4.4 [3.9, 5.1]	3.8 [3.2, 4.3]	0.001
MPG, mmHg	45 [35, 60]	32 [22, 41]	0.003
Indexed SV <35mL/m^2, n (%)	6 (21)	19 (18)	0.75
E/A	0.79 [0.61, 1.12]	0.87 [0.65, 1.10]	0.68
Deceleration Time	223 [200, 247]	207 [183, 247]	0.41
E/e'	16.8 [12.8, 24.4]	12.4 [9.8, 16.6]	0.023

LVOT Vm, m/s	1.0 [0.9,1.2]	1.0 [0.9, 1.2]	0.21
Bicuspid Aortic Valve n (%)	7 (24)	38 (35)	0.41
CARDIOVASCULAR MAGNETIC RESONANCE			
Indexed EDV, mL/m^2	71 [64, 80]	68 [61, 79]	0.50
Indexed ESV, mL/m^2	22 [18, 25]	23 [18, 27]	0.89
Indexed SV, mL/m^2	50±10	51±9	0.26
Indexed SV <35mL/m^2, n (%)	2 (7)	10 (9)	0.89
Ejection fraction, %	68 [65, 72]	67 [63, 71]	0.51
Longitudinal function, mm	10.9±2.5	12.5±2.9	0.02
Indexed LV mass, g/m^2	101 [89, 113]	96 [85, 107]	0.005
LV mass/EDV, g/mL	1.37 [1.24, 1.56]	1.23 [1.04, 1.43]	0.003
Mid-wall Fibrosis, n (%)	13 (44)	36 (32)	0.021
Extracellular volume fraction, %	28.7±2.7	27.7±2.6	0.13
Indexed Fibrosis volume, mL/m^2	24.9. [20.4, 28.7]	24.4 [20.1, 28.4]	0.48
BIOMARKERS			
HS-cTnI, ng/L	13.5 [8.0, 32.5]	5.35 [3.6, 11.2]	0.001
BNP, pg/mL	64.7.7 [28.1, 130.5]	24.3 [10.2, 52.9]	<0.001
OUTCOMES			
Combined Primary Outcome, n (%)	23 (79)	48 (43)	0.008
AVR, n (%)	20 (69)	42 (38)	0.024
Cardiac death, n (%)	1 (4)	2 (2)	NA
All cause death, n (%)	3 (10)	7 (6)	0.21

CAD, coronary artery disease; SBP, systolic blood pressure; MPG, mean pressure gradient; LVOT, left ventricular outflow track; EDV, end diastolic volume; ESV, end systolic volume; SV, stroke volume; HS-cTnI, high-sensitivity cardiac troponin I; AVR, aortic valve replacement

3.4.4 Clinical outcomes

Patients were followed up for a median of 28 [22,33] months and 86 events occurred (72 aortic valve replacements and 14 patients died). Using the magnetic resonance analysis, the primary end-point was higher in patients with asymmetric wall thickening (n=35, 81%) compared to both patients with concentric patterns (n=34, 51%) and to all patients who did not have asymmetric wall thickening (n=51, 42%). Indeed, asymmetric wall thickening was associated with worse outcomes independent of age, sex, left ventricular mass index, coronary artery disease and importantly aortic stenosis severity assessed with the mean aortic valve gradient (HR=2.15; 95 CI 1.29 to 3.59; P=0.003, Figure 12). Among patients that underwent aortic valve replacement, perioperative complications were also more frequently observed in individuals with asymmetric wall thickening than subjects without (55% vs. 13%; p=0.004; Figure 12).

Based upon the echocardiographic assessments, there were 23 outcome events (20 underwent aortic valve replacement and 3 died) in the 29 patients (79%) with asymmetrical wall thickening. This compared with 48 events in the 105 patients (46%) with concentric wall thickening. Using our combined primary outcome measure the asymmetric group on echo again had worse outcomes independent of age, sex, left ventricular mass index, coronary artery disease and the mean aortic valve gradient (HR=1.79; 95 CI 1.08 to 3.69; p=0.021). In patients that underwent aortic valve replacement, perioperative adverse outcomes were also more frequently reported in subjects with asymmetric wall thickening on echocardiographic (57% vs 19%; p=0.023).

Table 8. Hazard ratios predicting adverse events (aortic valve replacement or deaths) for asymmetric wall thickening on magnetic resonance and echocardiography in adjusted and unadjusted analyses.

	Asymmetric Wall Thickening on Magnetic Resonance		Asymmetric Wall Thickening on Echocardiography	
	Hazard ratio (95% CI)	p-value	Hazard ratio (95% CI)	p-value
Model 1	2.97 (1.87-4.69)	<0.001	2.28 (1.26-3.73)	0.008
Model 2	2.79 (1.73-4.59)	<0.001	2.08 (1.16-3.72)	0.014
Model 3	2.76 (1.69-4.52)	0.001	2.03 (1.11-3.70)	0.01
Model 4	2.21 (1.34-3.68)	0.004	1.86 (1.09-3.42)	0.014
Model 5	2.14 (1.28-3.57)	0.004	1.83 (1.10-3.53)	0.014
Model 6	2.15 (1.29-3.59)	0.003	1.79 (1.08-3.69)	0.021

Model 1 – unadjusted; Model 2 – adjusted for age and sex; Model 3 – similar to Model 2 additionally adjusted for indexed left ventricular mass; Model 4 – similar to Model 2 additionally adjusted for mean aortic valve pressure gradient; Model 5 – adjusted for age, sex, indexed left ventricular mass and mean aortic valve pressure gradient; Model 6 – similar to Model 5 additionally adjusted for Coronary Artery Disease

Table 9. Hazard ratios predicting adverse events (aortic valve replacement or deaths) for variables, which were used to construct the models, presented in Table 8 in unadjusted analysis.

Variable	Hazard ratio (95% CI)	p-value
Age	1.02 (1.00-1.05)	0.043
Gender	0.83 (0.51-1.33)	0.44
LV mass (indexed)	1.01 (0.99-1.02)	0.15
Mean Pressure Gradient	1.49 (1.23-1.82)	0.003
Coronary Artery Disease	1.15 (0.72-1.83)	0.56

Table 10. Perioperative Cardiac Complication in AS subjects.

Complication	Asymmetric Wall Thickening (n=35)	No Asymmetric Wall Thickening (n=37)	P value
Congestive Heart Failure, n (%)	5 (14)	1 (3)	NA
Atrial Fibrillation, n (%)	6 (17)	2 (5)	NA
Arrhythmia requiring Permanent Pacemaker Implantation, n (%)	5 (14)	2 (3)	NA
Perivalvular Leaks, n (%)	2 (6)	0	NA
Cardiac Tamponade, n (%)	1 (3)	0	NA
All Complications, n (%)	19 (55)	5 (13)	0.004

Figure 14. Outcome Data in Aortic Stenosis Patients With and Without Asymmetric Wall Thickening. Kaplan-Meier event estimates by adaptation patterns for the occurrence of death and AVR in aortic stenosis patients. Asymmetric thickening was associated with worse cardiac outcomes both when detected using magnetic resonance (A) (HR=2.15 (1.29-3.59); p=0.003) and echocardiography (B) (HR=1.79 (1.08-3.69); p=0.021). Peri-operative complications in aortic stenosis patients undergoing aortic valve replacement. Subjects with asymmetric wall thickening had more cardiac complications in the peri-operative period than those without based upon both magnetic resonance (C) 55% vs 13% (p=0.004) and echocardiographic (D) 57% vs 19% (p=0.023) assessments.

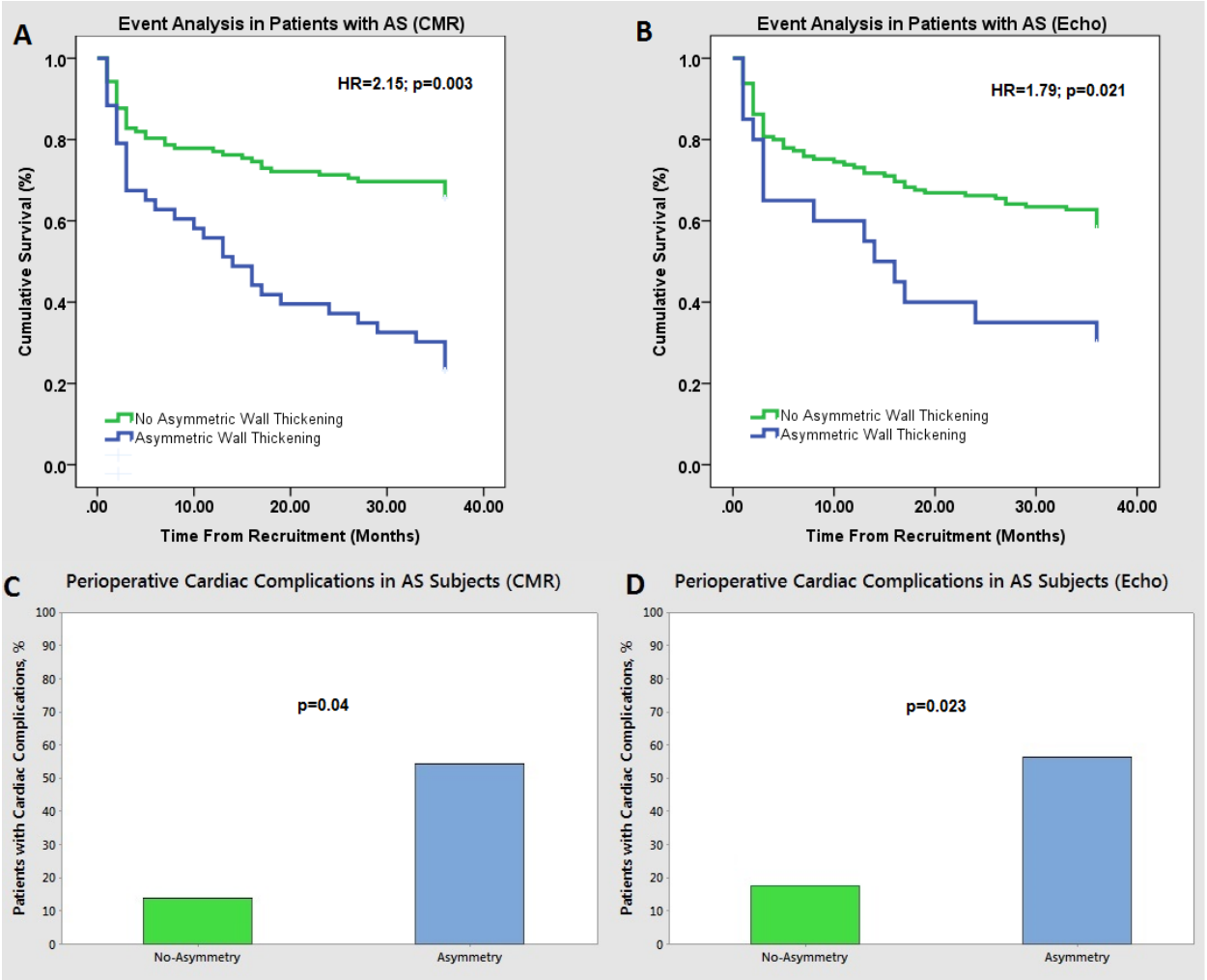

3.5 Discussion

We here provide a comprehensive multimodality imaging assessment of asymmetric wall thickening in 166 patients with aortic stenosis. In a prospective consecutive cohort we demonstrate that asymmetric wall thickening is common, affecting a quarter (n=43) of patients with mild-to-severe aortic stenosis when assessed using magnetic resonance. Echocardiography is less sensitive missing a third of these cases so that asymmetric wall thickening was only identified in 17% (n=29). Irrespective of the imaging modality used, patients with asymmetric wall thickening had evidence of more advanced left ventricular decompensation with elevated myocardial injury and increased BNP concentrations compared to those with concentric wall thickening. This was despite the two groups having similar co-morbidities, valve narrowing, myocardial fibrosis and left ventricular hypertrophy. Moreover, patients with asymmetric wall thickening (on both magnetic resonance and echocardiography) were found to have an adverse prognosis, with this form of remodelling acting as an independent predictor of aortic valve replacement or death after correction for age, sex, left ventricular mass index, coronary artery disease and aortic stenosis severity.

Magnetic resonance has emerged as the gold standard non-invasive assessment of left ventricular mass and wall thickness. This is the first study to evaluate the true prevalence of asymmetric wall thickening in a cohort of patients with aortic stenosis, free from referral bias. This is in contrast to the only previous magnetic resonance study examining this question where patients were referred for magnetic resonance on clinical grounds. Unusual patterns of remodelling could therefore have potentially triggered the referral. Our data have demonstrated that asymmetric wall thickening is indeed common amongst patients with aortic stenosis affecting approximately a quarter of subjects (40% in those with severe stenosis), and characterised by advanced wall thickness measurements (16 [14,17] mm).

Echocardiography is less well suited to measuring wall thickness and limited by the availability of acoustic windows. In this study it missed 14 cases of asymmetric wall thickening detected by magnetic resonance. In 8 patients this was because short-axis echocardiographic images were not interpretable. Overall our prevalence of asymmetric wall thickening on echocardiography is similar to that previously reported (B. J. Maron et al., 1977; Panza & Maron, 1988) and to a recent analysis of the Intensive Lipid Lowering with Simvastatin and Ezetimibe in AS SEAS trial (Tuseth et al., 2010). Importantly patients with asymmetric wall thickening on echocardiography demonstrated the same characteristics as those detected by magnetic resonance including the increased troponin and BNP levels as well as the adverse prognosis (Table 5). This is an important observation because echocardiography, unlike magnetic resonance, is performed routinely to assess all patients with aortic stenosis. It suggests that the presence of asymmetric wall thickening should therefore be actively looked for on echocardiography (not simply ignored and attributed to a "sigmoid septum") and used to help identify patients likely to require aortic valve replacement rapidly and who might therefore benefit from more regular clinical follow up.

Why do some patients develop asymmetric rather than concentric wall thickening in response to increased afterload? The explanation for this observation remains unclear. In this comprehensive evaluation we did not observe any clear differences in patient demographics, co-morbidity, bicuspid aortic valve prevalence or aortic stenosis severity between these two groups. Asymmetric wall thickening did appear reversible following surgery suggesting that it represents an adaptive response to an increased afterload. One potential theory relates to the bending radius of the septum and posterior wall of the left ventricle. It has been suggested that the larger radius of the septum leads to greater myocardial tensions during contraction, promoting a more

pronounced hypertrophic response (Grossman, Jones, & McLaurin, 1975; Heng, Janz, & Jobin, 1985). While this concept explains why asymmetric wall thickening is almost universally confined to the septum, it fails to account for inter-individual differences in the degree of asymmetric wall thickening. It is possible that patients may have a subtle genetic predisposition to regional wall thickening (similar to those driving the development of hypertrophic cardiomyopathy) that becomes clinically apparent with exposure to an increased left ventricular afterload (Calvin W. L. Chin, Anoop S. V. Shah, et al., 2014; Hess et al., 1983b). Unfortunately we do not have genetic data in this study to test this hypothesis. The mechanism for the adverse event rate in patients with asymmetric wall thickening also remains unclear, although it was predominantly driven by increased rates of aortic valve replacement. Asymmetric wall thickening was associated with evidence of increased myocardial injury (cTnI) and wall stress (BNP) suggesting that it is a marker of more advanced decompensation and that patients will be more likely to develop symptoms and progress towards aortic valve replacement. The increased wall thickening may predispose patients to supply-demand ischemia, increased myocyte injury and troponin levels, though this hypothesis requires confirmation. It is interesting that patients with asymmetric wall thickening did not have evidence of increased myocardial fibrosis, another useful marker of left ventricular decompensation.

3.5.1 Limitations

During follow up a total of 14 patients died, limiting our mortality assessments, the outcome data is therefore predominantly driven by aortic valve replacement. A large multicentre study with longer follow up is desirable. Further attention should also be paid to the mechanism underlying asymmetric wall thickening formation, including the underlying genetics and the explanation for the associated adverse prognosis.

Chapter 4. Progression and regression of left ventricular hypertrophy and myocardial fibrosis in a mouse model of pressure overload cardiomyopathy.

4.1 Summary

We aimed to develop a mouse model to study the development of left ventricular hypertrophy and myocardial fibrosis in response to increased afterload and to understand how these processes reverse remodel following normalisation of pressure loading.

We performed a longitudinal study with serial cardiac magnetic resonance (CMR) every 2 weeks in mice (n=31) subjected to angiotensin II-induced pressure overload for 6 weeks and investigated reverse remodelling following normalisation of afterload (n=9). Left ventricular volumes, mass, and function as well as myocardial fibrosis were measured using cine CMR and indexed extracellular volume (iECV) calculated from T1-relaxation times.

Increased pressure afterload (65.1±12.0 vs 84.7±9.2 mmHg; p<0.001) resulted in higher indices of left ventricular hypertrophy (0.091 [0.083, 0.105] vs 0.123 [0.111, 0.138] g; p<0.001) and myocardial fibrosis (iECV: 0.022 [0.019, 0.024] vs 0.039 [0.031, 0.043] mL; p<0.001) whilst left ventricular ejection fraction fell (LVEF, 59.3 [57.6, 59.9] vs 46.9 [38.5, 49.6] %; p<0.001).

Following normalisation of blood pressure (68.8±5.4 vs baseline 65.1±12.0 mmHg; p=0.42), LV mass (0.108 [0.098, 0.116] vs 0.091 [0.083, 0.105] g), iECV (0.034 [0.032, 0.036] vs 0.022 [0.019, 0.024] mL) and LVEF (51.1 [42.9, 52.8] vs 59.3 [57.6, 59.9] %) improved but remained impaired compared to baseline (p<0.05 for all). There was a strong inverse correlation between LVEF and iECV during both pressure overload (r=-0.88, p<0.001) and reverse remodelling (r=-0.74, p=0.001).

We have developed a mouse model of left ventricular hypertrophy and reverse remodelling in response to pressure overload and we demonstrate that changes in myocardial fibrosis can be assessed non-invasively by MRI and are closely linked with alterations in systolic function during both phases of the disease.

4.2 Introduction

Pressure overload heart disease with concomitant myocardial fibrosis is observed in multiple common cardiac conditions including hypertension and aortic stenosis (Adabag et al., 2008; Assomull et al., 2006; Iles et al., 2008; C.-Y. Liu et al., 2013; Puntmann et al., 2013). While there is growing evidence that excessive fibrosis is associated with adverse clinical outcomes, longitudinal human data regarding changes in left ventricular remodelling and fibrosis over time are sparse. The lack of such data is largely due to the natural history of pressure overload heart disease, with conditions such as hypertension and aortic stenosis progressing slowly over many years and decades and making longitudinal studies challenging. In addition, little is known about adverse remodelling reversibility once the trigger is removed (Stuckey Daniel et al., 2014). Such insights are of particular interest in aortic stenosis where there is growing interest in optimizing the timing of aortic valve replacement (AVR) ideally using novel objective biomarkers of LV decompensation (Baumgartner et al., 2017; Krayenbuehl et al., 1989; Nishimura Rick et al., 2017).

Rodent models of pressure overload cardiomyopathy have been developed and potentially allow monitoring of disease progression, from the onset of pressure overload out to the advanced stages of heart failure. These models can therefore provide longitudinal data that is lacking in humans and can potentially do so using advanced imaging techniques that can be directly translated in to humans (Camacho et al., 2016; Houser et al., 2012; Ku et al., 2018; Messroghli Daniel et al., 2011). One of most widely used model of pressure overload heart disease is transverse aortic constriction. Unfortunately, this approach involves a high dropout rate of animals related to surgery and with the band placed distal to the innominate artery causes coronary congestion and a disease state more similar to aortic coarctation than aortic stenosis (Stuckey Daniel et al., 2014). Furthermore, removal of the band is challenging, and results in incomplete relief of the obstruction making the study of

reverse remodelling difficult (Cho et al., 2014). As a consequence only a few studies have investigated reverse remodelling upon removal of the pressure overload state and these did not include advanced imaging techniques (Bjørnstad et al., 2012; Gao et al., 2005; Weinheimer Carla et al., 2018).

The purpose of this study was to develop a mouse model of reversible pressure overload cardiomyopathy and to use state-of-the-art *in vivo* imaging to interrogate left ventricular hypertrophy, myocardial fibrosis, and cardiac function both before and after afterload reversal. Ultimately, our aim was to create a model that might help develop novel non-invasive biomarkers of left ventricular decompensation in response to pressure overload and provide insight in to the optimal timing of aortic valve implantation in aortic stenosis.

4.3 Methods

Thirty-one male C57BL/6J mice (Envigo, UK) were subjected to a continuous angiotensin II (Ang II) infusion at 480±34 ng/kg/min. Animals were allocated into one of three groups with varying duration of infusion: 2 weeks (n=5), 4 weeks (n=3) and 6 weeks (n=23). Additionally, a subset (n=9) of the animals receiving a 6-week infusion were assessed for an additional 28 days after discontinuation of the infusion to allow investigation of reverse remodelling. Finally, a further control cohort of animals received a placebo infusion of saline (0.9% NaCl) (n=9, Figure 13). Throughout the experiments, animals were on a regular chow diet, housed 5 mice per cage in a 12h:12h light/dark cycle in animal facilities at the University of Edinburgh. All procedures conformed to Home Office guidance on the use of the animals (Scientific Procedures) Act of 1986 and were approved by the University of Edinburgh Animal Welfare and Ethical Review Board.

4.3.1 Animal model of pressure overload

To subject animals to pressure overload, subcutaneously implanted osmotic minipumps (Alzet, Cupertino, CA) were used (Herrlich, Spieth, Messner, & Zengerle, 2012). Minipumps were prepared to deliver angiotensin II (Ang-II, Sigma-Aldrich, Darmstadt, Germany) at predetermined rates of infusion (Table 11). Implantation was performed surgically under anaesthesia. To monitor pressure overload, animals underwent serial blood pressure measurements using a Letica LE 5002 Non-Invasive Blood Pressure System (Panlab, Cornellá, Spain) which operates on the same basis as clinically used sphygmomanometers (tail cuff method). Prior to study commencement, mice were trained for tail cuff plethysmography in order to decrease animal stress related to measurement acquisition and to improve reproducibility. During the experimental period, mice were subjected to plethysmography after each imaging session. After 2 preliminary measurements, at least three recordings of systolic, diastolic and mean arterial pressure were recorded in each animal.

Table 11. Alzet minipumps specifications.

Pump	Reservoir Volume	Infusion Duration	Flow rate
1002	100µl	14 days	0.25µl/hr
2004	200µl	28 days	0.25µl/hr
2006	200µl	42 days	0.125µl/hr

4.3.1.1 Osmotic Minipump Preparation

To subject animals to pressure overload subcutaneously implanted osmotic minipumps (Alzet, Cupertino, CA) were used. These minipumps operate on the basis of an osmotic pressure difference between the pump's osmotic compartment and the surrounding tissue environment. They consist of a fluid reservoir (containing the drug) which is encapsulated by an osmotic layer covered by a semipermeable membrane. The high osmolality of the osmotic layer attracts water from the surrounding environment and this influx leads to compression of the reservoir chamber and guarantees a continuous delivery of the solution at a predefined rate which is specific for each pump model (Herrlich et al., 2012). Minipumps were prepared to deliver Angiotensin II (Sigma-Aldrich, Darmstadt, Germany) at the rates and over a time which is characteristic for a given pump model (Table 11). The total dose of Angiotensin II was calculated considering the pump reservoir size, flow rate and the animal weight. All pumps were filled using the provided 25-gauge filling needle (Alzet, Cupertino, CA) and a 1mL syringe. Special care was taken to avoid transferring any air bubbles into the filling reservoir as these might impede drug delivery. To confirm that no substantial air bubbles were present in the solution once filled all pumps were weighed. Control animals (n=9) were implanted with osmotic minipumps filled with sterile saline.

4.3.1.2 Surgical Procedures

Subcutaneous minipump implantation was performed under a sterile technique. To anaesthetise the animal, the induction chamber was filled with 3% isoflurane in oxygen (flow rate: 1L/min) and the mouse was placed in the box. When induction was confirmed (by unresponsiveness to external stimuli and absence of the palpebral reflex) the animal was placed on a heated mat (to maintain body temperature at 37°C) under a face mask delivering 2-2.5% isoflurane in oxygen (flow rate 1L/min). Hair was removed from the interscapular part of the animals' back using a hair trimmer. Afterwards any residual hair was removed diligently with the vetasept chlorhexidine surgical disinfectant. A small horizontal incision was made in the interscapular region using sharp surgical scissors. Subsequently using blunt, straight dissection forceps a pocket under the skin was created for the placement of the Alzet minipump. In the next step the minipump was inserted into the newly established subcutaneous pocket with the flow moderator of the pump pointing caudally (away from the incision site). The wound was closed using Autoclips (Kent Scientific, Torrington, CT) and sterilised with Vetasept. The animal was then liberated from the face mask, an analgesic (0.05 mg/kg buprenorphine/Vetergesic, Alstoe, UK) was administered subcutaneously and the mouse was placed into a preheated recovery cage with soft food readily available.

4.3.1.3 Blood Pressure Measurements

Blood pressure measurements were carried using the Letica LE 5002 Non-Invasive Blood Pressure System (Panlab, Cornellá, Spain). The system operates on the same basis as clinically used sphygmomanometers. By inflation of the cuff placed around the proximal part of the tail the arterial blood flow is occluded and subsequently during controlled deflation a sensor measures both systolic and diastolic BP.

Prior to the start of the experimental protocol mice were trained to tail cuff plethysmography in order to decrease the load of stress related to taking the measurements and to improve reproducibility. During the experimental period animals were subjected to plethysmography after every imaging session. Mice were placed into a restraining chamber while recovering from anaesthesia. The plethysmograph cuff which has an inbuilt sensor was positioned at the proximal end of the tail. To maintain body temperature during the measurements mice were kept in a preheated recovery box (MediHEAT, Vet-Tech solutions, Congleton, UK). After 2 preliminary measurements, at least three recordings of systolic, diastolic and mean arterial pressure per animal were recorded. The time between measurements was >10 seconds - which was the time required for the system to deflate the cuff.

4.3.1.4 Sacrifice and Tissue Collection

After the final imaging session animals were kept under anaesthesia and transferred to a face mask delivering 3% isoflurane in oxygen (flow 1/L/min). Through a midline incision of the abdomen and chest the ribcage and (after cutting the sternum) the heart was visualised. Animals were then euthanized by exsanguination via cardiac puncture. Blood was collected into heparinized tubes (Multivette 600LH, Sarstedt, Nümbrecht, Germany). Death was confirmed by cessation of circulation. The heart was then removed and transferred into 10% neutral buffered formalin (Cellstor, CellPath, Newton, UK) for fixation for at least 20 hours. Blood was centrifuged at 8000 rpm for 6 minutes and then the plasma was carefully collected (with special care to avoid contamination by erythrocytes, leukocytes or platelets), aliquoted and stored in 1.5ml Eppendorf tubes at -80C for further analysis.

4.3.1.5 Histological Analysis

After fixation hearts were processed in a tissue processor by immersing in graded ethanol washes (70%,95%,100%), Xylene and then finally Paraffin wax. The wax infiltrated hearts were then placed in a mould containing molten paraffin which was allowed to cool. Samples were embedded in paraffin in a short axis orientation so that the sections cut would all show the ventricle lumen. For sectioning heart tissue blocks were chilled on ice and then cut on microtome. Prior to histological staining, sections were deparaffinized and rehydrated at room temperature according to the following protocol. For deparaffinization samples were immersed twice in xylene for 5 minutes. In the next step slides were rehydrated by sequentially immersing in graded ethanol washes (100%, 95%, 85%,70 and 50%) for 3 minutes each. Subsequently samples were washed in 0.85% NaCl for 5 minutes and immersed in phosphate buffered saline for 5 minutes. Slides were stained in a 0.1% sirius red solution in saturated picric acid (Picrosirius red, Sigma, Dorset, UK) in the dark for 90 minutes. Slides were then briefly washed three times in acidified water by quickly dipping 3 times and dehydrated by immersing in graded ethanol washes (50%, 70%, 85%, 95% 100%), cleared in xylene for 5 minutes and then finally mounted with permanent mounting media (Pertex, CellPath,Newtown, UK). All picrosirius red stained slides images were acquired on the AxioScan Z1 (Carl Zeiiss, Oberkochen, Germany) using an in-house developed protocol for bright field mouse myocardium slides. The .CZI files were then converted into tagged image file format (.TIFF) to facilitate image analysis using Image-Pro Premiere 9.1 (MediaCybernetics, Rockville, MD, USA). In the first step the pixel area occupied by fibrosis was calculated using the counting toll after manual protocol adjustment. A pixel intensity threshold of 204-245 on the Mono scale was applied. The highlighted area was inspected for any contamination by erythrocytes or endo/epicardium and if present these objects were removed before the final output was recorded. In a similar fashion the total area of the analysed tissue was calculated by considering the area within the threshold of 150-245 on the mono scale with the

exceptions outlined above made if necessary. Finally, the area of fibrosis was expressed as a percentage of the slide total myocardium area.

4.3.2 Cardiovascular Magnetic Resonance Imaging

All animals underwent serial CMR imaging to assess left ventricular structure and function as well as myocardial fibrosis. CMR was performed initially at baseline before the onset of pressure overload, and then every 2 weeks during angiotensin II infusion. In the reverse remodelling subgroup, a final CMR scan was performed 4 weeks after the Ang II infusion had been discontinued (Figure 13). At the end of the final imaging session, animals were culled by exsanguination under deep anaesthesia with the heart stored for further histological analysis.

Figure 15. Study outline. Top arrow: study timeframe. Second row: number of animals that underwent MRI at a given timepoint in bold. In brackets number of animals subjected to Angiotensin infusion and controls. In the bottom row, total number of animals culled in bold with numbers of experimental and control mice in brackets.

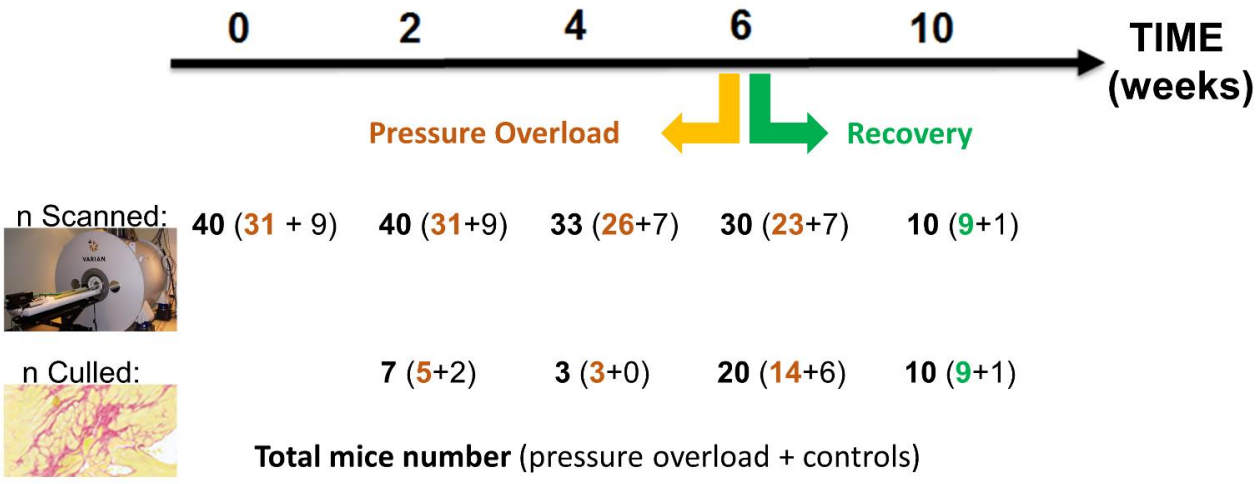

All MRI scans were performed on a 7-Tesla preclinical horizontal-bore MRI system (Agilent Technologies, Yarnton, UK) equipped with a 33-mm inner diameter radiofrequency coil for mice (Rapid Biomedical, Rimpar, Germany). Animals were anaesthetised using isoflurane (3% isoflurane in 1.0L/min oxygen for induction and 1.5-2% isoflurane in 0.5 L/min O2/0.5 L/min air for maintenance). Prior to imaging an Anicath 26G cannula (Millpledge Veterinary, Clarborough, UK) was placed intraperitoneally for administration of the gadolinium-based contrast agent (gadobenate dimeglumine 1 µL/g body weight [Multihance]; Bracco Diagnostics, Princeton, NJ). Animals were placed in an MRI cradle with electrocardiogram (ECG) leads placed subcutaneously. The animals were positioned supine with hearts in the centre of the coil, and in the centre of the MRI scanner. A pressure transducer was placed under the torso for constant monitoring of respiration (MR-compatible Small Animal Monitoring and Gating System, SA Instruments, Stony Brook, NY), and a rectal probe was inserted to monitor and maintain body temperature at 37±0.5 °C via a feedback-controlled warm air system (MR-compatible Small Animal Heating System, SA Instruments, Stony Brook, NY). Throughout the imaging session special care was taken to keep the heart rate stable at 530-600 beats/min and to maintain a respiratory rate of 45-75 breaths/min.

Scout images were taken to confirm correct positioning and to orientate 1.0-mm short axis slices covering the heart. T1 mapping for calculation of regional left ventricular myocardial T1 relaxation times was accomplished using a gradient-echo, cardiac-gated Modified Look-Locker Inversion recovery sequence (MoLLI) during which 30 images of a single mid-ventricular slice were acquired at unique inversion times (dependent on heart rate, ranging from approximately 0.10 to 3.00 s) with the recovery time after each inversion pulse > 3×T1 of myocardium. Imaging readout was with a cardiac fast gradient echo (repetition time 2.8 ms; echo time 1.4 ms; flip angle

10°, matrix 128×128; field of view 30×30 mm2; in-plane resolution=0.23×0.23 mm2; trigger delay 0.5×R-R; slice thickness 1.5 mm;). We acquired eight phase-encoding echos per segment and 8 signal averages were used to compensate for respiratory motion. After acquisition of a baseline T1 map, gadobenate dimeglimine was injected via the intraperitoneal cannula, and a second T1-mapping dataset was acquired 20 minutes post-injection. During the time between the T1-mapping acquisitions, cine images were acquired for structural and functional assessment. The short axis, vertical and horizontal long axis cardiac images were acquired using an ECG triggered and respiratory-gated gradient echo sequence (TR/TE = 5.2/1.3 ms, flip angle: 15°) with gradient and radiofrequency spoiling. Eighteen phases were acquired with a field of view of 30x30 mm, a 128x128 matrix, and 2 signal averages were used. For the left ventricular short axis, nine consecutive 1-mm-thick slices were acquired, which encompassed the entire heart from base to apex. Late gadolinium enhancement imaging was performed between 12 and 18 minutes after contrast administration with a short-axis cardiac-triggered/respiratory-gated T1-weighted gradient echo inversion-recovery scan with the following imaging parameters: TR: 1000ms (depending on respiration rate), TE: 1.45 ms, field of view: 30 x 30 mm, number of signal averages: 4, inversion time: 560 ms, flip angle: 90°, nine 1-mm thick slices covering the entire left ventricle.

4.3.3 Image analysis

Data were analysed using certified software (cvi42, Circle CVI, Calgary, Alberta, Canada). The short axis cine images of the LV were used for the assessment of left ventricular volumes, mass and ejection fraction. The epicardial and endocardial contours were carefully identified and planimetered in end-systole and end-diastole for left ventricular volume quantification. The left ventricular mass was calculated from the total myocardial volume (excluding trabeculations and papillary muscles) multiplied by the density of the myocardium (1.05 g/mL). Maximal wall thickness was evaluated in all 17 segments of the LV from cine images of the LV in end-diastole (Cerqueira et al., 2002). For LV diffuse fibrosis, we calculated the extracellular volume fraction (ECV%) derived from pre- and post-contrast myocardial T1 values corrected for blood-pool T1. The ECV% was calculated according to: ECV% = partition coefficient x [1-hematocrit]; where partition coefficient = [ΔR1myocardium/ΔR1blood-pool] and ΔR1 = (1/post-contrast T1-1/pre-contrast T1). In order to evaluate the total amount of interstitial fibrosis in each animal, we calculated the indexed ECV (iECV) in each animal using the following equation: ECV% x left ventricular myocardial volume, where left ventricular myocardium volume = left ventricular mass divided by the density of myocardium (1.05 g/mL) (7). To avoid blood-pool contamination and partial volume effects, we used a mid-myocardial region of interest for the T1-mapping analysis. A two-pixel wide myocardium and ventricular boundary zone was excluded from all applicable slices. Late gadolinium enhancement was used for detection of focal replacement fibrosis. Where present, it was quantified as an area of myocardium with a signal intensity exceeding the threshold of two standard deviations above the mean value of normal myocardium. All areas of inversion artefact or myocardial regions contaminated by blood pool or epicardial fat were excluded.

4.3.4 Histology

Histological validation was performed for each CMR technique used to measure myocardial fibrosis. After the final imaging session, animals were kept under anaesthesia and euthanized. The heart was removed and transferred into 10% neutral buffered formalin (Cellstor, CellPath, Newton, UK) for fixation for at least 20 hours. After fixation hearts were processed and embedded in paraffin in a short axis orientation so that the cut sections would all show the ventricle lumen. Slides were stained in a 0.1% sirius red solution in saturated picric acid (Picrosirius red, Sigma, Dorset, UK). All picrosirius red stained slides images were acquired on the AxioScan Z1 (Carl Zeiss, Oberkochen, Germany) and analysed using Image-Pro Premiere 9.1 (MediaCybernetics, Rockville, MD, USA) using tissue specific threshold. The area of fibrosis was expressed as a percentage of the total myocardial area (supplemental data). The total burden of myocardial fibrosis assessed by histology was calculated as the ECV% multiple by the mass of the heart weighed before fixation.

4.3.5 Statistical Analysis

Continuous variables were tested for distribution with the Shapiro-Wilk test. Data are presented as mean±SD, median [interquartile range] or percentages where appropriate. Differences between groups were assessed with the use of a 2-sided Student t-test, paired Student t-test, ANOVA for continuous variables, Wilcoxon rank-sum test for ordinal variables and the $\chi 2$ test or Fisher's exact test for categorical data. The relationship between 2 continuous variables was assessed using Pearson's correlation. A 2-sided $p<0.05$ was considered statistically significant.

4.4 Results

4.4.1 Left ventricular remodelling under pressure overload

Mean arterial pressure (MAP) was elevated after 2 weeks of Ang II infusion compared to baseline (84.2±13.6 vs 65.1±12.0 mmHg, $p<0.001$) and remained stable for the remainder of the infusion phase ($p>0.50$; Table 11). Both maximum wall thickness and LV mass increased during angiotensin II infusion (0.73 [0.71,0.76] vs 0.84 [0.81, 0.86] mm, $p=0.001$ and 0.091 [0.083, 0.105] vs 0.108 [0.101, 0.121] g, $p<0.001$ respectively). Wall thickness and LV mass were elevated after 2 weeks and further increased up to the 4-week time point (0.84 [0.81, 0.86] vs 0.88 [0.80, 0.95] mm, $p<0.001$ and 0.108 [0.101, 0.121] vs 0.121 [0.111, 0.136] g, $p<0.001$) after which both plateaued (Table 12).

Table 12. Left ventricular remodelling under pressure overload and after load normalization.

	Baseline	2 weeks	4 weeks	6 weeks	1 month post infusion	P value
MAP, mm Hg	65.1±12.0	84.2±13.6	86.5±7.1	84.7±9.2	68.8±5.4	<0.001
EDV, ml	0.058 [0.053, 0.063]	0.071 [0.066, 0.081]	0.074 [0.065, 0.086]	0.083 [0.073, 0.097]	0.081 [0.067, 0.095]	<0.001
ESV, ml	0.022 [0.020, 0.025]	0.033 [0.30, 0.040]	0.041 [0.034, 0.045]	0.048 [0.037, 0.055]	0.041 [0.032, 0.063]	<0.001
Wall Thickness, mm	0.73 [0.71,0.76]	0.84 [0.81, 0.86]	0.88 [0.80, 0.95]	0.86 [0.82, 0.91]	0.82 [0.80, 0.92]	0.001
LV mass, g	0.091 [0.083, 0.105]	0.108 [0.101, 0.121]	0.121 [0.111, 0.136]	0.123 [0.111, 0.138]	0.108 [0.098, 0.116]	<0.001
ECV, %	24.03±3.39	29.53±4.25	29.99±2.65	29.98±1.84	27.10±1.64	0.001
LV iECV, mL	0.022 [0.019, 0.024]	0.033 [0.029, 0.035]	0.036 [0.035, 0.040]	0.039 [0.031, 0.043]	0.034 [0.032, 0.036]	<0.001
SV, ml	0.031 [0.027, 0.035]	0.033 [0.029, 0.035]	0.034 [0.028, 0.036]	0.033 [0.031, 0.034]	0.035 [0.031, 0.036]	0.19
EF, %	59.3 [57.6, 59.9]	52.4 [47.7, 53.9]	49.5 [41.2, 51.7]	46.9 [38.5, 49.6]	51.1 [42.9, 52.8]	<0.001

4.4.2 Histological assessment of myocardial fibrosis

Hearts from 28 animals were available for histological analysis and validation of the CMR fibrosis measurements (n=13 culled during increased pressure overload, n=9 culled after reverse remodelling and six control animals) (Figure 14A). An increase in myocardial fibrosis was observed in animals exposed to the angiotensin II infusions compared to control animals (4.4, [3.5, 5.8] vs 10.1 [8.7, 12.9] %, $p<0.001$). There was a strong correlation between the histological assessment of myocardial fibrosis (% myocardium comprised of fibrosis) and the ECV% as measured by CMR ($r=0.89$, $p=0.001$; Figure 14B). Similar correlations were observed between histological fibrosis and native T1 ($r=0.80$, $p<0.001$), post contrast T1 ($r=-0.75$, $p<0.001$) and iECV ($r=0.82$, $p<0.001$). Finally, a close correlation was observed between the total volume of myocardial fibrosis in the left ventricle on histology (%myocardium comprised of fibrosis multiplied by the volume of the left ventricular myocardium) and the equivalent CMR parameter iECV ($r=0.90$, $p<0.001$; Figure 14E).

Figure 16. Fibrosis on histology and T1-mapping data. Examples of diffuse fibrosis on histology - picrosirius red staining (A). The relationship between fibrosis on histology and the native T1-values (B), post contrast T1-values (C), extracellular volume (D) and indexed ECV(E)

A.

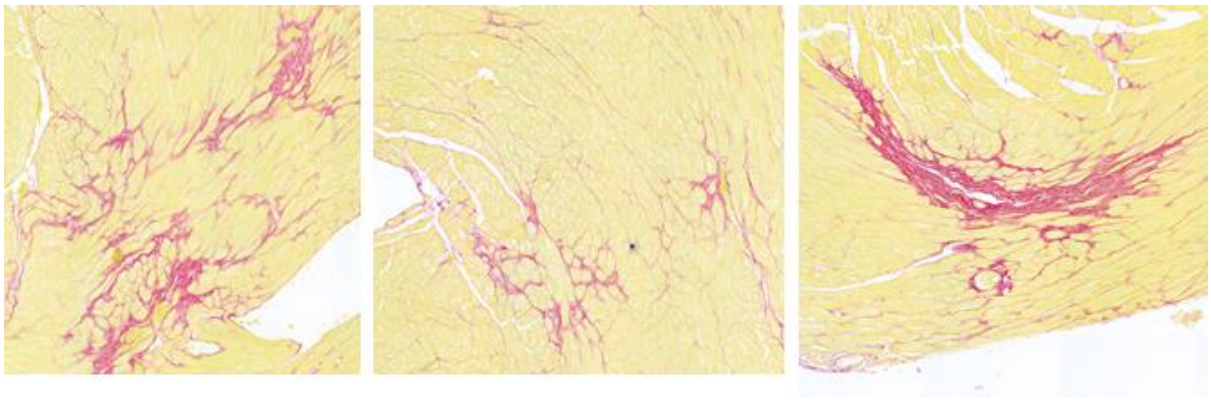

B.

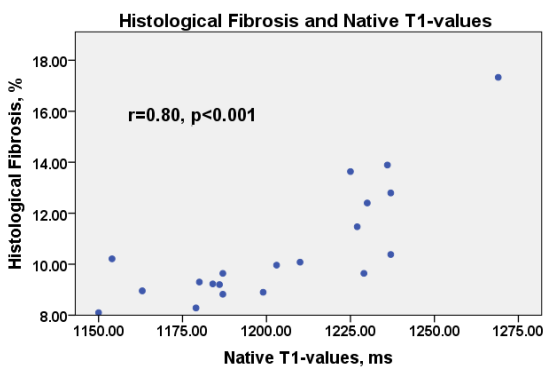

C.

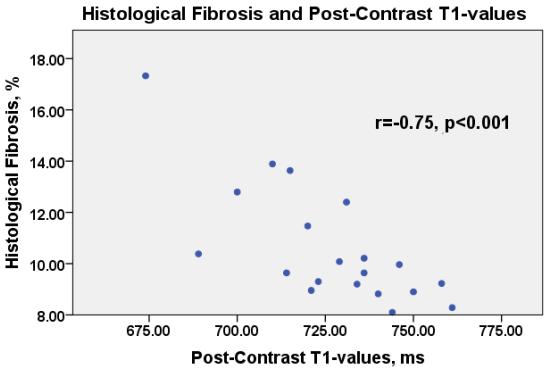

D.

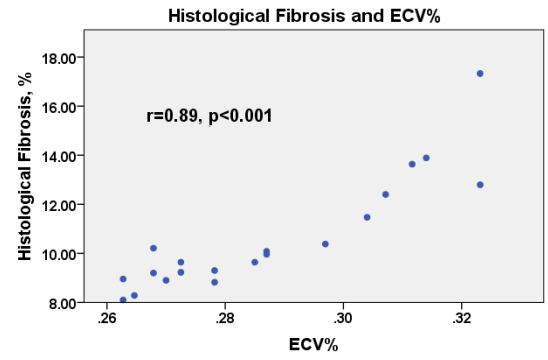

E.

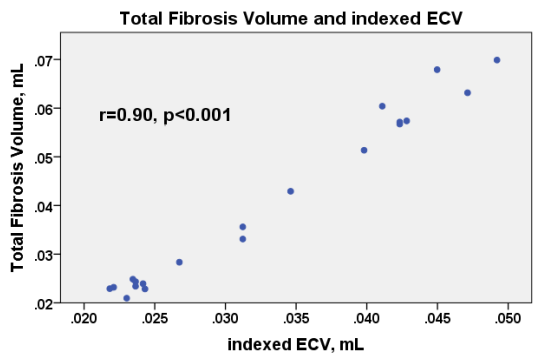

4.4.3 LV fibrosis and function under pressure overload

While there was no change in native T1 relaxation times during exposure to pressure overload (p=0.10), both ECV% and iECV demonstrated progressive increases. This increase in ECV% demonstrated a similar pattern of change as the blood pressure with an initial increase (24.28±3.35 vs 29.53±4.25 %, p=0.004) followed by a plateau phase after 4 weeks (p>0.40). By contrast iECV increased during the first 2 weeks (0.033 [0.029, 0.035] vs 0.022 [0.019, 0.024] mL, p<0.001), and then kept on expanding at 4 and 6 weeks (0.036 [0.035, 0.040] and 0.039 [0.031, 0.043] mL, p=0.041 and p=0.07 respectively) following a similar pattern to that demonstrated by EF, which also demonstrated an ongoing gradual reduction with time spent on the Ang II infusion (LVEF 59.3 [57.6, 59.9] % at baseline, 52.4 [47.7, 53.9] % at 2 weeks, 49.5 [41.2, 51.7] % at 4 weeks and 46.9 [38.5, 49.6] % at 6 weeks; p<0.001 for trend) (Figures 15 and 16). We did not observe late gadolinium enhancement in our experimental animals.

Figure 17. Cardiovascular magnetic resonance imaging of mice subjected to pressure overload. Modified Look-Locker Inversion Recovery T1-mapping (A). T1 relaxation times for the myocardium and bloodpool are generated from images shown in the upper row. The calculated T1 relaxation times can be used to generate native (**blue**) and postcontrast (**orange**) T1 maps. End-diastolic and end-systolic LV short axis images demonstrating adverse remodelling due to an increased afterload (B).

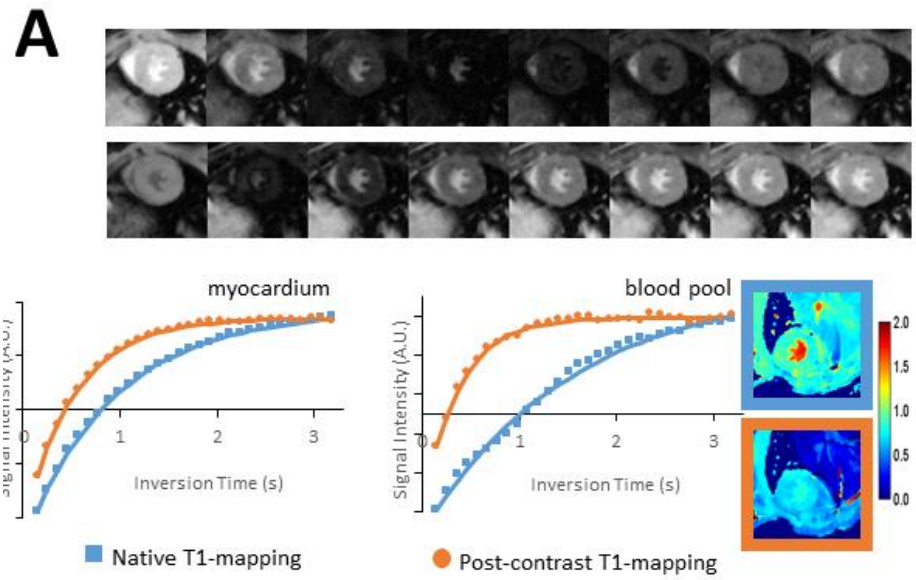

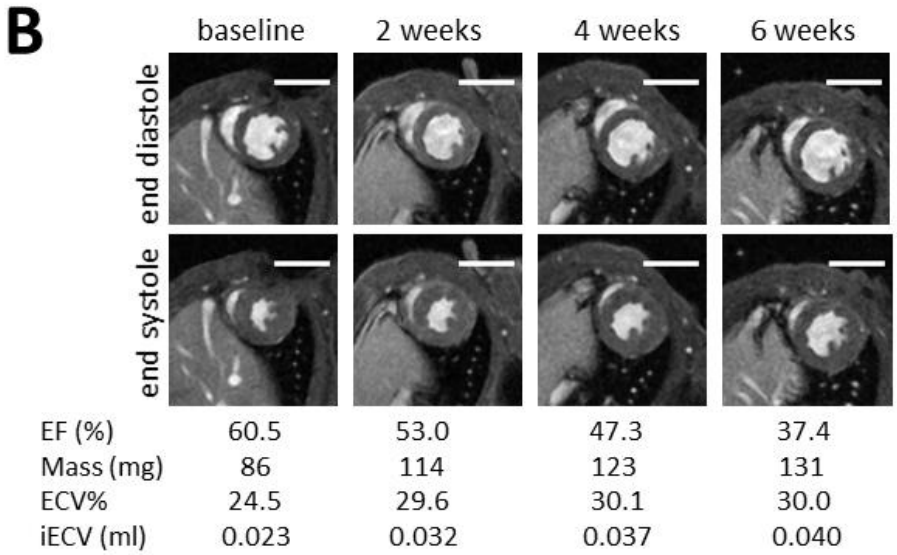

	baseline	2 weeks	4 weeks	6 weeks
EF (%)	60.5	53.0	47.3	37.4
Mass (mg)	86	114	123	131
ECV%	24.5	29.6	30.1	30.0
iECV (ml)	0.023	0.032	0.037	0.040

Figure 18. Adverse remodelling under pressure overload. Mean arterial pressure (A), Left ventricular mass (B) Extracellular volume fraction (C), iECV (D), LV ejection fraction (E), LV end diastolic volume

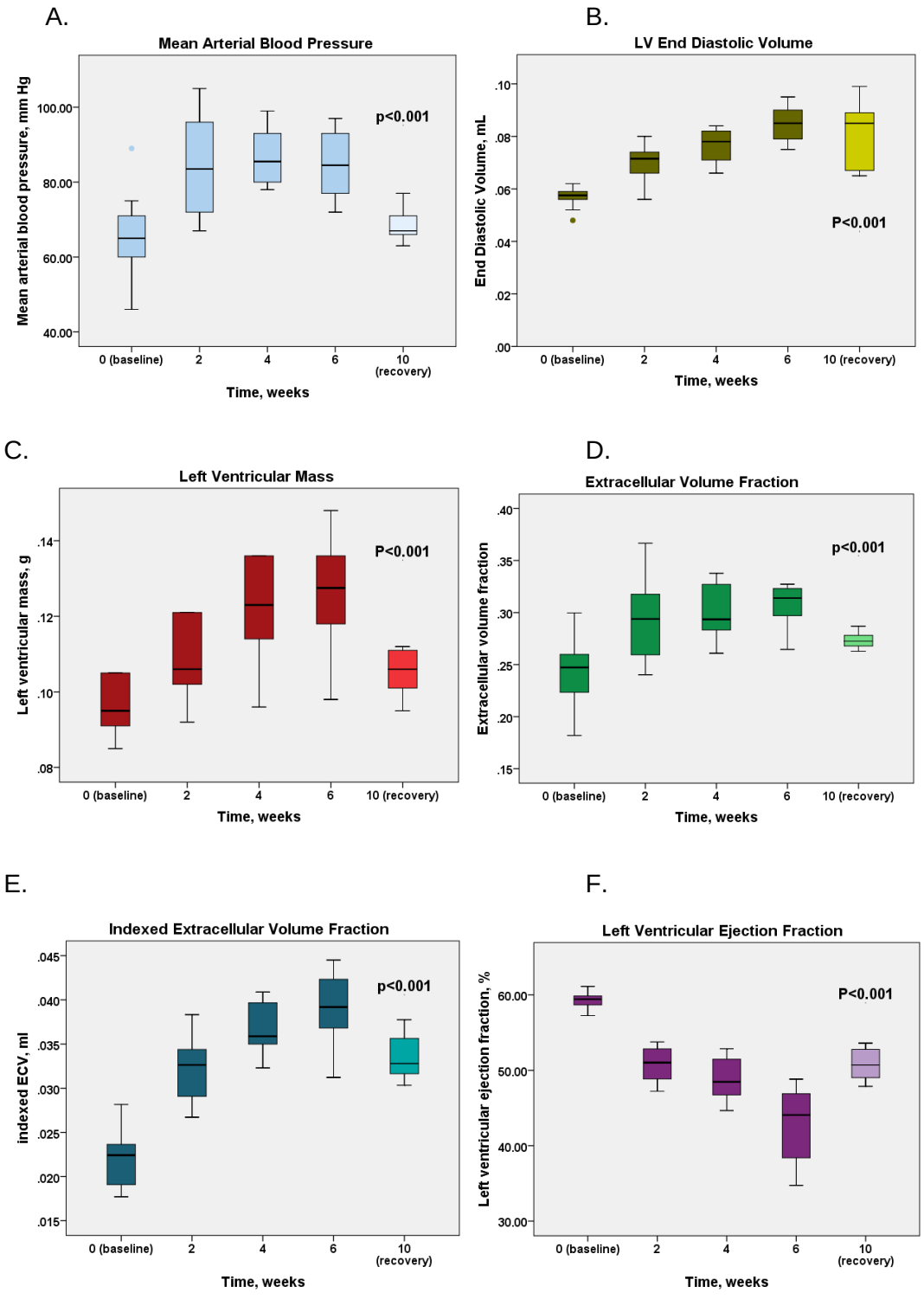

4.4.4 Reverse remodelling

Four weeks after the end of the Ang II infusion, reversal of the pressure overload state was observed with mean arterial blood pressure values returning to baseline (p=0.42 for difference, Figure 16A). In response LV mass, ECV% and iECV all regressed (p<0.01; Table 12). However, this reverse remodelling was only partial with none of these parameters returning to their baseline values (Figure 16). Indeed, ECV% only partially resolved, with values reducing from 30.0±1.8% during the infusion to 27.1±1.6% (p=0.001) 4 weeks following its discontinuation compared to baseline values of 24.0±3.4% (p=0.06). Similarly, iECV was lower than during angiotensin II infusion (0.030 [0.028, 0.036] vs. 0.039 [0.031, 0.043] mL, p=0.002) but remained higher than at baseline (0.022 [0.019, 0.024] vs. 0.034 [0.032, 0.036] mL, p=0.001; Table 1). Importantly the LV ejection fraction again demonstrated a similar pattern to iECV, showing a trend towards recovery (46.9 [38.5, 49.6] vs 51.1 [42.9, 52.8] %, p=0.10) yet remaining lower at 4 weeks than at baseline (59.3 [57.6, 59.9] vs 51.1 [42.9, 52.8] %, p=0.029; Table 1). The LV end-diastolic volume remained elevated: 0.081 [0.067, 0.095] mL compared to 0.083 [0.073, 0.097] mL during pressure overload (p=0.70).

4.4.5 ECV% is associated with systolic function

There was a strong inverse correlation between LVEF and iECV values during pressure loading ($r=-0.88$, $p<0.001$ at 6 weeks; Figure 17A). Whilst ECV% was also associated with LVEF at this timepoint, the observed correlation was only moderate ($r=-0.54$, $p<0.001$). Following reversal of pressure overload again a strong association was observed between iECV and ejection fraction ($r=-0.74$, $p=0.001$). On multivariable linear regression analysis, ECV%, and iECV were independently associated with LVEF independent of MAP and LV mass. Interestingly the model incorporating iECV had a higher R-Square (0.78) than the one with ECV% (0.54, Table 13).

We found a strong correlation between the increases in ECV% observed in the first two weeks of pressure overload (from baseline to week 2) and the reduced ejection fraction after 6 weeks ($r=-0.77$, $p<0.001$; Figure 17B).

Table 13. Univariable and multivariable linear regression analysis to examine association of variables with LV ejection fraction after 6 weeks of pressure overload.

Variables	Univariable		Multivariable – Model 1 (included early ECV% change) R-Sq = 0.62		Multivariable – Model 2 (included ECV% at 6 weeks) R-Sq =0.54		Multivariable – Model 3 (included iECV at 6 weeks) R-Sq =0.78	
	Relative change in LVEF (95% CI)	P-value	Relative change in LVEF (95% CI)	P-value	Relative change in LVEF (95% CI)	P-value	Relative change in LVEF (95% CI)	P-value
MAP, per 5mmHg	-2.8 (-5.4- -0.1)	0.04	-1.3 (3.0-0.4)	0.23	-1.9 (-3.9-0.1)	0.11	-0.5 (-1.9-0.8)	0.44
LV mass, per 1mg	0.1 (-0.05 - 0.3)	0.08	-0.2 (-0.5 - 0.1)	0.27	0.2 (-0.1-0.5)	0.21	-0.02 (-0.2-0.2)	0.68
Early change in ECV%, per 1%	-2.1 (-2.9- -1.3)	<0.001	-2.2 (-2.9 - -1.5)	<0.001				
ECV%	-1.6 (-2.3- -0.8)	<0.001			-1.5 (-2.2 - -0.7)	<0.001		
iECV, per 10µL	-6.3 (-7.7- -4.9)	<0.001					-6.0 (-7.7- -4.3)	<0.001

Figure 19. Diffuse fibrosis and systolic function. Indexed ECV is associated with ejection fraction under pressure overload (A). Early changes in ECV% predict later reductions in EF (B).

A.

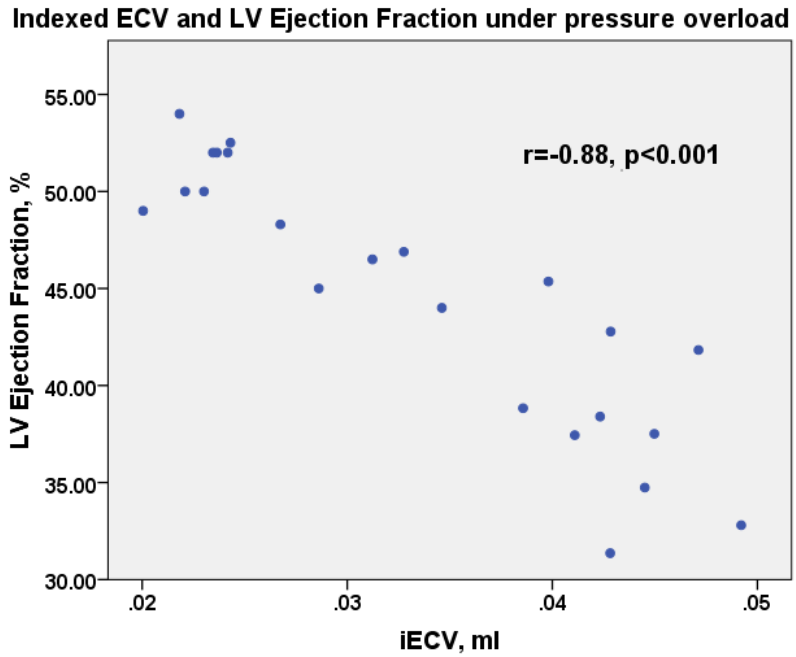

B.

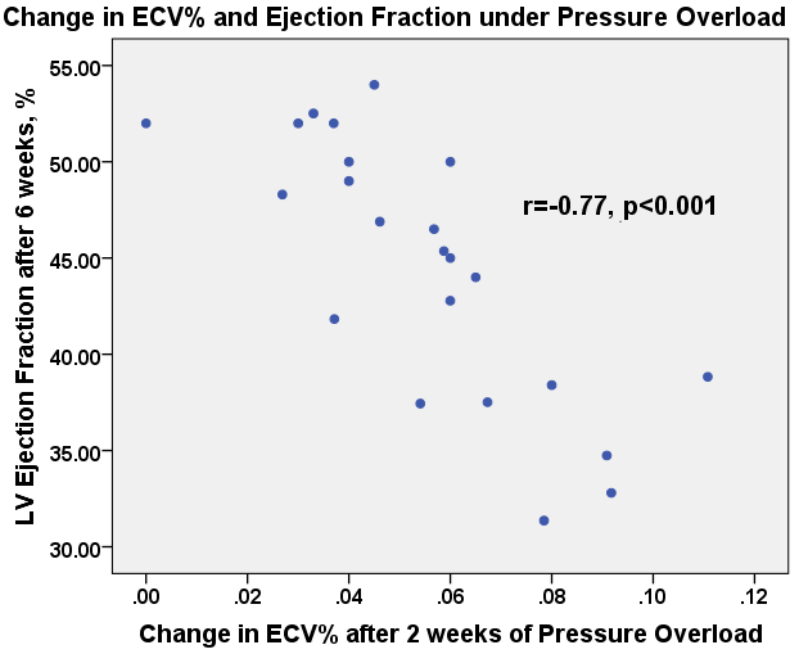

4.5 Discussion

In this study we have established reversible angiotensin II infusion as an animal model of left ventricular hypertrophy and reverse remodelling. This model has allowed us to assess how the hypertrophic response and myocardial fibrosis develop in response to an increased afterload and then reverse remodels once that stimulus is removed. We believe our model will allow improved understanding of the processes underlying LV decompensation in patients with aortic stenosis and hypertension that may ultimately help to optimise patient treatment including the timing of AVR. In this study we have demonstrated that myocardial fibrosis appears to be the primary determinant of LV dysfunction both before and after reversal of pressure overload. Further studies should investigate the optimum time to reverse pressure overload in order to ensure more complete recovery in left ventricular function.

Our preclinical model offers several important advantages, using state-of-the-art *in vivo* CMR imaging it enables longitudinal collection of data on remodelling in the same subject within a timespan of months rather than years or decades as observed in humans. Further it provides an almost unlimited amount of myocardium for histological evaluation, enabling validation of our CMR markers of fibrosis, including iECV confirmed for the first time as a biomarker of the total burden of left ventricular fibrosis. Finally, to the best of our knowledge, we have developed the first preclinical model to provide insight into both the hypertrophic response and reverse remodelling using state-of-the-art longitudinal imaging assessments. While several studies have utilized transverse aortic constriction as a model of aortic stenosis this model has several limitations. The surgical technique is associated with a 25% drop-out of animals in the peri-procedural period (Stuckey Daniel et al., 2014). With the aortic band placed between the origin of the innominate and left common carotid arteries the model recreates proximal aortic coarctation leading to significant hemodynamic consequences. These include elevated pressure in the innominate, right common

carotid, coronary and right subclavian arteries as opposed to a the left subclavian and carotids. In severe constriction perfusion of organs distal to the band can be maintained through the Willis circle yet this again is not typical for aortic valve stenosis.

Continuous infusion of Ang II leads to systemic hypertension and holds major promise in improving our understanding of LV decompensation in aortic stenosis and in the development of novel biomarkers and treatment strategies. Indeed, in this study we have demonstrated that reductions in ejection fraction in pressure overload conditions are more closely associated with the total burden of myocardial fibrosis (as measured with iECV) than the degree of pressure afterload. Moreover, we observed that reverse remodelling 1 month after load normalization is incomplete with residual fibrosis again closely associated with residual systolic impairment. Our findings are in line with the hypothesis that fibrosis is a principal driver of left ventricular decompensation in pressure overload (C. W. L. Chin et al., 2017), a key determinant of LV systolic function and an important potential therapeutic target. This is a particularly appealing target given that several drug therapies have already demonstrated their ability to reduce myocardial fibrosis in other contexts (Díez et al., 2002; Dweck et al., 2011). Indeed, our model could potentially be used to assess the efficacy of existing or novel anti-fibrotic therapies before proceeding to expensive clinical trials.

This model might also prove of value in determining the optimal timing of aortic valve replacement. The data presented here suggests that if pressure overload continues for too long then irreversible fibrosis will develop in the ventricle, leading to long term impairment of systolic function. Further studies should investigate whether reversing pressure overload earlier might potentially lead to complete recovery in left ventricular function and whether the optimal timing can be identified using imaging or other

biomarkers. This strategy could ultimately then be applied to aortic stenosis, thereby optimising the timing of aortic valve replacement.

4.5.1 Limitations

We acknowledge that our study has limitations. While our model recreates the myocardial response to increased afterload observed in patients with hypertension and aortic stenosis it is not a pure model for either. For T1-mapping we only acquired data from the mid-ventricle short axis slice potentially introducing a sampling error. In patients with aortic stenosis, data are usually obtained from 3 slices so that the basal, mid and apical segments are all interrogated. Since our model of pressure overload affects the entire left ventricle and due to animals' welfare, we chose to shorten the image acquisition by focusing on the mid-ventricle slice. We performed blood pressure measurements immediately after the imaging sessions at the time animals were recovering from anaesthesia. We found such an approach to be less stressful for mice whilst allowing for recording multiple readings.

Chapter 5. Sex-Related Differences in the Extent of Myocardial Fibrosis in Patients with Aortic Valve Stenosis

5.1. Summary

Previous studies reported sex-related differences in the left ventricular remodeling response to pressure overload in aortic stenosis. However, there are very few data regarding the effect of sex on myocardial fibrosis, a key marker of left ventricular decompensation and adverse cardiac events in aortic stenosis. The aim of this study was to assess the effect of sex on myocardial fibrosis as assessed by cardiac magnetic resonance in aortic stenosis.

Two hundred forty-nine patients (66±13 years, 30% women) with at least mild aortic stenosis were recruited from two prospective observational cohort studies and underwent comprehensive Doppler echocardiography and magnetic resonance exams. On cardiovascular magnetic resonance, T1 mapping was used to quantify extracellular volume fraction as a marker of diffuse fibrosis, and late gadolinium enhancement was used to assess focal fibrosis.

There was no difference in age between women and men (66±15 vs 66±12 years, p=0.78). However, women presented a better cardiovascular risk profile than men with less hypertension, dyslipidemia, diabetes, and coronary artery disease (all p≤0.10). As expected, left ventricular mass index measured by cardiovascular magnetic resonance was smaller in women than in men (p<0.0001). Despite less comorbidities, women presented larger extracellular volume fraction [29.0 (27.4-30.6) vs. 26.8 (25.1-28.7) %, p<0.0001] and similar late gadolinium enhancement [4.5 (2.3-7.0) vs. 2.8 (0.6-6.8) %, p=0.20] than men. In multivariable analysis, female sex remained an independent determinant of higher extracellular volume fraction and late gadolinium enhancement (all, p≤0.05).

Women have greater diffuse and focal myocardial fibrosis independent of the degree of aortic stenosis severity. These findings further emphasize the sex-related differences in left ventricular remodeling response to pressure overload.

5.2. Introduction

Calcific aortic stenosis (AS) is the most prevalent valvular heart disease in high income countries (Brian R. Lindman et al., 2016). In patients with AS, the development of symptoms and subsequent adverse cardiovascular events are essentially related to the increased left ventricular (LV) global hemodynamic load (Blase A. Carabello, 2013; Marc R. Dweck et al., 2012; Brian R. Lindman et al., 2016). In response to chronic pressure overload, LV remodeling and hypertrophy maintain normal LV wall stress and systolic function. However, this LV hypertrophic response is often maladaptive and leads to myocardial oxygen supply-demand mismatch, repetitive ischemia, and initiates a cascade of signalling pathways associated with inflammation, increased extracellular matrix remodeling, myocyte apoptosis or necrosis, and the development of myocardial fibrosis (Burchfield, Xie, & Hill, 2013; Hein et al., 2003; K. T. Weber, Sun, Bhattacharya, Ahokas, & Gerling, 2013; Westermann et al., 2011). To this regard, myocardial fibrosis by histopathology has been documented in patients with AS and has been associated with increased morbidity and mortality (Azevedo et al., 2010; Weidemann et al., 2009).

Cardiac magnetic resonance (CMR) imaging offers a non-invasive, accurate and reproducible assessment of LV architecture and function. CMR detects the presence of replacement myocardial fibrosis using late gadolinium enhancement (LGE), and diffuse reactive myocardial fibrosis using extracellular volume (ECV) fraction calculated from T1 mapping (Barone-Rochette et al., 2014; Dweck et al., 2011; Fontana et al., 2012; Singh et al., 2015; Taylor, Salerno, Dharmakumar, & Jerosch-Herold, 2016). Both LGE and ECV correlate strongly with collagen content as measured by histology, suggesting that they are both surrogate markers of myocardial fibrosis (Bull et al., 2013; Andrew S. Flett et al., 2011). Recent studies have reported an association between LGE and ECV with worse outcomes in patients with AS (C. W. L. Chin et al., 2017; Heesun Lee et al., 2018; S.-P. Lee et al., 2015).

Several factors, and in particular age and sex, may also have an effect on the expansion of diffuse myocardial fibrosis, a key marker of LV decompensation in AS (C. W. L. Chin et al., 2017; Treibel, Lopez, et al., 2018). The objectives of this study were thus to assess the determinants of diffuse (ECV) and focal (LGE) myocardial fibrosis in patients with AS, and in particular, to assess the effect of sex on these 2 types of fibrosis.

5.3 Methods

5.3.1 Patient Population

Patients were prospectively recruited in 2 centers: Quebec Heart and Lung Institute the (PROGRESSA study: Metabolic Determinants of the Progression of Aortic Stenosis [NCT01679431]), and Edinburgh Heart Centre (NCT01755936) (Romain Capoulade et al., 2015; C. W. L. Chin et al., 2017). The study inclusion criteria for the PROGRESSA study are age >21 years old and peak aortic jet velocity (Vpeak) >2.0 m/s. The exclusion criteria were symptomatic AS, significant (> mild) aortic regurgitation or mitral valve disease (mitral stenosis or regurgitation), LV ejection fraction (LVEF) <50% and if they are pregnant or lactating women (Romain Capoulade et al., 2015)(1). In Edinburgh, all stable patients with at least mild AS (Vpeak >2.0 m/s) were invited to participate in a prospective observational cohort study. The exclusion criteria were other forms of valvular heart disease (≥moderate severity), significant comorbidities with limited life expectancy, contraindications to gadolinium-enhanced cardiac magnetic resonance (CMR), acquired or inherited non-ischemic cardiomyopathies (C. W. L. Chin et al., 2017)(2). The present study included all patients from both centers with comprehensive echocardiography and CMR exams (Figure 18).

Figure 20. Study Flow Chart

Description of the inclusion of the study population. CMR = cardiac magnetic resonance; LGE = late gadolinium enhancement.

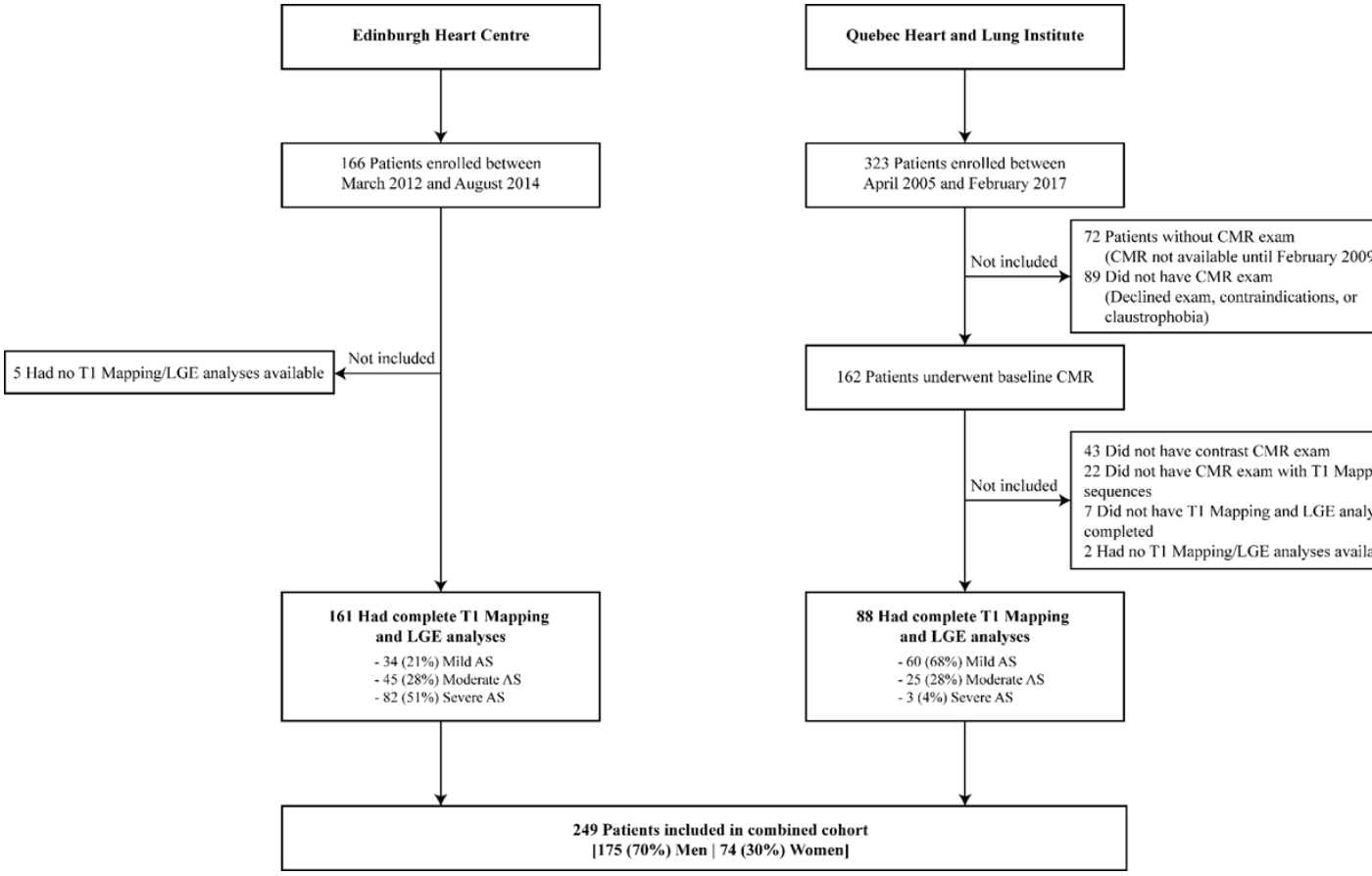

5.3.2 Clinical Data

The clinical data included age, sex, weight, height, body surface area (BSA), body-mass index (BMI), documented diagnoses of hypertension, dyslipidemia, diabetes mellitus, coronary artery disease, and renal function (plasma level of creatinine). Symptomatic status was assessed using the New York Heart Association (NYHA) functional classification.

5.3.3 Doppler Echocardiography

The aortic valve phenotype (i.e. bicuspid vs. tricuspid) was recorded. The Doppler-echocardiographic indices of AS severity included Vpeak, mean transvalvular pressure gradient (MG), and aortic valve area (AVA) calculated by the standard continuity equation and indexed to body surface area (AVAi). Stroke volume was calculated by multiplying the LV outflow tract area by the flow velocity-time integral and was indexed to BSA (SVi). LV mass was calculated with the corrected formula of the American Society of Echocardiography and European Association of Cardiovascular Imaging guidelines and was indexed to body surface area (3). Left ventricular hypertrophy (LVH) was defined as LV mass index >95 g/m² in women and >115 g/m² in men. Relative wall thickness (RWT) was calculated (i.e. RWT = [PWT+IVST]/LVID) and, as previously recommended, RWT >0.42 was used to define concentric remodeling (Lang et al., 2015). By taking into account both values of LV mass index and RWT, patients were classified into four different patterns using the following criteria: i) normal pattern: absence of LVH and RWT ≤0.42; ii) concentric remodeling: absence of LVH and RWT >0.42; iii) concentric hypertrophy: presence of LVH and RWT >0.42; iv) eccentric hypertrophy: presence of LVH and RWT ratio ≤0.42 (3).

Mitral annulus velocity was assessed using Doppler tissue imaging and diastolic function was classified according to guidelines (Lang et al., 2015).

As a measure of global LV hemodynamic load, we calculated the valvulo-arterial impedance: Zva = (SBP + MG)/SVi, where SBP is the systolic blood pressure.

5.3.4 Cardiac Magnetic Resonance

5.3.4.1 Acquisition

Magnetic resonance imaging was performed with 1.5 and 3 Tesla scanners (Quebec: Philips Achieva or Philips Ingenia, Philips Healthcare, Best, The Netherlands; Edinburgh: Magnetom Verio, Siemens AG, Erlangen, Germany). Short-axis cine images extending from the mitral valve to the left ventricular apex were obtained using a balanced steady-state free precession sequence (Quebec: 8-mm parallel slices with no gap; Edinburgh: 8-mm parallel slices with 2-mm spacing with temporal resolution ≤45 ms). Typical parameters at 1.5T were TR/TE 3.2/1.6ms, flip angle 60º. Equivalent acquisition parameters at 3T were TR/TE 2.8/1.3ms, flip angle 45º.

Focal replacement and diffuse interstitial myocardial fibrosis was assessed in all patients using late gadolinium enhancement (LGE) and myocardial T1 mapping, respectively. Late gadolinium enhancement was performed 15 min following gadobutrol (Gadovist, Bayer Pharma AG, Germany, 0.2 mmol/kg [Quebec], 0.1 mmol/kg [Edinburgh]) using an inversion-recovery fast gradient-echo sequence performed in two phase-encoding directions to differentiate true late enhancement from artefact (Larose et al., 2010). The inversion time was optimized to achieve satisfactory nulling of the myocardium.

Diffuse myocardial fibrosis was assessed using Modified Look-Locker Inversion-recovery (MOLLI) with built-in motion correction. The heart beat acquisition scheme was 5(3)-3 in Quebec (with a post-contrast acquisition scheme of 4(1)3(1)2 used in patients scanned at 3T) (Kellman et al., 2014), whilst the acquisition scheme was 3(3)-3(3)-5 in Edinburgh (flip angle 35□; minimum TI 100 ms; TI increment of 80 ms; time delay of 150 ms) (D. R. Messroghli et al., 2007; Daniel R. Messroghli et al., 2004;

Moon et al., 2013). A gradient echo field map and associated shim were performed to minimize off-frequency artefact.

5.3.4.2 Image analysis

Image analysis was performed offline in a core laboratory using a standardized approach (cmr42 version 3.4.1, Circle Vascular Imaging, Canada). In Quebec, images were quantified by trained operators supervised by an experienced cardiologist (Quebec: E.L.; Edinburgh: M.D.) (Cerqueira et al., 2002; Schulz-Menger et al., 2013). Left ventricular volume, mass and function measurements were performed using the contiguous short-axis multi-slice acquisition with delineation of atria/ventricles confirmed in matched long-axis planes. Papillary muscles and trabeculations were included when measuring mass (equivalent to weighting the LV) and excluded when measuring volumes (equivalent to blood pool techniques) in line with recommendations (Cerqueira et al., 2002).

LV hypertrophy was defined as LV mass indexed to BSA >95th centile using age- and sex-specific reference ranges (Kawel-Boehm et al., 2015). LV remodeling was determined as the ratio of LV mass index to LV end-diastolic volume index. By taking into account the presence of LV hypertrophy (LVH) and increased LV mass-volume ratio (i.e., ratio ≥1.15) (Kawel-Boehm et al., 2015; Treibel, Kozor, et al., 2018), four patterns of LV remodeling were defined: i) normal pattern: no LVH and LV mass-volume ratio <1.15; ii) concentric remodeling: no LVH and LV mass-volume ratio ≥1.15; iii) concentric hypertrophy: LVH and LV mass-volume ratio ≥1.15; iv) eccentric hypertrophy: LVH and LV mass-volume ratio <1.15.

Focal replacement fibrosis and extracellular volume (ECV) fraction were assessed using late gadolinium enhancement (LGE). LGE was performed 15 min following administration of gadobutrol (Gadovist, Bayer Pharma AG, Germany; 0.2 mmol/kg [Quebec], 0.1 mmol/kg [Edinburgh]). In Quebec, quantitative assessment of LGE was

performed on short-axis inversion recovery images by semi-automated signal intensity analysis, using the full width at half-maximum technique on the 17-segment model (4,9). In Edinburgh, a pattern of mid-wall fibrosis was determined qualitatively (2). LGE was quantified in a semi-automated manner using a signal intensity threshold of >3 standard deviations above the mean value in a region of normal myocardium. Areas of inversion artefact, infarct pattern LGE or signal contamination by epicardial fat or blood pool were manually excluded. Sub-endocardial LGE was also identified and quantified using the same analysis technique.

T1 mapping was performed using the Modified Look-Locker Inversion Recovery (Figure 19) (2). The regions of the endocardium and epicardium on the native motion-corrected T1 maps were manually contoured to avoid partial-volume or cardiac-motion-related blurring of the myocardium-blood boundary, where blood signal may contaminate myocardial data (Everett et al., 2018). These contours were then copied onto the corresponding post-contrast maps (Quebec: 15-min post-contrast maps; Edinburgh: 20-min post-contrast maps) with minor adjustments made to avoid partial volume effects. Regions of interest (ROIs) were then drawn in the blood, avoiding myocardium and papillary muscles. The extracellular volume (ECV) fraction was calculated according to: ECV fraction = partition coefficient x [1-hematocrit], where partition coefficient = [ΔR1myocardium/ΔR1blood-pool] and ΔR1 = (1/post-contrast T1-1/native T1). Hematocrit was measured as per protocol before cardiovascular magnetic resonance (2,5).

Figure 21. Assessment of T1 Mapping and Late Gadolinium Enhancement. Myocardial fibrosis assessment in a 70-year-old female with severe AS. The native (A) and post contrast (B) T1 relaxation time maps were used to calculate the extracellular volume (ECV) fraction. On late gadolinium enhancement (LGE) imaging, there was evidence of mid-wall enhancement in the basal inferolateral wall (C) which corresponded with areas of altered T1 relaxation times.

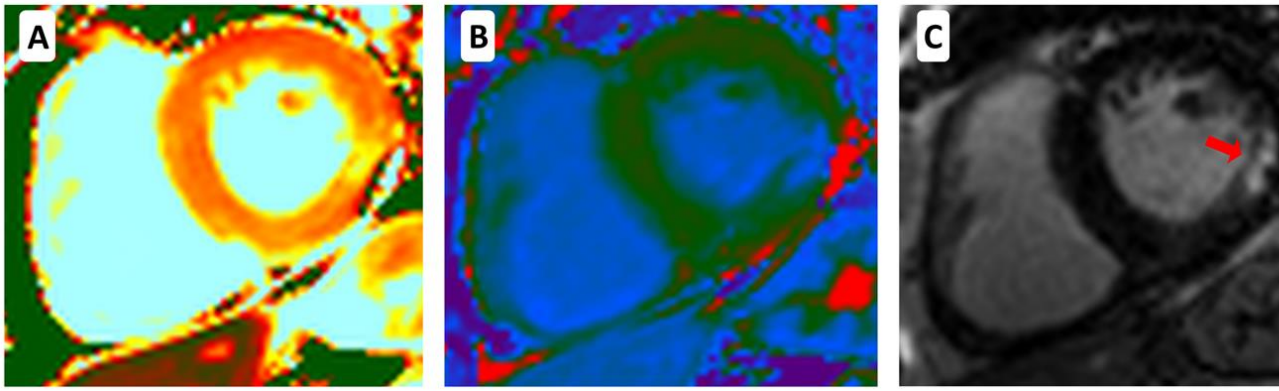

5.3.5 Statistical Analysis

Continuous data were expressed as mean ± SD or median (interquartile range), and were tested for normality of distribution and homogeneity of variances with the Shapiro-Wilk and Levene tests, respectively. Continuous data were compared between women and men using Student t test, Wilcoxon-Mann-Whitney test, one-way analysis of variance followed by Tukey post-hoc, or Kruskal-Wallis test followed by Dunn's post-hoc as appropriate. Categorical data were compared with the Chi-square test or Fisher's exact test as appropriate. Analysis of covariance (ANCOVA) was performed to assess the effect of sex on ECV fraction taking into account hemodynamic AS severity and LV mass index respectively. Univariable and multivariable linear regression analyses were performed to determine the predictors of diffuse myocardial fibrosis. Results were presented as standardized regression coefficients ± standard error (βeta coeff. ± SE). Traditional risk factors and/or clinically relevant variables and those with a p-value <0.10 in univariable analysis were included in the multivariable models. The explanatory variables entered in the multivariable models were age, sex, hypertension, diabetes, coronary artery disease, hemodynamic AS severity (i.e. Vpeak), Zva, and LV mass index measured by CMR. A frequency-matched analysis where patients were matched for age, cardiovascular risk factors, hemodynamic severity of AS, and prevalence of LVH was also performed to further compare the distribution of ECV and LGE between women and men. Statistical analyses were performed with STATA (V.14.2). A p value <0.05 was considered statistically significant.

5.4 Results

5.4.1 Population Characteristics

The study population had a mean age of 66±13 years and 30% were women (Table 14). Participants had a BMI of 28±5 kg/m², systolic blood pressure of 143±22 mmHg and 86% were in NYHA class I-II. The mean Vpeak was 3.4±1.0 m/s, 38% of patients had mild (Vpeak<3.0 m/s), 28% moderate (Vpeak 3.0-3.9 m/s), and 34% severe (Vpeak ≥4.0 m/s) AS.

Age was similar in women versus men (women: 66±15 vs. men: 66±12 years, p=0.78) but women presented with overall better clinical risk profile, particularly, lower prevalence of dyslipidemia (41% vs. 59%, p=0.004), diabetes (8% vs. 18%, p=0.04), and coronary artery disease (15% vs. 41%, p<0.0001; Table 14). Despite similar systolic (women: 146±25 vs. men: 142±21 mmHg, p=0.25) and diastolic (women: 81±12 vs. men: 81±11 mmHg, p=0.93) blood pressures, there was a trend toward less documented diagnosis of hypertension in women (59% vs. 70%, p=0.10) (Table 14). There was a trand for lesser use of anti-hypertensive medications (58% vs. 66%, p=0.26), and in particular of antagonists of the renin-angiotensin system (36% vs. 48%, p=0.10) in women versus men (Table 14).

The echocardiographic measures, and in particular AS severity (Vpeak: 3.3±1.0 vs. 3.5±0.9 m/s, p=0.32), were similar between women and men, (Table 14). However, women had a higher ratio of mitral E-wave and e' velocities (15.6±8.7 vs. 12.1±5.4, p=0.0002; Table 14).

As expected, the LV size and volumes quantified by CMR were smaller in women than in men (all, p≤0.04) but LV mass/volume ratio was lower in women compared with men [0.98 (0.80-1.20) vs. 1.12 (0.88-1.34), p=0.01] (Table 14). Despite lower LV mass index in women versus men [63 (56-80) vs. 82 (65-96) g/m², p<0.0001; Table 14 and Figure 20A), the prevalence of LVH was not different between sexes (27% vs.

36%, p=0.17; Table 14). However, there was a trend toward more LV concentric remodeling and concentric hypertrophy in men compared with women (Table 14). The systolic function as measured by LV ejection fraction was not different between sexes (p=0.16) (Table 14).

TABLE 14. Characteristics of the Study Population according to Sex

	All Patients (n = 249)	**Men (n = 175, 70%)**	**Women (n = 74, 30%)**	**p Value**
Clinical				
Age, years	66 ± 13	66 ± 12	66 ± 15	0.78
Body surface area, m^2	1.87 ± 0.19	1.94 ± 0.17	1.72 ± 0.15	**<0.0001**
Body mass index, kg/m^2	28 ± 5	29 ± 4	28 ± 6	0.43
Systolic blood pressure, mmHg	143 ± 22	142 ± 21	146 ± 25	0.26
Diastolic blood pressure, mmHg	81 ± 11	81 ± 11	81 ± 12	0.93
Hypertension, %	67	70	59	0.10
Dyslipidemia, %	53	59	41	**0.004**
Diabetes, %	15	18	8	**0.04**
Coronary artery disease, %	33	41	15	**<0.0001**
Creatinine, µmol/l	79 ± 18	84 ± 18	68 ± 12	**<0.0001**
Creatinine clairance, ml/min	87 ± 19	89 ± 20	84 ± 18	0.06
Hematocrit	0.41 ± 0.04	0.42 ± 0.04	0.38 ± 0.03	**<0.0001**
NYHA functional class, %				
I	51	54	46	0.61
II	35	33	41	
III	12	11	12	
IV	2	2	1	
Medication				
ACEIs/ARBs, %	45	48	36	0.10
Beta-blockers, %	30	31	27	0.55
Diuretics, %	28	25	35	0.11
Statins, %	52	58	39	**0.007**
Doppler-echocardiographic data				

Bicuspid aortic valve, %	26	26	27	0.85
Peak aortic jet velocity, m/s	3.4 ± 1.0	3.5 ± 0.9	3.3 ± 1.0	0.32
Mean transvalvular gradient, mmHg	28 ± 18	29 ± 17	27 ± 18	0.34
Aortic valve area, cm^2	1.05 ± 0.37	1.08 ± 0.39	0.96 ± 0.31	**0.02**
Indexed aortic valve area, cm^2/m^2	0.56 ± 0.19	0.56 ± 0.20	0.56 ± 0.18	0.99
AS severity, %				
Mild	38	34	46	0.22
Moderate	28	30	24	
Severe	34	36	30	
Valvulo-arterial impedance, $mmHg/mL/m^2$	4.2 ± 1.1	4.2 ± 1.1	4.2 ± 1.1	0.81
Mean e', cm/s	7.0 ± 2.2	7.1 ± 2.1	6.7 ± 2.5	0.18
Mean E/e' ratio	13.2 ± 6.7	12.1 ± 5.4	15.6 ± 8.7	**0.0002**
LV mass index, g/m^2	112 (93 - 132)	117 (97 - 135)	98 (83 - 119)	**<0.0001**
Relative wall thickness ratio	0.57 (0.48 - 0.66)	0.57 (0.48 - 0.66)	0.56 (0.44 - 0.67)	0.83
LV hypertrophy, %	53	53	54	0.97
LV remodeling patterns, %				
Normal pattern	11	9	14	0.43
Concentric remodeling	36	38	32	
Concentric hypertrophy	52	52	51	
Eccentric hypertrophy	2	1	3	
Cardiac magnetic resonance data				
End-diastolic volume index, ml/m^2	71 (62 - 82)	73 (64 - 85)	69 (61 - 78)	**0.01**
End-systolic volume index, ml/m^2	24 (19 - 28)	24 (21 - 29)	22 (17 - 27)	**0.005**
Stroke volume index, ml/m^2	47 (42 - 55)	49 (42 - 56)	46 (40 - 53)	**0.04**
LV ejection fraction, %	67 (63 - 71)	66 (62 - 70)	68 (63 - 72)	0.16
LV mass index, g/m^2	75 (61 - 93)	82 (65 - 96)	63 (56 - 80)	**<0.0001**

LV mass/volume ratio	1.06 (0.84 - 1.32)	1.12 (0.88 - 1.34)	0.98 (0.80 - 1.20)	**0.01**
LV hypertrophy, %	33	36	27	0.17
LV remodeling patterns, %				
Normal pattern	52	47	65	
Concentric remodeling	15	17	8	
Concentric hypertrophy	27	29	23	
Eccentric hypertrophy	6	7	4	
Presence of LGE, %	38	42	30	0.08
LGE, %	3.2 (0.7 - 7.0)	2.8 (0.6 - 6.8)	4.5 (2.3 - 7.0)	0.20
Presence of non-infarct LGE, %	34	37	27	0.12
Non-infarct LGE, %	2.8 (0.7 - 6.8)	2.1 (0.6 - 6.8)	4.5 (2.0 - 6.3)	0.22
Extracellular volume fraction				
Mean, %	27.8 ± 3.2	27.2 ± 3.0	29.2 ± 3.2	**<0.0001**
Median, %	27.6 (25.3 - 29.7)	26.8 (25.1 - 28.7)	29.0 (27.4 - 30.6)	**<0.0001**

Value are mean±SD, % or median [25th – 75th percentiles].

ACEIs = angiotensin-converting-enzyme inhibitors; ARBs = angiotensin receptor blockers; AS = aortic valve stenosis; LGE = late gadolinium enhancement; LV = left ventricular; NYHA = New York Heart Association.

Figure 22. Comparison of Extracellular Volume Fraction and Left Ventricular Mass Index According to Sex. Comparison of left ventricular (LV) mass index (A) and ECV fraction (B) in women (n = 74) versus men (n = 175). The box shows the 25th to 75th percentiles, the median line on the box shows the median value, and the error bars the 95th range; circles are outliers; the numbers of the top of the graph are median (25th percentile - 75th percentile).

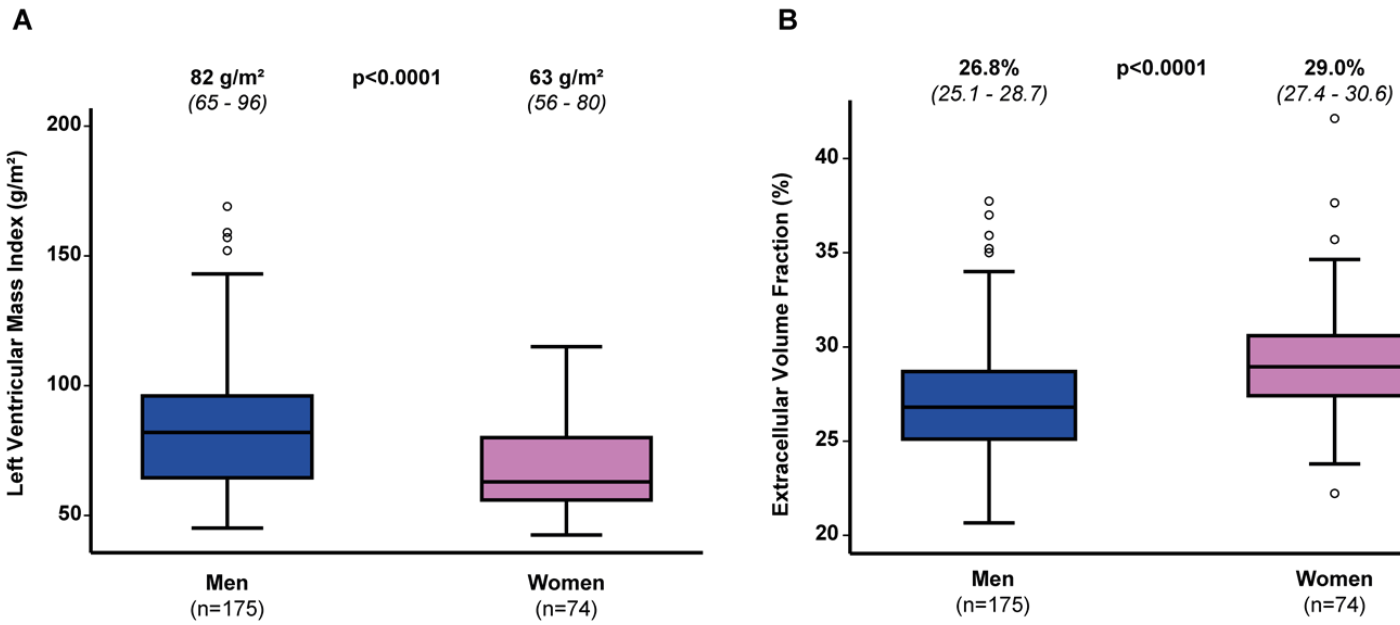

5.4.2 Association between Sex and Expansion of Late Gadolinium Enhancement.

In the study population, LGE was present in 95 (38%) patients and non-infarct LGE was present in 85 (34%) patients (Table 14). There was a trend towards higher proportion of patients with detectable LGE in men compared to women (42% vs. 30%, p=0.08), although the absolute value of LGE expressed in percentage was similar between sexes (2.8 [0.6-6.8] vs. 4.5 [2.3-7.0] %, p=0.20) (Table 14). Moreover, there was no significant difference in the proportion of LGE between sexes according to AS severity (p=0.58) but a trend according to tertiles of LV mass index defined using sex-specific thresholds (p=0.08) (Figure 21 A and B). Excluding the patients with areas of infarction provided similar results for the proportion of detectable LGE (Table 14), as well as the distribution of LGE according to AS severity (Figure 21C). However, there were significant differences between sexes according to tertiles of LV mass index (p=0.03) (Figure 21D).

Figure 23. Comparison of Late Gadolinium Enhancement between Women and Men According to Hemodynamic Severity of Aortic Valve Stenosis and Left Ventricular Mass Index. Caption: Comparison of LGE between women and men in each class of severity of AS (mild AS, Vpeak<3.0 m/s; moderate AS, Vpeak 3.0-3.9 m/s; Vpeak ≥4.0 m/s) (A) and in each tertile of LV mass index (B), and in the subset of patients with non-infarct LGE (C and D). The tertiles of LV mass index were designed according to sex: i) women: bottom tertile ≤58 g/m², mid tertile 59 g/m² - 73 g/m², top tertile >73 g/m²; ii) men: bottom tertile <70 g/m², mid tertile 70 g/m² - 92 g/m², top tertile ≥93 g/m².

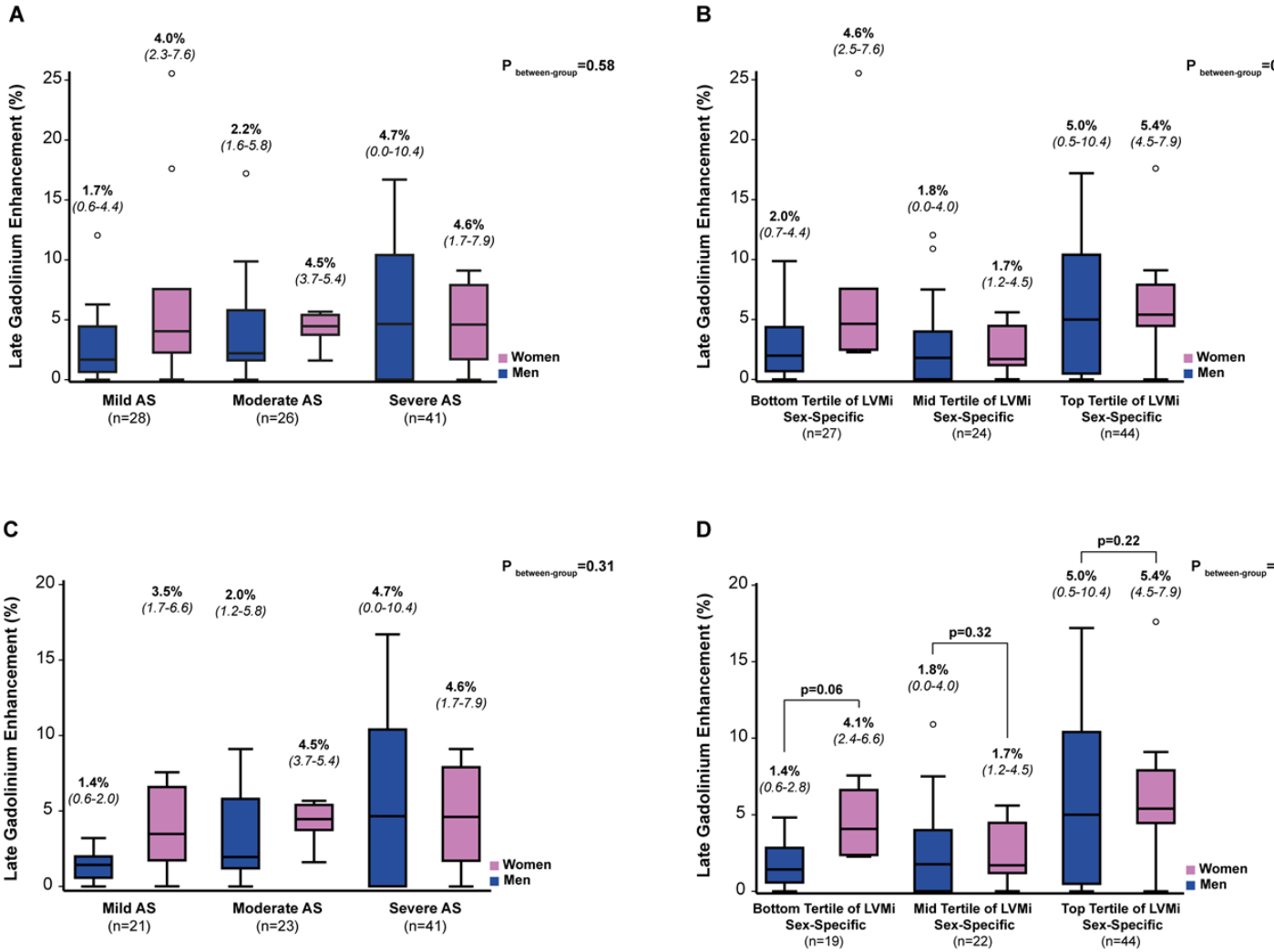

Univariable linear regression analysis in the whole study population showed that Vpeak and LV mass index were associated with higher LGE (both $p<0.0001$), while there was only a trend toward association between coronary artery disease and LGE ($p=0.07$; Table 15). On multivariable analysis, only female sex and LV mass index were associated with higher LGE (both $p\leq0.001$; Table 15). In women, univariable analysis demonstrated that age ($p=0.05$), coronary artery disease ($p=0.02$), and LV mass index ($p=0.007$) were associated with higher LGE (Table 15). After multivariable adjustment, age and LV mass index continued to be associated with higher LGE (all $p\leq0.03$), but there was only a trend towards an association with coronary artery disease ($p=0.07$; Table 15). Univariable analysis in men demonstrated that Vpeak ($p<0.0001$) and LV mass index ($p<0.0001$) were associated with higher LGE (Table 2). On multivariable analysis, only LV mass index remained associated with higher LGE ($p<0.0001$), with a trend toward an association with Vpeak ($p=0.09$; Table 15). Including Zva instead of Vpeak showed an association for Zva and LV mass index (both $p\leq0.009$) with higher LGE. The frequency-matched analysis showed that women with similar age, comorbidities as well as hemodynamic AS severity had similar amount of LGE [4.5 (2.5-7.6) vs. 3.2 (1.7-7.5) %, $p=0.46$] and non-infarct LGE [4.5 (2.3-7.6) vs. 3.0 (1.7-6.7) %, $p=0.52$] compared with men, despite higher LV mass index in men (Online Table 16). Results were similar when analyzed separately in each centre (Quebec Heart and Lung Institute versus Edinburgh Heart Centre) (Figure 22).

Table 15. Univariable and Multivariable Analyses of the Predictors of Higher Late Gadolinium Enhancement.

	All Patients (n = 249)				**Men** (n = 175)				**Women** (n = 74)			
	Univariable Analysis		**Multivariable Analysis**		**Univariable Analysis**		**Multivariable Analysis**		**Univariable Analysis**		**Multivariable Analysis**	
	βeta ±SE	p Value	βeta ±SE	p Value	βeta ±SE	p Value	βeta ±SE	p Value	βeta ±SE	p Value	βeta ±SE	p Value
Age, years	0.10±0.02	0.11	0.11±0.02	0.10	0.03±0.02	0.73	0.06±0.02	0.42	**0.23±0.03**	**0.05**	**0.30±0.04**	**0.03**
Female sex	-0.007±0.54	0.91	**0.21±0.54**	**0.001**	-	-	-	-	-	-	-	-
Hypertension	0.02±0.53	0.71	-0.02±0.54	0.76	0.03±0.63	0.73	0.08±0.62	0.32	0.02±0.99	0.89	-0.24±1.09	0.07
Diabetes	-0.08±0.69	0.22	-0.06±0.62	0.31	-0.06±0.74	0.40	-0.02±0.66	0.77	-0.13±1.77	0.27	-0.18±1.58	0.08
Coronary artery disease	0.12±0.52	0.07	0.10±0.52	0.11	0.07±0.58	0.36	0.04±0.57	0.58	**0.27±1.32**	**0.02**	0.20±1.24	0.07
V_{peak}, m/s	**0.25±0.21**	**<0.0001**	0.05±0.31	0.49	**0.34±0.29**	**<0.0001**	0.16±0.37	0.09	0.08±0.48	0.49	-0.18±0.56	0.19
LV mass index, g/ m^2	**0.39±0.01**	**<0.0001**	**0.61±0.01**	**<0.0001**	**0.45±0.01**	**<0.0001**	**0.56±0.02**	**<0.0001**	**0.31±0.03**	**0.007**	**0.59±0.03**	**<0.0001**

βeta are standardized regression coefficient ± SE.

V_{peak} = peak aortic jet velocity; other abbreviations as in Table 14.

Figure 24. Comparison of Late Gadolinium Enhancement between Women and Men According to Centre. Comparison of late gadolinium enhancement (LGE) between women and men (A) and non-infarct LGE (B) in the Quebec Centre, and non-infarct LGE in the Edinburgh Centre (C).

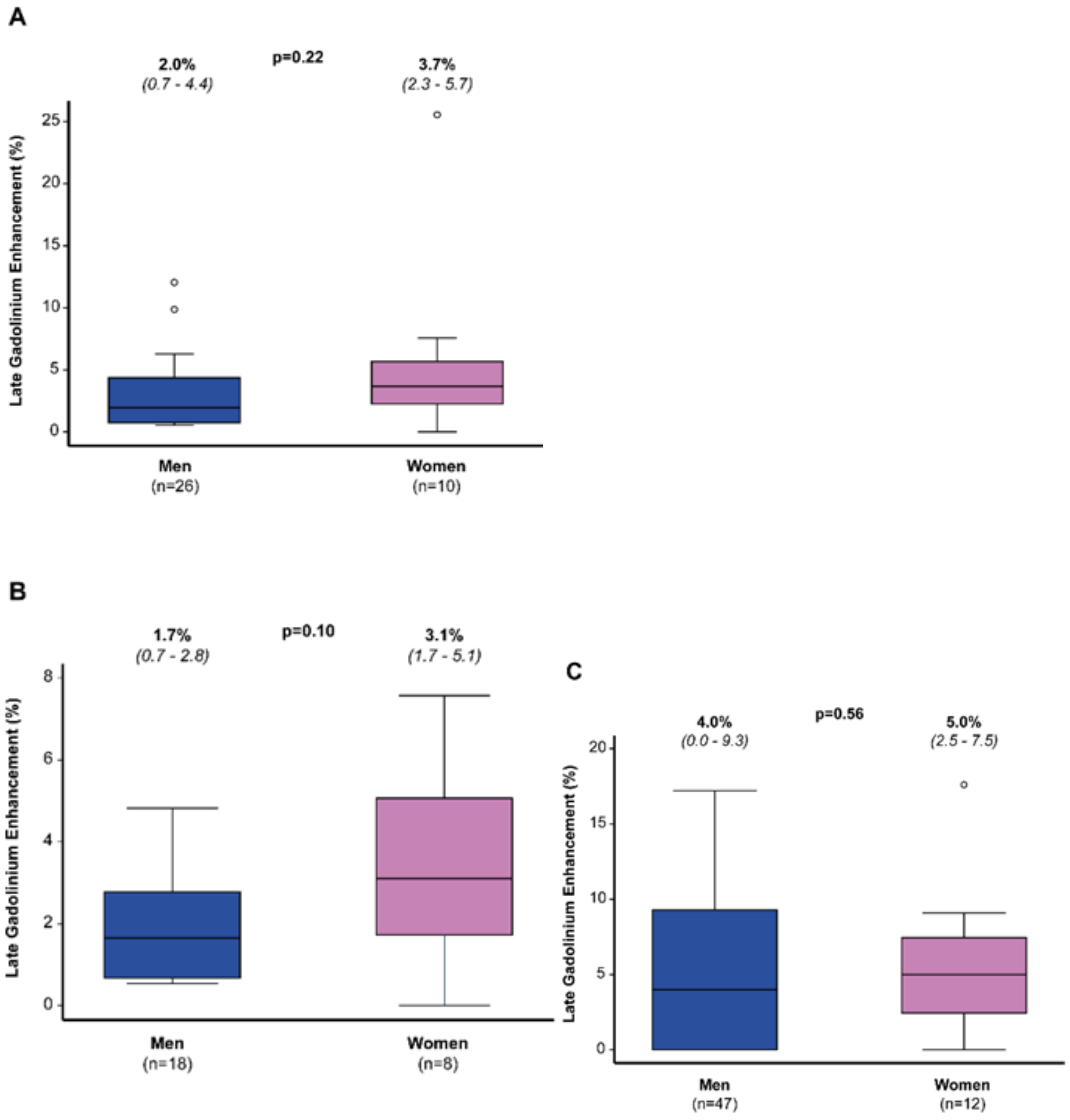

5.4.3 Association between Sex and Expansion of Extracellular Volume Fraction

As expected, LGE was associated with ECV fraction in the whole cohort as in each sex subset (whole cohort: r=0.35, p<0.0001; women: r=0.41, p=0.0003; men: r=0.35, p<0.0001). Compared with men, women presented higher ECV fraction in the whole cohort [29.0 (27.4-30.6) vs. 26.8 (25.1-28.7) %, p<0.0001] (Figure 20B) as well as in each hemodynamic AS severity stage (mild AS: [29.5 (26.8-32.5) vs. 26.4 (25.3-28.5) %, p=0.0004]; moderate AS: [28.7 (27.7-30.0) vs. 26.8 (25.0-29.1) %, p=0.002]; severe AS: [29.0 (27.7-30.1) vs. 26.8 (25.0-29.0)%, p=0.01]; Figure 24A). Furthermore, there was a significant effect of sex on the relationship between AS severity and ECV fraction (pancova<0.0001), suggesting a more pronounced impact of the AS-related pressure overload on LV fibrosis in women compared to men.

When ECV fraction was analyzed according to the tertiles of LV mass index, defined by sex-specific thresholds, women presented significantly higher ECV fraction than men in the lower and upper tertiles (lower tertile: [30.3 (28.1-32.5) vs. 26.0 (24.7-28.2) %, p<0.0001]); mid tertile: ([28.0 (26.4-28.7) vs. 26.8 (25.0-28.4)%, p=0.11); and upper tertile ([29.6 (28.3-30.2) vs. 28.0 (25.6-30.3)%, p=0.01]) (Figure 24B). There was also an effect of sex on the relationship between LV mass index and ECV (pancova<0.0001).

Figure 25. Comparison of Extracellular Volume Fraction between Women and Men According to Hemodynamic Severity of Aortic Valve Stenosis and Left Ventricular Mass Index. Comparison of ECV fraction between women and men in each class of severity of AS (A) and in each tertile of LV mass index (B). The figure shows that ECV fraction remains significantly higher in women as compared to men in each class of AS severity. Similarly, despite lower LV mass index, women present higher ECV fraction than men.

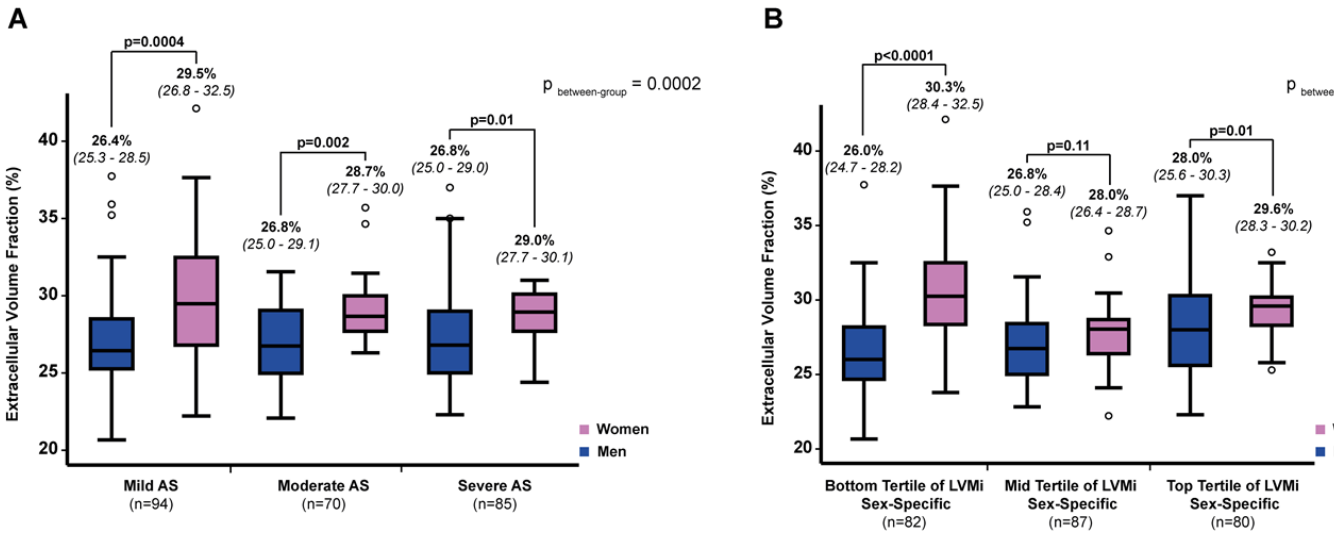

Interestingly, after frequency-matching of men and women for age, comorbidities and hemodynamic AS severity, women still had higher ECV fraction [28.9 (27.3-30.3) vs. 27.2 (25.0-29.2) %, p=0.002], but also higher ratio of mitral E-wave and e' velocities (16.2±9.3 vs. 12.6±7.1, p=0.02; Table 17).

The analyses of ECV fraction according to sex within each center provided similar results as those obtained by merging the data of the 2 centers (Figure 24).

Table 16. Frequency-Matched Characteristics of the Study Population according to Sex

	All Patients (n = 112)	**Men (n = 56, 50%)**	**Women (n = 56, 50%)**	**p Value**
Clinical				
Age, years	68 ± 12	68 ± 12	68 ± 12	0.98
Body surface area, m^2	1.83 ± 0.19	1.94 ± 0.17	1.73 ± 0.16	**<0.0001**
Body mass index, kg/m^2	28 ± 5	28 ± 4	28 ± 6	0.89
Systolic blood pressure, mmHg	145 ± 23	145 ± 22	145 ± 24	0.89
Diastolic blood pressure, mmHg	82 ± 12	83 ± 12	81 ± 13	0.58
Hypertension, %	62	61	63	0.85
Dyslipidemia, %	45	45	45	1.00
Diabetes, %	9	9	9	1.00
Coronary artery disease, %	20	20	20	1.00
Creatinine, µmol/l	76 ± 15	83 ± 15	69 ± 12	**<0.0001**
Hematocrit	0.40 ± 0.04	0.42 ± 0.04	0.38 ± 0.03	**<0.0001**
NYHA functional class, %				
I	57	64	50	0.19
II	30	29	32	
III	11	5	16	
IV	2	2	2	
Medication				
ACEIs/ARBs, %	32	29	36	0.42
Beta-blockers, %	29	29	29	1.00

Diuretics, %	28	36	20	0.06
Statins, %	46	45	48	0.71
Doppler-echocardiographic data				
Bicuspid aortic valve, %	25	27	23	0.63
Peak aortic jet velocity, m/s	3.4 ± 0.9	3.3 ± 0.8	3.4 ± 1.0	0.77
Mean transvalvular gradient, mmHg	27 ± 15	27 ± 13	27 ± 16	0.82
Aortic valve area, cm^2	1.01 ± 0.31	1.07 ± 0.31	0.96 ± 0.31	0.07
Indexed aortic valve area, cm^2/m^2	0.55 ± 0.17	0.55 ± 0.15	0.55 ± 0.18	0.98
AS severity, %				
Mild	45	43	46	0.78
Moderate	21	23	18	
Severe	35	34	36	
Valvulo-arterial impedance, $mmHg/mL/m^2$	4.3 ± 1.2	4.4 ± 1.2	4.2 ± 1.2	0.53
Mean e', cm/s	6.7 ± 2.1	7.1 ± 2.0	6.3 ± 2.1	0.06
Mean E/e' ratio	14.4 ± 8.4	12.6 ± 7.1	16.2 ± 9.3	**0.02**
LV mass index, g/m^2	108 (91 - 125)	115 (98 - 127)	101 (85 - 122)	0.06
Relative wall thickness ratio	0.57 (0.48 - 0.67)	0.55 (0.48 - 0.65)	0.57 (0.48 - 0.67)	0.98
LV hypertrophy, %	54	51	57	0.56
LV remodeling patterns, %				
Normal pattern	11	8	11	0.43
Concentric remodeling	36	42	32	
Concentric hypertrophy	52	51	53	

Eccentric hypertrophy	2	0	4	
Cardiac magnetic resonance data				
End-diastolic volume index, ml/m^2	69 (62 - 79)	73 (64 - 82)	68 (60 - 76)	0.05
End-systolic volume index, ml/m^2	22 (18 - 27)	23 (20 - 27)	22 (18 - 26)	0.09
Stroke volume index, ml/m^2	47 (41 - 54)	48 (42 - 56)	45 (40 - 52)	0.09
LV ejection fraction, %	67 (63 - 71)	67 (64 - 70)	68 (62 - 72)	0.84
LV mass index, g/m^2	70 (59 - 86)	74 (62 - 92)	63 (56 - 80)	**0.004**
LV mass/volume ratio	0.99 (0.80 - 1.31)	0.98 (0.80 - 1.41)	1.01 (0.81 - 1.25)	0.34
LV hypertrophy, %	29	29	29	1.00
LV remodeling patterns, %				
Normal pattern	60	57	63	0.80
Concentric remodeling	12	14	9	
Concentric hypertrophy	24	25	23	
Eccentric hypertrophy	4	4	5	
Presence of LGE, %	34	38	30	0.43
LGE, %	4.0 (1.9 - 7.6)	3.2 (1.7 - 7.5)	4.5 (2.5 - 7.6)	0.46
Presence of non-infarct LGE, %	31	36	27	0.31
Non-infarct LGE, %	3.4 (1.7 - 7.5)	3.0 (1.7 - 6.7)	4.5 (2.3 - 7.6)	0.52
Extracellular volume fraction				
Mean, %	28.1 ± 2.9	27.2 ± 2.9	29.0 ± 2.9	**0.002**
Median, %	28.4 (25.6 - 29.8)	27.2 (25.0 - 29.2)	28.9 (27.3 - 30.3)	**0.002**

Value are mean±SD, % or median [25th – 75th percentiles].

ACEIs = angiotensin-converting-enzyme inhibitors; ARBs = angiotensin receptor blockers; LGE = late gadolinium enhancement; LV = left ventricular; NYHA = New York Heart Association.

Figure 26. Comparison of Extracellular Volume Fraction between Women and Men According to Centre. Comparison of extracellular volume fraction between women and men in the Quebec Centre (A) and in the Edinburgh Centre (B).

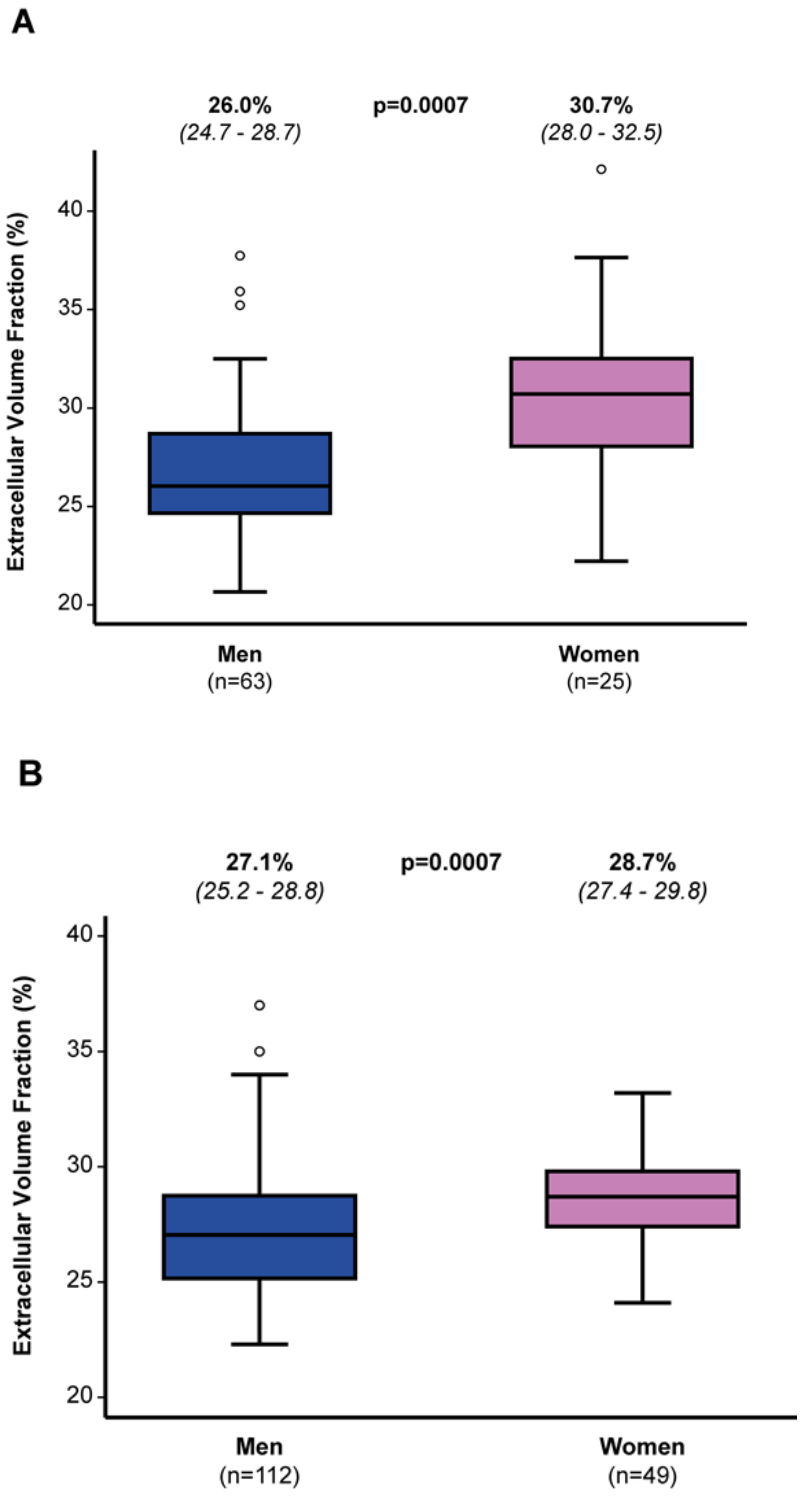

5.4.4 Factors Associated with Higher Extracellular Volume Fraction

In the whole cohort, age ($p=0.03$), female sex ($p<0.0001$), and hematocrit ($p<0.0001$) were significantly associated with ECV fraction (Table 18). After multivariable adjustment, female sex ($p<0.0001$), hematocrit ($p<0.0001$), and LV mass index ($p<0.0001$) were significantly associated with ECV fraction (Table 18). There was a trend toward significant association for age ($p=0.07$) (Table 18). In women, the univariable and multivariable analyses revealed no significant association between the explanatory variables and higher ECV fraction (Table 18), whereas in men, univariable analysis demonstrated that age, hematocrit, Vpeak, and LV mass index were associated with ECV fraction (all $p\leq0.02$; Table 18). On multivariable analysis, age, hematocrit and LV mass index remained significantly associated with ECV fraction (all $p\leq0.03$).

Table 17. Univariable and Multivariable Analyses of the Predictors of Higher Extracellular Volume Fraction

	All Patients (n = 249)				**Men** (n = 175)				**Women** (n = 74)			
	Univariable Analysis		**Multivariable Analysis**		**Univariable Analysis**		**Multivariable Analysis**		**Univariable Analysis**		**Multivariable Analysis**	
	βeta ±SE	p Value	βeta ±SE	p Value	βeta ±SE	p Value	βeta ±SE	p Value	βeta ±SE	p Value	βeta ±SE	p Value
Age, years	**0.14±0.02**	**0.03**	0.13±0.02	0.07	**0.21±0.02**	**0.006**	**0.19±0.02**	**0.03**	0.06±0.03	0.63	0.16±0.04	0.38
Female sex	**0.29±0.43**	**<0.001**	**0.30±0.49**	**<0.001**	-	-	-	-	-	-	-	-
Hypertension	-0.03±0.43	0.65	-0.10±0.45	0.12	0.05±0.50	0.51	-0.03±0.51	0.69	-0.10±0.77	0.40	-0.19±1.01	0.20
Diabetes	0.04±0.57	0.48	0.05±0.52	0.41	0.11±0.60	0.16	0.09±0.55	0.21	0.03±1.39	0.82	-0.04±1.45	0.77
Coronary artery disease	-0.03±0.43	0.64	0.04±0.43	0.53	0.05±0.47	0.49	-0.008±0.47	0.92	0.03±1.06	0.80	0.04±1.11	0.76
Creatinine clairance	-0.12±0.01	0.06	-0.07±0.01	0.24	-0.10±0.01	0.18	-0.07±0.01	0.31	-0.07±0.02	0.57	-0.08±0.03	0.61
Hematocrit	**-0.39±4.67**	**<0.001**	**-0.29±5.07**	**<0.001**	**-0.37±5.43**	**<0.001**	**-0.27±5.51**	**<0.001**	-0.18±12.2	0.12	-0.19±12.8	0.12
V_{peak}, m/s	0.05±0.21	0.48	-0.08±0.25	0.29	**0.17±0.24**	**0.02**	-0.03±0.30	0.78	-0.15±0.37	0.21	-0.12±0.53	0.47
LV mass index, g/ m^2	0.11±0.01	0.08	**0.42±0.01**	**<0.001**	**0.31±0.01**	**<0.001**	**0.47±0.01**	**<0.001**	-0.03±0.02	0.78	0.28±0.03	0.10

βeta are standardized regression coefficient ± SE. Abbreviations as in Table 14 and 15.

Further analyses including correlates of ECV fraction are presented in Table 18. There was significant association between higher ECV fraction and E/e' ratio (p=0.004) and NYHA class (p=0.04) in univariable analysis (Table 18). However, in multivariable analysis E/e' ratio was not significantly (p=0.61) associated with ECV%, whereas there was a trend for association with NYHA class (p=0.14) (Table 18).

Table 18. Correlates of Extracellular Volume Fraction.

	Univariable Analysis		**Multivariable Analysis**	
	βeta Coeff. ± SE	p value	βeta Coeff. ± SE	p value
Age, years	**0.14±0.02**	**0.03**	**0.14±0.02**	**0.05**
Female sex	**0.29±0.43**	**<0.0001**	**0.31±0.51**	**<0.0001**
Hypertension	-0.03±0.43	0.65	-0.10±0.45	0.12
Diabetes	0.04±57	0.48	0.05±0.53	0.41
Coronary artery disease	-0.03±0.43	0.64	0.03±0.43	0.68
Creatinine clairance	-0.12±0.01	0.06	-0.06±0.01	0.37
Hematocrit	**-0.39±4.67**	**<0.0001**	**-0.28±5.19**	**<0.0001**
NYHA functional class	**0.13±0.27**	**0.04**	0.09±0.28	0.14
Peak aortic jet velocity, m/s	0.05±0.21	0.48	-0.11±0.27	0.16
E/e' ratio	**0.18 ±0.03**	**0.004**	-0.03 ±0.03	0.61
LV mass index, g/m²	0.11 ±0.009	0.08	**0.45 ±0.01**	**<0.0001**

βeta coeff. are standardized regression coefficient.

Abbreviations as in Table 17.

5.5 Discussion

In this bicenter CMR prospective study of patients with AS, we have demonstrated that despite having smaller LV mass index, women have similar amounts of LGE but a larger ECV fraction across the range of disease severities. Moreover, this expansion of myocardial fibrosis appeared to be less dependent on LV mass than occurs in men.

5.5.1 Noninvasive Assessment of Myocardial Fibrosis in AS

Several studies have reported an association between expansion of ECV, a surrogate marker of diffuse myocardial fibrosis, and adverse cardiac events in patients with AS (C. W. L. Chin et al., 2017; Wong et al., 2012). As opposed to ECV, LGE is a marker of the expansion of dense focal extracellular matrix deposition and has been primarily related to ischemic heart disease (Ambale-Venkatesh & Lima, 2014). However, recent findings showed that a non-ischemic pattern of focal fibrosis is also detected using LGE and this pattern is mainly related to chronic pressure overload conditions such as AS or systemic arterial hypertension (Calvin W. L. Chin et al., 2016). We previously reported that mid-wall fibrosis pattern is present in 38% of patients with moderate to severe AS and is independently associated with increased risk of mortality (Dweck et al., 2011). However, few studies have examined the respective determinants of ECV and LGE fractions in patients with a large range of AS severity.

5.5.2 Factors associated with myocardial fibrosis in AS

Our analysis showed that LV mass index was the strongest determinant for both higher ECV fraction and higher amount of LGE. This is consistent with previous studies that have demonstrated an association between an advanced hypertrophic response and myocardial fibrosis as assessed by CMR (Shah et al., 2014). Moreover, histological investigations have demonstrated that fibrosis is a key pathological characteristic of the LV hypertrophic response to AS and an important driver to its decompensation and the transition to heart failure (Bull et al., 2013; Treibel, Lopez, et al., 2018). In the present study, traditional cardiovascular risk factors such as hypertension and coronary artery disease were not independently associated with diffuse or focal myocardial fibrosis. The lack of association between hypertension and the surrogate CMR markers of fibrosis could be related to the fact that the vast majority of patients with diagnosis of hypertension were treated with anti-hypertensive medications. In this study, few patients presented infarct-pattern of fibrosis and such pattern was also excluded from the analysis of LGE in one center, which could explain why coronary artery disease was not independently associated with higher ECV fraction or presence of LGE. Consistent with a previous study, we reported no association between hemodynamic severity of AS and both patterns of myocardial fibrosis (C. W. L. Chin et al., 2017). This suggests that the ability of the LV to adapt to AS-related pressure overload may vary from patient to patient, and is not solely determined by AS severity. An association was also observed between older age and higher ECV fraction, but not with LGE. The association between age and ECV fraction has been reported in previous studies (C.-Y. Liu et al., 2013; Ugander et al., 2012). This association could reflect age-dependent mechanisms of myocyte loss and increased proliferation of extracellular matrix and collagen (i.e. cardiac fibroblasts) (Keller & Howlett, 2016). The present study also reported a trend for association between

diabetes and higher ECV fraction. Increased ECV fraction has been previously reported in patients with diabetes (Wong et al., 2014). Indeed, the metabolic ‘milieu’ of diabetic patients may predispose to the expansion of extracellular matrix through the stimulation of cardiac fibroblast (Wong et al., 2014).

5.5.3 Sex Differences in LV Remodeling and Extent of Myocardial Fibrosis

Several studies have reported sex-related differences in the LV response to pressure overload (R. Capoulade et al., 2017; Dana Cramariuc et al., 2008; Dobson et al., 2016; Pamela S. Douglas et al., 1998; Petrov et al., 2014) . The present study provides further evidence to support the fundamental difference in LV remodeling between women and men with AS. Indeed, despite similar AS severity and LV global hemodynamic load as well as more favourable cardiovascular risk profile, women presented lower indexed LV mass but paradoxically a larger extent of diffuse myocardial fibrosis (ECV) and a similar amount of replacement myocardial fibrosis (LGE). Moreover, after comprehensive multivariable analyses, female sex remained an important independent determinant of higher ECV fraction and LGE. Noteworthy, the greater expansion of ECV fraction observed in women was also accompanied by higher estimated LV filling pressure (E/e' ratio), which may be related to reduced LV compliance and more advanced LV diastolic dysfunction in women (Dunlay, Roger, Weston, Jiang, & Redfield, 2012). A previous analysis of the Multi-Ethnic Study of Atherosclerosis also reported higher ECV fraction in women compared with men (31). In a recent study including 100 patients with severe AS undergoing AVR, women had smaller LV mass but similar amount of replacement myocardial fibrosis as assessed by LGE (Dobson et al., 2016)(38). Nevertheless, our findings differ from those of previous studies suggesting a greater propensity of men to develop myocardial fibrosis (Montalvo et al., 2012; Weinberg et al., 1999). In addition, a recent study including 168 patients with severe symptomatic AS reported higher LGE fraction as well as ECV fraction indexed to LV end diastolic volume in men, but similar extent of ECV fraction between sexes (Treibel, Kozor, et al., 2018). However, this previous study included only patients with severe AS planned for AVR in which men harbored a high proportion (>70%) of LVH. This could explain, at least in part, the larger

fibrotic burden observed in men versus women in this previous study. Similarly, in a recent study by Singh et al including patients with mainly severe AS, men presented larger LGE and indexed ECV fraction compared to women (Singh et al., 2017). However, despite the larger fibrotic burden reported in men, women presented higher incidence of symptoms. The main added value of our study is that we compared the expansion of LGE and ECV in men versus women subsets having similar cardiovascular risk profile and similar distribution of age, AS severity, and degree of LV hypertrophy/remodeling.

The susceptibility to fibrosis has been mostly attributed to sex hormones such as estrogen, which could exert a cardioprotective effect in the female hearts (Patten et al., 2004; Pedram, Razandi, Narayanan, & Levin, 2016; Satoh et al., 2007). However, most patients with AS are >60 years old and the effect of sex hormones on profibrotic process in post-menopausal women remains unknown. On the other hand, chronic activation of the renin-angiotensin-aldosterone system is thought to play a key role in the cardiac remodeling as well as profibrotic processs (Keller & Howlett, 2016). Some evidence suggests that these processes may predominantly affect the female hearts and thus may explain, at least in part, the sex differences observed in the LV remodeling and expansion of diffuse myocardial fibrosis (Greiten, Holditch, Arunachalam, & Miller, 2014). Further studies are needed to determine the underlying mechanisms for the sex differences in the magnitude of myocardial fibrosis in patients with AS.

This study is the first to perform separate analyses of explanatory variables for increased diffuse and replacement fibrosis in women and men. In women, there were no variables associated with higher ECV fraction, but interestingly older age, presence of coronary artery disease and LV mass index were associated with higher LGE. The latter findings could reflect the presence of impaired coronary microcirculation related to the LV hypertrophic response and increased LV transmural pressures associated with AS.

Some studies reported that among patients with AS, the coronary microcirculation is more frequently impaired in women (Reis et al., 2001). Hence, in older women with AS, repetitive myocardial ischemia related to chronic reduction of the coronary microcirculation could lead to apoptosis of myocyte cells and ultimately to the development of replacement fibrosis. In men, older age and higher LV mass index were associated with higher ECV fraction; whilst LV mass index was the strongest variable associated with higher LGE. Therefore, in men, the LV hypertrophic response due to chronic pressure overload appears to be the main factor for the adverse LV remodeling and subsequent fibrosis. This is consistent with a previous study that demonstrated a maladaptive LV remodeling associated with the activation of profibrotic markers predominantly in men with AS (Kararigas et al., 2014). The association of older age with higher ECV fraction in men has been previously reported (31). This is also supported by histological evidence suggesting that the ageing process associated with myocyte cell loss affects the myocardium of men but not women (Olivetti et al., 1995). All together these findings strongly support the existence of sex differences in the LV remodeling as well as the predictors of increased myocardial fibrosis in patients with AS.

5.5.4 Clinical implications

The noninvasive assessment of the expansion and pattern of myocardial fibrosis by CMR could help to determine the optimal timing of AVR in asymptomatic patients with severe AS. Future studies are needed to determine whether an earlier intervention based on the extent of diffuse fibrosis may be associated with better outcomes in these patients. However, the results of the present study suggest that women may develop greater extent of diffuse fibrosis than men independently of the degree of stenosis severity. Further studies are still needed to determine whether women larger expansion of diffuse myocardial fibrosis as measured by CMR could be a potential trigger for early valve replacement in women with severe AS.

These findings also suggest that adjuvant pharmacotherapy targeting pro-fibrotic pathways, such as inhibitors of renin-angiotensin system might help to improve outcomes in patients with AS, and particularly in women.

5.5.5 Study limitations

The present study is a cross-sectional analysis and thus have inherent limitations related to this type of design. In particular, the sex-related differences in LV remodeling and expansion of fibrosis reported in this study need to be confirmed by further studies with a longitudinal design. In addition, this study was not a prespecified analysis from our two prospective studies. The rationale for this study is, however, supported by recent evidences suggesting substantial sex-related differences in the pathophysiology of AS (Clavel et al., 2013; Hervault & Clavel, 2018; Simard et al., 2017). The CMR exams were performed with scanners from different vendors and there were some minor differences in the acquisition protocols. Moreover, the areas of infarction were excluded from LGE analysis by one center and included by the other. However, these limitations did not affect the main findings of this study. Furthermore, an analysis stratified according to the centre revealed that the results with respect to the sex-differences in LV remodeling and fibrosis were similar in the two centres, which indirectly supports the generalizability of the results of this study.

ECV fraction is not specific to fibrosis, thus it is possible that larger ECV fraction in women could be related to many other factors including the intravascular compartment rather than interstitial expansion due to diffuse myocardial fibrosis (Mahmod et al., 2014). However, multiple histological studies have demonstrated that T1 mapping parameters are closely correlated to myocardial fibrosis as quantified by biopsy, suggesting that ECV fraction is a non-invasive surrogate marker of fibrosis. Whereas, similar histological validation of T1 values as a surrogate of intravascular expansion are lacking.

Chapter 6. Feasibility of coronary ^{18}F-sodium fluoride PET assessment with the utilization of previously acquired CT angiography.

Published by Jacek Kwiecinski, Philip D Adamson, Martin L Lassen, Mhairi K Doris, Alastair J Moss, Sebastian Cadet, Maurits A Jansen, Damini Dey, Sang-Eun Lee, Mijin Yun, Hyuk-Jae Chang, Marc R Dweck, David E Newby, Daniel S Berman, Piotr J Slomka. Feasibility of coronary ^{18}F-sodium fluoride PET assessment with the utilization of previously acquired CT angiography. 2018 Circulation Cardiovascular Imaging

6.1 Summary

We assessed the feasibility of utilizing previously acquired computed tomography angiography (CTA) with a subsequent PET-only scan for the quantitative evaluation of ^{18}F-NaF PET coronary uptake.

Forty-five patients (age 67.1±6.9 years, 76% males) underwent CTA (CTA1) and combined ^{18}F-NaF PET/CTA (CTA2) imaging within 14[10,21] days. We fused CTA1 from visit one with ^{18}F-NaF PET from the second visit (PET) and compared visual pattern of activity, maximal standard uptake values (SUVmax) and target to background (TBR) measurements on (PET/CTA1) fused versus hybrid (PET/CTA2) data.

On PET/CTA2, 226 coronary plaques were identified. Fifty-eight coronary segments from 28(62%) patients had high ^{18}F-NaF uptake (TBR>1.25), whilst 168 segments had lesions with ^{18}F-NaF TBR ≤1.25. Uptake in all lesions was categorized identically on co-registered PET/CTA1. There was no significant difference in ^{18}F-NaF uptake values between PET/CTA1 and PET/CTA2 (SUVmax: 1.16±0.40 vs. 1.15±0.39,p=0.53; TBR:1.10±0.45 vs. 1.09±0.46,p=0.55). The intraclass correlation coefficient for SUVmax and TBR was 0.987 (95%CI 0.983 to 0.991) and 0.986 (95%CI 0.981 to 0.992). There was no fixed or proportional bias between PET/CTA1 and PET/CTA2 for SUVmax and TBR. Cardiac motion correction of PET scans improved reproducibility with tighter 95% limits of agreement (±0.14 for SUVmax and ±0.15 for TBR vs. ±0.20 and ±0.20 on diastolic imaging;p<0.001).

Coronary CTA/PET protocol with CTA first followed by PET-only allows for reliable and reproducible quantification of ^{18}F-NaF coronary uptake. This approach may facilitate selection of high-risk patients for PET-only imaging based on results from prior CTA, providing a practical workflow for clinical application.

6.2 Introduction

Coronary computed tomography angiography (CTA) has emerged as powerful method for accurately assessing coronary artery stenosis and characterizing coronary atherosclerosis, providing a wealth of diagnostic and prognostic information. These anatomic measurements, however, do not provide insight into the activity of the disease and fail to depict the biological processes implicated in plaque rupture (Dweck, Williams, Moss, Newby, & Fayad, 2016). Assessment of plaque activity may improve the patient risk prediction provided by CTA. Recently, it was shown that ^{18}F-sodium fluoride (^{18}F-NaF) PET imaging, providing an assessment of developing microcalcification within coronary plaque, might provide such an assessment (M. R. Dweck, M. W. L. Chow, et al., 2012). ^{18}F-NaF PET imaging, however, requires co-registered CTA images for precise anatomical localization of ^{18}F-NaF within coronary plaques (Joshi et al., 2014; Kitagawa et al., 2017; Thomas & Haraszti, 2014). Increased ^{18}F-NaF uptake has been observed with hybrid PET/CTA to localize in regions of recent plaque rupture in patients with acute myocardial infarction as well as in coronary plaques with high-risk features on intravascular ultrasound in patients with stable coronary artery disease (Joshi et al., 2014). Other PET tracers targeting different aspects of coronary plaque activity are increasingly becoming available (Tarkin et al., 2017).

The standard approach used to date for coronary ^{18}F-NaF PET/CT has several limitations which hamper its practical implementation into a meaningful clinical workflow (Thomas & Haraszti, 2014). Studies to date have utilized CTA acquired using hybrid PET/CTA scanner during the same imaging session (Joshi et al., 2014; Oliveira-Santos et al., 2017; T. A. Pawade et al., 2016; Vesey et al., 2017). This approach, however, does not lend itself to patient selection for imaging based on prior CTA findings. If the ^{18}F-NaF imaging becomes part of a clinical assessment strategy, it is likely that patients would be selected

for ^{18}F-NaF PET based on the findings of a CTA performed for clinical purposes (Motoyama et al., 2015; Nerlekar et al., 2018). Another key limitation of the single-session hybrid PET/CTA protocol is that it may not allow for the use of optimal CT equipment for CTA which may only be available on standalone CT scanners. Finally, the use of hybrid PET/CTA requires multi-faceted staff expertise in both PET and coronary CTA during a single session. To address these limitations, we assessed the feasibility of utilizing a previously acquired CTA with a subsequent PET-only coronary scan for the evaluation of coronary ^{18}F-NaF PET uptake.

6.3 Methods

6.3.1 Study Population

We analyzed scans of patients with stable coronary artery disease who first underwent CTA (CTA1) followed by a hybrid ^{18}F-NaF PET of the coronary arteries with second CTA (CTA2). We analyzed data from two cohorts of patients. Cohort 1 consisted of 20 subjects who underwent CTA 1 and hybrid PET/CTA on the same scanner within 14 days. Cohort 2 consisted of 25 patients whose initial CTA acquisition was performed on a standalone CT and had hybrid PET/CTA in a median of 17 days [14-37] after CTA 1. All subjects had angiographically proven multivessel coronary artery disease (defined as at least two major epicardial vessels with any combination of either >50% luminal stenosis, or previous revascularization (percutaneous coronary intervention or coronary artery bypass graft surgery). Exclusion criteria included an acute coronary syndrome within the previous 12 months, renal dysfunction (eGFR ≤30 mL/min/1.73 m2) and contraindication to iodinated contrast agents. The study was approved by the investigational review board, and written informed consent was obtained from all subjects. Study data can be made available to other researchers on request to the corresponding author.

6.3.2 Image acquisition and reconstruction

6.3.2.1 Initial Coronary CTA

Cohort 1 had the CTA1 scan performed on the 128-slice Biograph mCT scanner (Siemens Medical Systems, Erlangen, Germany) using the following settings: 330 ms rotation time, 100 or 120kV (depending on body mass index), 160-245 mAs. Cohort 2 underwent CTA1 on a dual source CT scanner (Definition; Siemens Medical Systems, Erlangen, Germany). The scan parameters were as follows: 330 ms gantry rotation time, reference tube current of 400 mAs per rotation, and a peak tube voltage of 120 kV. Patients in both cohorts received beta blockers (orally or intravenously) to achieve a target heart rate <60beats/min and sublingual nitrates. A bolus of 60-100 mL of contrast (300-400 mgI/mL; Iomeron) was power injected intravenously at 6 mL/s, after determining the appropriate trigger delay with a test bolus of 20 mL contrast. Transverse images were reconstructed with 0.75/0.6 mm slice thickness, 0.4 mm increment and a medium-soft convolution kernel.

6.3.3.2 ^{18}F-NaF PET /CTA

Prior to the PET imaging, 250 MBq of ^{18}F-sodium fluoride was injected intravenously and patients rested in a quiet environment for 60 minutes. Because emission scanning was followed by CTA during that hour subjects were administered with beta-blockers. Imaging was performed on 2 different PET/CTA scanners 128-slice Biograph mCT, Siemens Medical Systems (Cohort 1) and 128-slice Discovery 710 (GE Healthcare, Milwaukee, WI, USA (Cohort 2). In both cohorts low-dose CT attenuation correction scan (120 kV, 50 mAs, 3 mm slice thickness), a 30-min single bed position PET acquisition with ECG-gating in list mode was performed. Image corrections were applied for attenuation, dead time, scatter, and random coincidences. In Cohort 1 PET data were reconstructed using a Siemens implementation of iterative reconstruction algorithm (Ultra-HD; with Point Spread function correction and time of flight reconstruction, matrix 256, Gaussian filter of 5 mm and 2 iterations and 21 subsets). In Cohort 2 data were reconstructed with GE implementation of iterative reconstruction algorithm (Sharp IR with Point Spread function correction and time of flight reconstruction, matrix 256, Gaussian filter of 5 mm and 4 iterations and 24 subsets)(Mhairi K. Doris et al., 2018).
In both cohorts, a second CTA (CTA2) was obtained on the hybrid scanner with patient remaining on the table in the same position as during emission scanning. In Cohort 1 (Siemens Biograph mCT) imaging was performed on the same scanner and according to the same protocol as CTA1. In Cohort 2 (GE Discovery 710) CTA2 was acquired with rotation time 350ms, tube voltage 120 kV, tube current 150-250 mAs) and reconstructed with 0.625 mm thick slices, a 0.625 mm increment and a medium-soft convolution kernel.

6.3.4 Image analysis

6.3.4.1 Cardiac motion correction

In addition to assessing diastolic PET data, we also analyzed cardiac motion corrected ^{18}F-NaF PET images. This technique compensates for coronary artery motion by aligning all cardiac gates to the reference gate (the one which is used for PET and CTA co-registration - see below). This approach was shown to reduce image noise and improve target to background ratios(Rubeaux, Joshi, Dweck, Fletcher, Motwani, Thomson, Germano, Dey, Li, et al., 2016). To perform cardiac motion correction in the first step coronary artery centerlines were extracted from coronary CTA by applying a vessel tracking algorithm based on Bayesian maximal paths using dedicated software (Autoplaque version 2.0, Cedars Sinai Medical Center). Secondly, a diffeomorphic mass-preserving image registration algorithm was used to align the gates of PET data to the end-diastolic (reference) gate. As a result, all gates were summed back together providing a motion-free image containing counts from the entire duration of PET acquisition.

6.3.4.2 Image registration

Image registration was performed using FusionQuant Software (Cedars Sinai Medical Center, Los Angeles). PET and CTA reconstructions were reoriented, fused and carefully co-registered in all 3 planes (a X-Y-Z translation was performed) as described previously (T. A. Pawade et al., 2016; Vesey et al., 2017). Key points of reference were the sternum, vertebrae, blood pool in the left and right ventricle (based upon high ^{18}F-fluoride activity in the blood pool in comparison to the surrounding myocardium) and the great vessels. We fused CTA1 from the first visit with PET and also separately fused CTA2 with PET. Although CTA2 was obtained at the same imaging session as PET on the hybrid scanner, co-registration was performed to account for any possible patient motion between PET and CTA2. Both CTA1 and CTA2 were co-registered to PET in an identical fashion (Figure 25). This way, we could compare directly a clinical protocol using a CTA scan acquired up to 4 weeks before a PET-only ^{18}NaF scan, with a standard hybrid ^{18}NaF-CTA protocol in individual patients. To assess interobserver reproducibility of the CTA and PET registration both datasets of cohort 1 patients were fused and reoriented by 2 experienced observers (imaging cardiologists) blinded to each other's adjustments.

6.3.4.3 ^{18}F-NaF PET quantification

After registration of CTA1 and CTA2 to the PET, plaque activity was measured by defining 3-dimensional volumes of interest (spheres with a 5mm radius) around coronary plaques on both the fused PET/CTA2 and PET/CTA1 images. The maximum standard uptake value (SUVmax) was recorded from each coronary segment that had a diameter of at least 2 mm and included coronary atheroma with a >25% stenosis on CTA and had not been stented previously. Background blood pool activity was measured by delimiting a spherical volume of interest (radius 10-15 mm depending on atrium size) in the middle of the left atrium. Target to background ratios (TBRs) were calculated by dividing SUVmax by averaged background blood pool activity. To categorize lesions according to PET tracer uptake, we utilized the previously validated methodology (M. R. Dweck, M. W. L. Chow, et al., 2012; Joshi et al., 2014). In brief, plaques were considered to have high uptake if they presented with focal tracer uptake which followed the course of the vessel over more than one slice and their TBR on diastolic imaging was >1.25. Image noise was defined as the mean standard deviation of the blood pool activity. Signal to noise ratio was defined as the plaque SUVmax divided by image noise. To assess interobserver reproducibility of the uptake measurements on the PET/CTA1 datasets coronary ^{18}F-NaF activity of cohort 1 patients was assessed by 2 experienced observers (imaging cardiologists) blinded to each other's delineations.

6.3.4.4 Reproducibility analysis

Image analysis of PET/CTA1 and PET/CTA2 was carried out on diastolic and motion corrected images. To limit the potential for recall bias between PET/CTA1 and PET/CTA2, PET/CTA1 was anonymized against PET/CTA2 and there was at least a three-week interval between reading PET/CTA1 and PET/CTA2 images. For each scan, PET registration and regions of interest were saved using the reference CTA and the same registration position so that the same regions of interest could be measured in the diastolic and motion corrected images. Reproducibility was defined as the difference in PET SUV or TBR measured from PET/CTA1 and PET/CTA2 datasets.

Figure 27. Utilization of prior coronary CT angiography for the assessment ^{18}F-NaF PET coronary uptake. We fused (orange arrow) the CTA from the first visit (CTA1) with an ^{18}F-NaF PET from the second visit (PET). The PET/CTA imaging session comprised the acquisition of a low-dose attenuation correction scan (AC) followed by a 30min long PET registration (PET) and finally the coronary CT angiography (CTA).

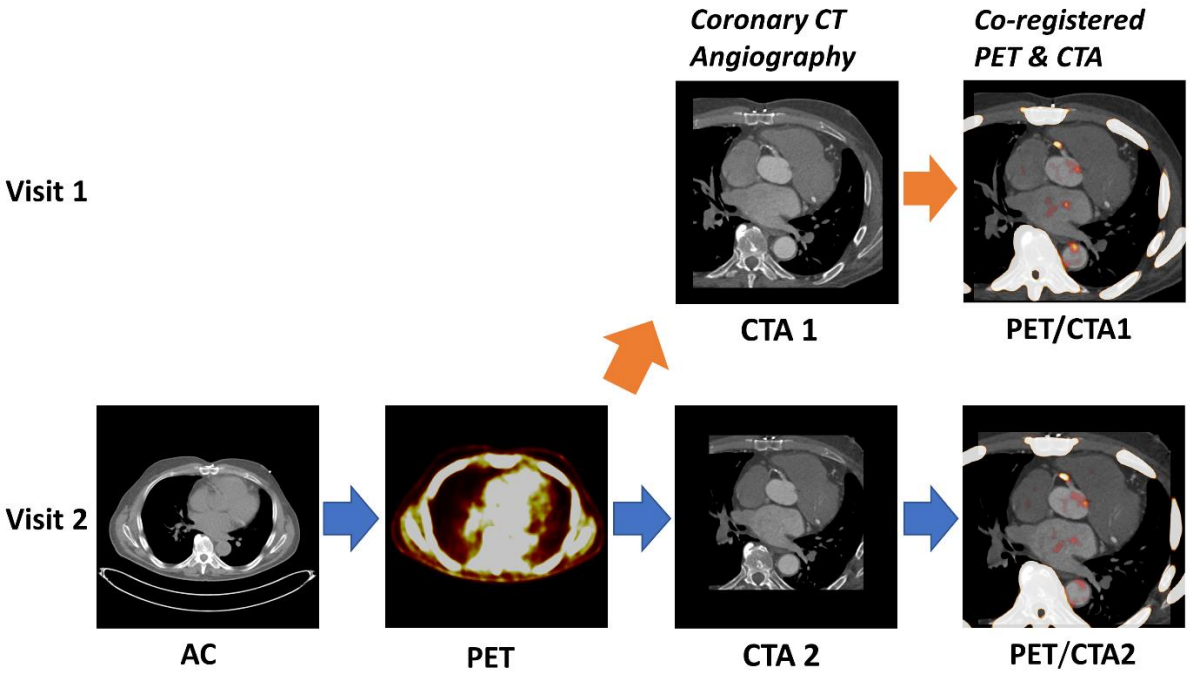

6.3.5 Statistical Analysis

Data was tested for normality using Shapiro Wilks test. Continuous variables were expressed as mean ±SD or median [interquartile range] and compared with paired Student t or Wilcoxon signed-rank test where appropriate. We presented all categorical variables as percentages and used the chi-square test for comparison. We used Bland-Altman plots to visualize reproducibility of measurements. The 95% normal range for differences between sets of SUV and TBR measurements (the limits of agreement) were estimated by multiplying the SD of the mean difference by 1.96 (W. A. Weber et al., 1999). Intra-class correlation coefficients with 95% confidence intervals (CIs) were calculated for PET/CTA1 vs. PET/CTA2 scan variation. The Pitman-Morgan test was used to compare the homogeneity of variance between uptake measurements derived from diastolic gate and motion corrected datasets. In our per lesion analysis we assumed independence of lesions within patients. A 2-sided p value <0.05 was regarded as statistically significant. Statistical analysis was performed with SPSS software (version 24, SPSS, Inc., Chicago, Illinois).

6.4 Results

A total of 45 patients (age 67.1±6.9 years, 76% males) underwent CTA1 and a subsequent PET/CT with CTA2 at a median of 14 [10,21] days. All patients had multivessel disease on CTA1 (Table 19).

Table 19. Patients baseline clinical characteristics

	Cohort 1, n=20	Cohort 2, n=25	Study population, n=45
Demographics			
Age (years)	69.5±7.3	65.0±6.1	67.1±6.9
Gender (male)	17 (85%)	17 (68%)	34 (76%)
Height (cm)	173.0±9.4	168.0±6.4	170.3±8.7
Weight (kg)	82.9±17.1	73.9±14.8	78.1±16.2
Cardiovascular risk factors			
Diabetes	2 (10%)	5 (20%)	7 (16%)
Hyperlipidemia	20 (100%)	8 (32%)	28 (62%)
Hypertension	14 (70%)	15 (60%)	29 (64%)
Tobacco use	14 (70%)	7 (28%)	21 (47%)
Family history of coronary heart disease	12 (60%)	4 (16%)	16 (36%)
Peripheral vascular disease	1 (5%)	1 (4%)	2 (4%)

SD= standard deviation.

6.4.1 Image registration

Compared to PET/CTA2 registration, PET/CTA1 registration required larger spatial adjustments in all three axes (0.5 [0.0, 1.5] vs 12.6 [2.5, 21.8] mm, p<0.001; 1.4 [0.0, 2.9] vs 6.3 [1.5, 14.1] mm, p=0.007; 3.2 [0.6, 5.9] vs 15.9 [5.1, 30.3] mm, p= 0.001; for the x, y, z axis respectively) (Figure 26A). The intraclass correlation coefficient for spatial adjustments between two observers was 0.92 (95% CI 0.87 to 0.95) for PET/CTA2 and 0.99 (95% CI 0.993 to 0.997) for PET/CTA1 (Figure 26D). There was no fixed or proportional bias between observers with limits of agreement of ±4.5mm for both the hybrid and the prior CTA dataset (Figure 26). Despite the need for larger adjustments of PET/CTA1 there was no significant difference in the reproducibility of adjustments between both datasets (p=0.76).

Figure 28. Co-registration of ^{18}F-NaF PET and CTA data**.** Boxplots presenting the translational adjustments in 3 axes (X,Y,Z) made to the PET images to align the two datasets for CTA (coronary CT angiography) acquired during hybrid PET/CTA session (Hybrid) and for prior-CTA fused with PET-only ^{18}F-NaF scan (Prior CTA). The prior CTA (PET/CTA1) dataset required bigger adjustments than the hybrid – single imaging session (PET/CTA2) dataset (all p<0.01) (A). Bland Altman plots presenting the interobserver variability of the co-registration adjustments of the hybrid (B) and prior CTA (C) datasets. There was no significant difference in the reproducibility of adjustments for hybrid vs prior datasets (p=0.76). Scatter plot presenting the co-registration adjustments made by two independent observers of the prior CTA dataset (D).

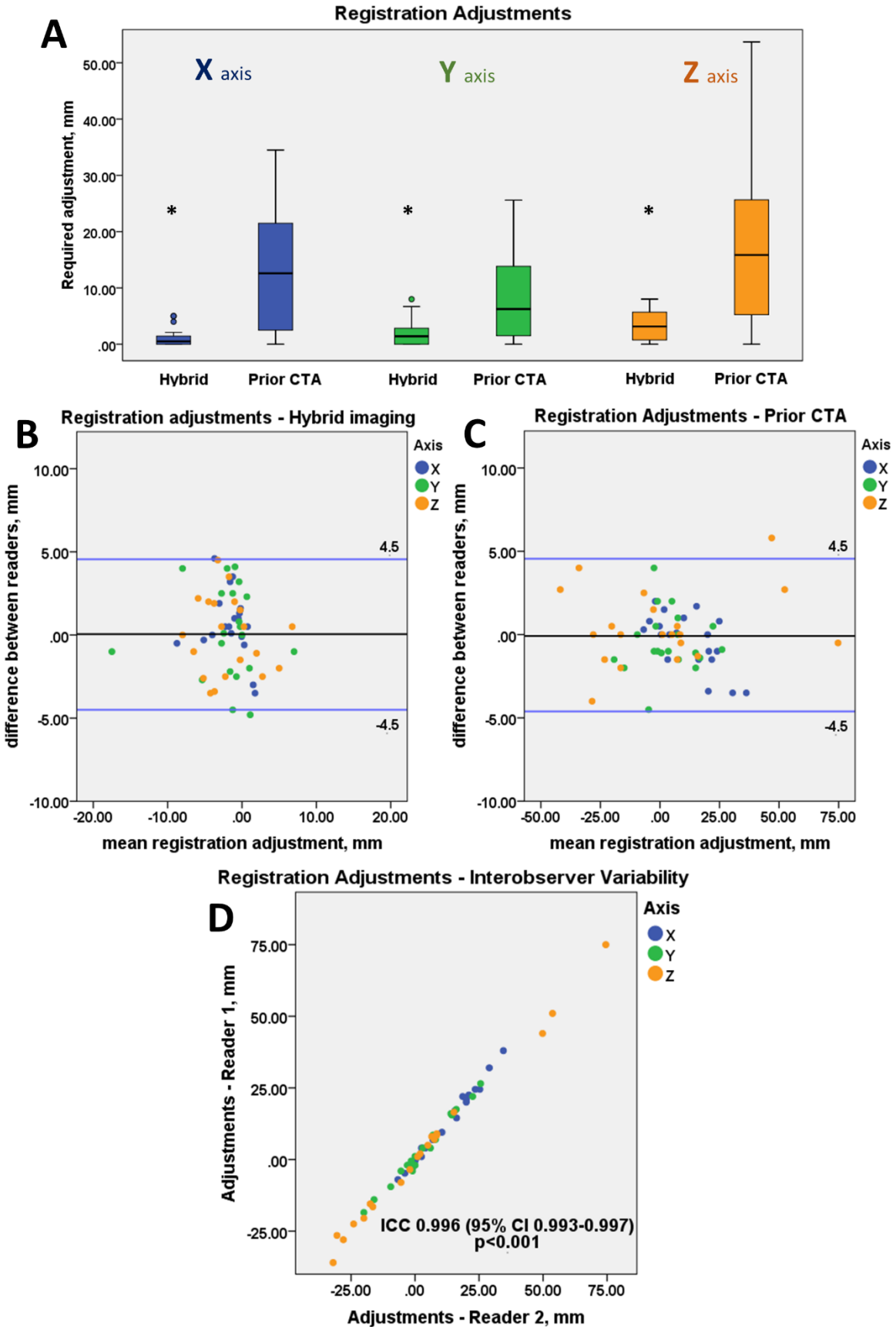
A
Registration Adjustments
X axis
Y axis
Z axis
Required adjustment, mm
50.00
40.00
30.00
20.00
10.00
.00
Hybrid
Prior CTA
Hybrid
Prior CTA
Hybrid
Prior CTA
B
Registration adjustments - Hybrid imaging
difference between readers, mm
mean registration adjustment, mm
Axis
X
Y
Z
4.5
-4.5
C
Registration Adjustments - Prior CTA
difference between readers, mm
mean registration adjustment, mm
Axis
X
Y
Z
4.5
-4.5
D
Registration Adjustments - Interobserver Variability
Adjustments - Reader 1, mm
Adjustments - Reader 2, mm
Axis
X
Y
Z
ICC 0.996 (95% CI 0.993-0.997)
p<0.001

6.4.2 ^{18}F-NaF PET quantification

Twenty-eight (62%) patients had high ^{18}F-NaF coronary uptake on PET/CTA2. Fifty-eight coronary segments showed high ^{18}F-NaF uptake (TBR>1.25). The remaining 168 segments with at least a 25% CTA stenosis, had PET TBR measurements ≤ 1.25. On PET/CTA1, all interrogated segments were classified identically as on PET/CTA2 (according to the 1.25 TBR cutoff; Figures 27, 31 and 32).

Figure 29. The assessment of coronary ^{18}F-NaF uptake on hybrid (PET/CTA2) and prior CTA (PET/CTA1). Both datasets were motion corrected after registration of CTA to PET. For the hybrid acquisition the required adjustments were 0.5, 2.5 and 0mm in the x,y and z axis respectively. For prior CTA dataset PET had to be moved by 2.5, 3 and 5mm in the corresponding axes. Lesions with increased tracer uptake were identified in the left main, lesion TBR 1.56 and 1.55 (A and A') and proximal right coronary artery, lesion TBR 1.60 and 1.60 (B and B'). CTA= coronary CT angiography. TBR= target to background ratio.

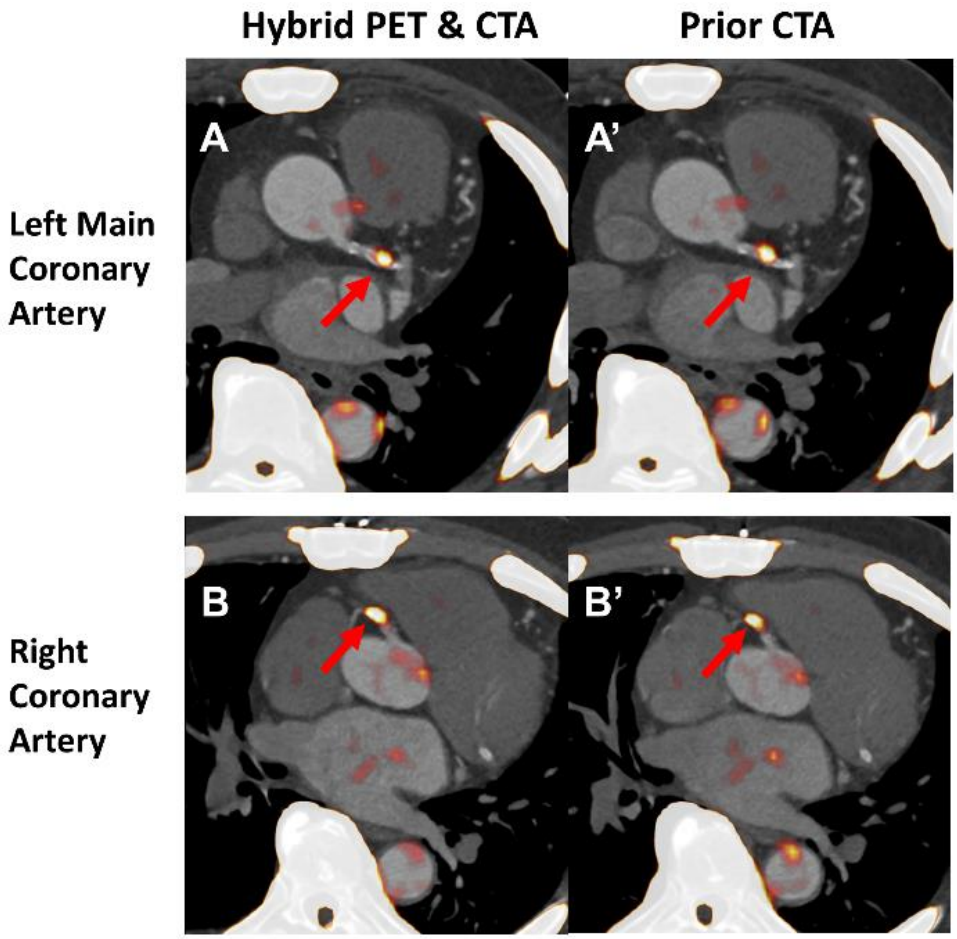

6.4.3 Diastolic imaging

There was no significant difference in SUVmax measurements across all identified lesions (n=226) on PET/CTA2 compared to PET/CTA1 (1.16±0.40 vs 1.15±0.39, p=0.53). Importantly, no significant difference was found when the TBR>1.25 and TBR<1.25 lesions were compared separately (1.71±0.44 vs 1.72±0.45, p=0.47 and 1.03±0.17 vs 1.05±0.18, p=0.48). In a similar fashion, there were no significant differences in measurements of coronary TBR (1.10±0.45 vs 1.09±0.46, p=0.55) or the signal to noise ratio (25.7±12.6 vs. 25.2±11.9, p=0.49).

6.4.4 Motion correction

After applying motion correction, the signal to noise ratio improved when compared to diastolic imaging (25.2±11.9 vs 30.8±17.2, p=0.01). On motion corrected images, SUVmax and TBR showed no significant difference between PET/CTA1 and PET/CTA2 (all p>0.40;). The intraclass correlation coefficient for uptake measurements in cohort 1 patients between two independent observers was 0.987 (95% CI 0.96 to 0.99) for SUVmax and 0.982 (95% CI 0.96 to 0.99) for TBR values (Figure 28).

Figure 30. Interobserver variability of uptake measurements on prior CTA (PET/CTA1). Scatter plots and Bland Altman plots of prior CTA (PET/CTA1) SUVmax (a, c) and TBR (b, d) measurements of lesion with (red) and without (blue) increased tracer uptake. SUVmax= maximal standard uptake, TBR = target to background ratio.

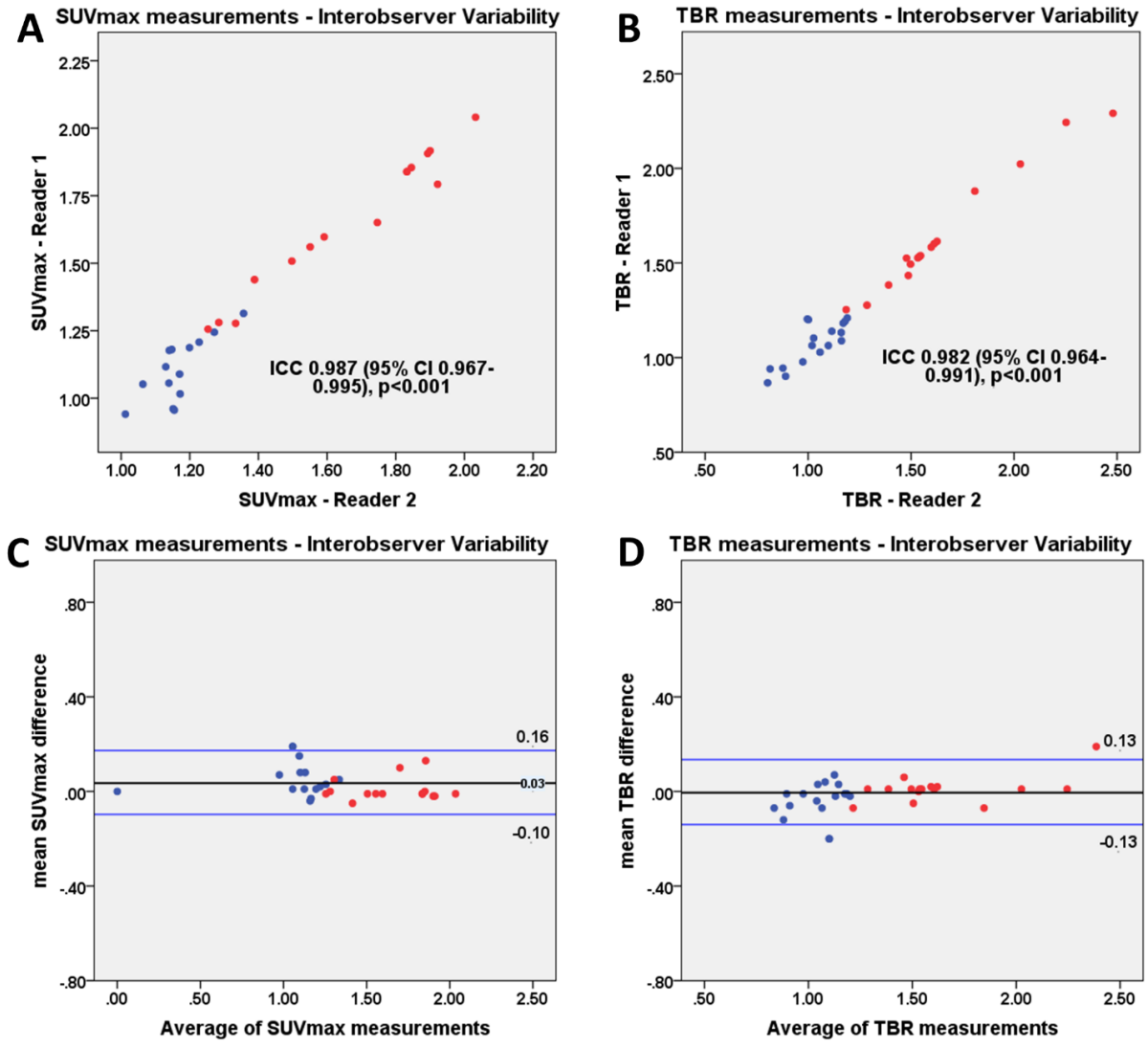

6.4.5 Reproducibility of measurements

On diastolic imaging the intraclass correlation coefficient for SUVmax and TBR between PET/CTA1 and PET/CTA2 measurements was 0.987 (95% CI 0.983 to 0.991) and 0.986 (95% CI 0.981 to 0.991). There was no fixed or proportional bias between PET/CTA1 and PET/CTA2 with limits of agreement of ±0.20 for SUVmax and ±0.20 for TBR measurements. On motion corrected images the intraclass correlation coefficients for SUVmax and TBR values on PET/CTA1 and PET/CTA2 was 0.991 (95% CI 0.988 to 0.994) and 0.992 (95% CI 0.989 to 0.994). Motion correction improved the reproducibility of measurements between PET/CTA1 and PET/CTA2. Compared to diastolic imaging, the limits of agreement decreased from ±0.20 to ±0.14 for SUVmax and from ±0.20 to ±0.15 for TBR ($p<0.001$; Figures 29 and 30).

Figure 31. SUVmax measurements. Scatter plots and Bland Altman plots of prior CTA (PET/CTA1) and hybrid (PET/CTA2) SUVmax values for diastolic gate (a, c) and motion corrected (b, d) data. SUVmax measurements of lesion with (red) and without (blue) increased tracer uptake are shown. Motion corrected analysis resulted in lower variation of the of SUVmax measurements, as compared to the diastolic gate analysis (p<0.001). SUVmax= maximal standard uptake, CTA=coronary CT angiography, ICC=intraclass correlation coefficient.

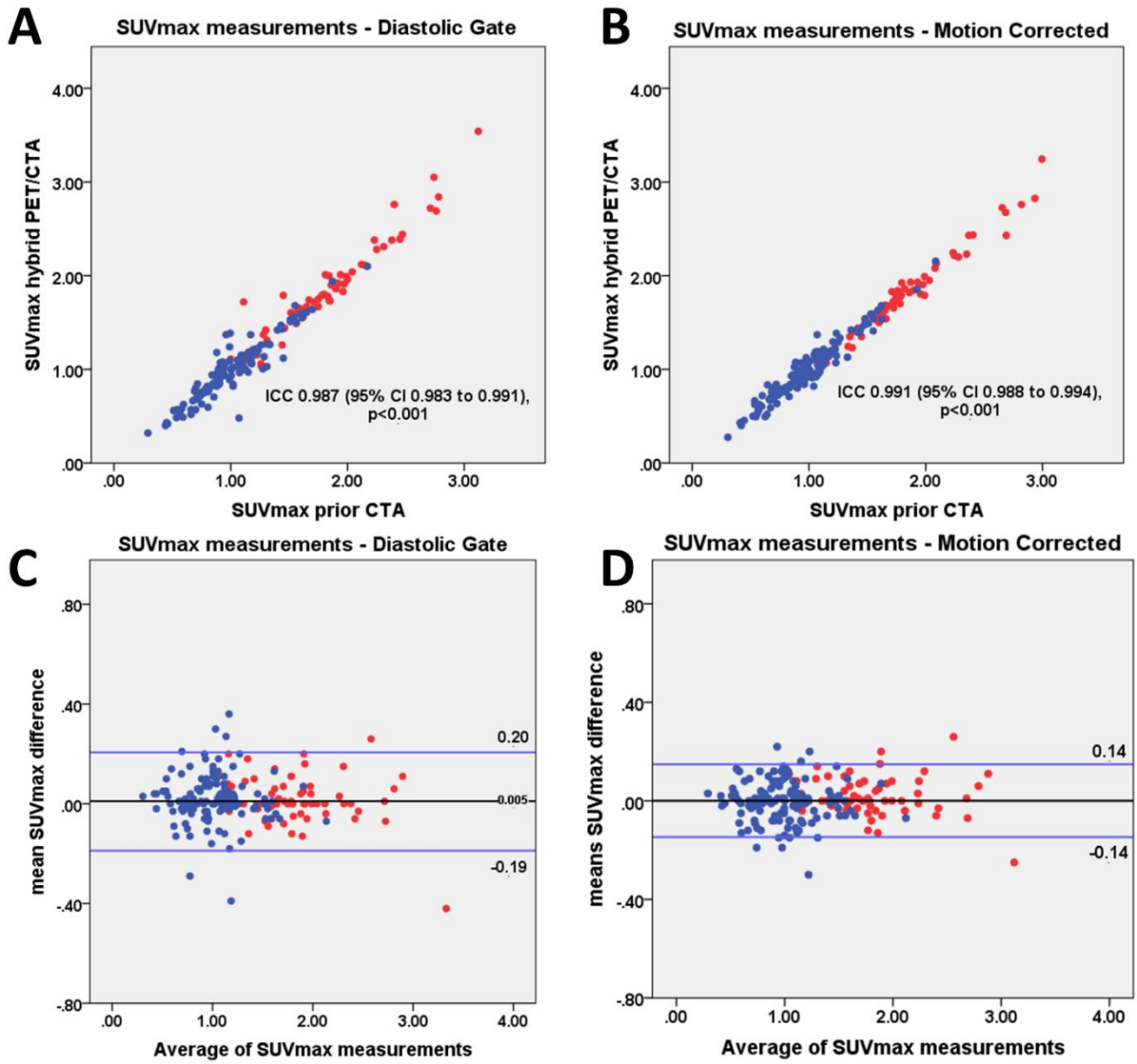

Figure 32. TBR measurements. Scatter plots and Bland Altman of prior CTA (PET/CTA1) and hybrid (PET/CTA2) TBR values for diastolic gate (a, c) and motion corrected (b, d) data. TBR measurements of lesion with (red) and without (blue) increased tracer uptake are shown. Motion corrected analysis resulted in reduced variation of TBR measurements compared to the diastolic gate imaging (p<0.001). TBR= target to background ratio, CTA= coronary CT angiography, ICC= intraclass correlation coefficient.

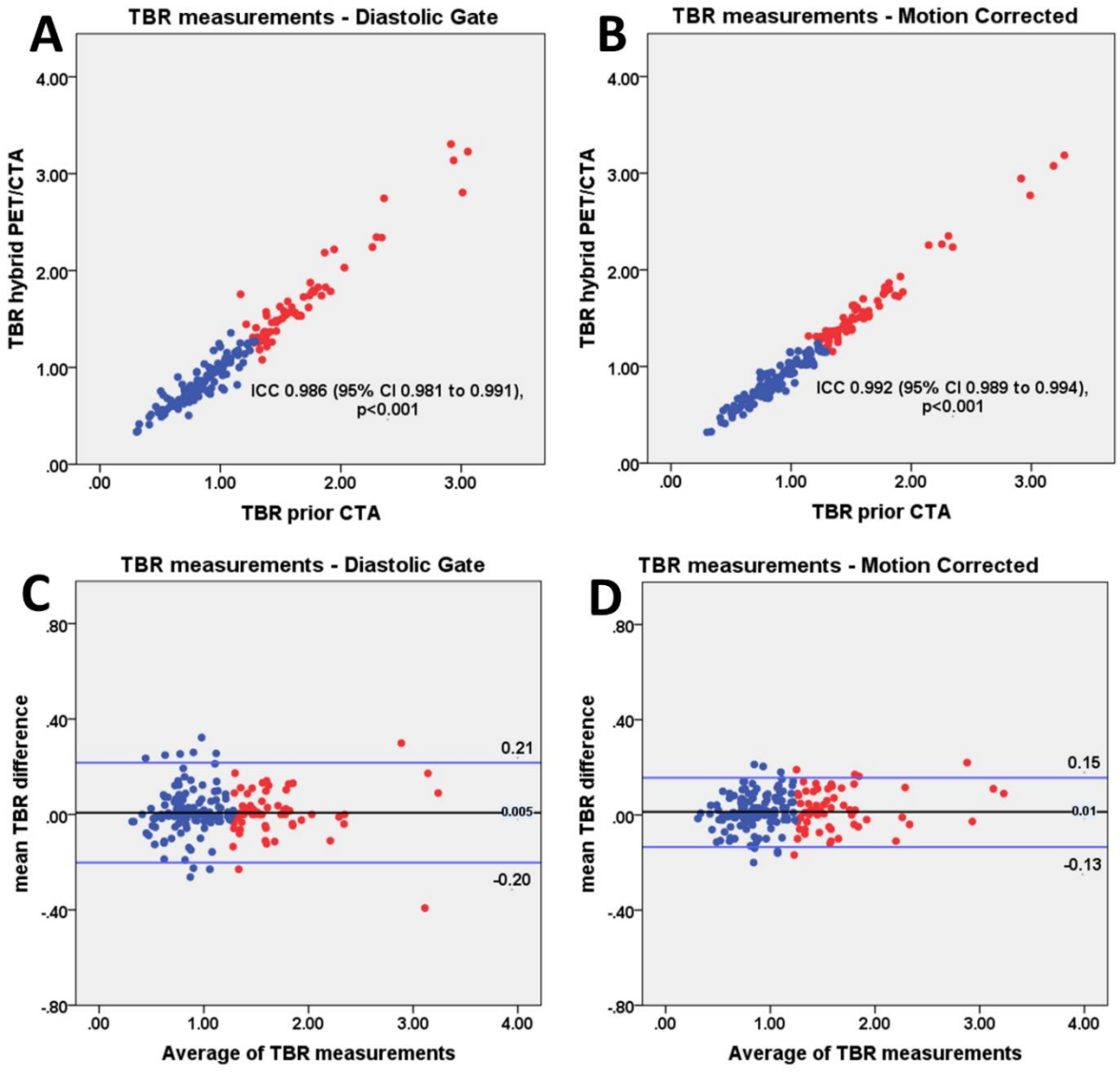

Figure 33. Examples of coronary ^{18}F-NaF uptake on hybrid (PET/CTA2) data (left column) and corresponding prior CTA (PET/CTA1) datasets (right column).

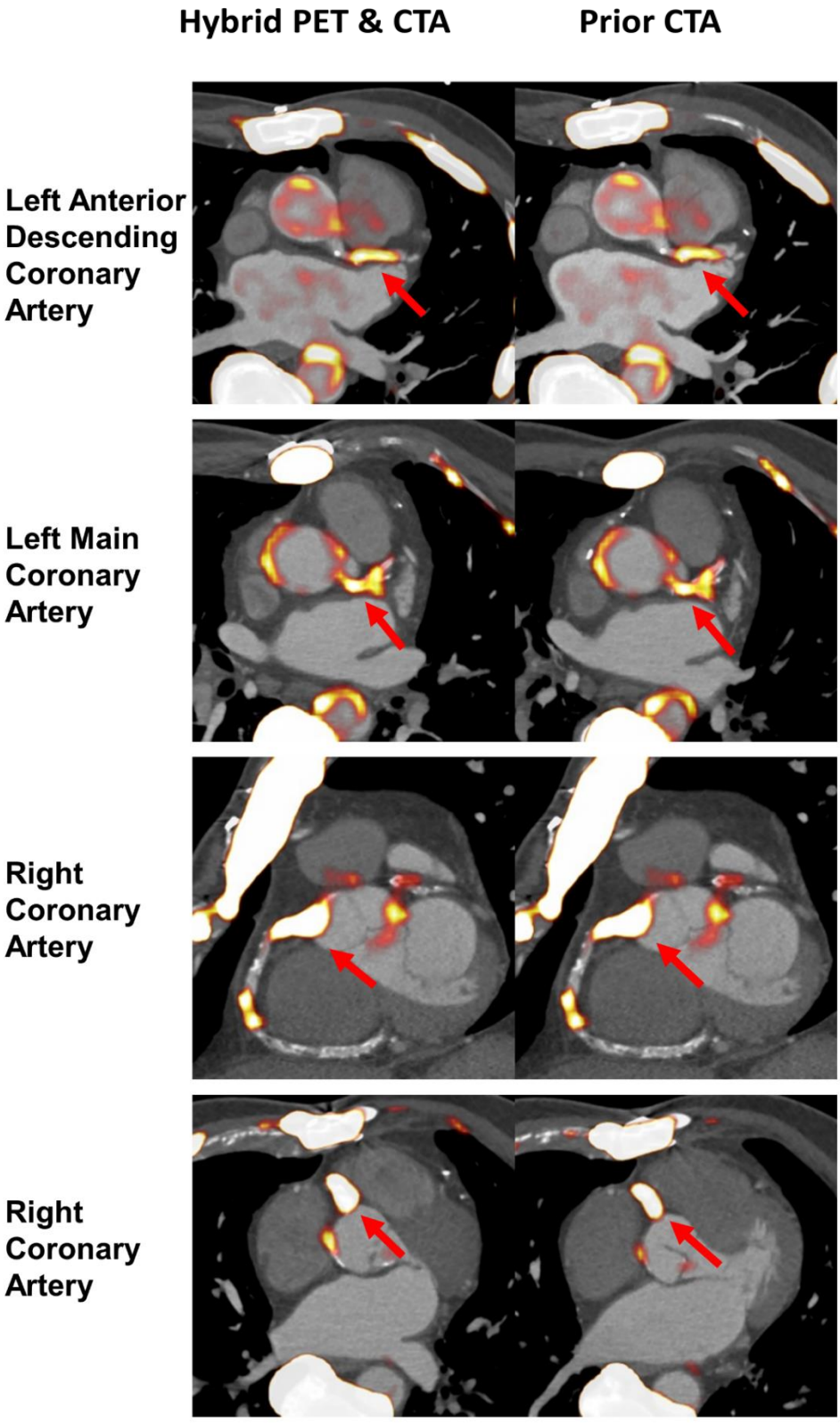

6.5 Discussion

In this multivendor and multicenter study, we report how utilizing a previously acquired CTA with a subsequent standalone PET-only coronary scan can be used for the evaluation of coronary ^{18}F-NaF PET uptake. On a population comprised of patients who underwent repeat CTA studies on the same PET/CT scanner (cohort 1) and a separate subset that had the initial CTA acquired on a solely CT machine (cohort 2) we show that a prior CTA and subsequent PET-only approach enables equivalent categorization of plaques with increased ^{18}F-NaF activity and accurate quantification of PET uptake. We demonstrate that staged coronary PET and CTA protocols can reliably and reproducibly generate quantitative ^{18}F-NaF PET coronary images, that are enhanced by motion correction.

These findings have important implications for future research and clinical coronary ^{18}F-NaF imaging. The prior CTA and subsequent PET-only acquisition protocol lends itself to a practical clinical workflow, with the initial CTA providing a basis for selection of patient for the coronary PET study. CTA is growing rapidly in a wide variety of clinical settings. Therefore, CTA will likely be the most common basis for selection of patients who might benefit from assessment of disease activity with coronary PET imaging. In this scenario, the requirement for a second CTA obtained at the time of coronary PET imaging would not be practical or economically feasible, and incurs unnecessary additional radiation exposure. In carefully selected populations at exceptionally high risk of adverse events, ^{18}F-NaF PET could provide insight into the biology of atherosclerosis and may prove to be of importance in patient management (Adamson, Vesey, Joshi, Newby, & Dweck, 2015; Raggi, Pontone, & Andreini, 2018). It has been shown that the presence of vulnerable plaque features predicts acute coronary syndromes and in the absence of significant stenosis and coronary calcification, the likelihood of adverse events is very

low (Greenland, LaBree, Azen, Doherty, & Detrano, 2004; Oliveira-Santos et al., 2017). Therefore, the CTA-first approach could limit unwarranted ^{18}F-NaF PET scans in low risk populations. On the other hand, a follow-up standalone ^{18}F-NaF PET scan could be warranted in individuals who present with a very high atherosclerotic plaque burden to differentiate active from burnt out stable disease, or in patients with high risk plaque features such as those with positive remodeling, low attenuation components and the napkin-ring sign on CTA (Kitagawa et al., 2017).

Importantly, CTA scans acquired on hybrid PET/CT are often of suboptimal quality due to limited CT performance in this configuration. In many PET laboratories, either the PET scanner does not have performance characteristics required for coronary CTA, or a standalone CT scanner with better imaging characteristics for coronary CTA is available. Since coronary CTA is strongly dependent on image quality, the most advanced CT scanners should be used for this application. While the current hybrid PET/CT scanners are at best 128-slice systems, the dedicated CTA equipment can be a 320-slice or dual source (196 slices) setup which can cover the entire heart in one gantry rotation (Einstein et al., 2010). Further, the scanning protocol for hybrid PET/CTA requires technical staff with expertise in both PET and coronary CTA to be present during a single session. In many centers that offer both PET and CTA scans, the imaging team performing PET studies does not have extensive experience in CTA. Thus, separate technologists with CTA expertise might be required to perform the CTA portion of the PET/CT examination, raising the cost and complexity of the procedure. With the utilization of CTA obtained prior to the ^{18}F-NaF PET, such inconvenience would no longer occur. A prior CTA approach to ^{18}F-NaF PET would also shorten the duration of image acquisition substantially and overall patient radiation exposure by avoiding repetition of the CTA scan.

As expected, we observed that larger registration adjustments were needed to achieve perfect alignment of CT acquired during a different imaging session from the PET compared to hybrid PET/CTA acquisition. However, with the image registration approach utilized, all images could be successfully registered and analyzed. Moreover, it is important to realize that even the hybrid PET/CTA approach requires substantial modification of image alignment for adequate co-registration (Figure 26). This is largely due to gross patient motion which occurs during the pause between PET and CTA acquisitions and differences in respiratory patterns. Indeed, no hybrid PET/CTA scan in this study was perfectly co-registered at baseline with each requiring such spatial adjustments.

In patients with multiple foci of increased ^{18}F-NaF activity achieving perfect registration of all lesions can be challenging. In our study, in such cases we observed a maximal misalignment of 5mm (from the center of vessel on CTA to the center of the hot spot on PET. Importantly misalignment was similarly common on both single visit acquisitions and when using prior CTA data. To offset for such issues, for the SUVmax measurements we used a spherical volume of interest (radius 5 mm) which encompasses the plaque in question (as seen on the CTA) and its immediate surroundings. As a result, in our study misregistration of 2-4 mm which can easily occur (Figure 26BC) had no adverse impact on the accuracy of the uptake measurement as shown on the scatterplots with interobserver variability of SUVmax and TBR measurements (Figure 28AB).

The sensitivity of SUVmax measurements on the accuracy of the registration varies from patient to patient and depends on the anatomy. In an ideal scenario (that is when uptake is only present within coronary arteries) since the volumes of interest utilized have a radius of 5 mm misregistration of up to ~5mm will not have an enormous impact. However, in patients with multiple non-coronary uptake foci within that distance from the

actual coronary lesions, such misregistration will potentially lead to false positive findings. For instance, when assessing ^{18}F-NaF activity in the left main or mid left anterior descending artery, special care should be taken to avoid assigning uptake originating from the ascending aorta and main pulmonary artery to the coronaries. Likewise, extra-coronary foci of uptake (in patients who suffered from pericardial, aortic or mitral disease which resulted in calcification outside of coronary arteries) need to be distinguished. Without anatomical reference provided by CTA accurate quantification of uptake is impossible as increased tracer activity of non-coronary microcalcifications can be erroneously classified (Figure 32).

Figure 34. Case example of coronary and non-coronary ^{18}F-NaF uptake. A 67-year-old-male with uptake in the distal RCA (yellow arrow) and non-coronary uptake in the inferomedial papillary muscle (red arrow) (A). The uptake in the papillary muscle is more pronounced than in the coronary plaque (B). In the transverse plane the extra coronary foci of uptake can be easily seen (red arrows) (C) and have higher activity than the RCA plaques (yellow arrows) (D).

Taking advantage of the CTA, which was used for anatomical reference, careful inspection of the dataset revealed an area of low attenuation within the inferior LV wall and the postero-medial papillary muscle (red arrow) as compared to the LV anteroseptum (blue arrow) (E&F). Such low attenuation can be seen in infarcted myocardium – which might, in the process of healing, develop foci of microcalcification (which attract ^{18}F-NaF). Without the reference of a CTA the foci of pronounced ^{18}F-NaF uptake could potentially be erroneously attributed to plaques in the posterior descending artery (PDA) or the posterior left ventricular (PLV) artery. Due to the findings on the PET study the patient underwent cardiac magnetic resonance imaging which revealed scarring of the inferior wall and postero-medial papillary muscle (area of delayed enhancement [white] as opposed to the remote myocardium [black]) (G).

While uptake situated within the myocardium is a rare finding, the same patient showed non-coronary ^{18}F-NaF activity in the aorta – which without anatomical reference could be easily attributed to one of the left coronary proximal plaques (H). Yellow arrows indicate coronary plaque uptake (in the distal RCA and proximal LAD). The red arrow highlights the infarcted postero-medial papillary muscle. The purple arrow indicates increased PET tracer activity in the ascending aorta and the blue arrow highlights uptake immediately adjacent to the left coronary cusp of the aortic valve.

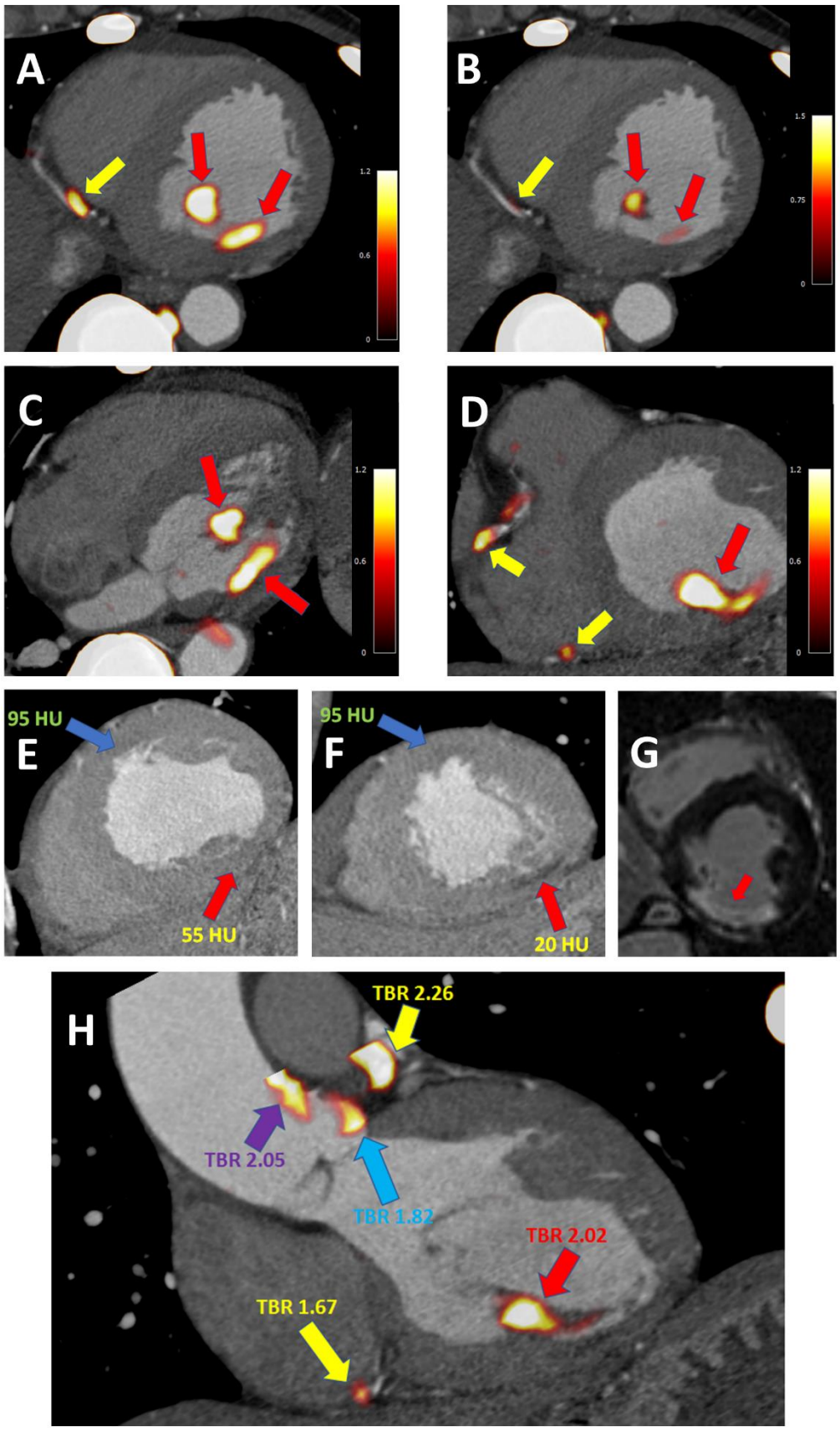
A
B
C
D
95 HU
E
55 HU
95 HU
F
20 HU
G
H
TBR 2.26
TBR 2.05
TBR 1.82
TBR 2.02
TBR 1.67

Finally, we have demonstrated that by applying correction for coronary artery motion, the reproducibility of such PET-only measurements with prior CTA are significantly improved. In fact, our limits of agreement between PET/CTA1 and PET/CTA2 are comparable to the inter-observer repeatability for uptake measurements in the same scan as shown by Dweck et al (M. R. Dweck, M. W. L. Chow, et al., 2012)(2). The improved PET/CTA2-PET/CTA1 reproducibility with motion correction is likely due to the higher signal to noise in the motion corrected PET images.

6.5.1 Study Limitations

There are several limitations of our work. Our motion correction method compensated only for cardiac motion; nevertheless, we have been able to demonstrate the utility of this technique in reducing the variation of ^{18}F-NaF PET quantification with prior CTA. In this study we have not performed any quality control to identify any gross patient motion during the 30-minute-long emission scan. While the significance of such motion during acquisition has not been explored for coronary PET imaging it is likely that it has a detrimental effect on image quality and hence should be addressed in future studies. It might be speculated that gross patient motion correction would make the co-registration of PET and CTA more straightforward as borders between high and low update areas could be better defined. Currently the PET-CT co-registration was performed manually with translations made in the X,Y and Z axis and no rotations between datasets. It is likely that automatization of this process could decrease the time and expertise required for image analysis and translate into rapid dissemination of coronary ^{18}F-NaF PET imaging beyond highly experienced academic centers. Nevertheless, in this study, despite the manual registration of CTA, we were already able to demonstrate excellent reproducibility of quantification ^{18}F-NaF PET with separately obtained CTA.

Chapter 7. Three-hour delayed imaging improves assessment of coronary ^{18}F-sodium fluoride PET.

Published by Jacek Kwiecinski, Daniel S Berman, Sang-Eun Lee, Damini Dey, Sebastien Cadet, Martin L Lassen, Guido Germano, Maurits A Jansen, Marc R Dweck, David E Newby, Hyuk-Jae Chang, Mijin Yun*, Piotr J Slomka* Three-hour delayed imaging improves assessment of coronary ^{18}F-sodium fluoride PET. 2018 Journal of Nuclear Medicine

7.1 Summary

Coronary ^{18}F-sodium fluoride (^{18}F-NaF) PET imaging identifies ruptured plaques in patients with recent myocardial infarction and localizes to atherosclerotic lesions with active calcification. Most studies to date performed the PET acquisition 1-hour (1h) post-injection. Although qualitative and semi-quantitative analysis is feasible with 1h images, often residual blood pool activity makes it difficult to discriminate plaques with ^{18}F-NaF uptake from noise. We aimed to assess whether delayed 3-hour (3h) post-injection PET scan improves image quality and uptake measurements.

Twenty patients (67±7years old, 55% male) with stable coronary artery disease underwent coronary CT angiography and PET/CT both 1 h and 3 h after the injection of 266.2±13.3 MBq of ^{18}F-NaF. We compared the visual pattern of coronary uptake, maximal background (blood pool) activity, noise, standard uptake values (SUVmax), corrected SUV (cSUVmax) and target to background (TBR) measurements in lesions defined by CTA on 1h vs 3h post injection ^{18}F-NaF PET.

On 1h PET 26 CTA lesions with ^{18}F-NaF PET uptake were identified in 12 (60%) patients. On 3h PET we detected ^{18}F-NaF PET uptake in 7 lesions which were not identified on the 1h PET. The median cSUVmax and TBR values of these lesions were 0.48 [interquartile range (IQR) 0.44-0.51] and 1.45 [IQR, 1.39-1.52] compared to -0.01 [IQR, -0.03-0.001] and 0.95 [IQR, 0.90-0.98] on 1h PET, both p<0.001. Across the entire cohort 3h PET SUVmax values were similar to 1h PET measurements 1.63 [IQR, 1.37-1.98] vs. 1.55 [IQR, 1.43-1.89], p=0.30 and the background activity was lower 0.71 [IQR, 0.65-0.81] vs. 1.24 [IQR, 1.05-1.31], p<0.001. On 3h PET, the TBR values, cSUVmax and the noise were significantly higher (2.30 [IQR, 1.70-2.68] vs 1.28 [IQR, 0.98-1.56], p<0.001; 0.38 [IQR, 0.27-0.70] vs 0.90 [IQR, 0.64-1.17], p<0.001 and 0.10 [IQR, 0.09-0.12] vs.

0.07 [IQR, 0.06-0.09], p=0.02). The median cSUVmax and TBR values increased by 92% (range: 33-225%) and 80% (range: 20-177%).

Blood-pool activity decreases on delayed imaging facilitating the assessment of ^{18}F-NaF uptake in coronary plaques. The median target to background ratios increase by 80% leading to the detection of more plaques with significant uptake compared to the standard 1h protocol. A greater than a 1h delay may improve the detection of ^{18}F-NaF uptake in coronary artery plaques.

7.2 Introduction

Coronary ^{18}F-sodium fluoride (^{18}F-NaF) PET imaging depicts biological processes involved in plaque formation and rupture in patients with coronary artery disease (M. R. Dweck, M. W. L. Chow, et al., 2012). Increased ^{18}F-NaF uptake has been observed with hybrid PET (positron emission tomography)/coronary CT angiography (CTA) to localize in regions of recent plaque rupture in patients with acute myocardial infarction as well as in coronary plaques with high-risk features on intravascular ultrasound in patients with stable coronary artery disease (CAD) (Joshi et al., 2014). As this promising imaging approach is still in its infancy, several technical aspects regarding ^{18}F-NaF coronary PET imaging remain to be addressed (Adamson et al., 2015; Thomas & Haraszti, 2014).

In the 1970s when ^{18}F-NaF was first used for bone scanning, Blau et al suggested that the optimal scanning time for ^{18}F-NaF is 2-4 hours post injection (Monte Blau et al., 1972; M. Blau et al., 1962). Nevertheless, whole-body ^{18}F-NaF PET is nowadays most often performed with imaging commencing 60 minutes after injection (Czernin et al., 2010; Grant et al., 2008; Hawkins et al., 1992; Segall et al., 2010). In cardiovascular PET, in most studies to date assessing ^{18}F-NaF uptake in atherosclerotic plaques, acquisition was performed 1-hour (1h) after tracer administration (Derlin et al., 2010; Derlin, Toth, et al., 2011; Derlin, Wisotzki, et al., 2011). Although semi-quantitative analysis is feasible with 1h images, it can be difficult to discriminate plaques with ^{18}F-NaF uptake from noise. Recently, it has been speculated that the optimal time for atherosclerotic plaque imaging with ^{18}F-sodium fluoride might differ from the 1h post injection time-point used for bone imaging (Derlin, Wisotzki, et al., 2011). Up to date only one study looked at the optimal timing for cardiovascular ^{18}F-NaF imaging, but performed the ungated low-count PET acquisition measuring overall uptake in the entire heart rather than in coronary plaques (Björn A. Blomberg et al., 2014). In this study, we aimed to quantitatively assess whether

delayed 3-hour (3h) post-injection state-of-the-art PET scanning improves image quality and coronary ^{18}F-NaF uptake measurements.

7.3 Methods

7.3.1 Patients

We analyzed scans of 20 patients with stable coronary artery disease who underwent coronary CTA and PET/CT imaging both 1h and 3h after a single injection of ^{18}F-NaF at Severance Cardiovascular Hospital. All study participants had angiographically proven CAD (defined as at least one >50% luminal stenosis). Exclusion criteria included, renal dysfunction (eGFR ≤30 mL/min/1.73 m2), contraindication to iodinated contrast agents, significant ventricular or atrial arrhythmia (which could compromise image quality), class III congestive heart failure and ejection fraction <35%. The study was approved by the investigational review board, and written informed consent was obtained from all enrolled patients.

7.3.2 Imaging acquisition and reconstruction

7.3.2.1 PET

All patients underwent ^{18}F-NaF PET/CT on a hybrid PET-CT scanner (Discovery 710, GE Healthcare, Milwaukee, WI, USA). Prior to imaging, subjects were administered with a target dose of 250 MBq of ^{18}F-NaF and rested in a quiet environment for 60 minutes. After the acquisition of a non-contrast attenuation correction scan, PET data was acquired in list mode for 30 minutes. The list mode dataset was reconstructed using a standard ordered expectation maximization algorithm with resolution recovery (SharpIR). Corrections were applied for attenuation, dead time, scatter and random coincidences. Utilizing 10 cardiac gates, the data were reconstructed on a 256x256 matrix (20x20cm field of view) using 24 subsets and applying 4 iterations along with 5mm Gaussian smoothing(Mhairi K. Doris et al., 2018). For standard uptake value (SUV) assessment, all analyzed values were decay-corrected to the injection time.

7.3.2.2 CT angiography

After the 1h PET acquisition, contrast-enhanced coronary CTA was performed with prospective ECG-triggering if the heart rate was <60 beats/min and regular or with ECG gated helical acquisition if the heart rate >60 beats/min or irregular. All patients received beta blockers and sublingual nitrates. For contrast-enhanced imaging iodinated contrast (65-130ml) was power injected at 5-6 ml/sec, followed by a saline flush. Transverse images were reconstructed using filtered back projection with 0.65-mm slice thickness, 0.4 mm increment, and a medium-soft convolution kernel.

7.3.2.3 Delayed PET

A second low-dose CT for attenuation correction and PET was performed 3h after tracer administration using the same protocol for imaging and the same reconstruction of PET datasets as used in the 1h study.

7.3.2.4 PET Motion correction

Cardiac motion correction was performed on the 1h and 3h ^{18}F-NaF PET/CT data. This technique compensates for coronary artery motion by aligning all gates to the end-diastolic position and has demonstrated its ability to reduce image noise and improve target to background ratio (TBR) (Rubeaux, Joshi, Dweck, Fletcher, Motwani, Thomson, Germano, Dey, Li, et al., 2016). First, anatomic coronary artery data was extracted from diastolic coronary CTA by applying a vessel tracking algorithm based on Bayesian maximal paths using dedicated software (Autoplaque version 2.0, Cedars-Sinai Medical Center). Second, a diffeomorphic mass-preserving image registration algorithm was used to align the 10 gates of PET data to the end-diastolic gate (gate 7 or 8 dependent on the timing of the CTA acquisition). After motion correction, the 10 gates were summed to build a motion-free image containing counts from the entire PET acquisition.

7.3.3 Image analysis

7.3.3.1 Coronary CTA

Evaluation of coronary artery plaques was conducted in accordance with the Society of Cardiovascular Computed Tomography guidelines (Leipsic et al., 2014). The extent of disease was characterized by lesion maximal stenosis (Autoplaque version 2.0, Cedars-Sinai Medical Center), plaque composition (non-calcified/partially calcified/totally calcified), the segment involvement score (SIS) and coronary calcium scoring (Agatston et al., 1990; Min et al., 2007).

7.3.3.2 Positron emission tomography

Coronary ^{18}F-NaF image analysis was performed on axial images using FusionQuant Software (Cedars Sinai Medical Center, Los Angeles). PET and CTA reconstructions were reoriented, fused and systematically co-registered in all 3 planes. Key points of reference were the sternum, vertebrae, blood pool in the ventricles and the great vessels. For each scan, plaque activity was measured by delimiting 3-dimensional volumes of interest on lesions. All segments with coronary plaque (at least a grade 2 stenosis [>25%]) and a lumen diameter ≥2 mm, as defined by CTA were interrogated. The maximum standard uptake value (SUVmax) was recorded from all these segments by delimiting a spherical volume of interest (radius=5mm). Background blood pool activity (SUVmean) was measured by delimiting a cylindrical volume of interest (radius=10mm, thickness = 5mm) in the right atrium on the level of the right coronary artery orifice (T. A. Pawade et al., 2016). TBRs were calculated by dividing SUVmax by averaged background blood pool activity. Corrected maximum standard uptake values (cSUVmax) were calculated by subtracting the blood-pool activity from SUVmax. Image noise was defined as the coefficient of variance of the blood pool activity. Coronary plaques were

considered clearly positive for ^{18}F-NaF uptake if they presented with focal tracer uptake arising from the coronary plaque which followed the course of the vessel in three dimensions over more than one slice and had a TBR>1.25 (Joshi et al., 2014). In addition to reporting decay corrected uptake values we also evaluated the raw counts. The PET acquisitions were analyzed independently with at least a 21-day interval between the reading of the 1h and the 3h after injection scan.

7.3.4 Statistical Analysis

Continuous data are expressed as mean (standard deviation) or median [interquartile range (IQR)] as appropriate. Parametric data were compared using student's T-test and paired student's T-test, non-parametric data were compared using Wilcoxon rank sum and Wilcoxon signed-rank test where appropriate. Categorical variables are presented as absolute numbers (percentage) and were compared using a Chi-squared test or Fisher's exact test where appropriate. A two-sided p value <0.05 was considered statistically significant. Statistical analyses were performed using SPSS (version 24, IBM, USA) software.

7.4 Results

Twenty patients (67±7 years old, 55% male) were recruited into the study. Patient baseline characteristics are shown in Table 20. On CTA, the median segment involvement and coronary calcium scores were 6 [IQR, 3-8] and 413 [IQR, 50-770] respectively. Exact PET tracer injected doses were 266.2±13.3 MBq of ^{18}F-NaF.

Table 20. Patients' baseline clinical characteristics.

	Study cohort (n=20)	SD, IQR, %
Baseline Characteristics		
Age, years	67	±7
Males, n (%)	11	(55%)
Diabetes, n (%)	4	(20%)
Hyperlipidemia, n (%)	5	(25%)
Hypertension, n (%)	12	(60%)
Tobacco use, n (%)	6	(30%)
Family history of CAD, n (%)	3	(15%)
Serum Biomarkers		
Total Cholesterol	162	[135-189]
HDL	43	[38-46]
LDL	93	[71-107]
Triglyceride	121	[86-140]
Creatine	0.8	[0.7-0.9]
Medications		

Aspirin, n (%)	13	(65%)
Statin, n (%)	6	(30%)
ACEI/ARB, n (%)	6	(30%)
Beta Blocker, n (%)	7	(35%)
Leading clinical indication for CTA		
Chest pain, n (%)	15	(75%)
Dyspnea, n (%)	3	(15%)
Risk assessment (asymptomatic patient), n (%)	2	(10%)
Coronary Computed Tomography Angiography		
Segment involvement score	6	[3-8]
Multivessel disease, n (%)	6	(30%)
Coronary calcium score	312	[50-770]

CAD: coronary artery disease; CTA: coronary computed tomography angiography; HDL – high density lipoprotein; LDL – low density lipoprotein; ACEI – angiotensin converting enzyme inhibitor; ARB – angiotensin receptor blocker; SD – standard deviation; IQR - Interquartile range.

7.4.1 1h post injection imaging

On 1h PET (acquisition 66.5 [IQR, 64.5-71.8] min post injection), coronary uptake exceeding the TBR=1.25 threshold was observed in 12 (60%) patients. Twenty-six CTA segments were considered positive for ^{18}F-NaF uptake. Eleven (41%) were in the left anterior descending, 6 (23%) in the left circumflex, 4 (16%) in the left main and 5 (20%) in the right coronary artery. The association between patients' baseline characteristics, risk-profiles and CTA findings are presented in supplementary Tables 21 and 22.

Table 21. Univariate and multivariate linear regression analysis to examine association of variables with maximum per patient 1h post injection target to background uptake measurements. Both multivariate models with: LDL levels, segment involvement scores, presence of multivessel disease, coronary calcium scores and quantitative stenosis. Model 1 additionally includes lipid lowering treatment; Model 2 includes partially calcified plaques.

Variables	Univariate		Multivariable – Model 1 (included: lipid lowering treatment)		Multivariable – Model 2 (included: plaque composition - mixed)	
	Relative change in TBR (95% CI)	P value	Relative change in TBR (95% CI)	P value	Relative change in TBR (95% CI)	P value
LDL	0.001 (-0.001-0.001)	0.97	0.001 (-0.006-0.005)	0.74	0.001 (-0.005-0.006)	0.80
Lipid lowering treatment	-0.30 (-0.60—0.004)	0.047	-0.331 (-0.68-0.023)	0.064		
Segment involvement score	0.04 (-0.05 – 0.67)	0.22	0.01 (-0.06-0.02)	0.53	0.02 (-0.03-0.06)	0.49
Multivessel disease	0.05 (-0.21-0.31)	0.30	0.09 (-0.43-0.27)	0.65	0.33 (-0.01-0.76)	0.11

Coronary calcium score	0.01 (0.001-0.02)	0.39	0.01 (-0.01-0.02)	0.43	0.01 (-0.01-0.02)	0.55
Stenosis	0.001 (-0.007 – 0.10)	0.75	0.002 (-0.007-0.011)	0.66	0.003 (-0.005-0.12)	0.44
Partially calcified plaque	0.30 (0.03-0.57)	0.030			0.56 (0.1-1.0)	0.020

CI: confidence interval, LDL: low density lipoprotein, TBR: maximum target to background ratios.

Table 22. Univariate and multivariate linear regression analysis to examine association of variables with maximum per patient 3h post injection target to background uptake measurements. Both multivariate models with: LDL levels, segment involvement scores, presence of multivessel disease, coronary calcium scores and quantitative stenosis. Model 1 additionally includes lipid lowering treatment; Model 2 includes partially calcified plaques.

Variables	Univariate		Multivariable – Model 1 (included: lipid lowering treatment)		Multivariable – Model 2 (included: plaque composition - mixed)	
	Relative change in TBR (95% CI)	P value	Relative change in TBR (95% CI)	P value	Relative change in TBR (95% CI)	P value
LDL	0.004 (-0.007-0.015)	0.43	0.002 (-0.01-0.01)	0.66	0.01(-0.001-0.015)	0.15
Lipid lowering treatment	-0.32 (-0.61--0.03)	0.041	-0.36 (-1.04-0.012)	0.079		
Segment involvement score	0.012 (-0.08-0.10)	0.78	0.04 (-0.05-0.13)	0.33	0.03 (-0.04-0.09)	0.40
Multivessel disease	0.09 (-0.61-0.79)	0.21	0.11 (-0.56-0.78)	0.32	0.67 (0.2-1.33)	0.02

Coronary calcium score	0.001 (-0.01-0.011)	0.37	0.001(-0.002-0.003)	0.77	0.001 (-0.001-0.002)	0.79
Stenosis	0.12 (-0.05-0.029)	0.15	0.1 (-0.01-0.03)	0.19	0.02 (0.001-0.03)	0.11
Partially calcified plaque	0.79 (0.27-1.30)	0.005			1.3 (0.7-1.9)	<0.001

CI: confidence interval, LDL: low density lipoprotein, TBR: maximum target to background ratios.

7.4.2 3h post injection imaging

On delayed PET imaging (acquisition 180.5 [IQR, 177.3-193.0] min post injection), by visual inspection background ^{18}F-NaF activity was markedly reduced, and coronary lesions were more conspicuous. We identified all segments which were detected on 1h post injection imaging (Figure 33). In addition, 7 new segments (median stenosis 48.6% [IQR, 35.7-60.2]) which were previously negative for ^{18}F-NaF uptake demonstrated focal uptake with TBR>1.25 (Figure 34). These lesions were found in 2 patients who had uptake elsewhere in the coronary vasculature and in 3 patients classified as negative for ^{18}F-NaF coronary uptake on 1h post injection imaging. While the SUVmax of these 7 new positive lesions was similar on 3h vs 1h PET (1.51 [IQR, 1.42-1.60] vs. 1.48 [IQR, 1.40-1.55], p=0.68), the cSUVmax and TBR values were higher on delayed imaging (0.48 [IQR, 0.44-0.51] vs. -0.01 [IQR, -0.03-0.001] and 1.45 [IQR, 1.39-1.52] vs. 0.95 [IQR, 0.90-0.98], both p<0.001).

Figure 35. Assessment of ^{18}F-NaF coronary uptake on 1h and 3h delayed PET.

Four patients with significant (TBR>1.25) on 1h post injection (left column) coronary uptake in the left anterior descending artery. Uptake can be difficult to differentiate in this region from blood pool in the adjacent pulmonary artery. On 3h PET (right column) the TBR increased significantly, and blood pool activity reduced improving image quality.

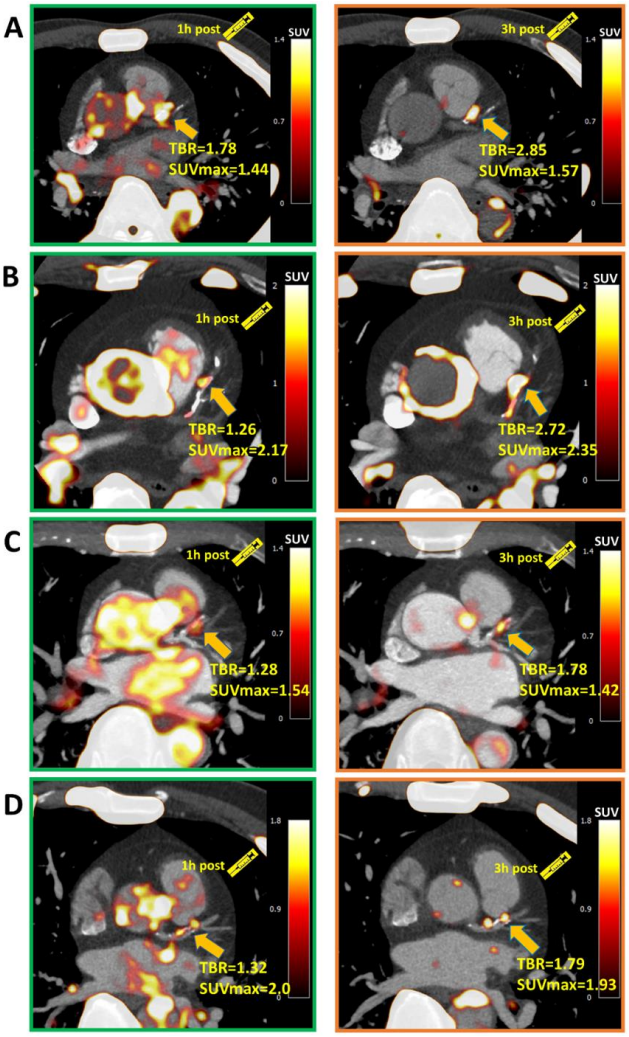

^{18}F-NaF: ^{18}F-sodium fluoride; PET: positron emission tomography; TBR: target to background ratios; SUV: standard uptake value

Figure 36. Examples of coronary plaques with significant uptake on 3h PET and low tracer activity of 1h post injection imaging.

Short axis images of proximal left anterior descending, proximal circumflex (A) and distal right coronary artery (B) plaques which had a TBR<1.0 on 1h PET (left column) and showed uptake exceeding the 1.25 TBR threshold at 3h

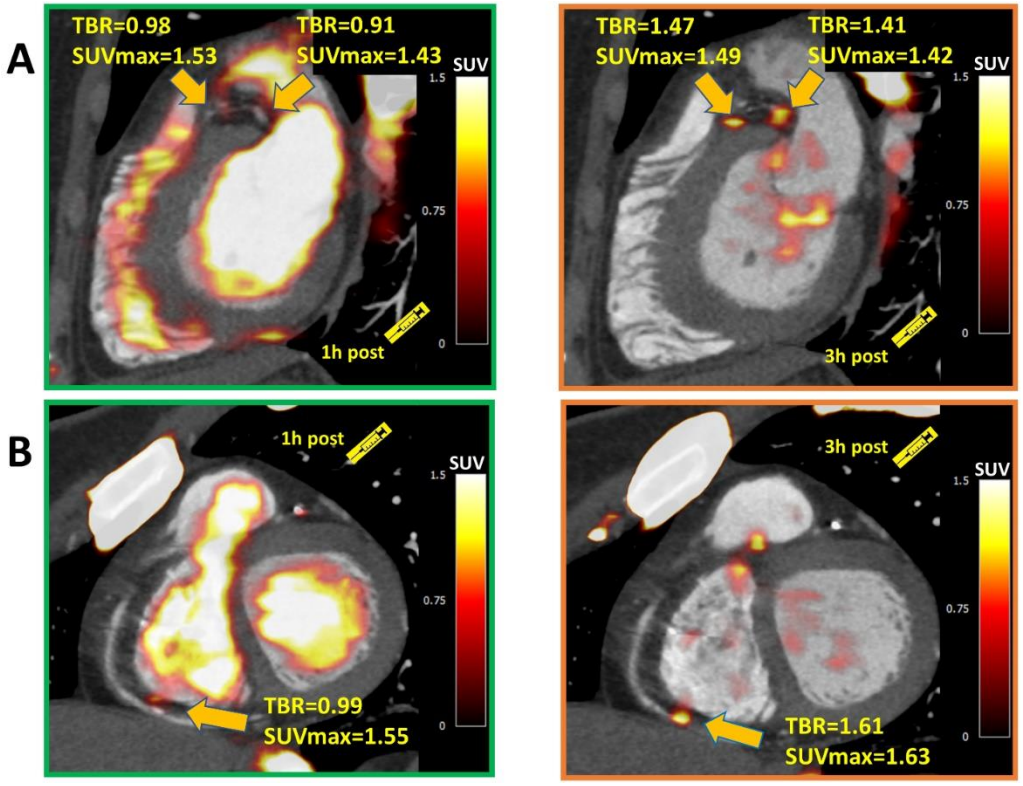

TBR: target to background ratios; PET: positron emission tomography

Across the entire cohort on 3h PET compared to 1h PET, the SUVmax of the detected lesions remained similar (1.63 [IQR, 1.37-1.98] vs. 1.55 [IQR, 1.43-1.89], p=0.30). However, the background activity decreased to 0.71 [IQR, 0.65-0.81] vs. 1.24 [IQR, 1.05-1.31], p<0.001 with a median decrease of 42% (range 18-48%). Consequently, the TBR values were higher (2.30 [IQR, 1.70-2.68] vs 1.28 [IQR, 0.98-1.56], p<0.001), with a median TBR increase of 80% (range: 20-177%, Figures: 35 and 36). A similar change was observed in the cSUVmax 0.38 [IQR, 0.27-0.70] vs 0.90 [IQR, 0.64-1.17], p<0.001; median cSUVmax increased by 92% (range: 33-225%, Figures 35 and 36). In accordance with the Poisson's distribution, we observed a 49.0±3.8% decrease in counts on delayed imaging compared to 1h PET. As expected due to fewer counts on 3h PET, noise increased 0.10 [IQR, 0.09-0.12] vs. 0.07 [IQR, 0.06-0.09], p=0.02.

Table 23. Comparison of ^{18}F-NaF motion corrected measurements on 1h and 3h post injection PET imaging.

	1-hour post injection PET	3-hour post injection PET	P Value
SUVmax	1.55 [1.43-1.89]	1.63 [1.37-1.98]	0.30
TBR	1.28 [0.98-1.56]	2.30 [1.70-2.68]	<0.001
Corrected SUVmax	0.38 [0.27-0.70]	0.90 [0.64-1.17]	<0.001
Background (blood pool)	1.24 [1.05-1.31]	0.71 [0.65-0.81]	<0.001
Noise	0.07 [0.06-0.09]	0.10 [0.09-0.12]	0.02
Segments with TBR>1.25, n (%)	26 (8%)	33 (10%)	0.01
Patients with TBR>1.25, n (%)	12 (60%)	15 (75%)	0.004

^{18}F-NaF: ^{18}F-sodium fluoride; PET: positron emission tomography; SUVmax: maximum standard uptake values; TBR: maximum target to background ratios.

Figure 37. ^{18}F-NaF coronary uptake measures on 1h and 3h delayed PET.

Maximum standard uptake values (SUVmax) values were comparable on both scans (A). The corrected SUVmax and target to background (TBR) values were higher on 3h post injection PET (B,C). The background (right atrium blood pool SUVmean) was lower on 3h imaging (D).

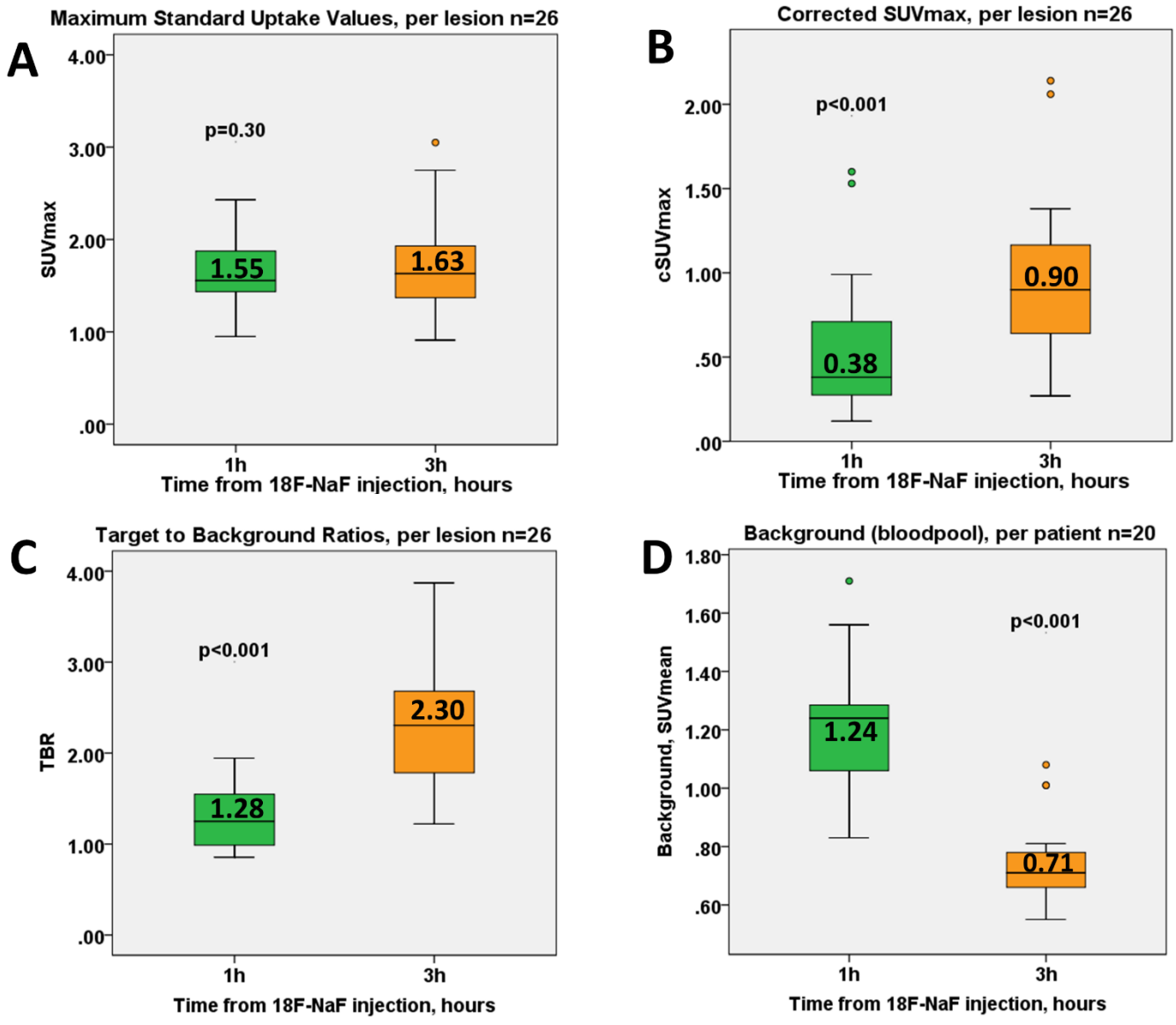

PET: positron emission tomography; ^{18}F-NaF: ^{18}F-sodium fluoride

Figure 38. Line-plots of ^{18}F-NaF coronary uptake measurements on 1h and 3h delayed PET.

Maximum standard uptake values (SUVmax) values were comparable on both scans (A). The corrected SUVmax and target to background (TBR) values were higher on 3h post injection PET (B,C). The background (right atrium blood pool SUVmean) was lower on 3h imaging (D).

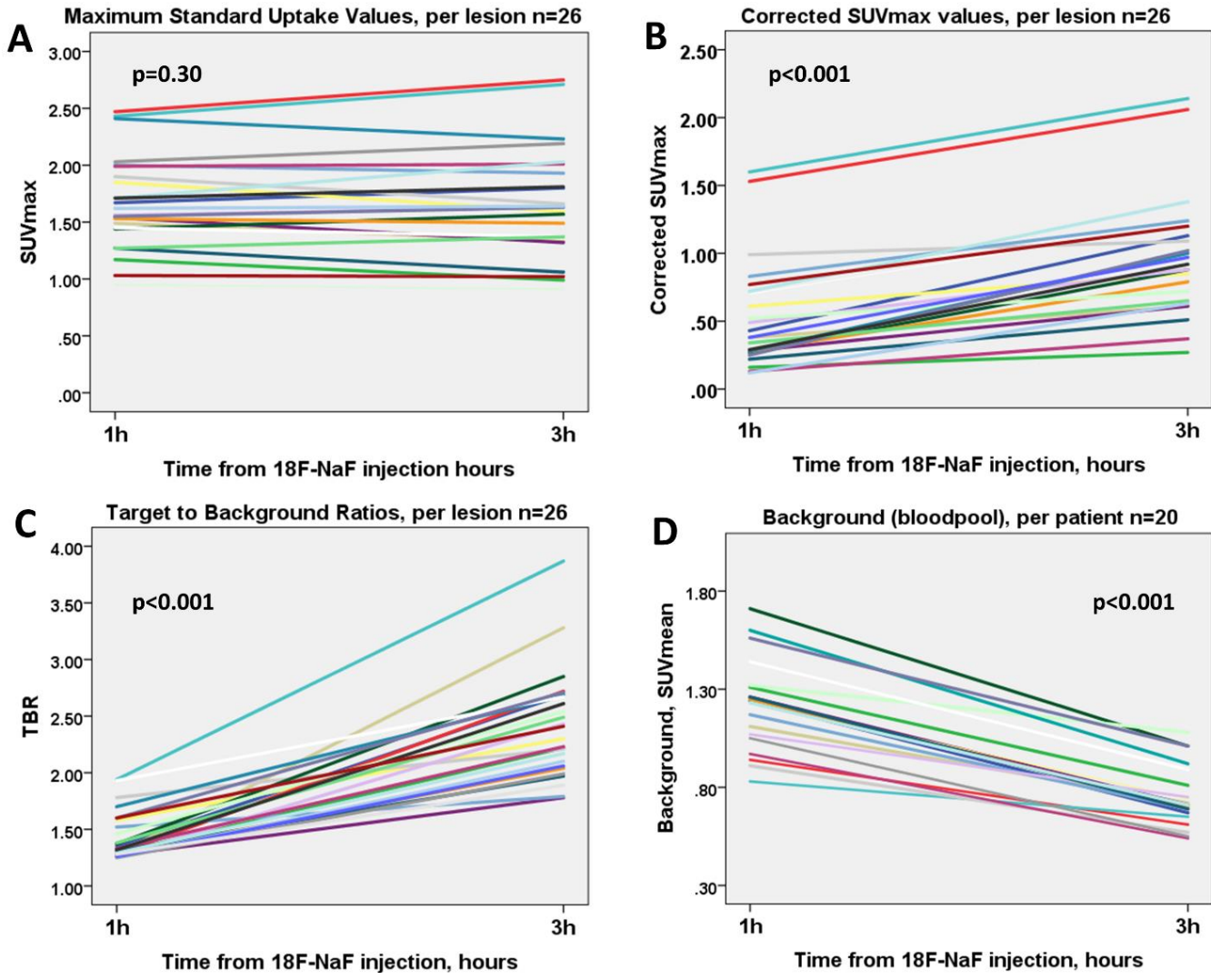

PET: positron emission tomography; ^{18}F-NaF: ^{18}F-sodium fluoride

7.5 Discussion

This is the first study which utilized a 30min acquisition cardiac-gated coronary PET protocol and compared the image quality and quantitative measures of ^{18}F-NaF coronary uptake on 1h vs 3h post injection PET images. We hereby show that prolonging the time from tracer injection to PET acquisition can facilitate image analysis and provide lower background activity, higher TBR and cSUV values compared to the currently utilized protocol. We demonstrate that by delaying image acquisition to 3h new lesions, categorized as false-negative on the 1h PET, were now readily identified.

By utilizing currently used imaging protocols with PET acquisition (1h post injection), the reader is often challenged to distinguish true coronary uptake from overspill from the surrounding structures. A large proportion of ^{18}F-NaF positive plaques present with uptake which is at or only slightly higher than the background activity. Visualization of these lesion is usually possible because of below blood-pool activity in the adjacent myocardium. However, analysis can often be difficult particularly in the proximal and mid-LAD which lies close to blood pool in the pulmonary artery (Figure 33) and in the proximal circumflex that lies adjacent to the left atrial appendage. Techniques to improve the detection of such lesions are therefore required. To some extent blurring of the tracer uptake which occurs due to cardiorespiratory and patient motion can be mitigated with end-diastolic imaging, improving the conspicuousness of lesions (M. R. Dweck, M. W. L. Chow, et al., 2012). Recently developed cardiac motion correction techniques further improve image quality by co-registration of all cardiac gates to the reference one and allowing all PET data rather than that from a single diastolic gate to be utilized (Rubeaux, Joshi, Dweck, Fletcher, Motwani, Thomson, Germano, Dey, Li, et al., 2016). In this study, we show that delaying ^{18}F-NaF coronary image acquisition further facilitates assessment

of coronary uptake, predominantly as a result of a decrease in the background blood pool activity.

Improved visual identification of the lesions on the delayed ^{18}F-NaF PET acquisition is accompanied by significant improvements in TBR and corrected SUVmax measurements. While the coronary SUVmax remained unchanged on 3h PET imaging, the TBR values improved significantly. We observed an increase in the noise on delayed imaging (as expected due to a lower count statistic), however given the favorable decrease in the background (blood pool) activity, the noise level on 3h PET does not impede image analysis.

The benefit of delayed PET acquisition for the detection of disease is widely appreciated in oncological applications with ^{18}F-fluorodeoxyglucose (FDG)(Caoduro et al., 2013; Kubota et al., 2004; W. Y. Lin et al., 2005; Nishiyama et al., 2005). There is good agreement that because background activity decreases on delayed imaging, the image quality improves. The lower background activity is a critical feature and advantage of delayed imaging, because it increases target to background ratios ((Cheng et al., 2013; Houshmand et al., 2016). It has been shown that a longer time window from injection to acquisition translates to higher signal to noise and therefore facilitates visual analysis providing higher diagnostic accuracy (Kubota et al., 2001). For coronary PET imaging, it was suggested that the optimal timing for acquisition with FDG is 2.5-3h after tracer administration (Bucerius et al., 2014; Rudd et al., 2002).

In case of ^{18}F-NaF PET bone imaging, since it has faster blood clearance and higher bone uptake compared to 99mTc-methylene diphosphonate, the SNM practice guideline recommends emission scanning for the axial skeleton as soon as 30-45 minutes after injection in patients with normal renal function (Segall et al., 2010) to decrease the overall time of the study. However, a longer waiting time of 90-120 minutes was recommended

to acquire high-quality images of the extremities. Compared to uptake in the bony skeleton, ^{18}F-NaF uptake due to active microcalcification formation in coronary plaque is very small in amount. Therefore, it is not surprising that a higher TBR in coronary plaques is observed with a longer waiting time from injection to acquisition. Longer delays for cardiovascular ^{18}F-NaF PET imaging were evaluated by only one study to date (Björn A. Blomberg et al., 2014). Blomberg et al. concluded that delayed ^{18}F-NaF PET imaging does not improve quantification of vascular calcification. However, the authors measured only overall heart ^{18}F-NaF activity (including blood pool) by placing regions of interest around the cardiac silhouette on ungated PET/CT images (excluding ^{18}F-NaF activity originating from bones and cardiac valves), and averaged the SUV values derived from all slices. As a result, identifying additional foci of uptake on delayed imaging was not feasible. Moreover, that study was performed without cardiac gating and motion correction. Further, with 2.5-minute scan time and a 2.2 MBq dose of ^{18}F-NaF per kilogram of body weight the authors had approximately 16 times less counts compared to our coronary scans (~3.4MBq dose per kg and 30-min long acquisition).

The utilization of coronary CT angiography in our study enabled measuring ^{18}F-NaF uptake in individual coronary plaques. It also provided an opportunity to evaluate potential predictors of uptake by means of regression modelling (supplemental Tables 21 and 22). While our study is slightly underpowered such analysis revealed that TBR is positively associated with partially calcified plaque and inversely with lipid lowering drugs (statins). These findings are in line with previously published data showing that active calcification, macrophage infiltration and partially calcified plaques are associated with ^{18}F-NaF uptake (Joshi et al., 2014; Kitagawa et al., 2017). On the contrary in our study completely calcified plaques did not attract the PET tracer which is in accordance with prior studies and supports the view that ^{18}F-NaF is a marker active calcification including

the stage before the development of advanced atherosclerotic lesions rather than established disease (McKenney-Drake et al., 2016; Oliveira-Santos et al., 2017). Interestingly, as shown by the explanatory uni- and multivariate analysis the associations with clinical and imaging data are stronger when 3h PET measures rather 1h post injection PET values are utilized (Tables 21 and 22).

Our findings have important clinical implications. Given the challenges that ^{18}F-NaF imaging faces, which include, but are not limited to small target lesion size, cardiac, respiratory and gross patient motion which collectively compromise image quality, a delayed acquisition protocol is an important step in mitigating the modest TBR reported in studies utilizing the 1h post injection protocol. By decreasing the background (blood pool) signal, not only do the TBR values improve, but also lesions which were difficult to detect 1h post injection can be easily identified. Additionally, by utilizing the 3 hours' post injection approach coronary uptake can be more readily assessed by less experienced readers. In our view, such a protocol can facilitate dissemination of this imaging techniques beyond academic institutions.

7.5.1 Limitations

We acknowledge that our study was based on a modest number of patients with stable CAD. Importantly, despite this limitation our findings are supported by statistically significant data. The normal limits applied to define an increase in TBR values in our population were based on those derived from 1h data; thus, it is likely that reference values for relevant uptake on 3h ^{18}F-NaF coronary PET will need to be derived for optimal use of delayed imaging (Joshi et al., 2014). The utilization of TBR as a measure of tracer uptake remains to some degree controversial (Chen & Dilsizian, 2015); however, we also evaluated corrected SUVmax measurements which have been suggested to be more robust for coronary imaging. The low TBR values in our study can be attributed to partial

volume effects as adjacent myocardium presents on average with 60% of the blood-pool uptake (Trivieri et al., 2016). We acknowledge that a 3h post injection PET protocol may lead to reorganizing the workflow within the nuclear medicine imaging facility and will prolong the time patients spend in the imaging facility. Nevertheless, the benefits of delayed PET acquisition for the assessment of ^{18}F-NaF coronary uptake undoubtedly outweigh the aforementioned workflow inconveniences.

Chapter 8. Conclusions and Future Directions

8.1 Summary of findings

Aortic stenosis is a disease of the valve and the myocardium. In the past years advanced cardiovascular imaging has greatly improved our understanding of the processes driving disease progression and enabled monitoring how the valve and the myocardium deteriorate over time. Both cardiovascular magnetic resonance and ^{18}F-sodium fluoride PET imaging showed promise in refining patients' diagnosis and providing early markers of disease progression. In this thesis I have demonstrated that in aortic stenosis asymmetric wall thickening is associated with adverse prognosis, I have shown that there are significant differences in the fibrosis burden between male and female patients and that the adverse remodeling of the ventricle can be reproduced in a simple animal model of pressure overload. Further I have demonstrated that utilizing a CT angiography acquired before the PET acquisition enables adequate ^{18}F-NaF uptake quantification and that delayed emission scanning facilitates image analysis.

8.1.1 Adverse Prognosis Associated with Asymmetric Myocardial Thickening in Aortic Stenosis.

Asymmetric wall thickening is most commonly associated with hypertrophic cardiomyopathy. However, this form of remodelling has recently been described in patients with increased afterload such as hypertension and aortic stenosis. An initial magnetic resonance study suggested that asymmetric wall thickening could be observed in around a quarter of aortic stenosis patients. In my multimodality imaging assessment of asymmetric wall thickening in 166 patients with aortic stenosis, I have demonstrated this pattern of remodeling is common, affecting a quarter of patients with mild-to-severe aortic stenosis when assessed using magnetic resonance. Echocardiography is less sensitive missing a third of these cases. Irrespective of the imaging modality used, patients with asymmetric wall thickening have evidence of more advanced left ventricular decompensation with elevated myocardial injury and increased BNP concentrations compared to those with concentric wall thickening. This is despite the two groups having similar co-morbidities, valve narrowing, myocardial fibrosis and left ventricular hypertrophy. Moreover, patients with asymmetric wall thickening (on both magnetic resonance and echocardiography) have an adverse prognosis, with this form of remodelling acting as an independent predictor of aortic valve replacement or death after correction for age, sex, left ventricular mass index, coronary artery disease and aortic stenosis severity. In the future further attention should be paid to the mechanism underlying asymmetric wall thickening formation, including the underlying genetics and the explanation for the associated adverse prognosis.

8.1.2 Progression and regression of left ventricular hypertrophy and myocardial fibrosis in a mouse model of pressure overload cardiomyopathy.

Rodent models of pressure overload cardiomyopathy have been developed and potentially allow monitoring of disease progression, from the onset of pressure overload out to the advanced stages of heart failure. These models can therefore provide longitudinal data that are lacking in humans and can potentially do so using advanced imaging techniques that can be directly translated in to humans. In a longitudinal preclinical study with serial cardiac magnetic resonance performed every 2 weeks in mice subjected to pressure overload and followed after cessation of the increased afterload I established an animal model of angiotensin II-induced left ventricular hypertrophy and subsequent reverse remodelling. This model allows to assess how the hypertrophic response and myocardial fibrosis develop in response to an increased afterload and then reverse remodels once that stimulus is removed. Using state-of-the-art *in vivo* CMR imaging, I have been able to obtain longitudinal data on myocardial remodelling within a timespan of months rather than years or decades as observed in humans. Importantly, the proposed model facilitates histological correlation with imaging findings, enabling validation of our CMR markers of fibrosis, including iECV, as biomarkers of left ventricular fibrosis. This model will allow improved understanding of the processes underlying LV decompensation in patients with aortic stenosis and hypertension. In this study I have demonstrated that myocardial fibrosis appears to be the primary determinant of LV dysfunction both before and after reversal of pressure overload. Further studies should investigate the optimum time to reverse pressure overload in order to ensure long-term preservation of left ventricular function.

8.1.3 Sex-Related Differences in the Extent of Myocardial Fibrosis in Patients with Aortic Valve Stenosis.

Cardiac magnetic resonance imaging detects the presence of replacement myocardial fibrosis using late gadolinium enhancement and diffuse reactive myocardial fibrosis using extracellular volume fraction calculated from T1 mapping. Both these surrogate measures of fibrosis correlate strongly with collagen content measured by histology. Recent studies have reported an association between LGE and ECV with worse outcomes in patients with aortic stenosis. In a multicenter prospective observational study of two hundred forty-nine patients with at least mild aortic stenosis I demonstrated that despite similar AS severity and LV global hemodynamic load as well as more favorable cardiovascular risk profile, women presented lower indexed LV mass but paradoxically a larger extent of diffuse myocardial fibrosis. While LV mass index was the strongest determinant for both higher ECV fraction and higher amount of LGE, in the present study, traditional cardiovascular risk factors such as hypertension and coronary artery disease were not independently associated with diffuse or focal myocardial fibrosis. This lack of association between hypertension and the surrogate CMR markers of fibrosis could be related to the fact that the vast majority of patients in the study with diagnosis of hypertension were treated with anti-hypertensive medications. After comprehensive multivariable analyses, female sex remained an important independent determinant of higher ECV fraction and LGE. Noteworthy, the greater expansion of ECV fraction observed in women was also accompanied by higher estimated LV filling pressure (E/e' ratio), which may be related to reduced LV compliance and more advanced LV diastolic dysfunction in women. Future studies should elucidate the underlying mechanisms for sex difference in LV remodeling and fibrosis.

8.1.4 Feasibility of coronary ^{18}F-sodium fluoride PET assessment with the utilization of previously acquired CT angiography.

^{18}F-NaF PET imaging has shown hope as a tool for predicting valve calcifications. For precise anatomical localization of ^{18}F-NaF uptake within the heart, this imaging modality requires co-registered CT angiography images. To date studies utilized CT angiography acquired using hybrid PET/CT scanners during the same imaging session. This approach has several limitations which hamper its practical implementation into a meaningful clinical workflow. For instance, an important limitation of the single-session hybrid PET/CT is that it may not allow for the use of optimal CT equipment for CT angiography which may only be available on standalone CT scanners. In a multivendor and multicenter study of 45 patients I report how utilizing a previously acquired CTA with a subsequent standalone PET-only scan can be used for the evaluation of ^{18}F-NaF PET uptake. On a population comprised of patients who underwent repeat CT angiography studies on the same PET/CT scanner and a separate subset that had the initial CTA acquired on a solely CT machine, I showed that a prior CT angiography and subsequent PET-only approach enables accurate quantification of ^{18}F-NaF PET uptake. This prior CT angiography and subsequent PET-only acquisition protocol lends itself to a practical clinical workflow, with the initial CT angiography providing a basis for selection of patient for the PET study. CT angiography is growing rapidly in a wide variety of clinical settings. It will likely be the most common basis for selection of patients who might benefit from assessment of disease activity with PET imaging. In this scenario, the requirement for a second CT angiography obtained at the time of PET imaging would not be practical or economically feasible and would incur unnecessary additional radiation exposure. Additionally, CT angiography scans acquired on hybrid PET/CT are often of suboptimal quality due to limited CT performance in this configuration. In many PET laboratories,

either the PET scanner does not have performance characteristics required for CT angiography, or a standalone CT scanner with better imaging characteristics for CT angiography is available. Further, the scanning protocol for hybrid PET/CT requires technical staff with expertise in both PET and CT angiography to be present during a single session. In many centers that offer both PET and CT angiography scans, the imaging team performing PET studies does not have extensive experience in CT angiography. Thus, separate technologists with CT angiography expertise might be required to perform the CT angiography portion of the PET/CT examination, raising the cost and complexity of the procedure. With the utilization of CT angiography obtained prior to the ^{18}F-NaF PET, such inconvenience would no longer occur.

8.1.5 Three-hour delayed imaging improves assessment of coronary ^{18}F-sodium fluoride PET.

As ^{18}F-sodium fluoride imaging is still in its infancy, several technical aspects remain to be addressed. One of these is the optimal timing for emission scanning. In the 1970s when ^{18}F-NaF was first used for bone scanning, it was suggested that the optimal scanning time for ^{18}F-NaF is 2-4 hours post injection. Nevertheless, whole-body ^{18}F-NaF PET is nowadays performed with imaging commencing 60 minutes after injection. In cardiovascular PET, in most studies to date assessing ^{18}F-NaF uptake in the cardiovascular system, acquisition was performed 1-hour (1h) after tracer administration. Up to date only one study looked at the optimal timing for cardiovascular ^{18}F-NaF imaging, but performed the ungated low-count PET acquisition measuring overall uptake in the entire heart rather than uptake localized to single foci of microcalfication. On a cohort of twenty patients with stable coronary artery disease who underwent PET/CT imaging both 1 h and 3 h after the injection of ^{18}F-NaF I demonstrate that prolonging the time from tracer injection to PET acquisition can facilitate image analysis. In the study, I show that delaying ^{18}F-NaF coronary image acquisition further facilitates assessment of coronary uptake, predominantly as a result of a decrease in the background blood pool activity. The improved visual identification of the lesions on the delayed ^{18}F-NaF PET acquisitions is accompanied by significant improvements in TBR and corrected SUVmax measurements. While I observed an increase in the noise on delayed imaging (as expected due to a lower count statistic), because of the favorable decrease in the background (blood pool) activity, the noise level on 3h PET did not impede image analysis.

8.2 Future Directions

Cardiovascular magnetic resonance imaging has provided a wealth of information regarding left ventricular reverse remodeling in aortic stenosis. The observations regarding the impact of fibrosis on disease progression and asymmetric wall thickening on outcome can potentially enable personalized decision making in this most common form of valve disease. However, before the non-invasive markers of left ventricular decompensation can be incorporated into clinical practice they should be formally validated in the context of multicenter randomized clinical trials. The currently ongoing Early Valve Replacement Guided by Biomarkers of LV Decompensation in Asymptomatic Patients With Severe AS (EVoLVeD, NCT03094143) study shall address this need. It will challenge the current clinical guidelines suggesting that aortic valve replacement should be performed only when symptoms develop or the heart presents with an impaired systolic function on echocardiography. Using cardiovascular magnetic resonance imaging the investigators shall actively search for early markers of decompensation including replacement fibrosis. Patients with such form of myocardial scarring will be randomised to routine clinical care, or referral for valve replacement surgery. The overarching hypothesis of the study is that early surgery will lead to fewer complications and reduced risk of death compared to standard care. The evolved trial aims to recruit 1000 participants and shall therefore provide a unique dataset for assessing gender differences in aortic stenosis. It will enable determining whether the larger expansion of diffuse myocardial fibrosis in women as measured by cardiovascular magnetic resonance could be a potential trigger for early valve replacement in women with severe aortic stenosis.

While in this thesis I provided a CT followed by PET workflow which enables maximizing the benefits of CT imaging and showed that delayed imaging is beneficial in terms of

image quality, several aspects regarding cardiovascular ^{18}F-NaF PET remain to be addressed. Cardiorespiratory and patient body motion create serious limitations to imaging cardiovascular microcalcifications with PET. Natural tidal breathing can cause the heart to move over 1 cm, normal heart systolic function can lead to motion up to 26 mm depending on the location. Additionally, typical gross patient motion (repositioning during emission scanning) can also result in a loss in the contrast to noise ratio. These joint motion effects need to be compensated for and to date only cardiac contractility has been addressed. Future research should aim to develop techniques correcting for tidal breathing and patient repositioning. Another aspect of ^{18}F-NaF cardiovascular PET which requires refinement is CT and PET co-registration which is essential for image analysis but requires a certain level of expertise and is time consuming. Automatization of this process would facilitate dissemination of this imaging modality. While in my thesis I have shown that 3-hour delayed emission scanning is beneficial the optimal timing for imaging remains to be comprehensively assessed. At the moment it is unclear whether a 2-hour delay would be equally robust. Likewise, potentially a longer interval between tracer injection and imaging could further facilitate uptake assessment.

In aortic stenosis ^{18}F-NaF has already been shown to predict disease progression in native and surgical bioprosthetic valves. Given the successful application of ^{18}F-NaF PET for early diagnosis of structural valve degeneration in patients post-surgical valve replacement translating this approach for TAVR imaging appears as the ultimate frontier for ^{18}F-NaF cardiovascular PET imaging. While a combined CT angiography and ^{18}F-NaF PET appear to be ideally suited for this purpose, imaging TAVR presents unique challenges. After TAVR deployment, leaflets of the native valve are displaced against the aortic wall making it difficult to discern PET tracer uptake within the implanted bioprosthesis from the native valve. Similarly, distinguishing TAVR calcifications from

stent struts and native valve calcium with non-contrast CT is impossible and requires high quality CT angiography.

Future studies should aim to further optimize ^{18}F-NaF imaging specifically for TAVR imaging. Two areas appear particularly relevant in this regard. Firstly, for anatomical reference and detection of overt prosthesis degeneration high quality CT angiography is required. While (according to the conventional protocol) ^{18}F-NaF and CT angiography are acquired during a single imaging session on a hybrid PET/CT scanner such an approach has several limitations. It may not allow for the use of optimal CT equipment (which may only be available on standalone CT scanners) and requires multi-faceted staff expertise in both PET and cardiac CT during a single session. As shown in chapter 6 of this thesis utilization of a previously acquired CT with a subsequent PET-only cardiac ^{18}F-NaF acquisition enables adequate categorization of coronary plaques with respect to the presence of increased tracer activity and accurate quantification of PET uptake (Kwiecinski et al., 2018). This CT first approach could be an important protocol refinement for ^{18}F-NaF TAVR imaging. Secondly, for precise evaluation of ^{18}F-NaF uptake a high contrast to noise ratio is of critical importance. For coronary imaging I have recently shown (chapter 7) that a greater interval between tracer injection and image acquisition facilitates images analysis (Kwiecinski et al., 2019). Delayed imaging leads to a decrease in the background bloodpool activity and therefore enables distinction of subtle ^{18}F-NaF uptake which on conventional 1-h post injection imaging can be difficult to discern from background signal. Given the proximity of the native valve to the bioprothesis and the overall only subtle PET tracer activity in the leaflets (as reported for surgical valves) delayed imaging is expected to considerably facilitate image analysis.

8.3 Clinical perspectives

The cardiovascular magnetic resonance based stratification of risk in severe aortic stenosis holds hope in offering timely aortic valve replacement. If the hypotheses of this thesis are successfully tested in the context of the Evolved trial ultimately important modifications in managing aortic valve stenosis would be mandated. A fibrosis burden guided referral for valve replacement as well as a gender specific approach in aortic stenosis could be an important step on the path to individualized medicine.

Whether ^{18}F-sodium fluoride PET becomes the holy grail of coronary artery disease and aortic stenosis remains to be assessed. With several ongoing trials utilizing this promising imaging approach in the following years we shall learn its true potential. The PREFFIR (Prediction of Recurrent Events With ^{18}F-Fluoride) and DIAMOND (Dual Antiplatelet Therapy to Reduce Myocardial Injury) trials will provide key insights in the field of coronary artery disease. The SALTIRE-2 (Study Investigating the Effect of Drugs Used to Treat Osteoporosis on the Progression of Calcific Aortic Stenosis) and FAABULOUS (^{18}F-Fluoride Assessment of Aortic Bioprosthesis Durability and Outcome) shall elucidate the role ^{18}F-NaF imaging could play in the assessment of native and bioprosthetic aortic valves.

Chapter 9. Bibliography and additional publications

9.1 List of publications

1. **Jacek Kwiecinski**, Calvin W L Chin, Russell J Everett, Audrey C White, Scott Semple, Emily Yeung, William J Jenkins, Anoop S V Shah, Maria Koo, Saeed Mirsadraee, Chim C Lang, Nicholas Mills, Sanjay K Prasad, Maurits A Jansen, Alan G Japp, David E Newby, Marc R Dweck; Adverse prognosis associated with asymmetric myocardial thickening in aortic stenosis, **European Heart Journal - Cardiovascular Imaging**, Volume 19, Issue 3, 1 March 2018, Pages 347–356
2. **Jacek Kwiecinski**, Daniel S. Berman, Sang-Eun Lee, Damini Dey, Sebastien Cadet, Martin L Lassen, Guido Germano, Maurits A Jansen, Marc R Dweck, David E Newby, Hyuk-Jae Chang, Mijin Yun, Piotr Slomka Three-hour delayed imaging improves assessment of coronary 18F-sodium fluoride PET. **Journal Nuclear Medicine** jnumed.118.217885 published ahead of print September 13, 2018
3. **Jacek Kwiecinski**, Philip D. Adamson, Martin L. Lassen, Mhairi K. Doris, Alastair J. Moss, Sebastian Cadet, Maurits A. Jansen, Damini Dey, Sang-Eun Lee, Mijin Yun, Hyuk-Jae Chang, Marc R. Dweck, David E. Newby, Daniel S. Berman, Piotr J. Slomka, Feasibility of Coronary 18F-Sodium Fluoride Positron-Emission Tomography Assessment With the Utilization of Previously Acquired Computed Tomography Angiography. **Circ Cardiovasc Imaging**. 2018 Dec; 11(12): e008325
4. **Jacek Kwiecinski**, Damini Dey, Sebastien Cadet, Sang-Eun Lee, Yuka Otaki, Phi T. Huynh, Mhairi K. Doris, Evann Eisenberg, Mijin Yun, Maurits A. Jansen, Michelle C. Williams, Balaji K. Tamarappoo, John D. Friedman, Marc R. Dweck, David E. Newby, Hyuk-Jae Chang, Piotr J. Slomka, Daniel S. Berman. Peri-Coronary Adipose Tissue Density Is Associated With 18F-Sodium Fluoride Coronary Uptake in Stable Patients With High-Risk Plaques. **JACC Cardiovascular Imaging** 2019 published ahead of print February 13, 2019
5. **Jacek Kwiecinski**, Yoon Jae Lee, Piotr J Slomka. Selection of abstracts from the scientific sessions of the Society of Nuclear Medicine and Molecular Imaging, Philadelphia PA June 23-26, 2018. **J Nucl Cardiol**. 2018 Dec;25(6):2168-2171
6. Martin Lyngby Lassen*, **Jacek Kwiecinski***, Piotr J. Slomka. Gating Approaches in Cardiac PET Imaging. **PET Clinics** 2019 in press
7. Marc R. Dweck, **Jacek Kwiecinski**. Emerging Sex Differences in Aortic Stenosis. **JACC Cardiovasc Imaging**. 2019 Jan;12(1):106-108..

8. Martin L. Lassen, **Jacek Kwiecinski**, Sebastien Cadet, Damini Dey, Wang C, Marc Dweck, Daniel Berman, Guido Germano , David Newby, Piotr J Slomka. Data-driven gross patient motion detection and compensation: implications for coronary 18F-NaF PET imaging. **Journal Nuclear Medicine** 2018 [published online ahead of print November 15, 2018]

9. Michael Olymbios, **Jacek Kwiecinski**, Daniel S. Berman, John A. Kobashigawa. Imaging in Heart Transplant Patients. **JACC Cardiovasc Imaging**. 2018 Oct;11(10):1514-1530.

10. Calvin W.L. Chin, Russell J. Everett, **Jacek Kwiecinski**, Alex T. Vesey, Emily Yeung, Gavin Esson, William Jenkins, Maria Koo, Saeed Mirsadraee, Audrey C. White, Alan G. Japp, Sanjay K. Prasad, Scott Semple, David E. Newby, Marc R. Dweck, Myocardial Fibrosis and Cardiac Decompensation in Aortic Stenosis. **JACC Cardiovasc Imaging**. 2017 Nov;10(11):1320-1333

11. Mhairi K. Doris, Yuka Otaki, Sandeep K. Krishnan, **Jacek Kwiecinski**, Mathieu Rubeaux, Adam Alessio, Tinsu Pan, Sebastien Cadet, Damini Dey, Marc R. Dweck, David E. Newby, Daniel S. Berman, Piotr J. Slomka. Optimization of reconstruction and quantification of motion-corrected coronary PET-CT. **J. Nucl. Cardiol.** (2018) June 11

12. Daniel Massera, Mhairi K. Doris, Sebastien Cadet, **Jacek Kwiecinski**, Tania A. Pawade, Frederique E. C. M. Peeters, Damini Dey, David E. Newby, Marc R. Dweck, Piotr J. Slomka. Analytical quantification of aortic valve 18F-sodium fluoride PET uptake. **J. Nucl. Cardiol.** (2018) November 29

13. Atul Anand, Calvin Chin, Anoop S V Shah, **Jacek Kwiecinski**, Alex Vesey, Joanna Cowell, Ekkehard Weber, Thomas Kaier, David E Newby, Marc Dweck, Michael S Marber, Nicholas L Mills. Cardiac myosin-binding protein C is a novel marker of myocardial injury and fibrosis in aortic stenosis. **Heart**. 2018 Jul; 104(13): 1101–1108

14. Russell J. Everett, Lionel Tastet, Marie-Annick Clavel, Calvin W.L. Chin, Romain Capoulade, Vassilios S. Vassiliou, **Jacek Kwiecinski**, Miquel Gomez, Edwin J.R. van Beek, Audrey C. White, Sanjay K. Prasad, Eric Larose, Christopher Tuck, Scott Semple, David E. Newby, Philippe Pibarot, Marc R. Dweck. Progression of Hypertrophy and Myocardial Fibrosis in Aortic Stenosis - A Multicenter Cardiac Magnetic Resonance Study. **Circ Cardiovasc Imaging.** 2018 Jun;11(6):e007451

Chapters 4 and 5 were under review at the time of thesis submission.

References

Adabag, A. S., Maron, B. J., Appelbaum, E., Harrigan, C. J., Buros, J. L., Gibson, C. M., . . . Maron, M. S. (2008). Occurrence and Frequency of Arrhythmias in Hypertrophic Cardiomyopathy in Relation to Delayed Enhancement on Cardiovascular Magnetic Resonance. *Journal of the American College of Cardiology, 51*(14), 1369-1374. doi:https://doi.org/10.1016/j.jacc.2007.11.071

Adamson, P. D., Vesey, A. T., Joshi, N. V., Newby, D. E., & Dweck, M. R. (2015). Salt in the wound: (18)F-fluoride positron emission tomography for identification of vulnerable coronary plaques. *Cardiovascular diagnosis and therapy, 5*(2), 150-155. doi:10.3978/j.issn.2223-3652.2015.03.01

Agatston, A. S., Janowitz, W. R., Hildner, F. J., Zusmer, N. R., Viamonte, M., & Detrano, R. (1990). QUANTIFICATION OF CORONARY-ARTERY CALCIUM USING ULTRAFAST COMPUTED-TOMOGRAPHY. *Journal of the American College of Cardiology, 15*(4), 827-832. doi:10.1016/0735-1097(90)90282-t

Aggarwal, S. R., Clavel, M. A., Messika-Zeitoun, D., Cueff, C., Malouf, J., Araoz, P. A., . . . Enriquez-Sarano, M. (2013). Sex Differences in Aortic Valve Calcification Measured by Multidetector Computed Tomography in Aortic Stenosis. *Circulation-Cardiovascular Imaging, 6*(1), 40-47. doi:10.1161/circimaging.112.980052

Alavi, A., Werner, T. J., & Høilund-Carlsen, P. F. (2017). What can be and what cannot be accomplished with PET to detect and characterize atherosclerotic plaques. *Journal of Nuclear Cardiology*. doi:10.1007/s12350-017-0977-x

AlJaroudi, W., Alraies, M. C., Hachamovitch, R., Jaber, W. A., Brunken, R., Cerqueira, M. D., & Marwick, T. (2012). Association of left ventricular mechanical dyssynchrony with survival benefit from revascularization: a study of gated positron emission tomography in patients with ischemic LV dysfunction and narrow QRS. *European Journal of Nuclear Medicine and Molecular Imaging, 39*(10), 1581-1591. doi:10.1007/s00259-012-2171-3

Ambale-Venkatesh, B., & Lima, J. A. C. (2014). Cardiac MRI: a central prognostic tool in myocardial fibrosis. *Nature Reviews Cardiology, 12*, 18. doi:10.1038/nrcardio.2014.159 https://www.nature.com/articles/nrcardio.2014.159#supplementary-information

Antonini-Canterin, F., Huang, G. Q., Cervesato, E., Faggiano, P., Pavan, D., Piazza, R., & Nicolosi, G. L. (2003). Symptomatic aortic stenosis - Does systemic hypertension play an additional role? *Hypertension, 41*(6), 1268-1272. doi:10.1161/01.hyp.0000070029.30058.59

Armstrong, I. S., Tonge, C. M., & Arumugam, P. (2014). Impact of point spread function modeling and time-of-flight on myocardial blood flow and myocardial flow reserve measurements for rubidium-82 cardiac PET. *Journal of Nuclear Cardiology, 21*(3), 467-474. doi:10.1007/s12350-014-9858-8

Assomull, R. G., Prasad, S. K., Lyne, J., Smith, G., Burman, E. D., Khan, M., . . . Pennell, D. J. (2006). Cardiovascular Magnetic Resonance, Fibrosis, and Prognosis in Dilated Cardiomyopathy. *Journal of the American College of Cardiology, 48*(10), 1977-1985. doi:https://doi.org/10.1016/j.jacc.2006.07.049

Attias, D., Macron, L., Dreyfus, J., Monin, J.-L., Brochet, E., Lepage, L., . . . Messika-Zeitoun, D. (2013). Relationship between Longitudinal Strain and Symptomatic Status in Aortic

Stenosis. *Journal of the American Society of Echocardiography, 26*(8), 868-874. doi:10.1016/j.echo.2013.05.004

Aurigemma, G. P., & Gaasch, W. H. (1995). GENDER DIFFERENCES IN OLDER PATIENTS WITH PRESSURE-OVERLOAD HYPERTROPHY OF THE LEFT-VENTRICLE. *Cardiology, 86*(4), 310-317. doi:10.1159/000176895

Azevedo, C. F., Nigri, M., Higuchi, M. L., Pomerantzeff, P. M., Spina, G. S., Sampaio, R. O., . . . Rochitte, C. E. (2010). Prognostic Significance of Myocardial Fibrosis Quantification by Histopathology and Magnetic Resonance Imaging in Patients With Severe Aortic Valve Disease. *Journal of the American College of Cardiology, 56*(4), 278-287. doi:10.1016/j.jacc.2009.12.074

Barone-Rochette, G., Pierard, S., de Ravenstein, C. D., Seldrum, S., Melchior, J., Maes, F., . . . Gerber, B. L. (2014). Prognostic Significance of LGE by CMR in Aortic Stenosis Patients Undergoing Valve Replacement. *Journal of the American College of Cardiology, 64*(2), 144-154. doi:10.1016/j.jacc.2014.02.612

Baumgartner, H., Falk, V., Bax, J. J., De Bonis, M., Hamm, C., Holm, P. J., . . . Group, E. S. C. S. D. (2017). 2017 ESC/EACTS Guidelines for the management of valvular heart disease. *European Heart Journal, 38*(36), 2739-2791. doi:10.1093/eurheartj/ehx391

Baumgartner, H., Hung, J., Bermejo, J., Chambers, J. B., Evangelista, A., Griffin, B. P., . . . Quiñones, M. (2009). Echocardiographic Assessment of Valve Stenosis: EAE/ASE Recommendations for Clinical Practice. *Journal of the American Society of Echocardiography, 22*(1), 1-23. doi:10.1016/j.echo.2008.11.029

Beheshti, M., Saboury, B., Mehta, N. N., Torigian, D. A., Werner, T., Mohler, E., . . . Alavi, A. (2011). Detection and global quantification of cardiovascular molecular calcification by fluoro-18-fluoride positron emission tomography/computed tomography-A novel concept. *Hellenic Journal of Nuclear Medicine, 14*(2), 114-120.

Bellinge, J. W., Francis, R. J., Majeed, K., Watts, G. F., & Schultz, C. J. (2018). In search of the vulnerable patient or the vulnerable plaque: 18F-sodium fluoride positron emission tomography for cardiovascular risk stratification. *Journal of Nuclear Cardiology, 25*(5), 1774-1783. doi:10.1007/s12350-018-1360-2

Beyer, T., Lassen, M. L., Boellaard, R., Delso, G., Yaqub, M., Sattler, B., & Quick, H. H. (2016). Investigating the state-of-the-art in whole-body MR-based attenuation correction: an intra-individual, inter-system, inventory study on three clinical PET/MR systems. *Magnetic Resonance Materials in Physics Biology and Medicine, 29*(1), 75-87. doi:10.1007/s10334-015-0505-4

Bjørnstad, J. L., Skrbic, B., Sjaastad, I., Bjørnstad, S., Christensen, G., & Tønnessen, T. (2012). A mouse model of reverse cardiac remodelling following banding-debanding of the ascending aorta. *Acta Physiologica, 205*(1), 92-102. doi:10.1111/j.1748-1716.2011.02369.x

Blankstein, R., Osborne, M., Naya, M., Waller, A., Kim, C. K., Murthy, V. L., . . . Di Carli, M. F. (2014). Cardiac Positron Emission Tomography Enhances Prognostic Assessments of Patients With Suspected Cardiac Sarcoidosis. *Journal of the American College of Cardiology, 63*(4), 329-336. doi:10.1016/j.jacc.2013.09.022

Blau, M., Ganatra, R., & Bender, M. A. (1972). 18F-fluoride for bone imaging. *Seminars in Nuclear Medicine, 2*(1), 31-37. doi:https://doi.org/10.1016/S0001-2998(72)80005-9

Blau, M., Nagler, W., & Bender, M. A. (1962). FLUORINE-18 - A NEW ISOTOPE FOR BONE SCANNING. *Journal of Nuclear Medicine, 3*(4), 332-334.

Blomberg, B. A., Thomassen, A., de Jong, P. A., Simonsen, J. A., Lam, M., Nielsen, A. L., . . . Hoilund-Carlsen, P. F. (2015). Impact of Personal Characteristics and Technical Factors

on Quantification of Sodium F-18-Fluoride Uptake in Human Arteries: Prospective Evaluation of Healthy Subjects. *Journal of Nuclear Medicine, 56*(10), 1534-1540. doi:10.2967/jnumed.115.159798

Blomberg, B. A., Thomassen, A., Takx, R. A. P., Vilstrup, M. H., Hess, S., Nielsen, A. L., . . . Høilund-Carlsen, P. F. (2014). Delayed sodium 18F-fluoride PET/CT imaging does not improve quantification of vascular calcification metabolism: Results from the CAMONA study. *Journal of Nuclear Cardiology, 21*(2), 293-304. doi:10.1007/s12350-013-9829-5

Boellaard, R., Krak, N. C., Hoekstra, O. S., & Lammertsma, A. A. (2004). Effects of noise, image resolution, and ROI definition on the accuracy of standard uptake values: A simulation study. *Journal of Nuclear Medicine, 45*(9), 1519-1527.

Braunwald, E. (1990). On the natural history of severe aortic stenosis. *Journal of the American College of Cardiology, 15*(5), 1018-1020. doi:https://doi.org/10.1016/0735-1097(90)90235-H

Brown, J. M., O'Brien, S. M., Wu, C., Sikora, J. A. H., Griffith, B. P., & Gammie, J. S. (2009). Isolated aortic valve replacement in North America comprising 108,687 patients in 10 years: Changes in risks, valve types, and outcomes in the Society of Thoracic Surgeons National Database. *Journal of Thoracic and Cardiovascular Surgery, 137*(1), 82-90. doi:10.1016/j.jtcvs.2008.08.015

Brown, T. L. Y., Merrill, J., Volokh, L., & Bengel, F. M. (2008). Determinants of the response of left ventricular ejection fraction to vasodilator stress in electrocardiographically gated (82)rubidium myocardial perfusion PET. *European Journal of Nuclear Medicine and Molecular Imaging, 35*(2), 336-342. doi:10.1007/s00259-007-0603-2

Bucerius, J., Mani, V., Moncrieff, C., Machac, J., Fuster, V., Farkouh, M. E., . . . Fayad, Z. A. (2014). Optimizing 18F-FDG PET/CT imaging of vessel wall inflammation: the impact of 18F-FDG circulation time, injected dose, uptake parameters, and fasting blood glucose levels. *European Journal of Nuclear Medicine and Molecular Imaging, 41*(2), 369-383. doi:10.1007/s00259-013-2569-6

Bull, S., White, S. K., Piechnik, S. K., Flett, A. S., Ferreira, V. M., Loudon, M., . . . Myerson, S. G. (2013). Human non-contrast T1 values and correlation with histology in diffuse fibrosis. *Heart, 99*(13), 932-937. doi:10.1136/heartjnl-2012-303052

Bundschuh, R. A., Martinez-Moeller, A., Essler, M., Martinez, M. J., Nekolla, S. G., Ziegler, S. I., & Schwaiger, M. (2007). Postacquisition detection of tumor motion in the lung and upper abdomen using list-mode PET data: A feasibility study. *Journal of Nuclear Medicine, 48*(5), 758-763. doi:10.2967/jnumed.106.035279

Burchfield, J. S., Xie, M., & Hill, J. A. (2013). Pathological ventricular remodeling: mechanisms: part 1 of 2. *Circulation, 128*(4), 388-400. doi:10.1161/CIRCULATIONAHA.113.001878

Buther, F., Dawood, M., Stegger, L., Wubbeling, F., Schafers, M., Schober, O., & Schafers, K. P. (2009). List Mode-Driven Cardiac and Respiratory Gating in PET. *Journal of Nuclear Medicine, 50*(5), 674-681. doi:10.2967/jnumed.108.059204

Buther, F., Ernst, I., Dawood, M., Kraxner, P., Schafers, M., Schober, O., & Schafers, K. P. (2010). Detection of respiratory tumour motion using intrinsic list mode-driven gating in positron emission tomography. *European Journal of Nuclear Medicine and Molecular Imaging, 37*(12), 2315-2327. doi:10.1007/s00259-010-1533-y

Cal-Gonzalez, J., Li, X., Heber, D., Rausch, I., Moore, S. C., Schäfers, K., . . . Beyer, T. (2018). Partial volume correction for improved PET quantification in 18F-NaF imaging of atherosclerotic plaques. *Journal of Nuclear Cardiology, 25*(5), 1742-1756. doi:10.1007/s12350-017-0778-2

Cal-Gonzalez, J., Rausch, I., Sundar, L. K. S., Lassen, M. L., Muzik, O., Moser, E., . . . Beyer, T. (2018). Hybrid Imaging: Instrumentation and Data Processing. *Frontiers in Physics, 6*. doi:10.3389/fphy.2018.00047

Camacho, P., Fan, H. M., Liu, Z. M., & He, J. Q. (2016). Small mammalian animal models of heart disease. *American Journal of Cardiovascular Disease, 6*(3), 70-80.

Caoduro, C., Porot, C., Vuitton, D. A., Bresson-Hadni, S., Grenouillet, F., Richou, C., . . . Blagosklonov, O. (2013). The Role of Delayed F-18-FDG PET Imaging in the Follow-up of Patients with Alveolar Echinococcosis. *Journal of Nuclear Medicine, 54*(3), 358-363. doi:10.2967/jnumed.112.109942

Capoulade, R., Clavel, M. A., Le Ven, F., Dahou, A., Thebault, C., Tastet, L., . . . Pibarot, P. (2017). Impact of left ventricular remodelling patterns on outcomes in patients with aortic stenosis. *European Heart Journal-Cardiovascular Imaging, 18*(12), 1378-1387. doi:10.1093/ehjci/jew288

Capoulade, R., Mahmut, A., Tastet, L., Arsenault, M., Bédard, É., Dumesnil, J. G., . . . Pibarot, P. (2015). Impact of Plasma Lp-PLA2 Activity on the Progression of Aortic Stenosis: The PROGRESSA Study. *JACC: Cardiovascular Imaging, 8*(1), 26-33. doi:https://doi.org/10.1016/j.jcmg.2014.09.016

Carabello, B. A. (2002). Aortic stenosis. *New England Journal of Medicine, 346*(9), 677-682. doi:10.1056/NEJMcp010846

Carabello, B. A. (2013). The Symptoms of Aortic Stenosis. *A Step Closer to Understanding Their Cause, 6*(2), 147-149. doi:10.1016/j.jcmg.2012.12.002

Carabello Blase, A. (2013). Introduction to Aortic Stenosis. *Circulation Research, 113*(2), 179-185. doi:10.1161/CIRCRESAHA.113.300156

Carroll, J. D., Carroll, E. P., Feldman, T., Ward, D. M., Lang, R. M., McGaughey, D., & Karp, R. B. (1992). SEX-ASSOCIATED DIFFERENCES IN LEFT-VENTRICULAR FUNCTION IN AORTIC-STENOSIS OF THE ELDERLY. *Circulation, 86*(4), 1099-1107. doi:10.1161/01.cir.86.4.1099

Cerqueira, M. D., Weissman, N. J., Dilsizian, V., Jacobs, A. K., Kaul, S., Laskey, W. K., . . . Verani, M. S. (2002). Standardized Myocardial Segmentation and Nomenclature for Tomographic Imaging of the Heart. *Circulation, 105*(4), 539-542. doi:doi:10.1161/hc0402.102975

Chambers, J. B., Myerson, S. G., Rajani, R., Morgan-Hughes, G. J., Dweck, M. R., & British Heart Valve, S. (2016). Multimodality imaging in heart valve disease. *Open Heart, 3*(1). doi:10.1136/openhrt-2015-000330

Chander, A., Brenner, M., Lautamaki, R., Voicu, C., Merrill, J., & Bengel, F. M. (2008). Comparison of Measures of Left Ventricular Function from Electrocardiographically Gated (82)Rb PET with Contrast-Enhanced CT Ventriculography: A Hybrid PET/CT Analysis. *Journal of Nuclear Medicine, 49*(10), 1643-1650. doi:10.2967/jnumed.108.053819

Chen, W. G., & Dilsizian, V. (2015). PET Assessment of Vascular Inflammation and Atherosclerotic Plaques: SUV or TBR? *Journal of Nuclear Medicine, 56*(4), 503-504. doi:10.2967/jnumed.115.154385

Cheng, G., Torigian, D., Zhuang, H. M., & Alavi, A. (2013). When should we recommend use of dual time-point and delayed time-point imaging techniques in FDG PET? *European Journal of Nuclear Medicine and Molecular Imaging, 40*(5), 779-787. doi:10.1007/s00259-013-2343-9

Chesler, D. A. (1971). 3-DIMENSIONAL ACTIVITY DISTRIBUTION FROM MULTIPLE POSITRON SCINTIGRAPHS. *Journal of Nuclear Medicine, 12*(6), 347-&.

Chin, C. W. L., Everett, R. J., Kwiecinski, J., Vesey, A. T., Yeung, E., Esson, G., . . . Dweck, M. R. (2017). Myocardial Fibrosis and Cardiac Decompensation in Aortic Stenosis. *Jacc-Cardiovascular Imaging, 10*(11), 1320-1333. doi:10.1016/j.jcmg.2016.10.007

Chin, C. W. L., Messika-Zeitoun, D., Shah, A. S. V., Lefevre, G., Bailleul, S., Yeung, E. N. W., . . . Dweck, M. R. (2016). A clinical risk score of myocardial fibrosis predicts adverse outcomes in aortic stenosis. *European Heart Journal, 37*(8), 713-723. doi:10.1093/eurheartj/ehv525

Chin, C. W. L., Semple, S., Malley, T., White, A. C., Mirsadraee, S., Weale, P. J., . . . Dweck, M. R. (2014). Optimization and comparison of myocardial T1 techniques at 3T in patients with aortic stenosis. *European Heart Journal-Cardiovascular Imaging, 15*(5), 556-565. doi:10.1093/ehjci/jet245

Chin, C. W. L., Shah, A. S. V., McAllister, D. A., Cowell, S. J., Alam, S., Langrish, J. P., . . . Dweck, M. R. (2014). High-sensitivity troponin I concentrations are a marker of an advanced hypertrophic response and adverse outcomes in patients with aortic stenosis. *European Heart Journal, 35*(34), 2312-2321. doi:10.1093/eurheartj/ehu189

Chin, C. W. L., Vassiliou, V., Jenkins, W. S. A., Prasad, S. K., Newby, D. E., & Dweck, M. R. (2014). Markers of left ventricular decompensation in aortic stenosis. *Expert Review of Cardiovascular Therapy, 12*(7), 901-912. doi:10.1586/14779072.2014.923307

Chizner, M. A., Pearle, D. L., & deLeon, A. C. (1980). The natural history of aortic stenosis in adults. *American Heart Journal, 99*(4), 419-424. doi:https://doi.org/10.1016/0002-8703(80)90375-0

Cho, J. S., Cho, E. J., Lee, J., Choi, H.-D., Park, K. C., Lee, K.-H., . . . Kim, C. J. (2014). Myocardial mechanics in a rat model with banding and debanding of the ascending aorta. *Journal of cardiovascular ultrasound, 22*(4), 189-195. doi:10.4250/jcu.2014.22.4.189

Cioffi, G., Faggiano, P., Vizzardi, E., Tarantini, L., Cramariuc, D., Gerdts, E., & de Simone, G. (2011). Prognostic effect of inappropriately high left ventricular mass in asymptomatic severe aortic stenosis. *Heart, 97*(4), 301-307. doi:10.1136/hrt.2010.192997

Cioffi, G., Mazzone, C., Faggiano, P., Tarantini, L., Di Lenarda, A., Russo, T. E., . . . Furlanello, F. (2013). Prognostic Stratification by Conventional Echocardiography of Patients with Aortic Stenosis: The "CAIMAN-ECHO Score". *Echocardiography-a Journal of Cardiovascular Ultrasound and Allied Techniques, 30*(4), 367-377. doi:10.1111/echo.12065

Cioffi, G., & Stefenelli, C. (2002). Comparison of left ventricular geometry and left atrial size and function in patients with aortic stenosis versus those with pure aortic regurgitation. *American Journal of Cardiology, 90*(6), 601-606. doi:10.1016/s0002-9149(02)02563-8

Clavel, M. A., Malouf, J., Michelena, H. I., Suri, R. M., Jaffe, A. S., Mahoney, D. W., & Enriquez-Sarano, M. (2014). B-Type Natriuretic Peptide Clinical Activation in Aortic Stenosis. *Journal of the American College of Cardiology, 63*(19), 2016-2025. doi:10.1016/j.jacc.2014.02.581

Clavel, M. A., Messika-Zeitoun, D., Pibarot, P., Aggarwal, S. R., Malouf, J., Araoz, P. A., . . . Enriquez-Sarano, M. (2013). The Complex Nature of Discordant Severe Calcified Aortic Valve Disease Grading New Insights From Combined Doppler Echocardiographic and Computed Tomographic Study. *Journal of the American College of Cardiology, 62*(24), 2329-2338. doi:10.1016/j.jacc.2013.08.1621

Clavel, M. A., Pibarot, P., Messika-Zeitoun, D., Capoulade, R., Malouf, J., Aggarval, S., . . . Enriquez-Sarano, M. (2014). Impact of Aortic Valve Calcification, as Measured by MDCT, on Survival in Patients With Aortic Stenosis. *Journal of the American College of Cardiology, 64*(12), 1202-1213. doi:10.1016/j.jacc.2014.05.066

Conti, M. (2011). Focus on time-of-flight PET: the benefits of improved time resolution. *European Journal of Nuclear Medicine and Molecular Imaging, 38*(6), 1147-1157. doi:10.1007/s00259-010-1711-y

Cote, N., Pibarot, P., Pepin, A., Fournier, D., Audet, A., Arsenault, B., . . . Mathieu, P. (2010). Oxidized low-density lipoprotein, angiotensin II and increased waist cirumference are associated with valve inflammation in prehypertensive patients with aortic stenosis. *International Journal of Cardiology, 145*(3), 444-449. doi:10.1016/j.ijcard.2009.05.054

Cramariuc, D., Gerdts, E., Davidsen, E. S., Segadal, L., & Matre, K. (2010). Myocardial deformation in aortic valve stenosis: relation to left ventricular geometry. *Heart, 96*(2), 106-112. doi:10.1136/hrt.2009.172569

Cramariuc, D., Rieck, Å. E., Staal, E. M., Wachtell, K., Eriksen, E., Rossebø, A. B., & Gerdts, E. (2008). Factors Influencing Left Ventricular Structure and Stress-Corrected Systolic Function in Men and Women With Asymptomatic Aortic Valve Stenosis (a SEAS Substudy). *American Journal of Cardiology, 101*(4), 510-515. doi:10.1016/j.amjcard.2007.09.100

Czernin, J., Satyamurthy, N., & Schiepers, C. (2010). Molecular Mechanisms of Bone F-18-NaF Deposition. *Journal of Nuclear Medicine, 51*(12), 1826-1829. doi:10.2967/jnumed.110.077933

Dahou, A., Bartko, P. E., Capoulade, R., Clavel, M.-A., Mundigler, G., Grondin, S. L., . . . Pibarot, P. (2015). Usefulness of Global Left Ventricular Longitudinal Strain for Risk Stratification in Low Ejection Fraction, Low-Gradient Aortic Stenosis. *Circulation: Cardiovascular Imaging, 8*(3), e002117. doi:doi:10.1161/CIRCIMAGING.114.002117

Dasari, P. K. R., Jones, J. P., Casey, M. E., Liang, Y., Dilsizian, V., & Smith, M. F. (2018). The effect of time-of-flight and point spread function modeling on 82Rb myocardial perfusion imaging of obese patients. *Journal of Nuclear Cardiology, 25*(5), 1521-1545. doi:10.1007/s12350-018-1311-y

Daubewitherspoon, M. E., & Muehllehner, G. (1987). TREATMENT OF AXIAL DATA IN 3-DIMENSIONAL PET. *Journal of Nuclear Medicine, 28*(11), 1717-1724.

Dawood, M., Buther, F., Lang, N., Schober, O., & Schafers, K. P. (2007). Respiratory gating in positron emission tomography: A quantitative comparison of different gating schemes. *Medical Physics, 34*(7), 3067-3076. doi:10.1118/1.2748104

Dawood, M., Buther, F., Stegger, L., Jiang, X. Y., Schober, O., Schafers, M., & Schafers, K. P. (2009). Optimal number of respiratory gates in positron emission tomography: A cardiac patient study. *Medical Physics, 36*(5), 1775-1784. doi:10.1118/1.3112422

Derlin, T., Richter, U., Bannas, P., Begemann, P., Buchert, R., Mester, J., & Klutmann, S. (2010). Feasibility of F-18-Sodium Fluoride PET/CT for Imaging of Atherosclerotic Plaque. *Journal of Nuclear Medicine, 51*(6), 862-865. doi:10.2967/jnumed.110.076471

Derlin, T., Toth, Z., Papp, L., Wisotzki, C., Apostolova, I., Habermann, C. R., . . . Klutmann, S. (2011). Correlation of Inflammation Assessed by F-18-FDG PET, Active Mineral Deposition Assessed by F-18-Fluoride PET, and Vascular Calcification in Atherosclerotic Plaque: A Dual-Tracer PET/CT Study. *Journal of Nuclear Medicine, 52*(7), 1020-1027. doi:10.2967/jnumed.111.087452

Derlin, T., Wisotzki, C., Richter, U., Apostolova, I., Bannas, P., Weber, C., . . . Klutmann, S. (2011). In Vivo Imaging of Mineral Deposition in Carotid Plaque Using F-18-Sodium Fluoride PET/CT: Correlation with Atherogenic Risk Factors. *Journal of Nuclear Medicine, 52*(3), 362-368. doi:10.2967/jnumed.110.081208

Díez, J., Querejeta, R., López, B., González, A., Larman, M., & Martínez Ubago José, L. (2002). Losartan-Dependent Regression of Myocardial Fibrosis Is Associated With Reduction of

Left Ventricular Chamber Stiffness in Hypertensive Patients. *Circulation, 105*(21), 2512-2517. doi:10.1161/01.CIR.0000017264.66561.3D

Dilsizian, V., Bacharach, S. L., Beanlands, R. S., Bergmann, S. R., Delbeke, D., Dorbala, S., . . . Travin, M. I. (2016). ASNC imaging guidelines/SNMMI procedure standard for positron emission tomography (PET) nuclear cardiology procedures. *Journal of Nuclear Cardiology, 23*(5), 1187-1226. doi:10.1007/s12350-016-0522-3

Dobson, L. E., Fairbairn, T. A., Musa, T. A., Uddin, A., Mundie, C. A., Swoboda, P. P., . . . Greenwood, J. P. (2016). Sex-related differences in left ventricular remodeling in severe aortic stenosis and reverse remodeling after aortic valve replacement: A cardiovascular magnetic resonance study. *American Heart Journal, 175*, 101-111. doi:10.1016/j.ahj.2016.02.010

Dorbala, S., Hachamovitch, R., Curillova, Z., Thomas, D., Vangala, D., Kwong, R. Y., & Di Carli, M. F. (2009). Incremental Prognostic Value of Gated Rb-82 Positron Emission Tomography Myocardial Perfusion Imaging Over Clinical Variables and Rest LVEF. *Jacc-Cardiovascular Imaging, 2*(7), 846-854. doi:10.1016/j.jcmg.2009.04.009

Dorbala, S., Vangala, D., Sampson, U., Limaye, A., Kwong, R., & Di Carli, M. F. (2007). Value of vasodilator left ventricular ejection fraction reserve in evaluating the magnitude of myocardium at risk and the extent of angiographic coronary artery disease: A Rb-82 PET/CT study. *Journal of Nuclear Medicine, 48*(3), 349-358.

Doris, M. K., Otaki, Y., Krishnan, S. K., Kwiecinski, J., Rubeaux, M., Alessio, A., . . . Slomka, P. J. (2018). Optimization of reconstruction and quantification of motion-corrected coronary PET-CT. *Journal of Nuclear Cardiology*. doi:10.1007/s12350-018-1317-5

Doris, M. K., Rubeaux, M., Pawade, T., Otaki, Y. K., Xie, Y. B., Li, D. B., . . . Dey, D. (2017). Motion-Corrected Imaging of the Aortic Valve with F-18-NaF PET/CT and PET/MRI: A Feasibility Study. *Journal of Nuclear Medicine, 58*(11), 1811-1814. doi:10.2967/jnumed.117.194597

Douglas, P. S., Katz, S. E., Weinberg, E. O., Chen, M. H., Bishop, S. P., & Lorell, B. H. (1998). Hypertrophic remodeling: gender differences in the early response to left ventricular pressure overload. *Journal of the American College of Cardiology, 32*(4), 1118-1125. doi:https://doi.org/10.1016/S0735-1097(98)00347-7

Douglas, P. S., Otto, C. M., Mickel, M. C., Labovitz, A., Reid, C. L., & Davis, K. B. (1995). GENDER DIFFERENCES IN LEFT-VENTRICLE GEOMETRY AND FUNCTION IN PATIENTS UNDERGOING BALLOON DILATATION OF THE AORTIC-VALVE FOR ISOLATED AORTIC-STENOSIS. *British Heart Journal, 73*(6), 548-554.

Dulgheru, R., Pibarot, P., Sengupta, P. P., Pierard, L. A., Rosenhek, R., Magne, J., . . . Lancellotti, P. (2016). Multimodality Imaging Strategies for the Assessment of Aortic Stenosis Viewpoint of the Heart Valve Clinic International Database (HAVEC) Group. *Circulation-Cardiovascular Imaging, 9*(2). doi:10.1161/circimaging.115.004352

Duncan, A. I., Lowe, B. S., Garcia, M. J., Xu, M., Gillinov, A. M., Mihaljevic, T., & Koch, C. G. (2008). Influence of concentric left ventricular remodeling on early mortality after aortic valve replacement. *Annals of Thoracic Surgery, 85*(6), 2030-2039. doi:10.1016/j.athoracsur.2008.02.075

Dunlay, S. M., Roger, V. L., Weston, S. A., Jiang, R., & Redfield, M. M. (2012). Longitudinal changes in ejection fraction in heart failure patients with preserved and reduced ejection fraction. *Circulation. Heart failure, 5*(6), 720-726. doi:10.1161/CIRCHEARTFAILURE.111.966366

Dweck, M. R., Boon, N. A., & Newby, D. E. (2012). Calcific Aortic Stenosis: A Disease of the Valve and the Myocardium. *Journal of the American College of Cardiology, 60*(19), 1854-1863. doi:https://doi.org/10.1016/j.jacc.2012.02.093

Dweck, M. R., Chow, M. W. L., Joshi, N. V., Williams, M. C., Jones, C., Fletcher, A. M., . . . Newby, D. E. (2012). Coronary Arterial 18F-Sodium Fluoride Uptake A Novel Marker of Plaque Biology. *Journal of the American College of Cardiology, 59*(17), 1539-1548. doi:10.1016/j.jacc.2011.12.037

Dweck, M. R., Jenkins, W. S. A., Vesey, A. T., Pringle, M. A. H., Chin, C. W. L., Malley, T. S., . . . Newby, D. E. (2014). 18F-Sodium Fluoride Uptake Is a Marker of Active Calcification and Disease Progression in Patients With Aortic Stenosis. *Circulation-Cardiovascular Imaging, 7*(2), 371-378. doi:10.1161/circimaging.113.001508

Dweck, M. R., Jones, C., Joshi, N. V., Fletcher, A. M., Richardson, H., White, A., . . . Newby, D. E. (2012). Assessment of Valvular Calcification and Inflammation by Positron Emission Tomography in Patients With Aortic Stenosis. *Circulation, 125*(1), 76-U424. doi:10.1161/circulationaha.111.051052

Dweck, M. R., Joshi, S., Murigu, T., Alpendurada, F., Jabbour, A., Melina, G., . . . Prasad, S. K. (2011). Midwall Fibrosis Is an Independent Predictor of Mortality in Patients With Aortic Stenosis. *Journal of the American College of Cardiology, 58*(12), 1271-1279. doi:10.1016/j.jacc.2011.03.064

Dweck, M. R., Joshi, S., Murigu, T., Gulati, A., Alpendurada, F., Jabbour, A., . . . Prasad, S. K. (2012). Left ventricular remodeling and hypertrophy in patients with aortic stenosis: insights from cardiovascular magnetic resonance. *Journal of Cardiovascular Magnetic Resonance, 14*. doi:10.1186/1532-429x-14-50

Dweck, M. R., Williams, M. C., Moss, A. J., Newby, D. E., & Fayad, Z. A. (2016). Computed Tomography and Cardiac Magnetic Resonance in Ischemic Heart Disease. *Journal of the American College of Cardiology, 68*(20), 2201-2216. doi:10.1016/j.jacc.2016.08.047

Einstein, A. J., Elliston, C. D., Arai, A. E., Chen, M. Y., Mather, R., Pearson, G. D. N., . . . Brenner, D. J. (2010). Radiation dose from single-heartbeat coronary CT angiography performed with a 320-detector row volume scanner. *Radiology, 254*(3), 698-706. doi:10.1148/radiol.09090779

Eriksson, L., Townsend, D., Conti, M., Eriksson, M., Rothfuss, H., Schmand, M., . . . Bendriem, B. (2007). An investigation of sensitivity limits in PET scanners. *Nuclear Instruments & Methods in Physics Research Section a-Accelerators Spectrometers Detectors and Associated Equipment, 580*(2), 836-842. doi:10.1016/j.nima.2007.06.112

Eveborn, G. W., Schirmer, H., Heggelund, G., Lunde, P., & Rasmussen, K. (2013). The evolving epidemiology of valvular aortic stenosis. The Tromsø Study. *Heart, 99*(6), 396-400. doi:10.1136/heartjnl-2012-302265

Everett, R. J., Tastet, L., Clavel, M.-A., Chin, C. W. L., Capoulade, R., Vassiliou, V. S., . . . Dweck, M. R. (2018). Progression of Hypertrophy and Myocardial Fibrosis in Aortic Stenosis: A Multicenter Cardiac Magnetic Resonance Study. *Circulation. Cardiovascular imaging, 11*(6), e007451-e007451. doi:10.1161/CIRCIMAGING.117.007451

Flett, A. S., Hasleton, J., Cook, C., Hausenloy, D., Quarta, G., Ariti, C., . . . Moon, J. C. (2011). Evaluation of Techniques for the Quantification of Myocardial Scar of Differing Etiology Using Cardiac Magnetic Resonance. *JACC: Cardiovascular Imaging, 4*(2), 150-156. doi:https://doi.org/10.1016/j.jcmg.2010.11.015

Flett, A. S., Hayward, M. P., Ashworth, M. T., Hansen, M. S., Taylor, A. M., Elliott, P. M., . . . Moon, J. C. (2010). Equilibrium Contrast Cardiovascular Magnetic Resonance for the

Measurement of Diffuse Myocardial Fibrosis Preliminary Validation in Humans. *Circulation, 122*(2), 138-U172. doi:10.1161/circulationaha.109.930636

Fontana, M., White, S. K., Banypersad, S. M., Sado, D. M., Maestrini, V., Flett, A. S., . . . Moon, J. C. (2012). Comparison of T1 mapping techniques for ECV quantification. Histological validation and reproducibility of ShMOLLI versus multibreath-hold T1 quantification equilibrium contrast CMR. *Journal of cardiovascular magnetic resonance : official journal of the Society for Cardiovascular Magnetic Resonance, 14*(1), 88-88. doi:10.1186/1532-429X-14-88

Forsythe, R. O., Dweck, M. R., McBride, O. M. B., Vesey, A. T., Semple, S. I., Shah, A. S. V., . . . Newby, D. E. (2018). F-18-Sodium Fluoride Uptake in Abdominal Aortic Aneurysms The SoFIA(3) Study. *Journal of the American College of Cardiology, 71*(5), 513-523. doi:10.1016/j.jacc.2017.11.053

Fujisaka, T., Hoshiga, M., Hotchi, J., Takeda, Y., Jin, D. N., Takai, S., . . . Ishizaka, N. (2013). Angiotensin II promotes aortic valve thickening independent of elevated blood pressure in apolipoprotein-E deficient mice. *Atherosclerosis, 226*(1), 82-87. doi:10.1016/j.atherosclerosis.2012.10.055

Gaasch, W. H., & Zile, M. R. (2011). Left Ventricular Structural Remodeling in Health and Disease With Special Emphasis on Volume, Mass, and Geometry. *Journal of the American College of Cardiology, 58*(17), 1733-1740. doi:10.1016/j.jacc.2011.07.022

Galiuto, L., Lotrionte, M., Crea, F., Anselmi, A., Biondi-Zoccai, G. G. L., De Giorgio, F., . . . Abbate, A. (2006). Impaired coronary and myocardial flow in severe aortic stenosis is associated with increased apoptosis: a transthoracic Doppler and myocardial contrast echocardiography study. *Heart, 92*(2), 208-212. doi:10.1136/hrt.2005.062422

Ganau, A., Devereux, R. B., Roman, M. J., Desimone, G., Pickering, T. G., Saba, P. S., . . . Laragh, J. H. (1992). PATTERNS OF LEFT-VENTRICULAR HYPERTROPHY AND GEOMETRIC REMODELING IN ESSENTIAL-HYPERTENSION. *Journal of the American College of Cardiology, 19*(7), 1550-1558. doi:10.1016/0735-1097(92)90617-v

Gao, X.-M., Kiriazis, H., Moore, X.-L., Feng, X.-H., Sheppard, K., Dart, A., & Du, X.-J. (2005). Regression of pressure overload-induced left ventricular hypertrophy in mice. *American Journal of Physiology-Heart and Circulatory Physiology, 288*(6), H2702-H2707. doi:10.1152/ajpheart.00836.2004

Gasser, P., Voegel, J. C., & Gramain, P. (1993). SURFACE-REACTIONS ON HYDROXYAPATITE IN THE PRESENCE OF FLUORIDE IONS .1. SATURATED AND CONGRUENT CONDITIONS. *Colloids and Surfaces a-Physicochemical and Engineering Aspects, 74*(2-3), 275-286. doi:10.1016/0927-7757(93)80271-f

Gigengack, F., Ruthotto, L., Burger, M., Wolters, C. H., Jiang, X., & Schafers, K. P. (2012). Motion Correction in Dual Gated Cardiac PET Using Mass-Preserving Image Registration. *Ieee Transactions on Medical Imaging, 31*(3), 698-712. doi:10.1109/TMI.2011.2175402

Giraud, P., & Garcia, R. (2010). Respiratory gating for radiotherapy: main technical aspects and clinical benefits. *Bulletin Du Cancer, 97*(7), 847-856. doi:10.1684/bdc.2010.1143

Gong, W., Ma, R., Mei, D., Jing, P., Dong, X., Li, B., . . . Hu, F.-Q. (2014). A novel subcutaneous infusion delivery system based on osmotic pump: in vitro and in vivo evaluation. *Drug Delivery, 21*(1), 1-7. doi:10.3109/10717544.2013.838718

Gosse, P. (2005). Left ventricular hypertrophy as a predictor of cardiovascular risk. *Journal of Hypertension, 23*, S27-S33. doi:10.1097/01.hjh.0000165625.79933.9a

Gould, K. L. (2017). Optimizing quantitative myocardial perfusion by positron emission tomography for guiding CAD management. *Journal of Nuclear Cardiology, 24*(6), 1950-1954. doi:10.1007/s12350-016-0666-1

Gould, K. L., Pan, T., Loghin, C., Johnson, N. P., Guha, A., & Sdringola, S. (2007). Frequent diagnostic errors in cardiac PET/CT due to misregistration of CT attenuation and emission PET images: A definitive analysis of causes, consequences, and corrections. *Journal of Nuclear Medicine, 48*(7), 1112-1121. doi:10.2967/jnumed.107.039792

Gradman, A. H., & Alfayoumi, F. (2006). From left ventricular hypertrophy to congestive heart failure: Management of hypertensive heart disease. *Progress in Cardiovascular Diseases, 48*(5), 326-341. doi:10.1016/j.pcad.2006.02.001

Grant, F. D., Fahey, F. H., Packard, A. B., Davis, R. T., Alavi, A., & Treves, S. T. (2008). Skeletal PET with F-18-fluoride: Applying new technology to an old tracer. *Journal of Nuclear Medicine, 49*(1), 68-78. doi:10.2967/jnumed.106.037200

Greenland, P., LaBree, L., Azen, S. P., Doherty, T. M., & Detrano, R. C. (2004). Coronary artery calcium score combined with framingham score for risk prediction in asymptomatic individuals. *JAMA, 291*(2), 210-215. doi:10.1001/jama.291.2.210

Greiten, L. E., Holditch, S. J., Arunachalam, S. P., & Miller, V. M. (2014). Should There Be Sex-Specific Criteria for the Diagnosis and Treatment of Heart Failure? *Journal of Cardiovascular Translational Research, 7*(2), 139-155. doi:10.1007/s12265-013-9514-8

Greve, A. M., Boman, K., Gohlke-Baerwolf, C., Kesaniemi, Y. A., Nienaber, C., Ray, S., . . . Wachtell, K. (2012). Clinical Implications of Electrocardiographic Left Ventricular Strain and Hypertrophy in Asymptomatic Patients With Aortic Stenosis The Simvastatin and Ezetimibe in Aortic Stenosis Study. *Circulation, 125*(2), 346-353. doi:10.1161/circulationaha.111.049759

Grossman, W., Jones, D., & McLaurin, L. P. (1975). Wall stress and patterns of hypertrophy in human left-ventricle. *Journal of Clinical Investigation, 56*(1), 56-64. doi:10.1172/jci108079

Gunther, S., & Grossman, W. (1979). Determinants of ventricular function in pressure-overload hypertrophy in man. *Circulation, 59*(4), 679-688. doi:doi:10.1161/01.CIR.59.4.679

Hawkins, R. A., Choi, Y., Huang, S. C., Hoh, C. K., Dahlbom, M., Schiepers, C., . . . Phelps, M. E. (1992). EVALUATION OF THE SKELETAL KINETICS OF FLUORINE-18-FLUORIDE ION WITH PET. *Journal of Nuclear Medicine, 33*(5), 633-642.

He, J. F., O'Keefe, G. J., Gong, S. J., Jones, G., Saunder, T., Scott, A. M., & Geso, M. (2008). A Novel Method for Respiratory Motion Gated With Geometric Sensitivity of the Scanner in 3D PET. *Ieee Transactions on Nuclear Science, 55*(5), 2557-2565. doi:10.1109/tns.2008.2001187

Hein, S., Arnon, E., Kostin, S., Schönburg, M., Elsässer, A., Polyakova, V., . . . Schaper, J. (2003). Progression From Compensated Hypertrophy to Failure in the Pressure-Overloaded Human Heart. *Circulation, 107*(7), 984-991. doi:10.1161/01.CIR.0000051865.66123.B7

Helske, S., Lindstedt, K. A., Laine, M., Mayranpaa, M., Werkkala, K., Lommi, J., . . . Kovanen, P. T. (2004). Induction of local angiotensin II-producing systems in stenotic aortic valves. *Journal of the American College of Cardiology, 44*(9), 1859-1866. doi:10.1016/j.jacc.2004.07.054

Heng, M. K., Janz, R. F., & Jobin, J. (1985). Estimation of regional stress in the left-ventricular septum and free wall - as echocardiographic study suggesting a mechanism for for asymmetric septal hypertrophy. *American Heart Journal, 110*(1), 84-90. doi:10.1016/0002-8703(85)90519-8

Herrlich, S., Spieth, S., Messner, S., & Zengerle, R. (2012). *Osmotic micropumps for drug delivery* (Vol. 64).

Herrmann, S., Fries, B., Salinger, T., Liu, D., Hu, K., Gensler, D., . . . Nordbeck, P. (2018). Myocardial Fibrosis Predicts 10-Year Survival in Patients Undergoing Aortic Valve

Replacement. *Circulation-Cardiovascular Imaging, 11*(8). doi:10.1161/circimaging.117.007131

Hervault, M., & Clavel, M.-A. (2018). Sex-related Differences in Calcific Aortic Valve Stenosis: Pathophysiology, Epidemiology, Etiology, Diagnosis, Presentation, and Outcomes. *Structural Heart, 2*(2), 102-113. doi:10.1080/24748706.2017.1420273

Hess, O. M., Schneider, J., Turina, M., Carroll, J. D., Rothlin, M., & Krayenbuehl, H. P. (1983a). ASYMMETRIC SEPTAL HYPERTROPHY IN PATIENTS WITH AORTIC-STENOSIS - AN ADAPTIVE MECHANISM OR A COEXISTENCE OF HYPERTROPHIC CARDIOMYOPATHY. *Journal of the American College of Cardiology, 1*(3), 783-789. doi:10.1016/s0735-1097(83)80191-0

Hess, O. M., Schneider, J., Turina, M., Carroll, J. D., Rothlin, M., & Krayenbuehl, H. P. (1983b). Asymmetric septal hypertrophy in patients with aortic stenosis - an adaptive mechanism or a coexistence of hypertophic cardiomyopathy. *Journal of the American College of Cardiology, 1*(3), 783-789.

Holme, I., Pedersen, T. R., Boman, K., Egstrup, K., Gerdts, E., Kesaniemi, Y. A., . . . Gohlke-Barwolf, C. (2012). A risk score for predicting mortality in patients with asymptomatic mild to moderate aortic stenosis. *Heart, 98*(5), 377-383. doi:10.1136/heartjnl-2011-300475

Houser, S. R., Margulies, K. B., Murphy, A. M., Spinale, F. G., Francis, G. S., Prabhu, S. D., . . . Council Functional, G. (2012). Animal Models of Heart Failure A Scientific Statement From the American Heart Association. *Circulation Research, 111*(1), 131-150. doi:10.1161/RES.0b013e3182582523

Houshmand, S., Salavati, A., Segtnan, E. A., Grupe, P., Hoilund-Carlsen, P. F., & Alavi, A. (2016). Dual-time-point Imaging and Delayed-time-point Fluorodeoxyglucose-PET/Computed Tomography Imaging in Various Clinical Settings. *PET Clinics, 11*(1), 65-+. doi:10.1016/j.cpet.2015.07.003

Huet, P., Burg, S., Le Guludec, D., Hyafil, F., & Buvat, I. (2015). Variability and Uncertainty of F-18-FDG PET Imaging Protocols for Assessing Inflammation in Atherosclerosis: Suggestions for Improvement. *Journal of Nuclear Medicine, 56*(4), 552-559. doi:10.2967/jnumed.114.142596

Hyun, M. C., Gerlach, J., Rubeaux, M., & Slomka, P. J. (2017). Technical consideration for dual ECG/respiratory-gated cardiac PET imaging. *Journal of Nuclear Cardiology, 24*(4), 1246-1252. doi:10.1007/s12350-016-0741-7

Iles, L., Pfluger, H., Phrommintikul, A., Cherayath, J., Aksit, P., Gupta, S. N., . . . Taylor, A. J. (2008). Evaluation of Diffuse Myocardial Fibrosis in Heart Failure With Cardiac Magnetic Resonance Contrast-Enhanced T1 Mapping. *Journal of the American College of Cardiology, 52*(19), 1574-1580. doi:https://doi.org/10.1016/j.jacc.2008.06.049

Irkle, A., Vesey, A. T., Lewis, D. Y., Skepper, J. N., Bird, J. L. E., Dweck, M. R., . . . Davenport, A. P. (2015). Identifying active vascular microcalcification by F-18-sodium fluoride positron emission tomography. *Nature Communications, 6*. doi:10.1038/ncomms8495

Jadvar, H., Desai, B., & Conti, P. S. (2015). Sodium F-18-Fluoride PET/CT of Bone, Joint, and Other Disorders. *Seminars in Nuclear Medicine, 45*(1), 58-65. doi:10.1053/j.semnuclmed.2014.07.008

Jaskowiak, C. J., Bianco, J. A., Perlman, S. B., & Fine, J. P. (2005). Influence of reconstruction iterations on F-18-FDG PET/CT standardized uptake values. *Journal of Nuclear Medicine, 46*(3), 424-428.

Jerosch-Herold, M., Sheridan, D. C., Kushner, J. D., Nauman, D., Burgess, D., Dutton, D., . . . Hershberger, R. E. (2008). Cardiac magnetic resonance imaging of myocardial contrast

uptake and blood flow in patients affected with idiopathic or familial dilated cardiomyopathy. *American Journal of Physiology-Heart and Circulatory Physiology, 295*(3), H1234-H1242. doi:10.1152/ajpheart.00429.2008

Joshi, N. V., Vesey, A. T., Williams, M. C., Shah, A. S. V., Calvert, P. A., Craighead, F. H. M., . . . Newby, D. E. (2014). F-18-fluoride positron emission tomography for identification of ruptured and high-risk coronary atherosclerotic plaques: a prospective clinical trial. *Lancet, 383*(9918), 705-713. doi:10.1016/s0140-6736(13)61754-7

Kang, D. H., Park, S. J., Rim, J. H., Yun, S. C., Kim, D. H., Song, J. M., . . . Park, P. W. (2010). Early Surgery Versus Conventional Treatment in Asymptomatic Very Severe Aortic Stenosis. *Circulation, 121*(13), 1502-1509. doi:10.1161/circulationaha.109.909903

Kang, D. H., Rim, J. H., Yun, S. C., Kim, D. H., Song, J. M., Choo, S. J., . . . Park, P. W. (2010). Response to Letter Regarding Article, "Early Surgery Versus Conventional Treatment in Asymptomatic Very Severe Aortic Stenosis". *Circulation, 122*(25), E639-E639. doi:10.1161/circulationaha.110.975821

Kararigas, G., Dworatzek, E., Petrov, G., Summer, H., Schulze, T. M., Baczko, I., . . . Regitz-Zagrosek, V. (2014). Sex-dependent regulation of fibrosis and inflammation in human left ventricular remodelling under pressure overload. *European Journal of Heart Failure, 16*(11), 1160-1167. doi:doi:10.1002/ejhf.171

Kawel-Boehm, N., Maceira, A., Valsangiacomo-Buechel, E. R., Vogel-Claussen, J., Turkbey, E. B., Williams, R., . . . Bluemke, D. A. (2015). Normal values for cardiovascular magnetic resonance in adults and children. *Journal of Cardiovascular Magnetic Resonance, 17*(1), 29. doi:10.1186/s12968-015-0111-7

Kearney, L. G., Lu, K., Ord, M., Patel, S. K., Profitis, K., Matalanis, G., . . . Srivastava, P. M. (2012). Global longitudinal strain is a strong independent predictor of all-cause mortality in patients with aortic stenosis. *European Heart Journal - Cardiovascular Imaging, 13*(10), 827-833. doi:10.1093/ehjci/jes115

Keller, K. M., & Howlett, S. E. (2016). Sex Differences in the Biology and Pathology of the Aging Heart. *Canadian Journal of Cardiology, 32*(9), 1065-1073. doi:10.1016/j.cjca.2016.03.017

Kellman, P., Xue, H., Chow, K., Spottiswoode, B. S., Arai, A. E., & Thompson, R. B. (2014). Optimized saturation recovery protocols for T1-mapping in the heart: influence of sampling strategies on precision. *Journal of cardiovascular magnetic resonance : official journal of the Society for Cardiovascular Magnetic Resonance, 16*(1), 55-55. doi:10.1186/s12968-014-0055-3

Kesner, A. L., & Kuntner, C. (2010). A new fast and fully automated software based algorithm for extracting respiratory signal from raw PET data and its comparison to other methods. *Medical Physics, 37*(10), 5550-5559. doi:10.1118/1.3483784

Kesner, A. L., Schleyer, P. J., Büther, F., Walter, M. A., Schäfers, K. P., & Koo, P. J. (2014). On transcending the impasse of respiratory motion correction applications in routine clinical imaging - a consideration of a fully automated data driven motion control framework. *EJNMMI Physics, 1*, 8. doi:10.1186/2197-7364-1-8

Kinahan, P. E., Hasegawa, B. H., & Beyer, T. (2003). X-ray-based attenuation correction for positron emission tomography/computed tomography scanners. *Seminars in Nuclear Medicine, 33*(3), 166-179. doi:10.1053/snuc.2003.127307

Kitagawa, T., Yamamoto, H., Toshimitsu, S., Sasaki, K., Senoo, A., Kubo, Y., . . . Kihara, Y. (2017). ¹⁸F-sodium fluoride positron emission tomography for molecular imaging of coronary atherosclerosis based on computed tomography analysis. *Atherosclerosis, 263*, 385-392. doi:10.1016/j.atherosclerosis.2017.04.024

Koos, R., Kuhl, H. P., Muhlenbruch, G., & Mahnken, A. H. (2006). Prevalence and clinical importance of aortic valve calcification detected incidentally on CT scans: Comparison with echocardiography. *Radiology, 241*(1), 76-82. doi:10.1148/radio1.2411051163

Kostin, S., Pool, L., Elsasser, A., Hein, S., Drexler, H. C. A., Arnon, E., . . . Schaper, J. (2003). Myocytes die by multiple mechanisms in failing human hearts. *Circulation Research, 92*(7), 715-724. doi:10.1161/01.res.0000067471.95890.5c

Krayenbuehl, H. P., Hess, O. M., Monrad, E. S., Schneider, J., Mall, G., & Turina, M. (1989). Left ventricular myocardial structure in aortic valve disease before, intermediate, and late after aortic valve replacement. *Circulation, 79*(4), 744-755. doi:10.1161/01.CIR.79.4.744

Ku, M. C., Huelnhagen, T., Niendorf, T., & Pohlmann, A. (2018). Cardiac MRI in Small Animals. In M. L. GarciaMartin & P. LopezLarrubia (Eds.), *Preclinical Mri: Methods and Protocols* (Vol. 1718, pp. 269-284).

Kubota, K., Itoh, M., Ozaki, K., Ono, S., Tashiro, M., Yamaguchi, K., . . . Fukuda, H. (2001). Advantage of delayed whole-body FDG-PET imaging for tumour detection. *European Journal of Nuclear Medicine, 28*(6), 696-703. doi:10.1007/s002590100537

Kubota, K., Yokoyama, J., Yamaguchi, K., Ono, S., Qureshy, A., Itoh, M., & Fukuda, H. (2004). FDG-PET delayed imaging for the detection of head and neck cancer recurrence after radio-chemotherapy: comparison with MRI/CT. *European Journal of Nuclear Medicine and Molecular Imaging, 31*(4), 590-595. doi:10.1007/s00259-003-1408-6

Lamare, F., Le Maitre, A., Dawood, M., Schäfers, K. P., Fernandez, P., Rimoldi, O. E., & Visvikis, D. (2014). Evaluation of respiratory and cardiac motion correction schemes in dual gated PET/CT cardiac imaging. *Medical Physics, 41*(7), 072504. doi:doi:10.1118/1.4881099

Lang, R. M., Badano, L. P., Mor-Avi, V., Afilalo, J., Armstrong, A., Ernande, L., . . . Voigt, J.-U. (2015). Recommendations for Cardiac Chamber Quantification by Echocardiography in Adults: An Update from the American Society of Echocardiography and the European Association of Cardiovascular Imaging. *Journal of the American Society of Echocardiography, 28*(1), 1-39.e14. doi:10.1016/j.echo.2014.10.003

Larose, E., Rodés-Cabau, J., Pibarot, P., Rinfret, S., Proulx, G., Nguyen, C. M., . . . Bertrand, O. F. (2010). Predicting Late Myocardial Recovery and Outcomes in the Early Hours of ST-Segment Elevation Myocardial Infarction: Traditional Measures Compared With Microvascular Obstruction, Salvaged Myocardium, and Necrosis Characteristics by Cardiovascular Magnetic Resonance. *Journal of the American College of Cardiology, 55*(22), 2459-2469. doi:https://doi.org/10.1016/j.jacc.2010.02.033

Lassen, M. L., Kwiecinski, J., Cadet, S., Dey, D., Wang, C., Dweck, M. R., . . . Slomka, P. J. (2018). Data-driven gross patient motion detection and compensation: Implications for coronary 18F-NaF PET imaging. *Journal of Nuclear Medicine*. doi:10.2967/jnumed.118.217877

Lassen, M. L., Rasmussen, T., Christensen, T. E., Kjaer, A., & Hasbak, P. (2017). Respiratory gating in cardiac PET: Effects of adenosine and dipyridamole. *Journal of Nuclear Cardiology, 24*(6), 1941-1949. doi:10.1007/s12350-016-0631-z

Lassen, M. L., Rasul, S., Beitzke, D., Stelzmüller, M.-E., Cal-Gonzalez, J., Hacker, M., & Beyer, T. (2017). Assessment of attenuation correction for myocardial PET imaging using combined PET/MRI. *Journal of Nuclear Cardiology*. doi:10.1007/s12350-017-1118-2

Lassnigg, A., Hiesmayr, M., Frantal, S., Brannath, W., Mouhieddine, M., Presterl, E., . . . Schmidlin, D. (2013). Long-term absolute and relative survival after aortic valve

replacement: A prospective cohort study. *European Journal of Anaesthesiology (EJA), 30*(11), 695-703. doi:10.1097/EJA.0b013e3283657829

Le Meunier, L., Slomka, P. J., Dey, D., Ramesh, A., Thomson, L. E. J., Hayes, S. W., . . . Berman, D. S. (2011). Motion frozen F-18-FDG cardiac PET. *Journal of Nuclear Cardiology, 18*(2), 259-266. doi:10.1007/s12350-010-9322-3

Le Ven, F., Bibeau, K., De Larochellière, É., Tizón-Marcos, H., Deneault-Bissonnette, S., Pibarot, P., . . . Larose, É. (2016). Cardiac morphology and function reference values derived from a large subset of healthy young Caucasian adults by magnetic resonance imaging. *European heart journal cardiovascular Imaging, 17*(9), 981-990. doi:10.1093/ehjci/jev217

Lee, H., Park, J.-B., Yoon, Y. E., Park, E.-A., Kim, H.-K., Lee, W., . . . Lee, S.-P. (2018). Noncontrast Myocardial T1 Mapping by Cardiac Magnetic Resonance Predicts Outcome in Patients With Aortic Stenosis. *JACC: Cardiovascular Imaging, 11*(7), 974-983. doi:https://doi.org/10.1016/j.jcmg.2017.09.005

Lee, H., Park, J. B., Yoon, Y. E., Park, E. A., Kim, H. K., Lee, W., . . . Lee, S. P. (2018). Noncontrast Myocardial T1 Mapping by Cardiac Magnetic Resonance Predicts Outcome in Patients With Aortic Stenosis. *Jacc-Cardiovascular Imaging, 11*(7), 974-983. doi:10.1016/j.jcmg.2017.09.005

Lee, J. M., Bang, J. I., Koo, B. K., Hwang, D., Park, J., Zhang, J. L., . . . Akasaka, T. (2017). Clinical Relevance of F-18-Sodium Fluoride Positron-Emission Tomography in Noninvasive Identification of High-Risk Plaque in Patients With Coronary Artery Disease. *Circulation-Cardiovascular Imaging, 10*(11). doi:10.1161/circimaging.117.006704

Lee, J. M., Park, S. J., Lee, S. P., Park, E., Chang, S. A., Kim, H. K., . . . Choe, Y. H. (2015). Gender Difference in Ventricular Response to Aortic Stenosis: Insight from Cardiovascular Magnetic Resonance. *Plos One, 10*(3). doi:10.1371/journal.pone.0121684

Lee, S.-P., Lee, W., Lee, J. M., Park, E.-A., Kim, H.-K., Kim, Y.-J., & Sohn, D.-W. (2015). Assessment of Diffuse Myocardial Fibrosis by Using MR Imaging in Asymptomatic Patients with Aortic Stenosis. *Radiology, 274*(2), 359-369. doi:10.1148/radiol.14141120

Leipsic, J., Abbara, S., Achenbach, S., Cury, R., Earls, J. P., Mancini, G. B. J., . . . Raff, G. L. (2014). SCCT guidelines for the interpretation and reporting of coronary CT angiography: A report of the Society of Cardiovascular Computed Tomography Guidelines Committee. *Journal of Cardiovascular Computed Tomography, 8*(5), 342-358. doi:10.1016/j.jcct.2014.07.003

Lertsburapa, K., Ahlberg, A. W., Bateman, T. M., Katten, D., Volker, L., Cullom, S. J., & Heller, G. V. (2008). Independent and incremental prognostic value of left ventricular ejection fraction determined by stress gated rubidium 82 PET imaging in patients with known or suspected coronary artery disease. *Journal of Nuclear Cardiology, 15*(6), 745-753. doi:10.1007/bf03007355

Lin, J., Raghavan, S., & Fuerstenau, D. W. (1981). THE ADSORPTION OF FLUORIDE IONS BY HYDROXYAPATITE FROM AQUEOUS-SOLUTION. *Colloids and Surfaces, 3*(4), 357-370. doi:10.1016/0166-6622(81)80062-5

Lin, W. Y., Tsai, S. C., & Hung, G. U. (2005). Value of delayed F-18-FDG-PET imaging in the detection of hepatocellular carcinoma. *Nuclear Medicine Communications, 26*(4), 315-321. doi:10.1097/00006231-200504000-00003

Lindman, B. R., Clavel, M.-A., Mathieu, P., Iung, B., Lancellotti, P., Otto, C. M., & Pibarot, P. (2016). Calcific aortic stenosis. *Nature reviews. Disease primers, 2*, 16006-16006. doi:10.1038/nrdp.2016.6

Lindman, B. R., Stewart, W. J., Pibarot, P., Hahn, R. T., Otto, C. M., Xu, K., . . . Douglas, P. S. (2014). Early Regression of Severe Left Ventricular Hypertrophy After Transcatheter Aortic Valve Replacement Is Associated With Decreased Hospitalizations. *Jacc-Cardiovascular Interventions, 7*(6), 662-673. doi:10.1016/j.jcin.2014.02.011

Liu, C.-Y., Liu, Y.-C., Wu, C., Armstrong, A., Volpe, G. J., van der Geest, R. J., . . . Lima, J. A. C. (2013). Evaluation of age-related interstitial myocardial fibrosis with cardiac magnetic resonance contrast-enhanced T1 mapping: MESA (Multi-Ethnic Study of Atherosclerosis). *Journal of the American College of Cardiology, 62*(14), 1280-1287. doi:10.1016/j.jacc.2013.05.078

Liu, C., Alessio, A., Pierce, L., Thielemans, K., Wollenweber, S., Ganin, A., & Kinahan, P. (2010). Quiescent period respiratory gating for PET/CT. *Medical Physics, 37*(9), 5037-5043. doi:10.1118/1.3480508

Liu, C., Pierce, L. A., Alessio, A. M., & Kinahan, P. E. (2009). The impact of respiratory motion on tumor quantification and delineation in static PET/CT imaging. *Physics in Medicine and Biology, 54*(24), 7345-7362. doi:10.1088/0031-9155/54/24/007

Liu, F., Coursey, C. A., Grahame-Clarke, C., Sciacca, R. R., Rozenshtein, A., Homma, S., & Austin, J. H. M. (2006). Aortic valve calcification as an incidental finding at CT of the elderly: Severity and location as predictors of aortic stenosis. *American Journal of Roentgenology, 186*(2), 342-349. doi:10.2214/ajr.04.1366

Lluri, G., Renella, P., Finn, J. P., Vorobiof, G., Aboulhosn, J., & Deb, A. (2017). Prognostic Significance of Left Ventricular Fibrosis in Patients With Congenital Bicuspid Aortic Valve. *American Journal of Cardiology, 120*(7), 1176-1179. doi:10.1016/j.amjcard.2017.06.060

M Otto, C., Kuusisto, J., D Reichenbach, D., Gown, A., & D O'Brien, K. (1994). *Characterization of the early lesion of 'degenerative' valvular aortic stenosis Histological and immunohistochemical studies* (Vol. 90).

Mahmod, M., Piechnik, S. K., Levelt, E., Ferreira, V. M., Francis, J. M., Lewis, A., . . . Karamitsos, T. D. (2014). Adenosine stress native T1 mapping in severe aortic stenosis: evidence for a role of the intravascular compartment on myocardial T1 values. *Journal of Cardiovascular Magnetic Resonance, 16*(1), 92. doi:10.1186/s12968-014-0092-y

Manber, R., Thielemans, K., Hutton, B. F., Wan, S., McClelland, J., Barnes, A., . . . Atkinson, D. (2016). Joint PET-MR respiratory motion models for clinical PET motion correction. *Physics in Medicine and Biology, 61*(17), 6515-6530. doi:10.1088/0031-9155/61/17/6515

Marcus, M. L., Koyanagi, S., Harrison, D. G., Doty, D. B., Hiratzka, L. F., & Eastham, C. L. (1983). ABNORMALITIES IN THE CORONARY CIRCULATION THAT OCCUR AS A CONSEQUENCE OF CARDIAC-HYPERTROPHY. *American Journal of Medicine, 75*(3A), 62-66. doi:10.1016/0002-9343(83)90120-1

Maron, B. J. (2002). Hypertrophic cardiomyopathy: A systematic review. *JAMA, 287*(10), 1308-1320. doi:10.1001/jama.287.10.1308

Maron, B. J., Clark, C. E., Henry, W. L., Fukuda, T., Edwards, J. E., Mathews, E. C., . . . Epstein, S. E. (1977). Prevalence and characteristics of disproportionate ventricular septal thickening in patients with acquired or congenital heart diseases - echocardiographic and morphological findings. *Circulation, 55*(3), 489-496.

Maron, M. S., Maron, B. J., Harrigan, C., Buros, J., Gibson, C. M., Olivotto, I., . . . Appelbaum, E. (2009). Hypertrophic Cardiomyopathy Phenotype Revisited After 50 Years With Cardiovascular Magnetic Resonance. *Journal of the American College of Cardiology, 54*(3), 220-228. doi:10.1016/j.jacc.2009.05.006

Martinez-Moller, A., Souvatzoglou, M., Delso, G., Bundschuh, R. A., Chefd'hotel, C., Ziegler, S. I., . . . Nekolla, S. G. (2009). Tissue Classification as a Potential Approach for Attenuation Correction in Whole-Body PET/MRI: Evaluation with PET/CT Data. *Journal of Nuclear Medicine, 50*(4), 520-526. doi:10.2967/jnumed.108.054726

Martinez-Moller, A., Souvatzoglou, M., Navab, N., Schwaiger, M., & Nekolla, S. G. (2007). Artifacts from misaligned CT in cardiac perfusion PET/CT studies: Frequency, effects, and potential solutions. *Journal of Nuclear Medicine, 48*(2), 188-193.

Martinez-Moller, A., Zikic, D., Botnar, R. M., Bundschuh, R. A., Howe, W., Ziegler, S. I., . . . Nekolla, S. G. (2007). Dual cardiac-respiratory gated PET: implementation and results from a feasibility study. *European Journal of Nuclear Medicine and Molecular Imaging, 34*(9), 1447-1454. doi:10.1007/s00259-007-0374-9

McKenney-Drake, M. L., Territo, P. R., Salavati, A., Houshmand, S., Persohn, S., Liang, Y., . . . Sturek, M. (2016). 18F-NaF PET Imaging of Early Coronary Artery Calcification. *JACC: Cardiovascular Imaging, 9*(5), 627-628. doi:https://doi.org/10.1016/j.jcmg.2015.02.026

Memmott, M. J., Tonge, C. M., Saint, K. J., & Arumugam, P. (2018). Impact of pharmacological stress agent on patient motion during rubidium-82 myocardial perfusion PET/CT. *Journal of Nuclear Cardiology, 25*(4), 1286-1295. doi:10.1007/s12350-016-0767-x

Messika-Zeitoun, D., Aubry, M. C., Detaint, D., Bielak, L. F., Peyser, P. A., Sheedy, P. F., . . . Enriquez-Sarano, M. (2004). Evaluation and clinical implications of aortic valve calcification measured by electron-beam computed tomography. *Circulation, 110*(3), 356-362. doi:10.1161/01.cir.0000135469.82545.d0

Messroghli Daniel, R., Nordmeyer, S., Dietrich, T., Dirsch, O., Kaschina, E., Savvatis, K., . . . Kuehne, T. (2011). Assessment of Diffuse Myocardial Fibrosis in Rats Using Small-Animal Look-Locker Inversion Recovery T1 Mapping. *Circulation: Cardiovascular Imaging, 4*(6), 636-640. doi:10.1161/CIRCIMAGING.111.966796

Messroghli, D. R., Greiser, A., Frohlich, M., Dietz, R., & Schulz-Menger, J. (2007). Optimization and validation of a fully-integrated pulse sequence for modified look-locker inversion-recovery (MOLLI) T1 mapping of the heart. *Journal of Magnetic Resonance Imaging, 26*(4), 1081-1086. doi:10.1002/jmri.21119

Messroghli, D. R., Radjenovic, A., Kozerke, S., Higgins, D. M., Sivananthan, M. U., & Ridgway, J. P. (2004). Modified Look-Locker inversion recovery (MOLLI) for high-resolution T1 mapping of the heart. *Magnetic Resonance in Medicine, 52*(1), 141-146. doi:doi:10.1002/mrm.20110

Milano, A. D., Faggian, G., Dodonov, M., Golia, G., Tomezzoli, A., Bortolotti, U., & Mazzucco, A. (2012). Prognostic value of myocardial fibrosis in patients with severe aortic valve stenosis. *Journal of Thoracic and Cardiovascular Surgery, 144*(4), 830-837. doi:10.1016/j.jtcvs.2011.11.024

Min, J. K., Shaw, L. J., Devereux, R. B., Okin, P. M., Weinsaft, J. W., Russo, D. J., . . . Callister, T. Q. (2007). Prognostic Value of Multidetector Coronary Computed Tomographic Angiography for Prediction of All-Cause Mortality. *Journal of the American College of Cardiology, 50*(12), 1161-1170. doi:https://doi.org/10.1016/j.jacc.2007.03.067

Mitchell, A. M., Sackett, C. H., Hunzicker, W. J., & Levine, S. A. (1954). The clinical features of aortic stenosis. *American Heart Journal, 48*(5), 684-720. doi:https://doi.org/10.1016/0002-8703(54)90063-0

Mohler Emile, R., Gannon, F., Reynolds, C., Zimmerman, R., Keane Martin, G., & Kaplan Frederick, S. (2001). Bone Formation and Inflammation in Cardiac Valves. *Circulation, 103*(11), 1522-1528. doi:10.1161/01.CIR.103.11.1522

Montalvo, C., Villar, A. V., Merino, D., García, R., Ares, M., Llano, M., . . . Nistal, J. F. (2012). Androgens Contribute to Sex Differences in Myocardial Remodeling under Pressure Overload by a Mechanism Involving TGF-β. *Plos One, 7*(4), e35635. doi:10.1371/journal.pone.0035635

Moon, J. C., Messroghli, D. R., Kellman, P., Piechnik, S. K., Robson, M. D., Ugander, M., . . . Schelbert, E. B. (2013). Myocardial T1 mapping and extracellular volume quantification: a Society for Cardiovascular Magnetic Resonance (SCMR) and CMR Working Group of the European Society of Cardiology consensus statement. *Journal of Cardiovascular Magnetic Resonance, 15*(1), 92. doi:10.1186/1532-429x-15-92

Morris, J. J., Schaff, H. V., Mullany, C. J., Morris, P. B., Frye, R. L., & Orszulak, T. A. (1994). GENDER DIFFERENCES IN LEFT-VENTRICULAR FUNCTIONAL-RESPONSE TO AORTIC-VALVE REPLACEMENT. *Circulation, 90*(5), 183-189.

Motoyama, S., Ito, H., Sarai, M., Kondo, T., Kawai, H., Nagahara, Y., . . . Narula, J. (2015). Plaque Characterization by Coronary Computed Tomography Angiography and the Likelihood of Acute Coronary Events in Mid-Term Follow-Up. *Journal of the American College of Cardiology, 66*(4), 337-346. doi:https://doi.org/10.1016/j.jacc.2015.05.069

Myerson, S. G., Bellenger, N. G., & Pennell, D. J. (2002). Assessment of left ventricular mass by cardiovascular magnetic resonance. *Hypertension, 39*(3), 750-755. doi:10.1161/hy0302.104674

Nadjiri, J., Nieberler, H., Hendrich, E., Will, A., Pellegrini, C., Husser, O., . . . Hadamitzky, M. (2016). Prognostic value of T1-mapping in TAVR patients: extra-cellular volume as a possible predictor for peri- and post-TAVR adverse events. *International Journal of Cardiovascular Imaging, 32*(11), 1625-1633. doi:10.1007/s10554-016-0948-3

Nadra, I., Mason Justin, C., Philippidis, P., Florey, O., Smythe Cheryl, D. W., McCarthy Geraldine, M., . . . Haskard Dorian, O. (2005). Proinflammatory Activation of Macrophages by Basic Calcium Phosphate Crystals via Protein Kinase C and MAP Kinase Pathways. *Circulation Research, 96*(12), 1248-1256. doi:10.1161/01.RES.0000171451.88616.c2

Nagel, E., & Chandrashekhar, Y. (2018). Is it Time to Look Beyond the Valve and Ventricular Function for Assessing Patients With Aortic Stenosis? *Jacc-Cardiovascular Imaging, 11*(7), 1041-1043. doi:10.1016/j.jcmg.2018.06.001

Nehmeh, S. A., & Erdi, Y. E. (2008). Respiratory motion in positron emission tomography/computed tomography: A review. *Seminars in Nuclear Medicine, 38*(3), 167-176. doi:10.1053/j.semnuclmed.2008.01.002

Nekolla, S. G., Dinges, J., & Rischpler, C. (2013). Clinical Impact of Cardiac-Gated PET Imaging. *PET Clinics, 8*(1), 69-79. doi:10.1016/j.cpet.2012.10.002

Nensa, F., Bamberg, F., Rischpler, C., Menezes, L., Poeppel, T. D., la Fougere, C., . . . European Assoc Nucl Med, E. C. (2018). Hybrid cardiac imaging using PET/MRI: a joint position statement by the European Society of Cardiovascular Radiology (ESCR) and the European Association of Nuclear Medicine (EANM). *European Radiology, 28*(10), 4086-4101. doi:10.1007/s00330-017-5008-4

Nerlekar, N., Ha, F. J., Cheshire, C., Rashid, H., Cameron, J. D., Wong, D. T., . . . Brown, A. J. (2018). Computed Tomographic Coronary Angiography–Derived Plaque Characteristics Predict Major Adverse Cardiovascular Events. *Circulation: Cardiovascular Imaging, 11*(1), e006973. doi:doi:10.1161/CIRCIMAGING.117.006973

Neubauer, S., & Bull, S. (2017). Myocardial Fibrosis in Aortic Stenosis. *Jacc-Cardiovascular Imaging, 10*(11), 1334-1336. doi:10.1016/j.jcmg.2016.09.022

Nishimura Rick, A., Otto Catherine, M., Bonow Robert, O., Carabello Blase, A., Erwin John, P., Fleisher Lee, A., . . . Thompson, A. (2017). 2017 AHA/ACC Focused Update of the 2014

AHA/ACC Guideline for the Management of Patients With Valvular Heart Disease: A Report of the American College of Cardiology/American Heart Association Task Force on Clinical Practice Guidelines. *Circulation, 135*(25), e1159-e1195. doi:10.1161/CIR.0000000000000503

Nishiyama, Y., Yamamotoa, Y., Monden, T., Sasakawa, Y., Tsutsui, K., Wakabayashi, H., & Ohkawa, M. (2005). Evaluation of delayed additional FDG PET imaging in patients with pancreatic tumour. *Nuclear Medicine Communications, 26*(10), 893-899.

Nkomo, V. T., Gardin, J. M., Skelton, T. N., Gottdiener, J. S., Scott, C. G., & Enriquez-Sarano, M. (2006). Burden of valvular heart diseases: a population-based study. *The Lancet, 368*(9540), 1005-1011. doi:10.1016/S0140-6736(06)69208-8

Oliveira-Santos, M. d., Castelo-Branco, M., Silva, R., Gomes, A., Chichorro, N., Abrunhosa, A., . . . Ferreira, M. J. (2017). Atherosclerotic plaque metabolism in high cardiovascular risk subjects – A subclinical atherosclerosis imaging study with ¹⁸F-NaF PET-CT. *Atherosclerosis, 260*, 41-46. doi:10.1016/j.atherosclerosis.2017.03.014

Olivetti, G., Giordano, G., Corradi, D., Melissari, M., Lagrasta, C., Gambert, S. R., & Anversa, P. (1995). Gender differences and aging: Effects on the human heart. *Journal of the American College of Cardiology, 26*(4), 1068-1079. doi:https://doi.org/10.1016/0735-1097(95)00282-8

Onorati, F., D'Errigo, P., Barbanti, M., Rosato, S., Covello, R. D., Maraschini, A., . . . Grp, O. R. (2014). Different impact of sex on baseline characteristics and major periprocedural outcomes of transcatheter and surgical aortic valve interventions: Results of the multicenter Italian OBSERVANT Registry. *Journal of Thoracic and Cardiovascular Surgery, 147*(5), 1529-1539. doi:10.1016/j.jtcvs.2013.05.039

Orsinelli, D. A., Aurigemma, G. P., Battista, S., Krendel, S., & Gaasch, W. H. (1993). LEFT-VENTRICULAR HYPERTROPHY AND MORTALITY AFTER AORTIC-VALVE REPLACEMENT FOR AORTIC-STENOSIS - A HIGH-RISK SUBGROUP IDENTIFIED BY PREOPERATIVE RELATIVE WALL THICKNESS. *Journal of the American College of Cardiology, 22*(6), 1679-1683. doi:10.1016/0735-1097(93)90595-r

Osnabrugge, R. L. J., Mylotte, D., Head, S. J., Van Mieghem, N. M., Nkomo, V. T., LeReun, C. M., . . . Kappetein, A. P. (2013). Aortic Stenosis in the Elderly: Disease Prevalence and Number of Candidates for Transcatheter Aortic Valve Replacement: A Meta-Analysis and Modeling Study. *Journal of the American College of Cardiology, 62*(11), 1002-1012. doi:https://doi.org/10.1016/j.jacc.2013.05.015

Otto, C. M., Burwash, I. G., Legget, M. E., Munt, B. I., Fujioka, M., Healy, N. L., . . . Schwaegler, R. G. (1997). Prospective Study of Asymptomatic Valvular Aortic Stenosis. *Circulation, 95*(9), 2262-2270. doi:doi:10.1161/01.CIR.95.9.2262

Pan, T. S., Mawlawi, O., Luo, D., Liu, H. H., Chi, P. C. M., Mar, M. V., . . . Macapinlac, H. A. (2006). Attenuation correction of PET cardiac data with low-dose average CT in PET/CT. *Medical Physics, 33*(10), 3931-3938. doi:10.1118/1.2349843

Panza, J. A., & Maron, B. J. (1988). Valvular aortic stenosis and asymmetric septal hypertrophy - diagnostic considerations and clinical and therapeutic implications. *European Heart Journal, 9*, 71-76.

Patten, R. D., Pourati, I., Aronovitz, M. J., Baur, J., Celestin, F., Chen, X., . . . Karas, R. H. (2004). 17β-Estradiol Reduces Cardiomyocyte Apoptosis In Vivo and In Vitro via Activation of Phospho-Inositide-3 Kinase/Akt Signaling. *Circulation Research, 95*(7), 692-699. doi:doi:10.1161/01.RES.0000144126.57786.89

Pawade, T., Clavel, M. A., Tribouilloy, C., Dreyfus, J., Mathieu, T., Tastet, L., . . . Dweck, M. R. (2018). Computed Tomography Aortic Valve Calcium Scoring in Patients With Aortic

Stenosis. *Circulation-Cardiovascular Imaging, 11*(3). doi:10.1161/circimaging.117.007146

Pawade, T. A., Cartlidge, T. R. G., Jenkins, W. S. A., Adamson, P. D., Robson, P., Lucatelli, C., . . . Dweck, M. R. (2016). Optimization and Reproducibility of Aortic Valve 18F-Fluoride Positron Emission Tomography in Patients With Aortic Stenosis. *Circulation-Cardiovascular Imaging, 9*(10). doi:10.1161/circimaging.116.005131

Pawade, T. A., Newby, D. E., & Dweck, M. R. (2015). Calcification in Aortic Stenosis: The Skeleton Key. *Journal of the American College of Cardiology, 66*(5), 561-577. doi:https://doi.org/10.1016/j.jacc.2015.05.066

Pazhenkottil, A. P., Buechel, R. R., Nkoulou, R., Ghadri, J.-R., Herzog, B. A., Husmann, L., . . . Kaufmann, P. A. (2011). Left ventricular dyssynchrony assessment by phase analysis from gated PET-FDG scans. *Journal of Nuclear Cardiology, 18*(5), 920-925. doi:10.1007/s12350-011-9411-y

Pedram, A., Razandi, M., Narayanan, R., & Levin, E. R. (2016). Estrogen receptor beta signals to inhibition of cardiac fibrosis. *Molecular and Cellular Endocrinology, 434*, 57-68. doi:https://doi.org/10.1016/j.mce.2016.06.018

Pellikka, P. A., Sarano, M. E., Nishimura, R. A., Malouf, J. F., Bailey, K. R., Scott, C. G., . . . Tajik, A. J. (2005). Outcome of 622 adults with asymptomatic, hemodynamically significant aortic stenosis during prolonged follow-up. *Circulation, 111*(24), 3290-3295. doi:10.1161/circulationaha.104.495903

Petersen, S. E., Aung, N., Sanghvi, M. M., Zemrak, F., Fung, K., Paiva, J. M., . . . Neubauer, S. (2017). Reference ranges for cardiac structure and function using cardiovascular magnetic resonance (CMR) in Caucasians from the UK Biobank population cohort. *Journal of Cardiovascular Magnetic Resonance, 19*(1), 18. doi:10.1186/s12968-017-0327-9

Petrov, G., Dworatzek, E., Schulze, T. M., Dandel, M., Kararigas, G., Mahmoodzadeh, S., . . . Regitz-Zagrosek, V. (2014). Maladaptive Remodeling Is Associated With Impaired Survival in Women But Not in Men After Aortic Valve Replacement. *Jacc-Cardiovascular Imaging, 7*(11), 1073-1080. doi:10.1016/j.jcmg.2014.06.017

Piccinelli, M., Votaw, J. R., & Garcia, E. V. (2018). Motion Correction and Its Impact on Absolute Myocardial Blood Flow Measures with PET. *Current Cardiology Reports, 20*(5). doi:10.1007/s11886-018-0977-8

Piechnik, S. K., Ferreira, V. M., Dall'Armellina, E., Cochlin, L. E., Greiser, A., Neubauer, S., & Robson, M. D. (2010). Shortened Modified Look-Locker Inversion recovery (ShMOLLI) for clinical myocardial T1-mapping at 1.5 and 3 T within a 9 heartbeat breathhold. *Journal of cardiovascular magnetic resonance : official journal of the Society for Cardiovascular Magnetic Resonance, 12*(1), 69-69. doi:10.1186/1532-429X-12-69

Puntmann, V. O., Voigt, T., Chen, Z., Mayr, M., Karim, R., Rhode, K., . . . Nagel, E. (2013). Native T1 Mapping in Differentiation of Normal Myocardium From Diffuse Disease in Hypertrophic and Dilated Cardiomyopathy. *JACC: Cardiovascular Imaging, 6*(4), 475-484. doi:https://doi.org/10.1016/j.jcmg.2012.08.019

Quarto, C., Dweck, M. R., Murigu, T., Joshi, S., Melina, G., Angeloni, E., . . . Pepper, J. R. (2012). Late gadolinium enhancement as a potential marker of increased perioperative risk in aortic valve replacement. *Interactive Cardiovascular and Thoracic Surgery, 15*(1), 45-50. doi:10.1093/icvts/ivs098

Raggi, P., Pontone, G., & Andreini, D. (2018). Role of new imaging modalities in pursuit of the vulnerable plaque and the vulnerable patient. *International Journal of Cardiology, 250*, 278-283. doi:10.1016/j.ijcard.2017.10.046

Rahmim, A., Rousset, O., & Zaidi, H. (2007). Strategies for Motion Tracking and Correction in PET. *PET Clinics, 2*(2), 251-266. doi:10.1016/j.cpet.2007.08.002

Rajamannan, N. M., Subramaniam, M., Rickard, D., Stock, S. R., Donovan, J., Springett, M., . . . Spelsberg, T. (2003). Human aortic valve calcification is associated with an osteoblast phenotype. *Circulation, 107*(17), 2181-2184. doi:10.1161/01.CIR.0000070591.21548.69

Rajamannan, N. M., Subramaniam, M., Springett, M., Sebo, T. C., Niekrasz, M., McConnell, J. P., . . . Spelsberg, T. C. (2002). Atorvastatin inhibits hypercholesterolemia-induced cellular proliferation and bone matrix production in the rabbit aortic valve. *Circulation, 105*(22), 2660-2665.

Reis, S. E., Holubkov, R., Smith, A. J. C., Kelsey, S. F., Sharaf, B. L., Reichek, N., . . . Pepine, C. J. (2001). Coronary microvascular dysfunction is highly prevalent in women with chest pain in the absence of coronary artery disease: Results from the NHLBI WISE study. *American Heart Journal, 141*(5), 735-741. doi:https://doi.org/10.1067/mhj.2001.114198

Rieck, A. E., Cramariuc, D., Boman, K., Gohlke-Barwolf, C., Staal, E. M., Lonnebakken, M. T., . . . Gerdts, E. (2012). Hypertension in Aortic Stenosis Implications for Left Ventricular Structure and Cardiovascular Events. *Hypertension, 60*(1), 90-97. doi:10.1161/hypertensionaha.112.194878

Rohde, L. E. P., Zhi, G., Aranki, S. F., Beckel, N. E., Lee, R. T., & Reimold, S. C. (1997). Gender-associated differences in left ventricular geometry in patients with aortic valve disease and effect of distinct overload subsets. *American Journal of Cardiology, 80*(4), 475-480. doi:10.1016/s0002-9149(97)00398-6

Rosenhek, R., Klaar, U., Schemper, M., Scholten, C., Heger, M., Gabriel, H., . . . Baumgartner, H. (2004). Mild and moderate aortic stenosis - Natural history and risk stratification by echocardiography. *European Heart Journal, 25*(3), 199-205. doi:10.1016/j.ehj.2003.12.002

Rosenhek, R., Zilberszac, R., Schemper, M., Czerny, M., Mundigler, G., Graf, S., . . . Maurer, G. (2010). Natural History of Very Severe Aortic Stenosis. *Circulation, 121*(1), 151-156. doi:10.1161/circulationaha.109.894170

Rubeaux, M., Doris, M. K., Alessio, A., & Slomka, P. J. (2017). Enhancing Cardiac PET by Motion Correction Techniques. *Current Cardiology Reports, 19*(2). doi:10.1007/s11886-017-0825-2

Rubeaux, M., Joshi, N., Dweck, M. R., Fletcher, A., Motwani, M., Thomson, L. E., . . . Slomk, P. J. (2016). Demons versus Level-Set motion registration for coronary F-18-sodium fluoride PET. In M. A. Styner & E. D. Angelini (Eds.), *Medical Imaging 2016: Image Processing* (Vol. 9784).

Rubeaux, M., Joshi, N. V., Dweck, M. R., Fletcher, A., Motwani, M., Thomson, L. E., . . . Slomka, P. J. (2016). Motion Correction of F-18-NaF PET for Imaging Coronary Atherosclerotic Plaques. *Journal of Nuclear Medicine, 57*(1), 54-59. doi:10.2967/jnumed.115.162990

Rudd, J. H. F., Warburton, E. A., Fryer, T. D., Jones, H. A., Clark, J. C., Antoun, N., . . . Weissberg, P. L. (2002). Imaging atherosclerotic plaque inflammation with F-18 - fluorodeoxyglucose positron emission tomography. *Circulation, 105*(23), 2708-2711. doi:10.1161/01.cir.0000020548.60110.76

Satoh, M., Matter, C. M., Ogita, H., Takeshita, K., Wang, C.-Y., Dorn, G. W., 2nd, & Liao, J. K. (2007). Inhibition of apoptosis-regulated signaling kinase-1 and prevention of congestive heart failure by estrogen. *Circulation, 115*(25), 3197-3204. doi:10.1161/CIRCULATIONAHA.106.657981

Schulz-Menger, J., Bluemke, D. A., Bremerich, J., Flamm, S. D., Fogel, M. A., Friedrich, M. G., . . . Nagel, E. (2013). Standardized image interpretation and post processing in cardiovascular magnetic resonance: Society for Cardiovascular Magnetic Resonance (SCMR) board of trustees task force on standardized post processing. *Journal of cardiovascular magnetic resonance : official journal of the Society for Cardiovascular Magnetic Resonance, 15*(1), 35-35. doi:10.1186/1532-429X-15-35

Segall, G., Delbeke, D., Stabin, M. G., Even-Sapir, E., Fair, J., Sajdak, R., & Smith, G. T. (2010). SNM Practice Guideline for Sodium F-18-Fluoride PET/CT Bone Scans 1.0. *Journal of Nuclear Medicine, 51*(11), 1813-1820. doi:10.2967/jnumed.110.082263

Shah, A. S. V., Chin, C. W. L., Vassiliou, V., Cowell, S. J., Doris, M., Kwok, T. C., . . . Dweck, M. R. (2014). Left Ventricular Hypertrophy With Strain and Aortic Stenosis. *Circulation, 130*(18), 1607-+. doi:10.1161/circulationaha.114.011085

Shechter, G., Resar, J. R., & McVeigh, E. R. (2006). Displacement and velocity of the coronary arteries: Cardiac and respiratory motion. *Ieee Transactions on Medical Imaging, 25*(3), 369-375. doi:10.1109/tmi.2005.862752

Shirani, J., Pick, R., Roberts, W. C., & Maron, B. J. (2000). Morphology and significance of the left ventricular collagen network in young patients with hypertrophic cardiomyopathy and sudden cardiac death. *Journal of the American College of Cardiology, 35*(1), 36-44. doi:10.1016/s0735-1097(99)00492-1

Simard, L., Côté, N., Dagenais, F., Mathieu, P., Couture, C., Trahan, S., . . . Clavel, M.-A. (2017). Sex-Related Discordance Between Aortic Valve Calcification and Hemodynamic Severity of Aortic Stenosis. *Circulation Research, 120*(4), 681-691. doi:doi:10.1161/CIRCRESAHA.116.309306

Singh, A., Chan, D. C. S., Greenwood, J. P., Dawson, D. K., Sonecki, P., Hogrefe, K., . . . McCann, G. P. (2017). Symptom Onset in Aortic Stenosis. *Relation to Sex Differences in Left Ventricular Remodeling*. doi:10.1016/j.jcmg.2017.09.019

Singh, A., Horsfield, M. A., Bekele, S., Khan, J. N., Greiser, A., & McCann, G. P. (2015). Myocardial T1 and extracellular volume fraction measurement in asymptomatic patients with aortic stenosis: reproducibility and comparison with age-matched controls. *European Heart Journal - Cardiovascular Imaging, 16*(7), 763-770. doi:10.1093/ehjci/jev007

Slomka, P. J., Pan, T. S., Berman, D. S., & Germano, G. (2015). Advances in SPECT and PET Hardware. *Progress in Cardiovascular Diseases, 57*(6), 566-578. doi:10.1016/j.pcad.2015.02.002

Slomka, P. J., Rubeaux, M., Le Meunier, L., Dey, D., Lazewatsky, J. L., Pan, T., . . . Berman, D. S. (2015). Dual-Gated Motion-Frozen Cardiac PET with Flurpiridaz F 18. *Journal of Nuclear Medicine, 56*(12), 1876-1881. doi:10.2967/jnumed.115.164285

Stamou, S. C., Robich, M., Wolf, R. E., Lovett, A., Normand, S. L. T., & Sellke, F. W. (2012). Effects of gender and ethnicity on outcomes after aortic valve replacement. *Journal of Thoracic and Cardiovascular Surgery, 144*(2), 486-492. doi:10.1016/j.jtcvs.2011.11.023

Stuckey Daniel, J., McSweeney Sara, J., Thin May, Z., Habib, J., Price Anthony, N., Fiedler Lorna, R., . . . Schneider Michael, D. (2014). T1 Mapping Detects Pharmacological Retardation of Diffuse Cardiac Fibrosis in Mouse Pressure-Overload Hypertrophy. *Circulation: Cardiovascular Imaging, 7*(2), 240-249. doi:10.1161/CIRCIMAGING.113.000993

Tarkin, J. M., Joshi, F. R., Evans, N. R., Chowdhury, M. M., Figg, N. L., Shah, A. V., . . . Rudd, J. H. F. (2017). Detection of Atherosclerotic Inflammation by (68)Ga-DOTATATE PET Compared to [(18)F]FDG PET Imaging. *Journal of the American College of Cardiology, 69*(14), 1774-1791. doi:10.1016/j.jacc.2017.01.060

Taylor, A. J., Salerno, M., Dharmakumar, R., & Jerosch-Herold, M. (2016). T1 Mapping: Basic Techniques and Clinical Applications. *JACC: Cardiovascular Imaging, 9*(1), 67-81. doi:https://doi.org/10.1016/j.jcmg.2015.11.005

Teras, M., Kokki, T., Durand-Schaefer, N., Noponen, T., Pietila, M., Kiss, J., . . . Knuuti, J. (2010). Dual-gated cardiac PET-Clinical feasibility study. *European Journal of Nuclear Medicine and Molecular Imaging, 37*(3), 505-516. doi:10.1007/s00259-009-1252-4

Terpogossian, M. M., Bergmann, S. R., & Sobel, B. E. (1982). INFLUENCE OF CARDIAC AND RESPIRATORY MOTION ON TOMOGRAPHIC RECONSTRUCTIONS OF THE HEART - IMPLICATIONS FOR QUANTITATIVE NUCLEAR CARDIOLOGY. *Journal of Computer Assisted Tomography, 6*(6), 1148-1155. doi:10.1097/00004728-198212000-00016

Thaden, J. J., Nkomo, V. T., & Enriquez-Sarano, M. (2014). The Global Burden of Aortic Stenosis. *Progress in Cardiovascular Diseases, 56*(6), 565-571. doi:https://doi.org/10.1016/j.pcad.2014.02.006

Thie, J. A. (2004). Understanding the standardized uptake value, its methods, and implications for usage. *Journal of Nuclear Medicine, 45*(9), 1431-1434.

Thielemans, K., Schleyer, P., Marsden, P. K., Teuho, J., Teras, M., Bettinardi, V., . . . Ieee. (2014). *Data-driven Dual-gating for Cardiac PET*.

Thomas, G. S., & Haraszti, R. A. (2014). A new frontier in atherosclerotic coronary imaging. *Lancet, 383*(9918), 674-675. doi:10.1016/s0140-6736(13)61911-x

Treibel, T. A., Kozor, R., Fontana, M., Torlasco, C., Reant, P., Badiani, S., . . . Moon, J. C. (2018). Sex Dimorphism in the Myocardial Response to Aortic Stenosis. *Jacc-Cardiovascular Imaging, 11*(7), 962-973. doi:10.1016/j.jcmg.2017.08.025

Treibel, T. A., Lopez, B., Gonzalez, A., Menacho, K., Schofield, R. S., Ravassa, S., . . . Moon, J. C. (2018). Reappraising myocardial fibrosis in severe aortic stenosis: an invasive and non-invasive study in 133 patients. *European Heart Journal, 39*(8), 699-+. doi:10.1093/eurheartj/ehx353

Trivieri, M. G., Dweck, M. R., Abgral, R., Robson, P. M., Karakatsanis, N. A., Lala, A., . . . Fayad, Z. A. (2016). (18)F-Sodium Fluoride PET/MR for the Assessment of Cardiac Amyloidosis. *Journal of the American College of Cardiology, 68*(24), 2712-2714. doi:10.1016/j.jacc.2016.09.953

Turina, J., Hess, O., Sepulcri, F., & P Krayenbuehl, H. (1987). *Spontaneous course of aortic valve disease* (Vol. 8).

Tuseth, N., Cramariuc, D., Rieck, A. E., Wachtell, K., & Gerdts, E. (2010). Asymmetric septal hypertrophy - a marker of hypertension in aortic stenosis (a SEAS substudy). *Blood Pressure, 19*(3), 140-144. doi:10.3109/08037051.2010.481816

Ugander, M., Oki, A. J., Hsu, L.-Y., Kellman, P., Greiser, A., Aletras, A. H., . . . Arai, A. E. (2012). Extracellular volume imaging by magnetic resonance imaging provides insights into overt and sub-clinical myocardial pathology. *European Heart Journal, 33*(10), 1268-1278. doi:10.1093/eurheartj/ehr481

Vassiliou, V. S., Perperoglou, A., Raphael, C. E., Joshi, S., Malley, T., Everett, R., . . . Prasad, S. K. (2017). Midwall Fibrosis and 5-Year Outcome in Moderate and Severe Aortic Stenosis. *Journal of the American College of Cardiology, 69*(13), 1755-1756. doi:10.1016/j.jacc.2017.01.034

Vesey, A. T., Jenkins, W. S. A., Irkle, A., Moss, A., Sng, G., Forsythe, R. O., . . . Newby, D. E. (2017). F-18-Fluoride and F-18-Fluorodeoxyglucose Positron Emission Tomography After Transient Ischemic Attack or Minor Ischemic Stroke: Case-Control Study. *Circulation-Cardiovascular Imaging, 10*(3). doi:10.1161/circimaging.116.004976

Vigliano, C. A., Meckert, P. M. C., Diez, M., Favaloro, L. E., Cortes, C., Fazzi, L., . . . Laguens, R. P. (2011). Cardiomyocyte Hypertrophy, Oncosis, and Autophagic Vacuolization Predict Mortality in Idiopathic Dilated Cardiomyopathy With Advanced Heart Failure. *Journal of the American College of Cardiology, 57*(14), 1523-1531. doi:10.1016/j.jacc.2010.09.080

Villari, B., Campbell, S. E., Schneider, J., Vassalli, G., Chiariello, M., & Hess, O. M. (1995). SEX-DEPENDENT DIFFERENCES IN LEFT-VENTRICULAR FUNCTION AND STRUCTURE IN CHRONIC PRESSURE-OVERLOAD. *European Heart Journal, 16*(10), 1410-1419. doi:10.1093/oxfordjournals.eurheartj.a060749

Watt, A. H., & Routledge, P. A. (1985). ADENOSINE STIMULATES RESPIRATION IN MAN. *British Journal of Clinical Pharmacology, 20*(5), 503-506. doi:10.1111/j.1365-2125.1985.tb05108.x

Weber, K. T., Sun, Y., Bhattacharya, S. K., Ahokas, R. A., & Gerling, I. C. (2013). Myofibroblast-mediated mechanisms of pathological remodelling of the heart. *Nature reviews. Cardiology, 10*(1), 15-26. doi:10.1038/nrcardio.2012.158

Weber, W. A., Ziegler, S. I., Thödtmann, R., Hanauske, A.-R., & Schwaiger, M. (1999). Reproducibility of Metabolic Measurements in Malignant Tumors Using FDG PET. *Journal of Nuclear Medicine, 40*(11), 1771-1777.

Weidemann, F., Herrmann, S., Stork, S., Niemann, M., Frantz, S., Lange, V., . . . Strotmann, J. M. (2009). Impact of Myocardial Fibrosis in Patients With Symptomatic Severe Aortic Stenosis. *Circulation, 120*(7), 577-584. doi:10.1161/circulationaha.108.847772

Weinberg, E. O., Thienelt, C. D., Katz, S. E., Bartunek, J., Tajima, M., Rohrbach, S., . . . Lorell, B. H. (1999). Gender differences in molecular remodeling in pressure overload hypertrophy. *Journal of the American College of Cardiology, 34*(1), 264-273. doi:https://doi.org/10.1016/S0735-1097(99)00165-5

Weinheimer Carla, J., Kovacs, A., Evans, S., Matkovich Scot, J., Barger Philip, M., & Mann Douglas, L. (2018). Load-Dependent Changes in Left Ventricular Structure and Function in a Pathophysiologically Relevant Murine Model of Reversible Heart Failure. *Circulation: Heart Failure, 11*(5), e004351. doi:10.1161/CIRCHEARTFAILURE.117.004351

Weiss Robert, M., Ohashi, M., Miller Jordan, D., Young Stephen, G., & Heistad Donald, D. (2006). Calcific Aortic Valve Stenosis in Old Hypercholesterolemic Mice. *Circulation, 114*(19), 2065-2069. doi:10.1161/CIRCULATIONAHA.106.634139

Westermann, D., Lindner, D., Kasner, M., Zietsch, C., Savvatis, K., Escher, F., . . . Tschöpe, C. (2011). Cardiac Inflammation Contributes to Changes in the Extracellular Matrix in Patients With Heart Failure and Normal Ejection Fraction. *Circulation: Heart Failure, 4*(1), 44-52. doi:doi:10.1161/CIRCHEARTFAILURE.109.931451

Wong, T. C., Piehler, K., Meier, C. G., Testa, S. M., Klock, A. M., Aneizi, A. A., . . . Schelbert, E. B. (2012). Association between extracellular matrix expansion quantified by cardiovascular magnetic resonance and short-term mortality. *Circulation, 126*(10), 1206-1216. doi:10.1161/CIRCULATIONAHA.111.089409

Wong, T. C., Piehler, K. M., Kang, I. A., Kadakkal, A., Kellman, P., Schwartzman, D. S., . . . Schelbert, E. B. (2014). Myocardial extracellular volume fraction quantified by cardiovascular magnetic resonance is increased in diabetes and associated with mortality and incident heart failure admission. *European Heart Journal, 35*(10), 657-664. doi:10.1093/eurheartj/eht193

Zhu, D. X., Hadoke, P. W. F., Wu, J. X., Vesey, A. T., Lerman, D. A., Dweck, M. R., . . . MacRae, V. E. (2016). Ablation of the androgen receptor from vascular smooth muscle cells

demonstrates a role for testosterone in vascular calcification. *Scientific Reports, 6*. doi:10.1038/srep24807